

A Platform for High-Speed Biomechanical Analysis Using Wearable Wireless Sensors

by

Michael T Lapinski

S.M., Massachusetts Institute of Technology (2008)

M.S., Rensselaer Polytechnic Institute(2002)

B.S., Rensselaer Polytechnic Institute(2000)

Submitted to the Program in Media Arts and Sciences,
School of Architecture and Planning,
in partial fulfillment of the requirements for the degree of
Doctor of Philosophy in Media Arts and Sciences

at the

MASSACHUSETTS INSTITUTE OF TECHNOLOGY

September 2013

© Massachusetts Institute of Technology 2013. All rights reserved.


Signature redacted

Author

Program in Media Arts and Sciences

August 9, 2013


Signature redacted

Certified by



Joseph A. Paradiso
Associate Professor of Media Arts and Sciences

MIT Media Lab

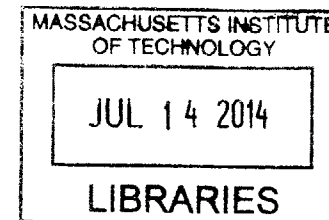
Thesis Supervisor


Signature redacted

Accepted by


Prof. Patricia Maes
Associate Academic Head
Program in Media Arts and Sciences

ARCHIVES



A Platform for High-Speed Biomechanical Analysis Using Wearable Wireless Sensors

by

Michael T Lapinski

Submitted to the Program in Media Arts and Sciences,
School of Architecture and Planning, on August 9, 2013
in partial fulfillment of the requirements for the degree of
Doctor of Philosophy in Media Arts and Sciences

Abstract

Humanity's desire to capture and understand motion started in 1878 and has continually evolved. Today, the best-of-breed technology for capturing motion are marker based optical systems that leverage high speed cameras. While these systems are excellent at providing positional information, they suffer from an innate inability to accurately provide fundamental parameters such as velocity and acceleration. The problem is further compounded when the target of capture is high-speed human motion. When applied to biomechanical study, this inaccuracy is magnified when higher order parameters, such as torque and force, are calculated using optical information.

This dissertation presents a first-of-its-kind wearable dual-range inertial sensor platform that allows end-to-end investigation of high level biomechanical parameters. The platform takes a novel approach by providing these parameters more accurately and at a higher fidelity than the current state of the art. The dual-range sensing approach allows accurate capture of both slow-moving motion and rapid movement which pushes the limits of human ability. The platform addresses inherent problems with scaling clinical biomechanical analysis to tens-of-thousands of trials using the sensor platform's data. This end-to-end approach provides mechanisms for rapid player instrumentation, en masse data translation and calculation of clinically relevant joint forces and torques. I present design details for this platform along with kinematic testing and some early biomechanical insight gleaned from system measurements.

Thesis Supervisor: Joseph A. Paradiso

Title: Associate Professor, Program in Media Arts and Sciences

**A Platform for High-Speed Biomechanical Analysis Using Wearable Wireless
Sensors**

by

Michael T Lapinski

The following people served as readers for this thesis:

Thesis Reader Signature redacted

Thomas M. Kepple
Chief Science Officer
C-Motion, Incorporated

Thesis Reader Signature redacted

Dr. Eric Berkson
Director, Mass General Orthopedics Sports Performance Center
Assistant in Orthopedic Surgery
Massachusetts General Hospital
Instructor
Harvard School of Medicine

Acknowledgments

Asia for all of the support and everything else that you know you did along the way.

Mom and Dad, looks like I will end up in San Francisco anyway, but not as a pro skateboarder living in a cardboard box like I promised 18 years ago...

The entire Responsive Environments group. The nerds who taught me so much and helped me unlock the magic of those little black chips on that are found on circuit boards and helping me create my own magic, especially Mat Laibowitz. Without your guidance I probably wouldn't have finished this thing.

Brian Mayton for the analog and digital separation of powers and grounds and all the great advice along the way. Your patience with clowns like me guarantees you will be a great professor someday.

Matt Aldrich for all of the math help and guidance. Also for 4 years of putting up with the Slayer, tupperwares, speaker phone and other countless annoying things.

Nan-Wei, just for being Nan-Wei.

Matt Xmal, whose words "voltage is like water" stick with me to this day.

Mark Feldmeier, I suspect you and your pile will never disappear from the lab and it makes me smile.

Tom Kepple, the shining beacon of light who taught me more about motion capture in half a year than I figured out on my own in 5 years. Your insight, timeliness and guidance were invaluable.

Eric, for expecting more from me than I thought I was capable of, the shoulder and knee surgeries and direction along this 7 year trip.

John Geen @ Analog Devices, you know much more about MEMs than I ever will, but had no problem sharing some of that knowledge with me.

Analog Devices and Grace Pigott and John Memishiam, for all the free gyros, accelerometers and connections to the people in the know.

Steve Buckley from Corflex, the neoprene attachment system still lives and will live for a long time to come.

Sean Driscoll, its in there and up to you to find it.

Clemens, Why that?

Donna and Hollie for the time in the sport performance lab and all of the help.

Linda P, you are the bestest and that's it.

Cornelle King and Kevin Davis, you guys are waaaay under appreciated. I appreciate everything you guys do to keep the media lab going.

To all my sponsors that kept me racing:

- The MIT GSC
- Colleen Asch at Asterisk
- Richard Basinger at Yoshimura
- Steve-O, Zak and Ziggy at Factory Connection
- Devin Leblanc from MSR and Pro Taper
- Tim Sprague from S4MX
- Rich Taylor at EKS Brand goggles
- Ryan at Works Connection
- Dunlop Tires
- Acerbis Plastics
- Gaerne Boots
- Leatt Brace for keeping my neck in one piece
- Magura Clutches

CONTENTS



he end of the beginning or the beginning of the
end?

The *Contents* chapter contains the spoilers, in other words
the Table of Contents and List of Figures.

TABLE OF CONTENTS

Contents	9
Table of Contents	10
Chapter 1 - Introduction	17
1.1.1 A Few Words on Biomechanics	19
1.1.2 Optical System Synopsis	19
1.2 Consumers of Sensor Fruit [Motivations]	20
1.2.1 Injury Mechanisms	23
1.2.2 Motivations for Using Inertial Sensors	24
1.3 Research Guidelines	25
1.3.1 Hardware Guidelines	26
1.3.2 Data Management Guidelines	27
1.3.3 Data Processing Fundamentals	28
1.3.4 Biomechanically Relevant Data Processing	29
Chapter 2 - Prologue	31
2.1 Related Work	32
2.1.1 Motion Capture Systems	32
2.1.2 Marker Based Optical Trackers	35
2.1.2.1 Active Systems	35
2.1.2.2 Semi-Passive Systems	36
2.1.2.3 Fully Passive Systems	37
2.1.3 Inertial Systems for Motion Capture	37
2.1.4 Current Pitcher Development	39
2.1.5 Precision of Biomechanical Research	40
2.1.5.1 Tracking Marker and the Underlying Skeleton	41
2.1.5.2 Marker Set Used	42

2.1.5.3 Position and Orientation Calculation Methods.....42
2.1.5.4 Inertial Parameter Estimation43

Chapter 3 - Taxonomy, High Level Architecture & Kinetic Model45

3.1 Taxonomy 46
3.1.0.1 Player46
3.1.0.2 Session47
3.1.0.3 Gesture.....49
3.1.0.4 Purposes of Player and Gesture Annotation50
3.2 System Architecture..... 51
3.2.1 Field Deployment.....51
3.2.2 μ SD Data Retrieval Interface52
3.2.3 Data Import Engine52
3.2.4 Visualization, Analysis and Modeling54
3.3 Physical (Kinematic) Model 54
3.3.1 Coordinate Systems.....54
3.3.2 Landmark Definition55
3.3.3 Segment Definition56
3.3.4 Joint Definition.....58
3.3.5 Performing the Kinematics.....59
3.4 Kinetic Model 59

Chapter 4 - The Tangible61

4.1 Wireless Inertial Measurement Node..... 62
4.1.1 Main Board.....63
4.1.2 Inertial High Range Daughterboards.....65
4.1.3 Wireless Expansion Board65
4.1.4 Putting It All Together66
4.1.5 System Evolution68
4.2 Calibration..... 69

4.2.1	Rotation Based Calibration	70
4.2.1.1	Gyroscopes.....	70
4.2.1.2	Accelerometers	71
4.2.2	Calibration Rig	75
4.2.2.1	Motor and Controller	77
4.2.2.2	Motor Containment.....	78
4.2.2.3	Per Axis Node Motor Attachment	79
4.2.3	Calibration Process.....	80
4.2.4	Calibration Results	81
4.3	Network Control Basestation	83
4.3.1	Optical System Synchronization	84
4.4	Data Translator.....	85

Chapter 5 - The Intangible87

5.1	Basestation	88
5.1.1	Optical System Synchronization	93
5.2	Node Startup.....	95
5.2.1	Flash Memory	97
5.2.2	Error Handling Subsystem	97
5.2.3	Clocks and Peripheral Bus	98
5.2.4	Communication Peripherals	98
5.2.5	Hardware Devices	100
5.2.5.1	μSD Card	100
5.2.5.2	High Range Gyroscopes	100
5.2.5.3	High Range Accelerometer.....	100
5.2.5.4	Analog-to-Digital Converter.....	101
5.2.5.5	Low Range Gyroscope.....	102
5.2.5.6	Low Range Accelerometer	102
5.2.5.7	Magnetometer	103
5.2.5.8	RF Transceiver.....	103
5.3	Node Operation	104
5.3.0.1	Error Commands.....	104
5.3.0.2	Idle Command.....	105
5.3.0.3	Next Packet Command	105

5.3.0.4	Erase Flash Command	105
5.3.0.5	Sample to Flash Command	105
5.3.0.6	Pseudo-Command Continuous Mode	107
5.3.0.7	Sample Count Command	108
5.3.0.8	Get Filename Command	108
5.4	Data Translator	109

Chapter 6 - Tangible Intangibles111

6.1	Network Control Application.....	112
6.1.1	USB Connection.....	114
6.1.2	Network Configuration	114
6.1.3	Erasing Flash	115
6.1.4	Sampling Gesture Data.....	115
6.1.5	Continuous Sampling	116
6.1.6	Error Management.....	116
6.1.7	Reading Node Contents.....	117
6.1.8	Optical System Synchronization	117
6.2	Data Translation Application	117
6.2.1	USB Connection.....	119
6.2.2	Translating Data	120
6.3	Data Model.....	123
6.3.1	Player Data Model.....	125
6.3.2	Session Data Model.....	127
6.3.3	Gesture Data Model	127
6.3.4	Node Data Model	130
6.3.5	Visual3D Data Model.....	132
6.4	Data Processing and Import Application - Operator View..	134
6.4.1	Database Connectivity.....	134
6.4.2	Player Management.....	136
6.4.3	Session Management.....	138
6.4.4	Gesture Handling.....	138

6.4.4.1	Gesture Import Process	139
6.4.4.2	Gesture Annotation and Management	141
6.4.5	Miscellaneous Operator Features	143
6.5	Data Processing and Import Application - User View	145

Chapter 7 - Experimental Methods147

7.1	Body Attachment	148
7.1.1	2009	148
7.1.2	2010	153
7.2	Pitching Protocol	160
7.3	Batting Protocol	163
7.3.1	Directed Batting Protocol	163
7.3.2	Batting Practice Protocol	168
7.4	Dual System Experiments	169
7.5	Data Translation and Annotation	170
7.5.1	Pitch Annotation	172
7.5.2	Swing Annotation	173
7.5.3	Dual System Annotation	174

Chapter 8 - Validation and Error Sources175


8.1	Error Quantification	176
8.1.1	Calibration	176
8.1.2	Application (Coordinate System Misalignment)	179
8.1.3	Soft Tissue Artifacts	180
8.1.4	Acceleration Induced Gyroscope Error	184
8.2	System Validation	186
8.2.1	The Inertial Gold Standard	188
8.2.2	The Eyeball Comparison	192
8.2.3	Angular Velocity Comparison	196
8.2.4	Angular Acceleration and Deceleration	200

Chapter 9 - Analytics and Biomechanical Metrics ... 203

9.1	Data Processing Fundamentals	204
9.2	Data Viewing	206
9.3	Segment Gesture Statistics.....	210
9.3.1	Gesture Duration Determination	210
9.3.2	Individual Segment Analysis	211
9.3.3	Inter-Segment Timing	212
9.3.4	Segment Velocity Estimation.....	212
9.4	Session Aggregation and Statistics	215
9.4.1	Session Stat Sheet	215
9.4.2	Segment Timing Analysis Application	218
9.5	Like Modality Sensor Fusion.....	221
9.6	Biomechanical Metrics	225
9.6.1	Jerk	226
9.6.2	Shoulder Distraction Jerk	231
9.6.3	Shoulder Internal and External Rotation Acceleration	232
9.7	Calculation of Kinetics and Dynamics.....	237
9.7.1	Visual3D Integration	237
9.7.2	Example Data	240
9.7.3	Shoulder Distraction and Compression Forces	246
9.7.4	Elbow Valgus and Varus Torque	249
9.7.5	The Fine Print.....	253

Chapter 10 - Contributions & Conclusions255

10.1	Contributions.....	256
10.2	Future Work	258
10.2.1	Differentiation Between Real Motion & Soft Tissue Artifacts....	258



10.2.2	Coordinate System Alignment Protocols	258
10.2.3	Joint Angles.....	259
10.2.4	Lower Cost Hybrid Systems	260
10.2.5	Continued Data Acquisition.....	261

References	263
------------------	-----

INTRODUCTION

It's not going to write itself.

- Michael Lapinski

Here we set the stage and lead the reader into what the entire body of work will be about.

1.1 A SEASON FOR SENSING

Whether you know it or not, you don't have to look further than your pocket to find a device that is capable of tracking you and providing a complete description of everything you have done today, how fast you have done it and can nearly predict what you will do tomorrow.

From the large seeds of early sensor systems a new generation of miniature sensor sprouts has grown (FIGURE 1-1, FIGURE 1-2). This miniaturization is the first step in the explosion of the once cumbersome science of sensing morphing to a level where integration of modalities has become so pervasive that most people aren't aware they are using them.

Trivial exploitation of this integration permits realization of new methods of human interaction with everyday objects that contain sensors [1]. Further, they allow these objects to behave in a smarter manner to ease the cumbersome task of knowing how to properly interact with them. An excellent example of this is managing the content displayed on any screen-equipped device using a two axis accelerometer that determines tilt. This behavior, along with other commonplace features, has transitioned from state-of-the-art and novel to being the norm and is expected to be ubiquitous. Our sensor sprouts have grown roots in our everyday devices and are now looking to start growing upwards by providing data to create more complex orchestrations of contextual awareness.

A more advanced exploitation of sensed data reaches towards tracking finer grains than those of an entire human body, allowing individual body segments to be precisely tracked and studied. Most existing systems [2][3][4][5][6] are only capable of recording relatively slow motion that doesn't exceed a slow jog. Regardless, the metaphorical stem is strong and its bud has gotten fuller.



FIGURE 1-1 Invensense IMU-3000 3-Axis Gyroscopes (2012)

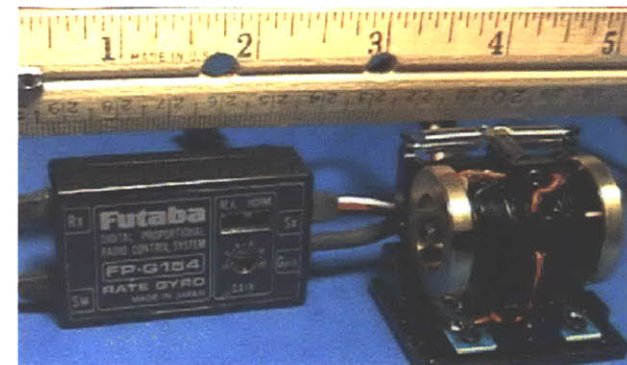


FIGURE 1-2 Futaba FP-G154 Single Axis Gyroscope (Circa 1990)

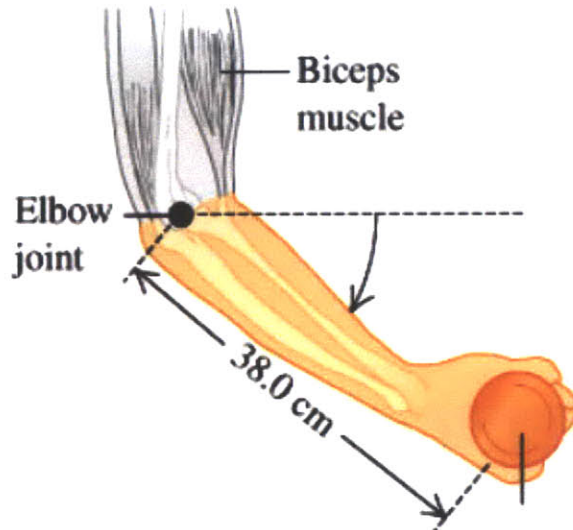


Figure 1-3 Elbow Joint Musculoskeletal System

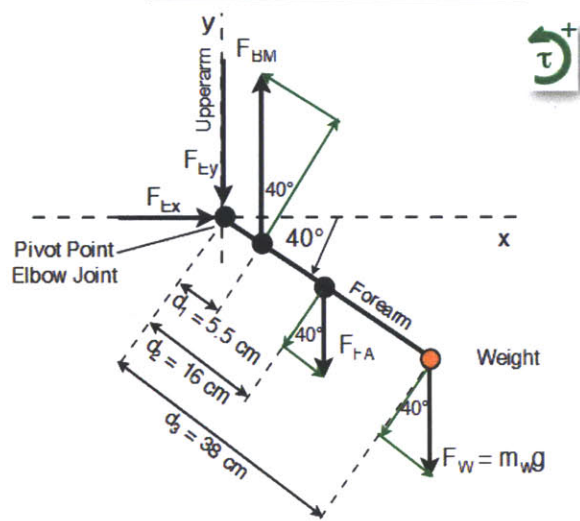


FIGURE 1-4 Mechanical Free Body Diagram for the same elbow joint.

We have reached the point or where this bud wants to blossom into a fully featured sensor “fruit” that is capable of tracking the most extreme motions that a human can perform.

1.1.1 A Few Words on Biomechanics

Biomechanics focuses on applying mechanical principals (FIGURE 1-4) to biological systems (Figure 1-3), and research in this field is the driving force in helping coaches, doctors, trainers and therapists understand both how the body moves and the good or bad forces associated with specific motion. Questions that arise are those seeking to characterize the stresses on given joints[11], bones[12], ligaments and muscles during various activities of daily living; these range from sitting in a chair to walking (gait) to running and playing sports. An important question (Q1) that is asked is what is the magnitude of the load on specific tissues during any of these activities? Another is; (Q2) Given that these activities will be performed regardless of risk, professionally or as a leisure activity, can it be determined if there are factors in mechanics and technique that result in potentially less damaging loads on the body? Further questions seek to assess the effectiveness of rehabilitation, the quality of surgical reconstruction and athletic performance.

The first (Q1) is answered by creating a model of the specific joint, ligament or muscular system and performing a biomechanical analysis based on given input forces and the resulting motion. The second (Q2) is answered by applying the model to a variety of trials taken from a representative population of test subjects. These techniques can be considered a method of preparing freshly harvested “fruit”, and a good recipe yields good results.

1.1.2 Optical System Synopsis

At its root, the concept of the optical capture system is simple; a more in-depth examination is presented in the Section 2.1.2. Early systems, such is the

Vanguard Motion Analyzer (FIGURE 1-5), enabled measurement of angles between body segments based on film projected on a screen, without any on-body markers. Currently, the most common system is based on a combination of strobing lights and cameras that work in unison to capture frames of data that show the positions of optical markers illuminated by the pulses of light. This data, taken from several different camera angles (20 or more for high speed motion), is reconstructed to build a three dimensional path for each of the markers. The paths of several markers can be combined to represent segments and joints of the human body, allowing for tracking individual and relative positions of body segments. The first derivative of segment or marker position provides velocity and a second order derivative provides acceleration. This positional, velocity and acceleration data is used to drive biomechanical models and study motion. An optical system is simply a different method of sowing, tending and reaping metaphorical fruit to be cooked, perhaps to be considered organic vs fertilized farming.

1.2 CONSUMERS OF SENSOR FRUIT [MOTIVATIONS]

Medical professionals performing biomechanical research and professional athletes, including their coaches, looking for a competitive edge are eager consumers of the fruits of wearable wireless sensing platforms.

Biomechanical analysis of fast-moving athletes has historically been performed using optical video capture systems that were hand digitized into stick figure representations frame by frame . These have evolved into passive marker based systems that reconstruct the paths of markers to generate a three

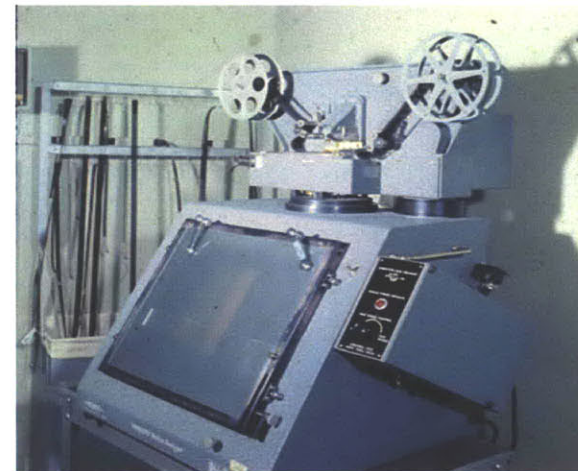


**FIGURE 1-5 Vanguard Motion Analyzer
Manual Digitization Platform (circa 1971)**

dimensional representation of the motion that occurred [8][9][10]. While these systems are excellent at creating 3D images, they are lacking in the ability to accurately provide accelerations and angular velocities; Section 2.1.5 discusses this in detail. These are the starting points of any serious biomechanical analysis that wishes to assess the dynamics and calculate the forces and torques experienced by the body during high speed activity.

Meeting the need of directly obtaining the fundamental parameters to build the better biomechanical model independent of a lab-situated optical tracker is one of two primary motivations of this dissertation.

This concept is not new and was partially addressed by this author's Master's Thesis [7] which had a similar philosophy but did not fully realize an end-to-end system:

“A better understanding of the forces, torques and speeds enables the creation of precise biomechanical model of, for example, the shoulder and elbow. Using these models to understand the difference between proper and improper motion would give athletes the opportunity to avoid getting injured and coaches the ability to train athletes with techniques that avoid injury. Further, if there is a patient history of such motion in existence, it would be possible for physical and occupational therapists to better help athletes by refining rehabilitation protocols that accurately define the forces and torques on a body segment over time.

Even further, a system such as this can recognize that an athlete is beginning to fatigue and is in danger of injuring themselves. If this can be recognized, then the athlete can be advised as to what motion is 'safer' or be advised to stop the activity, thus avoiding injury. Another step further, if athletes can be characterized and compared in a scientific manner, it is then possible to recognize traits which lead to better performance, hence such data could act as an aid in selecting up and coming athletes.”

Further discussion of motivations to use inertial sensors appears in Section 1.2.2. After realization of such a tool, there is a final motivation, to determine if the tool fits the job. There are two avenues that must be followed. The first is to compare the outputs of the sensor-based system to the current “gold standard”, an optical tracker. By comparing the two, optical and sensor, it will be possible to quantify the strengths and weaknesses of each. The second is to apply the system to athletes and use its data to generate meaningful and useful results that can be used in real-world clinical research.

Complete implementation, validation and proof of concept application of such a system is the first step in changing the way that clinical research is performed by taking it from the laboratory to the athletes’ native environment, the playing field. It should be considered as a tool available to researchers, not an answer to a single research question.

Further, it is also the first step in allowing coaches and trainers to change the archaic paradigm of how athletes are developed. While there exist documented techniques for developing overhead throwing athletes [13][14], coaching is traditionally very similar to the art of ancient storytelling. Knowledge of the correct techniques and what is thought to be the proper motion has been passed down from coach to player and player to coach by word of mouth generation after generation. Again, a system such as this would be the tool that would be used to prove or disprove specific training and coaching myths in a quantitative manner without a singular answer.

Lastly, this dissertation and its models focus on baseball players and examining the motion of the upper body because they truly push the limits of what the human body can do. In principal, such a system could be applied to any sport or any athlete anywhere in the world; the only thing that is necessary is the appropriate biomechanical model to interpret and analyze the data.

1.2.1 Injury Mechanisms

Most injury can be divided into two categories: acute injury and repetitive microtrauma. A torn Anterior Cruciate Ligament (ACL) from falling off of a ladder falls into the first and a torn ulnar collateral ligament from baseball pitching into the second. It is possible to study acute trauma, however this research focuses on repetitive microtrauma because of the science behind it, the questions it leads to, together with its huge relevance to sports. Repetitive microtrauma is defined as submaximal loading of the soft tissues. It often leads to cumulative microtrauma and eventual tissue failure. A good analogy in understanding repetitive microtrauma is to consider a rope. If you consistently yank the rope close to the point of it ripping, it will fatigue and eventually fail. This yanking is analogous to submaximal loading of the soft tissue. If tissue is constantly submaximally loaded, it will eventually fail. A specific milestone of this dissertation's research is to gather more accurate data that is representative of this loading, thus allowing researchers to better understand the damage occurring using techniques discussed above. This allows for measurement of ongoing injury and allows prediction of future injury.

This research focuses on the overhead throwing athlete, specifically professional baseball pitchers, and the swinging athlete, professional baseball batters. The primary reason for targeting these athletes is that their motion pushes the limits of what the human body can do; throwing a baseball at 100MPH or hitting a baseball 410 feet over the green monster (a huge wall at the furthest point of the outfield in Boston's Fenway Park) puts extreme forces on an athlete's body and musculoskeletal system. Relatively easy access to professional players via an existing research collaboration with Massachusetts General Hospital (MGH) and a major league baseball team also plays a factor in focusing on these target subjects.

A factor in allowing these athletes to perform at such a high level repeatedly and consistently is the mechanics, or technique, that they have developed over time. Given a large dataset over several players, it is important to determine what it is in the mechanics of an elite player that differentiates them from others.

1.2.2 Motivations for Using Inertial Sensors

A brief glance at the specifications of the most ubiquitous optical tracker shows that it has the capability to capture frame rates as high as 2000 frames per second (FPS) [8] with the caveat that as frame rate increases the capture volume decreases. The Qualisys Oqus camera is capable of 10,000FPS at a 4MPixel resolution, but with a reduced field of view. The field of view is not defined in their product literature, so this is not considered in the graph presented in **FIGURE 1-6**. There is a natural trade-off between camera fidelity and capture rate. In practice for extreme activity, such as baseball pitching, the frame rates that are used are in between 180 and 360 FPS. These capabilities are ideal for capturing motion that is not extreme in nature (i.e. walking, jogging) and for examining high level body segment positioning.

However, when the studied activity begins to push the limits of the human body and researchers seek to accurately and precisely measure not only segment positions, but also the forces involved, optical systems fall short. Further, optical systems require considerable time to set up and calibrate, take up a large dedicated area, cannot be trivially moved, and are sensitive to background IR light and reflections.

This research takes a different approach to capturing motion, utilizing an array of wearable wireless inertial sensors, and seeks to enable researchers to more precisely measure any motion of any athlete in their native environment.

There are several advantages to using inertial sensors. First, optical information must be doubly differentiated in order to obtain acceleration data,

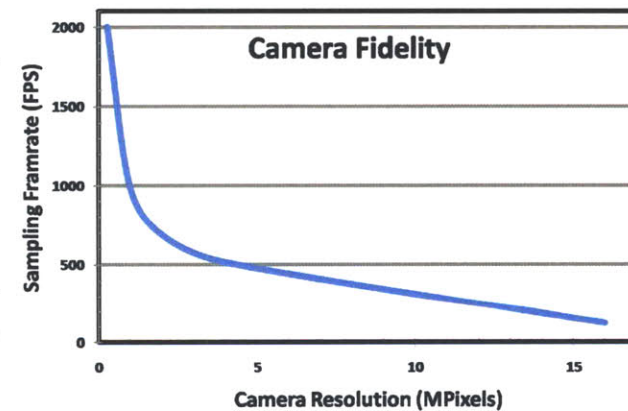


FIGURE 1-6 Frame rate is at best inversely proportional to the size of the capture volume. This is not ideal for sports, which require both high frame rates and a large capture volume.

hence any high frequency noise present in the data stream will be heavily magnified. In the case of inertial sensors, they are actually measuring the accelerations and angular velocities that are occurring (which are proportional to the induced forces) and each sensor is precisely calibrated. There is no differentiation necessary to obtain the desired measurements. The second major advantage is that a wearable system is extremely portable and can be applied wherever activity is occurring, in contrast to optical systems which require that the activity be brought into a controlled lab environment. Lastly, the maximum effective sampling rate for analog inertial sensors is strictly limited by the speed at which their output can be stored along with their intrinsic analog bandwidth. The latest generation of my inertial system is capable of sampling rates of 2 kilohertz or more, which ensures that fast changes in the studied motion will not be missed.

The study of human motion is nothing new and the de facto technology used to do this is well equipped to enable examination of most physical activity. When the activity begins to push the limits of human capability, the available systems fall short. This work seeks to apply wearable wireless inertial sensing technology, paired with massive data storage and high sampling rates, as a replacement or complementary tool to enable medical professionals to more accurately and precisely conduct research.

1.3 RESEARCH GUIDELINES

In order to build something it is always necessary to have some high-level goals and vision for how the system should behave and what it should consist of. These research guidelines drive what the system is and more importantly what the system is not.

1.3.1 Hardware Guidelines

The logical place to start is the hardware that generates the data. Its criteria are:

- 1 Mobile - The system should be capable of being applied and recording data anywhere that athletes train and play. The system should seamlessly integrate with the athlete's daily activities, rather than the athlete fit their activities to the system.
- 2 Wearable - The sensing nodes should be easily and quickly attached to the body. Fairly obvious, yet crucially important. Comfort and placement point stability against inertial forces are all important when attaching nodes.
- 3 Wireless - There should be no wires to link the nodes. Wires are undesirable because they impede motion and make the system more of a suit than a set of small wearable devices.
- 4 Rich with Sensing Modalities - Both high range and low range gyroscopes and accelerometers should be present on all three axes of sensing to measure inertial parameters. Additionally, a three-axis magnetometer is needed in order to calculate orientation of each node.
- 5 Synchronized - Data streams for each sensing axis intra-node should be synchronized. Data streams between each worn node should also be synchronized. Additionally, the system should be capable of synchronizing with other systems, such as optical ones with a minimum accuracy of within $\pm 5\text{ms}$ to adequately compare features from both data streams.
- 6 Large Data Storage - As a single node may be used on several players for tens of minutes each, there should be enough space to store at least this amount of data.

- 7 Fast Sampling - In order to capture all the information possible, fast sampling, 1 kilohertz or more, is necessary. From previous experience, well defined peaks can be observed at this rate.
- 8 Precision - The data from each sensed axis should be translated from unitless analog signals to real world inertial and magnetic heading parameters. This requires a rigorous calibration.
- 9 Command and Control - A network is nothing if you cannot control its behavior. There should be a mechanism for issuing commands that govern the behavior of nodes attached to the body.

1.3.2 Data Management Guidelines

With a set of hardware that can fulfill these functions, the amount of data that is generated grows very quickly. For example, a 5 node network sampling on 3 axes at 1 kilohertz yields about 15,000 variable-size (12-16 bit) data points per second. ¹

¹The system described above needs to sample 12 discrete axes.

Further, each group of nodes will record several hundred 5 second to 8 second sets of data. Simple probability leads to the conclusion that a once the hardware problem is addressed a new problem emerges, stressing the data management protocol. Fundamental needs that must be met to manage this large amount of data are:

- 1 Security is Paramount - Per IRB and the MIT Committee on Use of Humans as Experimental Subjects. All data must be stored in a secure manner with authorization and authentication in order to access it. Further, as this technology is applied to health and injury questions, biomechanics data becomes a measure of one's health and may be subject to HIPPA requirements as well.
- 2 Identifiable - Each sensed axis must be identifiable and be linked to the node and identifiable as coming from that node. Each group of nodes must be linked to the athlete that was wearing them when data was

recorded. Individual motions must also be discretely defined to allow for creation of metadata for each motion.

- 3 Metadata - Necessary metadata must also be stored and linked to a given data stream from a node and group of nodes. This includes anthropometric data, measurements of where nodes were placed, information regarding classification of different motions
- 4 Selectable - based on the identifiable traits, there must be a mechanism to query and select individual data streams en masse or individually.
- 5 Calibratable² - all calibrated data must adhere to the above 4 requirements.

Needs 1 through 4 are readily addressed by creating a data schema and storing all of the data in a relational database. Adhering to Need 5 requires a calibration process and is discussed in 4.2.

1.3.3 Data Processing Fundamentals

With a structured data set that fulfills the necessary data management guidelines, it is natural to create methods of viewing and manipulating the data. Once the data has been processed, it is necessary to store the results of any compute-heavy processing to avoid the need to repeat them. The database mentioned in the previous section is an ideal hub for meeting these needs. There are three abilities and one *ality* that need to be fulfilled by this part of the system.

- 1 Viewability - The ability to view data for individual sensor streams. Desirable as a simple sanity check to examine each axis of sensed data on each node. Realtime viewability is also highly desirable.
- 2 Aggregatability - The ability to merge different inertial data streams is a simple yet powerful tool for examining data and drawing conclusions.

²It is important to note that the mentioned requirements take into account **only** the raw analog sensor data that makes up the bulk of what needs to be organized and stored. The amount of data that is to be managed more than doubles when the it is converted from the analog values to real calibrated angular velocities, acceleration and magnetic field readings.

- 3 Repeatability - There should exist a standard set of reusable data access components for viewing and aggregating to avoid forcing each analyst of data to create their own.
- 4 Neutrality - These reusable components should be language and location neutral. A minimum supported subset of programming languages is MATLAB, C/C++ and Visual Basic. Each should be capable of accessing the data in a location-neutral manner over the network.

These four are the building blocks that allow consumers of our budding sensor fruit access to perform their own research or professional activities.

1.3.4 Biomechanically Relevant Data Processing

The previous sections have laid out a very application generic vision and design requirements in order to guide the development of a wearable wireless sensor network. This section outlines concepts relevant to performing a concrete biomechanical analysis, which is an eventual desired output for the specific audience of the Medical Researchers and Coaches mentioned in the introduction.

The inertial measurement unit (IMU) described in 1.3.1 is an excellent platform for tracking orientation and acceleration over time. The drawback of the IMU is that it is not aware of the context of this orientation and velocity, it does not have any idea of where it started or what it is attached to. For example, how do you compute a torque if you don't know the radius? In order to make the IMU, or groups of IMUS, contextually aware of itself and permit tracking of it in a three dimensional space there are two requirements:

- 1 Mechanical Model - Information regarding the fixed locations of IMU's in relation to each other. Including joint locations, joint types and the IMU's distance from these.

- 2 Starting Point or Initial Position- A mechanism for obtaining an absolute orientation of each IMU. This allows for tracking each node from a known configuration.

With an initial position, it is possible to drive the mechanical model using the inertial data. In addition to yielding three dimensional positions of segments, this provides one of the key elements of a non-trivial biomechanical analysis: **joint angles of body segments over time**. A detailed overview of the mechanical model is presented in Section 3.3

Tackling the kinematics of the body segments leads to the real “pot of gold” for biomechanical studies, kinetic analysis. In order to calculate the kinetics of a given model, there are three requirements:

- 1 Joint Angles - The relation of body segments to each other
- 2 Center(s) of Mass - Of a single body segment or groups of them.
- 3 Forces - Segment masses paired with accelerations and angular velocities acting on the segment, or group of segments.

Putting these three pieces together allows for calculation of dynamics that are the common language for describing the severity of loads experienced by joints, ligaments and tendons. A preliminary introduction as to how kinetics are calculated is presented in Section 3.4 and a more detailed discussion is presented in Section 9.7.

PROLOGUE



The *Prologue* chapter contains the related work to frame this research in the larger field. It is not meant to be a criticism of existing work and technology, but seeks to help readers understand how the author’s work is novel and not “reinventing the wheel”.

2.1 RELATED WORK

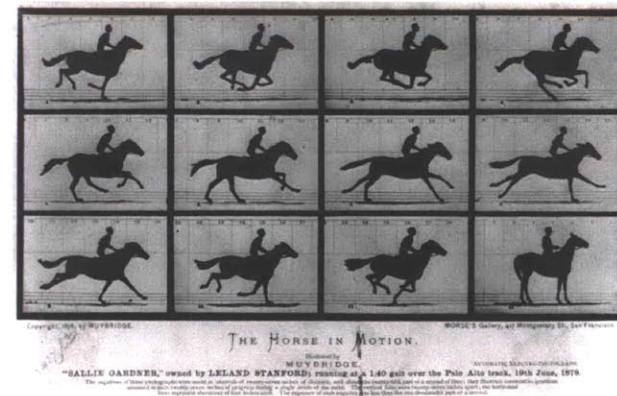
Other than preliminary work done in the authors Master Thesis[7], the research guidelines presented in Section 1.3 have no precedent due to the difficulty in orchestrating a standalone end-to-end wearable sensor system capable of providing complex biomechanical analysis. This does not mean that there does not exist a body of work peripheral to this dissertation from which the new technology draws.

2.1.1 Motion Capture Systems

One of the first known motion capture systems can be traced back to 1872 and was built by Eadweard Muybridge, an admitted and acquitted murderer³. The system was built to answer the question of whether all four of a horse's hooves are off the ground at the same time during a trot. It consisted of an array of cameras that the horses hooves would trigger sequentially via pieces of thread strung across a racetrack. Additionally, Muybridge built a device to study the captured motion: the Zoopraxiscope rotated the strip of sequential images and allowed them to be viewed in the order they were taken [17]. The system was further perfected by his research partner Etienne Jules Marey and became what is the first motion picture camera. It is interesting that the root of the massive filmmaking industry was based on this desire to learn and understand animal, and later human, movement.

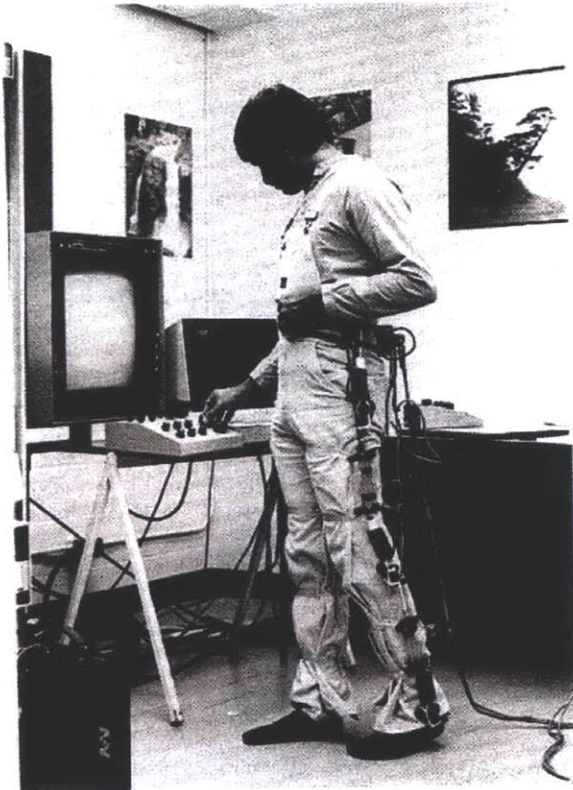
The next notable step was taken in the early 1900's with a technique called rotoscoping[18], developed by Max Fliescher, in which recorded motion is projected onto frosted glass and used as the basis for creating animated effects in movies.

In 1917, Etienne Oehmichen patented an electric stroboscope that was coupled to a camera capable of capturing 1,000 frames per second. This was



Muybridge's *The Horse in Motion*, 1878

³http://en.wikipedia.org/wiki/Eadweard_Muybridge#Murder.2C_acquittal_and_paternity



An early potentiometer based goniometer exoskeleton for the lower body.

taken one step further by Harold ‘Doc’ Edgerton in 1931 when he introduced the electronic stroboscope and used it to study the motion of high speed motors in motion. This work culminated and was documented in his Sc.D dissertation that he received from MIT [19]. He did not limit his interests to mechanical systems and is also known for mid 1930’s photographs ranging from golfers swinging to animals in flight.

Not much occurred in the field until 1953, where Zeller used interrupted light markers in order to trace the motion of an athlete in a long stereo exposure [20]. This is the first mention that could be found of a ‘Witness Point’, or marker-based system.

Moving forward, different types of systems began to emerge, the majority of work being focused on optical systems, with passive and active markers. Others used potentiometer-based goniometers developed in the late 1970’s [21] that consisted of exoskeletons with encoders at each joint and others still used a magnetic field to track motion (Polhemus, 1969).

Magnetic field tracking technology was developed in the 1960’s by Bill Polhemus. It is still commonly used today due to its excellent static (non-moving) positional and angular orientation accuracy (0.005in and 0.020 degrees) in small (2’x2’x2’) capture volumes [69] and relatively low cost (sub \$3k). This system is based on a sending (transmitting) unit that generates a changing magnetic field and groups (up to 16) of wired or wireless receiving sensors. The system’s sensors each read the generated magnetic field and estimate their orientation from these readings at a sampling rate of 240Hz and a latency of 3.5ms.

The Polhemus Liberty system or the Ascension Flock of Birds are commonly used in conjunction with an optical tracker in medical research to enhance the precision of optical system data. These systems would be ideal, as they are fairly mobile and the on-body nodes are wireless. However, a 240Hz sampling rate is not enough to capture all information that is present in

extremely high speed motion. A second drawback is that positional data must be doubly differentiated⁴ in order to obtain inertial parameters, such as acceleration. They also suffer calibration issues near ferrous metal and may require specialized rooms in which to perform data collection. These systems currently require direct AC power.

A wearable goniometer is a device to measure joint angles. The work of Calvert et al [22] fused electronic goniometer data with hand annotated camera information and developed a language, Labnotation, in an effort to describe motion and drive stick figure animations. The electronic goniometer, a simple device by today's standards, is a potentiometer mounted at the rotating joint of a standard goniometer. As the goniometer's angle changes, the resistance of the potentiometer also changes, which is reflected in the output voltage of the potentiometer and can be mapped to an angle. Goniometers prove to be too bulky and restrictive for the complex motion of throwing or batting.

In the mid 1980's, an extended version of rotoscoping was developed. The system used visible markers attached to the subject that were manually encoded on a 3D representation of a character in a computer. This technique is known as photogrammetry in two dimensions and stereo photogrammetry in three [23]. Digital rotoscoping, developed and patented in 1994 by Smoking Car Productions, allowed for any number of frames captured by a camera to be turned into black and white digital images with the use of a computer algorithm, enabling them to be used as rotoscoping masks. This opened the door for large-scale rotoscoping, rather than the previous technique of hand drawing each frame. Also of note is Bob Sabiston's "interpolated rotoscoping" technology that was developed at the MIT Media Lab in the early 1990's [24][25]. The interpolated technique allowed for only the key frames of an animation to be drawn, and then an interpolation is done automatically between the key frames.

⁴It is important to note that double differentiation of position, which greatly magnifies any noise present in positional data, is a drawback of any system that gathers data purely based on the position of markers or wearable magnetic nodes. This includes active, passive, semi-passive and markerless optical systems.

Optotrak Certus active marker optical system. There are two flavors of markers, wired and wireless.



2.1.2 Marker Based Optical Trackers

During the time that these technologies were developed and actively used, optical motion capture systems were experiencing rapid development in two major areas: camera technology and algorithm development. Both were significantly aided by the rapid advances in the speed and miniaturization of integrated circuits. Additionally, optical systems became very popular in the film industry, as evidenced by the Academy Awards received by Vicon and Motion Analysis Corp. in 2005.

In 1985 it took a Sun 1 computer 17 hours to compute 8 points from 4 cameras on a 3-second trial [20] while a current Vicon system can perform the same analysis in real time. The mathematics developed for stereo photogrammetry starting in the late 1800's have been heavily optimized and extended in order to allow this.

The computation of the positions of bodily segments or objects has also been aided by the ability to capture the locations of markers faster and more precisely. Several different capture schemes have been developed: active, passive, semi-passive and markerless approaches have also been attempted and implemented.

2.1.2.1 Active Systems

Active marker systems are based on illuminating groups of LEDs worn on the body and triangulating their position from several camera angles. Each marker or group of markers is larger than their passive counterparts because each need to have power and logic controlling the timing, illumination duration and power of each LED. They have been used successfully in the film industry and allow for capture to occur outdoors with synchronous illumination and detection, something that passive systems have difficulty achieving.

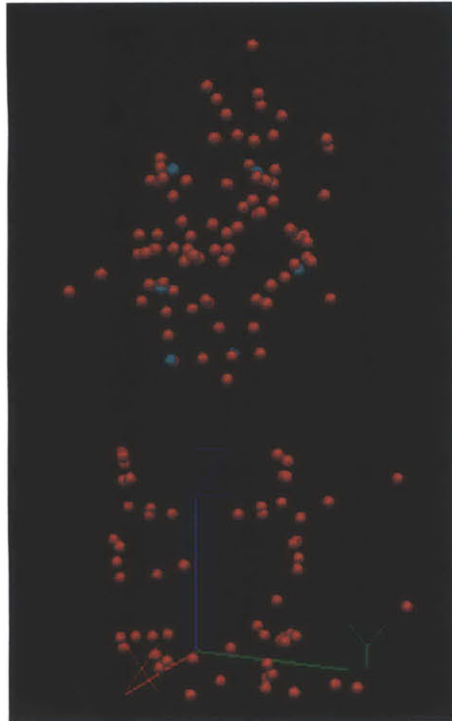


FIGURE 2-7 Optical Markers in X, Y, Z with targets placed over a human subject

The first active system, SELSPOT, was developed by Selcom in 1975 and is the ancestor of the SELSPOT II system released in 1982. Northern Digital introduced the Watsmart system in the mid-1980s and the Optotrak system around 1990. Both were active systems based on linear CCD array technology that produces high resolution. These are highly accurate systems and represent a significant development that occurred in active systems after Selspot's introduction. In 1994, Charynwood Dynamics released their Cartesian Optoelectronic Dynamic Anthropometer (CODA) active system that was successfully used in gait studies [26]. Lastly, as recently as 2012, Qualisys [10] has developed a hardwired active marker system. That sequence-coded active markers, and applied it in outdoor environments to analyze equine lameness and performance.

2.1.2.2 Semi-Passive Systems

Semi-Passive (or *Semi-Active*) systems, also labeled *Time Modulated Active Marker* and *Semi-Passive Imperceptible Marker*, also fall into the active category due to the necessity of having control software and power at each tag or marker. Prakash, a system developed by the Camera Culture Group at the MIT Media Lab, is labeled as a semi passive imperceptible marker system [27]. The scene is successfully illuminated by a series of structured IR light projections; the wearable sensors transmit via RF whether they see this illumination or not. By stitching several of these frames together, the location of the sensors can precisely and rapidly be determined. One issue is that occlusions are a problem because the sensor node must see all of the structured light to calculate the orientation and position. Considering that the received data is transmitted wirelessly back to a master host to later be integrated with

video that may or may not be captured of the scene, this system resembles a wireless sensor network more than a motion capture system.



FIGURE 2-8 Inferring the skin surface location from marker position allows for segment definition.

2.1.2.3 Fully Passive Systems

Passive marker systems are the dominant technology in motion capture; possibly due to the simplicity and flexibility of attachment and subject instrumentation. Vicon, Motion Analysis Corp and Qualysis are the major commercial players in this space and their systems are mainly used for medical research and in the film industry, with engineering (unmanned vehicles, meteorology, video game development) being the largest growing market.

The technology is based on a combination of strobing lights and cameras that work in unison to capture frames of data that show the positions of optical markers illuminated by the pulses of light. This data, taken from several different camera angles (20 or more for high speed motion), is reconstructed to build a three dimensional path for each of the markers [FIGURE 2-8](#) . The paths of several markers can be integrated to represent segments of the human body by building an interpolated virtual ‘skin’ which the markers determine, [FIGURE 2-8](#) . Augmenting this with anthropometric information such as diameters and lengths of segments allows inference of bone location and joint centers [FIGURE 2-9](#) .

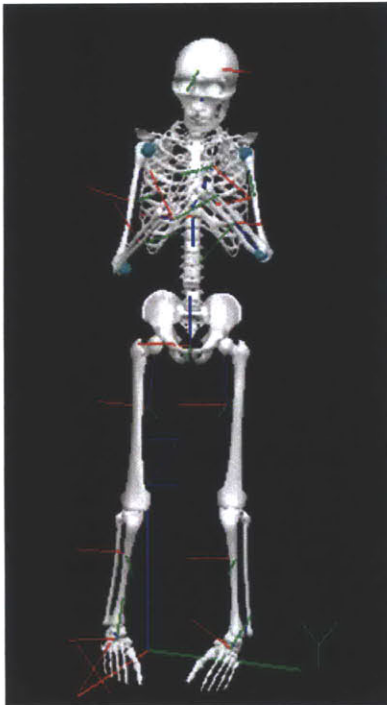


FIGURE 2-9 Skeleton defined from segment locations

2.1.3 Inertial Systems for Motion Capture

Inertial systems are not nearly as pervasive as optical in the medical and film communities. This is not a surprise, as the size of an inertial sensor 20 years ago made it difficult to even consider instrumentation of a human. There have been several domain-specific prototype tools for research [\[36\]\[37\]\[38\]](#) rather than fully built commercial products. These implementations are specific to a certain application and are not capable of capturing detailed motion information.

Ghasemzadeh et als. work [\[36\]](#) uses 50Hz sampling to characterize the timing of a batter’s swing and reaffirm some of the rote rules of batting. As part of a larger body of work that addressed personal health monitoring [\[38\]](#),

Gerasimov created Swings that Think [37]. He instrumented a bat with a gyroscope and accelerometer to measure the angular and acceleration parameters. Several other systems are focused on gait analysis [60], some on posture [61] and others on golf swing analysis[62]. None utilize high range sensors and instrument more than two body segments, and none attempt to reconstruct motion except for Orient-2 [63], which tracks slow moving poses over time using inertial sensing. The system has been utilized to analyze golf swings [64] and dancers of the Argentinian tango [70]. However, the range of its inertial sensors is too low to handle more extreme motion, $\pm 300^\circ/\text{sec}$ and $\pm 6G$.

As recently as 2010, work published in the Journal of Sports Engineering, whose purpose is to advance engineering in the area of sports including inertial sensors that were used to analyze tennis serves[59]. Unfortunately this work claims that, as of 2010, there does not exist a gyroscope with a range greater than $\pm 300^\circ/\text{sec}$ and the authors had to create a *virtual gyroscope* based on optical system marker data. While this statement is false because gyroscopes with much higher ranges were available at this time, it does indicate that the cutting edge of sports engineering is not at the cutting edge of inertial measurement unit development. It also indicates a disconnect between these two fields.

There is one main player in the commercial arena, Xsens [4], and a some lesser known companies such as Animazoo [5] and KinetiSense[6].

The Xsens system is more robust in terms of hardware, as it is comprised of gyroscopes, accelerometers and magnetometers, while the Animazoo system is based only on gyroscopes. Both systems are equipped with gyroscopes capable of sensing $\pm 1200^\circ/\text{sec}$ and the Xsens system also has a $\pm 16G$ accelerometer. Both are limited to 120Hz sampling rates, which is far below the capability of optical technology.

The technology is ideally suited for studying ergonomics and gait, and while the systems claim to be usable for sports there is much to be desired with such low sampling rates, which appear to be limited by the need to have the systems operate in real time. When examining an activity that pushes the limits of human ability, such as pitching, these systems fall short. From previous work, I have observed that during an 85MPH fastball a pitcher's hand experiences acceleration forces in excess of 110Gs and angular velocities of over 6,000 degrees/second. This is far beyond the sensing limits of the Xsens and Animazoo systems. Further, at 1000Hz sampling, the peak of the pitch consists of 3 data points or lasts 3ms. At 120Hz, each sample is taken every 8.3ms and there is a good probability that this peak would not even be detected with either existing inertial system or be extremely filtered by an anti-aliasing front-end. These simple facts dictate the need for a high-performance wearable wireless inertial sensor network.

2.1.4 Current Pitcher Development

In order to use a wearable sensor network on a pitcher to improve their performance, it is important to understand the state of the art in molding pitchers. As alluded to in section 1.2, techniques used to develop pitchers have been passed on as rote practice from coach to coach and player to coach. Most available information is not based on any hard numbers; rules for pitching are simply preached without an explanation of why and how these rules-of-thumb were established. For example, "Coaching Pitchers" [28] states five "90 degree Rules" for pitchers that:

"A coach should be able to measure these angles with the naked eye, and by doing so he can determine whether a pitcher is mechanically sound."

Each of the rules is described briefly, with little or no explanation of what effects improper angles would have on the pitch and no discussion of how these rules were determined.

From the two sources studied by the author [28][29], the first has 23 pages dedicated to mechanics and the latter has 10. It is difficult to understand how the most important part of the pitch can be completely described with such brevity. Hence, there is a lot of opportunity in performing research that validates and explains in a quantitative manner these rules of thumb.

Along with mechanics, fatigue is another factor that is considered by coaches, because it is thought to be a contributing factor in injury. Again, the metrics associated with measuring fatigue are vague at best and the methods of controlling it are not based on numerical or scientific data. There are simply preset maximum pitch counts established. The actual count limit is not explained, again just a rule of thumb. Hence, an opportunity for future research.

It is difficult to these “rules” such as prior work because there is not much hard science behind them, however they are relevant as they are the only existing methods for player development.

2.1.5 Precision of Biomechanical Research

There exists a large body of biomechanical research regarding throwing. Most of it is focused on forces, torques and angular velocities experienced at the shoulder and elbow [30][31][32][33][34][35] [94][95][96] and how different mechanics effect these parameters. They do not focus on understanding what makes one pitch ‘better’ than another. Further, the relationship between injury and mechanics has also not been thoroughly explored. An in-depth review of

each prior study would be a dissertation in itself. The focus in this section is different.

⁵Thank you Mr.Kepple

In order to understand the precision of a wearable sensor network, it is important to focus on the precision of the velocities and accelerations used to perform the biomechanical analysis in these studies and compare both systems. Most examined literature leverages techniques developed by Feltner and Dapena [39][40][41][42] to calculate joint forces and torques in the upper body, with the target activity being overhead throwing or swinging. Unfortunately, sources of error are not discussed in any significant detail in these papers.

While there is not much information regarding acceleration and velocity precision in known literature, there are four factors that should be considered when trying to answer the question of how good optical systems are⁵.

2.1.5.1 Tracking Marker and the Underlying Skeleton

Characterizing how well markers on the surface of the skin represent the underlying skeleton and understanding errors present due to soft tissue artifacts (STA's)(markers moving on the skin surface) has been widely studied[43][44][45][46][47].

The general consensus is that even with current inexpensive technology [44], marker location is within a $\pm 0.5\text{mm}$ difference in precision between systems using a man made calibration rig. With smaller capture volumes ($180 \times 180 \times 150 \text{ mm}^3$) the accuracy is as good as $63 \pm 5 \mu\text{m}$ and precision of $15 \mu\text{m}$ [47] using a robotic test apparatus. It is important to note that these studies were all performed with slow moving trials.

The gold standard method to understand and characterize soft tissue artifacts (STAs) involves using bone pins, FIGURE 2-10 , or external fixator devices that are surgically attached to the underlying skeleton [97]. Using this method, Anderson et al[48] found statistically significant error in their

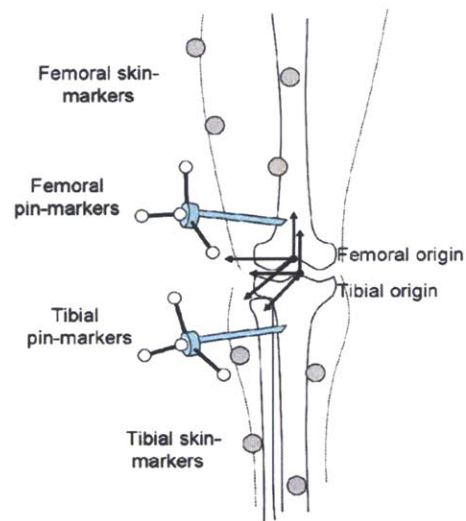


FIGURE 2-10 Surgically implanted bone pins - the most accurate method of comparing surface markers to the skeleton [45]

measurements of joint angle of the knee. However, in reality the error was about 1 degree of the

angular measurement, which is not significant for studies of gait. Again, the caveat with this work is that the trials studied were slow walking gait.

While not close in terms of angular velocity and acceleration, running with bone pins has been studied by Reinschmidt et al [46] with drastically different results. Errors relative to the range of motion during running stance were 21% for flexion/extension, 63% for internal/external rotation and 70% for abduction/adduction.

2.1.5.2 Marker Set Used

In order to reduce error due to STAs, different configurations and placement points for marker sets have been studied and optimized. Much of this work relates to gait[49][50], some relates to the entire skeleton [51]. The conclusions from this research is that the correct marker set makes the estimation of the joint centers and segment orientation more accurate.

Upper body marker sets for the specific purpose of throwing [71][72][73] have been developed. The primary focus of this research is to mitigate soft tissues artifacts by placing markers on bony prominences.

2.1.5.3 Position and Orientation Calculation Methods

Different approaches have been developed to correct for STAs and errors from marker movement. The seminal paper is that of Lu and O'Connor [52], that exploits a technique named *global optimization*, which uses a least squares fit for every segment and adds joint constraints to avoid joint dislocation. Converse to global optimization is Stagni et al's[53] leveraging of double calibration [54] for more precisely estimating slow moving activities. Also noteworthy is a probabilistic approach of Alexander and Andriacchi. Their interval deformation technique [43] makes assumptions regarding the

⁶Slow moving activities involve walking, sit-to-stand, step-up/step-down.

performed activities, and uses this information to provide a better estimate of position and orientation. While there is no single ‘*correct*’ method, the general takeaway is that the methodology used to accommodate for skin tissue artifacts and how data is processed when estimating orientation and position will effect the accuracy of estimation.

2.1.5.4 Inertial Parameter Estimation

Directly related to the estimation of position and orientation is calculating first and second order derivatives to obtain velocities and accelerations. Any errors present in position estimation will be magnified and manifest themselves as noise when these derivatives are taken.

Inertial models of the human body[55][56] have been developed along with methods of determining angular momentum[57][58] by Yeadon. As mentioned in the start of section 2.1.5, existing literature does not attempt to quantify error in moment and acceleration calculations. This does make sense because the goal of researchers studying gait and human movement is not to research the quality of their measurement equipment, but to study human movement. They appear to simply accept the best tools available and put them to use, but they need to understand the limits of accuracy.

One of the main motivations in utilizing inertial sensors is because they measure acceleration and angular velocity, currently inferred via derivatives, directly. Although inferring absolute position and/or joint angles with inertial systems involves its own complications (discussed in Section 10.2.3), thorough calibration virtually eliminates error in inertial data streams and allows for kinetic calculation that is much more accurate and precise than optical systems.



PROLOGUE

Related Work

TAXONOMY, HIGH LEVEL ARCHITECTURE & KINETIC MODEL

You say toe-may-toe, I say toe-mah-toe. I say
poh-tay-toe, you say poh-tah-toe.

- George & Ira Gershwin

This chapter contains the naming conventions used and stitches these together to define high level system concepts to allow for a better understanding of the overall system. The system architecture is presented at high-level along with the upper body model used to represent motion.

3.1 TAXONOMY

Mean or average? Standard deviation or sigma? Stochastic or random? Integration or summation? Sampled data or observation? Different branches of science define the same or similar concepts using different words and very rarely acknowledge it or attempt to rectify them. This leads to confusion for novices who are attempting to learn a new field.

This dissertation also has its own, albeit small, taxonomy and the purpose of this section is to define it and describe its analogs in existing scientific or practiced fields.

3.1.0.1 Player

The term *player* is used to describe the person that the sensor network is applied to. Its analog in the in medical research is *subject*. The goal of the system is to analyze athletes and, until now, each athlete has been a *player* on a baseball team, hence the name *player*. Each *player's* definition consists of standard biometric information:

- 1 First Name
- 2 Last Name
- 3 Player ID - unique player identifier
- 4 Age
- 5 Height
- 6 Weight
- 7 Player Number
- 8 Throwing Hand (Left or Right)
- 9 Batting Hand (Left or Right)

- 10 Player Type - Batter or Pitcher
- 11 Has had previous shoulder pain?
- 12 Has had previous shoulder surgery?

In order to perform accurate biomechanical analysis, anthropometric data is also recorded for each *player* and measured using a flexible tape measure between manually identified biomechanical landmarks. At this level, data consists of measurements that do not change greatly over time for a *player*:

- 13 Forearm Length - lateral epicondyle to radial styloid
- 14 Upper Arm Length - lateral acromion to lateral epicondyle
- 15 Chest Width - sternal notch to lateral acromion
- 16 Pelvis Width
- 17 Elbow Circumference
- 18 Wrist Circumference

As part of the experimental process all of these items are recorded in a logbook at the time of player instrumentation and entered into a database at a later time. Each *player* has a collection of *sessions* (Section 3.1.0.2) associated with themselves.

3.1.0.2 Session

Each time a *player* is instrumented and data is gathered, a new *session* is defined. A *session* is a collection of *gestures* (Section 3.1.0.3). The concept of the *session* does not have an analog in other fields, but is important because and each time a player is instrumented, sensor placement and certain anthropometric measurements may be different between *sessions*. The need to store this information dictated the definition of *session*. Each session contains general session information:

- 1 Session Name
- 2 Session ID - unique session identifier
- 3 Hand Node ID
- 4 Forearm Node ID
- 5 Upper Arm Node ID
- 6 Chest Node ID
- 7 Waist Node ID

As mentioned previously, each session also contains anthropometric data and node location information that changes from *session* to *session*:⁷

- 8 Radial Styloid to Hand Node Location
- 9 Lateral Epicondyle to Forearm Node Location
- 10 Lateral Acromion to Upper Arm Node Location
- 11 Sternal Notch to Chest Node Location
- 12 Chest Node Location to Waist Node Location
- 13 Arm Circumference
- 14 Chest Circumference
- 15 Waist Circumference
- 16 Waist Node to Floor Distance
- 17 Stomach to Lower Back Thickness
- 18 Chest Thickness
- 19 Depth from Stomach to Chest - (Stomach to Lower Back Thickness)
minus (Chest Thickness)

Additionally, for batting, two additional measurements are performed:

- 20 Bat Length

⁷Future applications of this technology may use more specific technology to measure node location.

21 Bat Tip to Bat Node Location on Bat

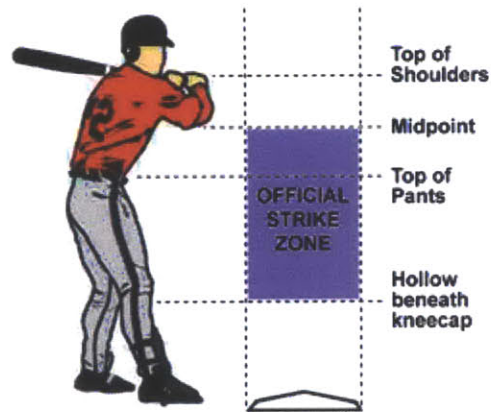


FIGURE 3-11 Major League Baseball Strike Zone Definition



FIGURE 3-12 Pitch location annotation. Red is outside of the Strike Zone and Green is inside of the Strike Zone.

3.1.0.3 Gesture

Each *gesture* consists of the inertial data sampled from the nodes that a *player* is instrumented with. This data is described in detail in Section 4.1.1. Each gesture also has annotation data associated with it which, like *session* data is logged and entered into a database. The first set of annotations define general gesture properties:

- 1 Gesture Type - Pitch/Swing/Other
- 2 Gesture Name
- 3 Gesture Comment - freehand text annotations about the gesture that do not fit any other categories

Specifically for *Swing* gestures, the following classification parameters are recorded:

- 4 Swing Type - Free Swing/Hit from Tee/Soft Toss Hit/Batting Practice Hit/Normal Full Speed Pitch Hit/Strike (missed hit)
- 5 Hit Location - What direction the ball went when hit. Center Field/Left Field/Right Field/Strike (missed hit)
- 6 Hit Trajectory - How the ball flew when hit. Ground Ball/Line Drive/Normal Trajectory/Pop-Up/Strike (missed hit)
- 7 Bat Instrumentation - Is the bat instrumented with an IMU?
- 8 Incoming Pitch Speed - in MPH measured by radar
- 9 Outgoing Hit Speed - in MPH measured by radar

Specifically for *Pitch* gestures, the following classification parameters are recorded:

- 10 Pitch Type - Fastball (regular/ 2 Seam/ 4 Seam)/Changeup/Breaking Ball/Curveball/Slider/Unknown
- 11 Pitch Location - Where the pitch was in relation to the strike zone. See FIGURE 3-11 and FIGURE 3-12

To synchronize the system with optical systems, two additional parameters are recorded

- 12 Milliseconds From Inertial System Start -The number of milliseconds the optical system started recording after the inertial system started recording.
- 13 Frame rate - The number of frames per second that the optical system is recording.

3.1.0.4 Purposes of Player and Gesture Annotation

Annotation is crucial for moving beyond reconstructing motion and analysis of single gestures. Given a large data set of different Players and several Gestures per player, the next logical step is to take different views of the data to see if patterns can be discovered based on different pitches, players, swings, pitch speeds, etc. This opens the door for a “big data” approach to understanding what makes an elite player elite and beginning to explore if it is possible to bring other players up to his level, gaining that constantly desired performance advantage. Further, using the same approach, it is possible to understand what aspects of motion affect the magnitude of torques and stress on the joints, then attempt to change player mechanics to lessen these loads while maintaining the same elite level of performance.

FIGURE 3-13 Node placement. Visible placement is on the top of the hand, volar on the forearm above the wrist and at the waist. Not visible are chest and upper arm nodes placed under the players jersey.

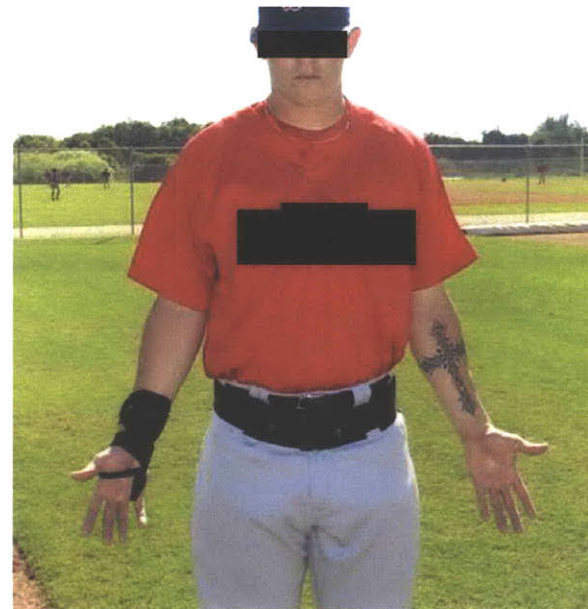
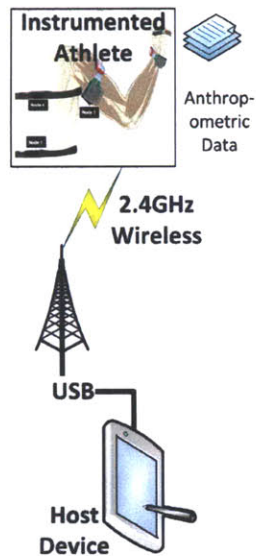


FIGURE 3-14 Field Deployment Architecture.

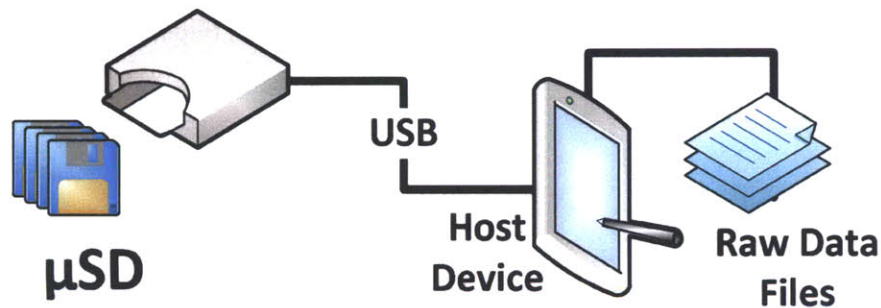


3.2 SYSTEM ARCHITECTURE

3.2.1 Field Deployment

A high level block diagram of the data gathering field deployment is depicted in FIGURE 3-14 . It is purposely very simple. Any USB-enabled host device connects to the wireless basestation and performs command, control and synchronization of the network of nodes that an instrumented athlete wears. Each node has local data storage in the form of μ SD for sampled data. To maximize the speed of writes, the data is stored as raw. This requires a custom SD interface to read it from the cards. Additionally all anthropometric measurements for each athlete are preformed and recorded for future use.

FIGURE 3-15 Data Retrieval Interface



3.2.2 μ SD Data Retrieval Interface

The data retrieval interface (FIGURE 3-15) relies on a custom piece of hardware that consists of a microcontroller with an internal SD peripheral, a physical SD card slot and is capable of acting as a USB slave. The microcontroller is programmed to read the data on the card sector-by-sector and serve it to a host device via USB. The host device decodes the data contained in the received sectors and creates files containing the raw analog sensor data for each gesture that is on the card.

3.2.3 Data Import Engine

Once raw data is present in the filesystem, the data import engine can be used to populate this data into the database. The import engine (FIGURE 3-16) is essentially a sophisticated parser with an interface to a relational database.

Additionally, while it is parsing the raw sensor data files, it creates a second copy of the data in the database to which calibration constants are applied. This process converts raw analog sensor data to actual angular velocities and linear accelerations.

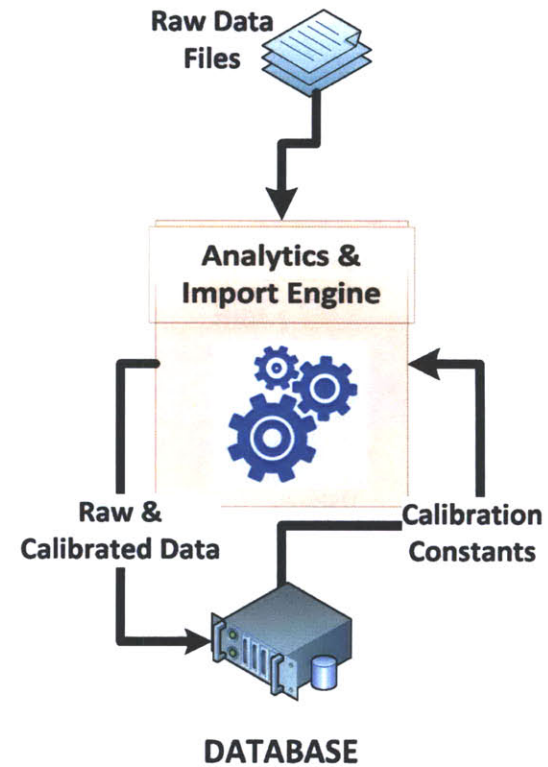
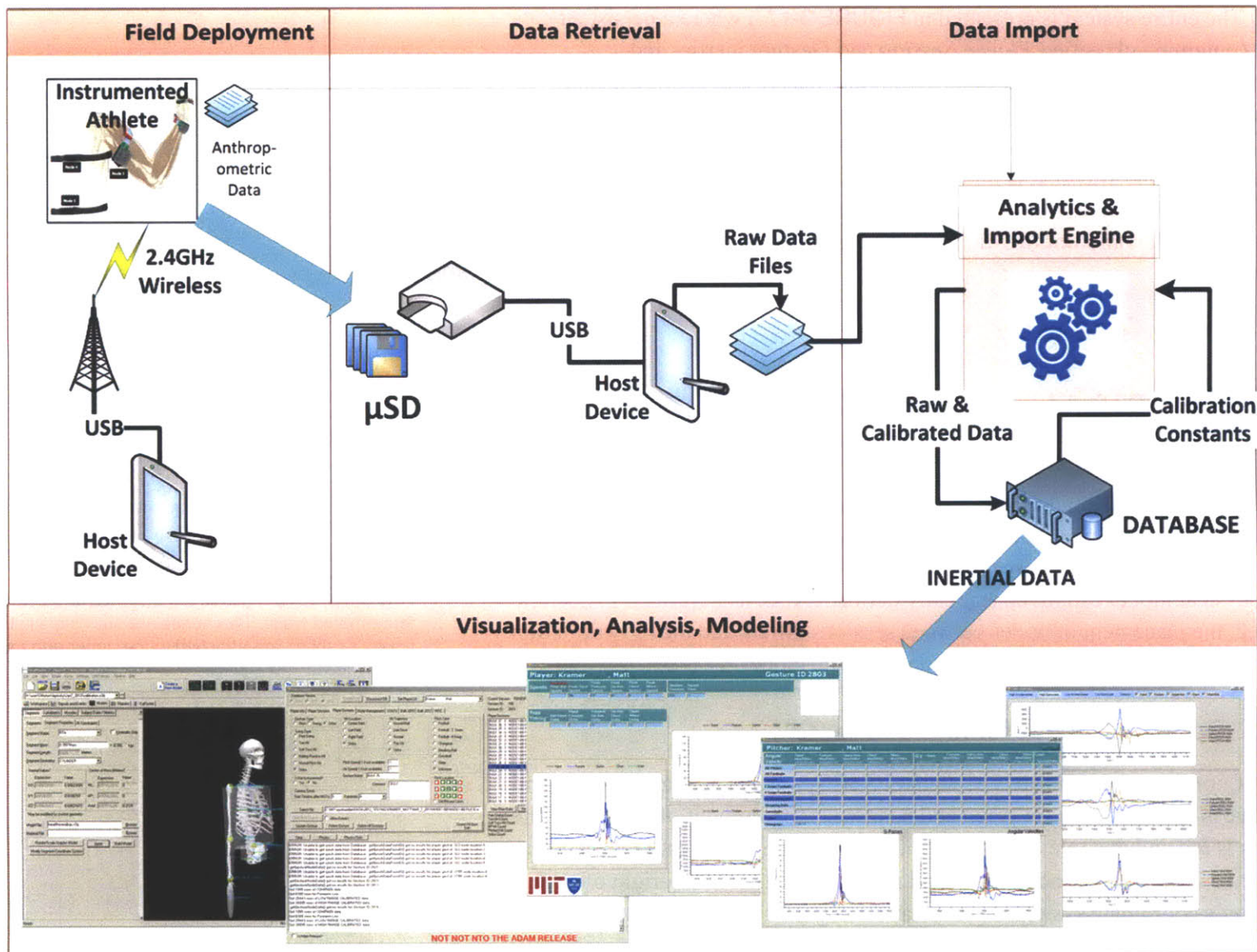


FIGURE 3-16 Data Import Engine

FIGURE 3-17 Complete System Architecture



3.2.4 Visualization, Analysis and Modeling

The entire system is presented in FIGURE 3-17 , where a persistent data store containing classified *Player*, *Session* and *Gesture* inertial and anthropometric data opens the door to building player-and-gesture-specific-models and performing medically significant research. An interface has been built for C/C++, Matlab and Visual Basic in order to retrieve, slice, dice and visualize data any way that is imaginable. The granularity of the data can be per athlete, per session, per gesture, per segment, per sensor and even per sensed axis. The only limiting factor is the capability and imagination of the model builder.

3.3 PHYSICAL (KINEMATIC) MODEL

At the opposite end of the spectrum from the *Player*, *Session* and *Gesture* taxonomy is the physical kinematic model that is driven by data from the sensor network. In order to accommodate different players of different sizes, this physical model cannot be statically defined. Also, as described in Section 3.1.0.2, the placement of nodes between sessions differs and the representation of this placement⁸ must also be encoded into the model.

⁸The evolution of node attachment to player's bodies is covered in-depth in Section 7.1, here we will briefly describe node placement to set the context for understanding the physical model. As visible in FIGURE 3-13 , nodes are attached to the hand, forearm and waist. Two nodes are not visible in the figure, as these are attached to the upper arm and on the chest.

3.3.1 Coordinate Systems

Coordinate systems are visible in FIGURE 3-19 . The Z axis is Blue and positive is up. The Y axis is green and positive is forward out of the chest. The X axis is red and positive extends out of the right arm. For rotations, the right-hand rule is used to define positive and negative rotation. The origin of each segment's coordinate system is placed at the segment's center of mass. In

anatomical terms the, X axis is medial/lateral, the Y axis is anterior/posterior and the Z is proximal/distal.

3.3.2 Landmark Definition

The physical model starts with biometric and anthropometric measurements that are performed for each *player* (Section 3.1.0.1) and each *session* (Section 3.1.0.2). Based on this data, a set of landmarks, which can be processed by a visualization and dynamics engine [65], are generated.

These landmarks, visible in FIGURE 3-18 are calculated starting at the **LAB ORIGIN**, which is defined as (0, 0, 0) in X, Y, Z 3-dimensional space and not shown in the figure. The rest of the landmarks are based on this **LAB ORIGIN** working up to the pelvis and to the chest and then down the arm. Measurements from the Player and Session section are referenced in each landmarks definition and refer to the numbered points in Section 3.1.0.1 and Section 3.1.0.2.

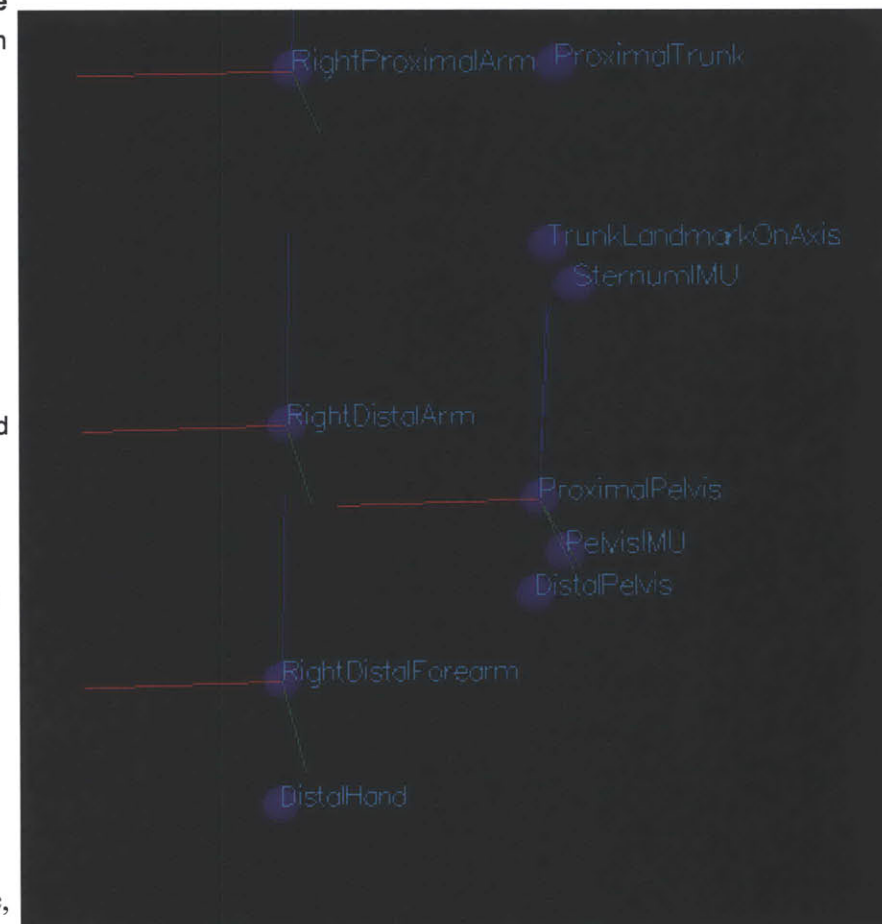
- 1 **PelvisIMU** - Directly above the **LAB ORIGIN** along the **Z** axis. This distance is based on the **Waist Node to Floor Distance** (Session Nr. 15) measurement. **X** and **Y** locations are unchanged (0, 0)
- 2 **ProximalPelvis** - Same **X** and **Z** coordinates as **PelvisIMU**, displaced along the **Y** axis by negative **Stomach to Lower Back Thickness/2** (Session Nr.17) measurement.
- 3 **DistalPelvis** - Construction marker to create a coordinate system for the Pelvis. Shares **X** and **Y** coordinates with the **ProximalPelvis** and is displaced 10cm negatively along the **Z** axis.
- 4 **SternumIMU** - Same **X** coordinate as **PelvisIMU**. **Y** coordinate is **PelvisIMU Y** displaced by negative **Depth from Stomach to Chest** (Session Nr 19). The **Z** coordinate is **PelvisIMU Z** plus **Chest Node Location to Waist Node Location** (Session Nr.12).

- 5 **TrunkLandmarkOnAxis** (a.k.a. center of the trunk) - **X** and **Z** are the same as **SternumIMU X** and **Z**. **Y** coordinate is **SternumIMU Y** minus **Chest Thickness/2** (Session Nr.18)
- 6 **ProximalTrunk** (a.k.a location of the sternal notch at trunk center) - Created along the line formed by **ProximalPelvis** and **TrunkLandmarkOnAxis** and starting at **ProximalPelvis**. The landmark is displaced by a distance of **Sternal Notch to Chest Node Location** (Session Nr.11) + **Waist Node to Floor Distance** (Session Nr.15) along the defined line.
- 7 **RightProximalArm** - **Y** and **Z** coordinates are the same as **ProximalTrunk Y** and **Z**. The **X** coordinate is the **ProximalTrunk X** plus **Chest Width** (Player Nr.15).
- 8 **RightDistalArm** - **X** and **Y** are inherited from the **RightProximalArm**. The **Z** component consists of the **RightProximalArm Z** subtracted from the **Upper Arm Length** (Player Nr.14) .
- 9 **RightDistalForearm** - Created along the line formed by **RightProximalArm** and **RightDistalArm**. The landmark is displaced by a distance of **Upper Arm Length** (Player Nr.14) + **Forearm Length** (Player Nr.13) along the defined line starting at **RightProximalArm**.
- 10 **DistalHand** - Created along the line formed by **RightDistalArm** and **RightDistalForearm**. The landmark is displaced by a distance of **Forearm Length** (Player Nr.13) + **Diameter of a Baseball** + **Hand Thickness** (2.5cm).

3.3.3 Segment Definition

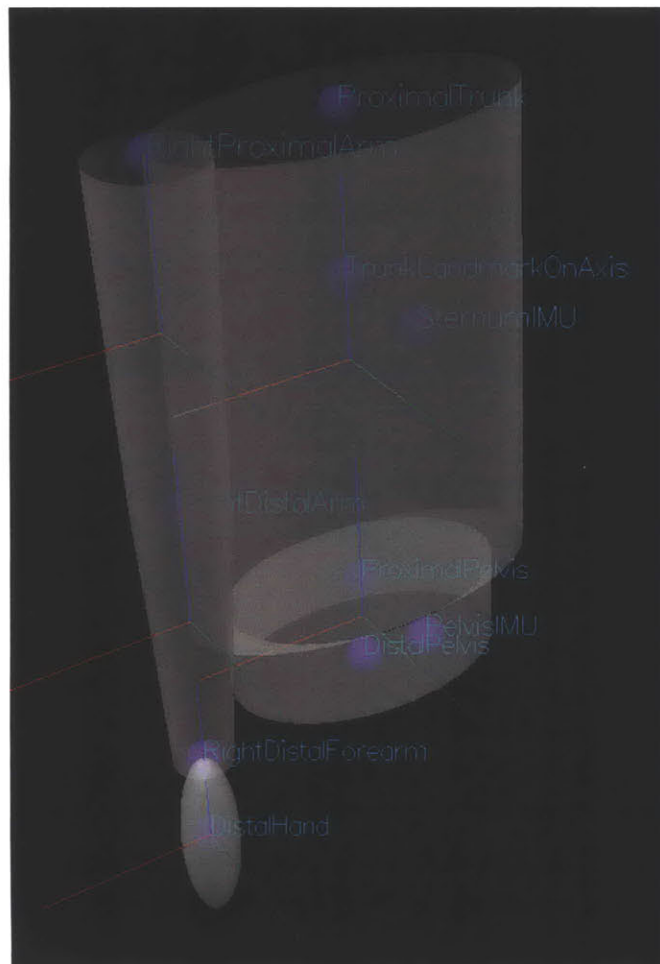
With relevant landmarks defined, each of the upper body segments are defined based on the landmarks. Each segment has a short name, a long name,

FIGURE 3-18 , **Model Landmarks (Lab origin is not shown)**
Coordinate systems are described in 3.3.1



geometry and mass. This section documents each, except for mass, which is based on standard percentages of body mass as presented on pages 64 & 65 of [66].

FIGURE 3-19 Segment Definitions for a Right Handed Athlete



- 1 **Pelvis - RPV** - The pelvis is the root segment and because of this it is allowed XYZ translation and rotation about all three of its axes. It is constructed from the **ProximalPelvis**, **DistalPelvis** and **PelvisIMU** landmarks. Its geometry is an ellipsoid cylinder with a height of **ProximalPelvis + DistalPelvis**, an **X** radius of **Pelvis Width/2** and a **Y** radius of 10cm, if kinetics are not calculated for this segment. An actual measurement of the width of this segment divided by two is used if kinetics will be calculated.
- 1 **Trunk - RTA** - Constructed based on the **ProximalPelvis** and **ProximalTrunk** landmarks with a cylindrical ellipsoid geometry. The **X** radius of this segment is the distance from **ProximalTrunk** to **RightProximalArm**. The **Y** radius is 10cm, if kinetics are not calculated for this segment. An actual measurement of the width of this segment divided by two is used if kinetics will be calculated.
- 2 **Upper Arm - RAR/LAR** - Modeled as a cone and defined by the **RightProximalArm**, **RightDistalArm** and **ProximalTrunk**. The proximal radius of the segment is defined by the **Arm Circumference** (Session Nr.13) divided by $\pi/2$. The distal cone radius is defined by **Elbow Circumference** (Player Nr.17) divided by $\pi/2$.
- 3 **Forearm - RFA/LFA** - Also modeled as a cone. Defined by the **RightDistalArm**, **RightDistalForearm** and **ProximalTrunk**. The proximal radius of the forearm is defined by the **Elbow Circumference** (Player Nr. 17) divided by $\pi/2$. The distal cone radius is defined by **Wrist Circumference** (Player Nr.18) divided by $\pi/2$.
- 4 **Hand - RHA/RFA** - Defined by the **RightDistalForearm**, **DistalHand** and **ProximalTrunk** and modeled as a sphere with a radius of **Wrist Circumference** (Player Nr.18) divided by $\pi/2$.

3.3.4 Joint Definition

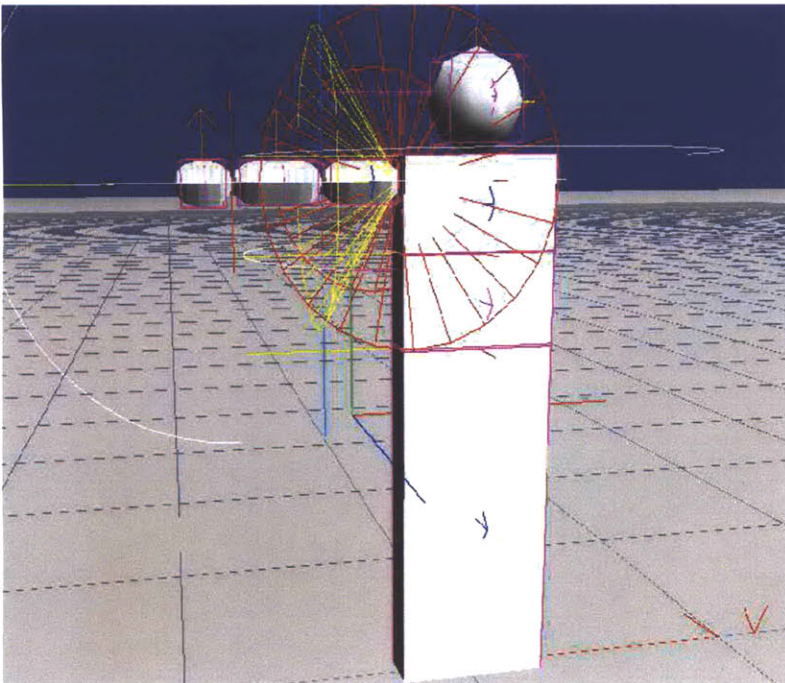
There are four joints for the upper body model. Each is modeled as a ball and socket with no possibility of translation. This means that each joint has 3 DOF, but does not mean that the joint cannot translate in 3 dimensional space. Joint and segment translation is driven by the root segment, the **Pelvis**.

Further, each joint has a given order of rotation angle application. The joints and their rotation sequences are as follows:

- 1 **Spine Joint** - for lack of a better name, the joint between the **Pelvis** and **Trunk** is named the Spine Joint. Its Euler rotation sequence is XYZ
- 2 **Shoulder Joint** - this is the joint between the **Trunk** and **Upper Arm** and has an Euler sequence of ZYZ⁹.
- 3 **Elbow Joint** - the joint between the **Upper Arm** and **Forearm** with an Euler sequence of XYZ.
- 4 **Wrist Joint** - the joint between the **Forearm** and **Hand** segments. Also with an Euler sequence of XYZ.

⁹this is based on the recommendations of the International Shoulder Group [67][68]

FIGURE 3-20 Clemens Satzger's Kinematic Model [91]. Complete with range of motion limits (yellow and red cone shaped objects) placed on each upper body segment.



3.3.5 Performing the Kinematics

An attempt to build a kinematic model was made by Clemens Satzger as part of his Diplom work [91] while at the MIT Media Lab. Satzger put many of the pieces in place and created a good three dimensional model (shown in FIGURE 3-20). His Kalman filter used individual node orientations along with accelerometer data to drive the model. This approach worked well for slow-moving gestures. It fell short in reconstructing complex motion, partially due to the filtering approach and partially to the immature state of the node hardware, which did not yet provide accurate data.

A new version of the kinematic model is generated from measured data on a per-player, per-session basis in a format that is readable by *C-Motions Visual3D*[65], the chosen visualization and dynamics package. Both FIGURE 3-18 and FIGURE 3-19 are actual player models imported by Visual3D. It is important to note that *Visual3D* inputs the necessary rotations and possible translations for each segment and joint via a custom plug-in (developed as part of a collaboration between *C-Motion* and the author), and creates a skeletal visualization of the model and its motion.

3.4 KINETIC MODEL

Creating a three dimensional kinematic model of the of the pelvis, trunk, upper arm, forearm and hand and the associated filtering algorithms necessary in order to drive this model using inertial and magnetic data is a massive undertaking in and of itself. Once such a model has been built, the next logical step is to begin calculating the kinetic forces and torques that are the causes kinematic motion. This analysis bridges the fields of physics and mechanics in

a non-trivial manner because all calculations must be performed in three dimensions and the underlying mechanical model has multiple rigid bodies and joints. Fortunately for this author, there exist systems, built to process optical system data, that implement and execute the kinetic modeling necessary for obtaining the desired forces and torques.

One of these is *Visual3D* from *C-Motion Incorporated* [65], who, as previously mentioned, is a collaborator on this project in three ways. Tom Kepple, Chief Science Officer at *C-Motion*, is a biomechanics expert, an invaluable mentor for all things optical and biomechanical and also a reader on the committee for this dissertation. Second, as described in Section 3.3.5, the physical model is generated in a manner that is readable by *Visual3D* and is driven via a custom plug-in. The last facet of the collaboration is to pair *Visual3D*'s proprietary kinetics engine with the inertial data gathered from each instrumented segment and perform kinetic calculations.

Internally, and because it is built to process X, Y, Z marker positions, *Visual3D* calculates its own angular velocities, along with angular and linear accelerations based on the markers and 'feeds' these into its kinetics engine. In order to use inertial data to 'feed' this model, *Visual3D* has been modified to import such data from our database and analytics engine via the custom plug-in. Once this data is paired with kinematic data, the entire suite of *Visual3D*'s kinetics algorithms are available for generating results. It is important to note that in keeping with the spirit of keeping athletes in their native environment while studying them, a goal of this work is to keep the medical researcher in their native environment when acquiring research data. Using the familiar and well known *Visual3D* environment as the interface researchers will interact with aligns itself ideally with this philosophy.

THE TANGIBLE

t

The combination of various tangible electronic parts forms the inertial sensing node into an instrument used to measure various motion parameters. This chapter details the instrument that has been tuned to capture the symphony of forces experienced by an athlete's body as he plays.

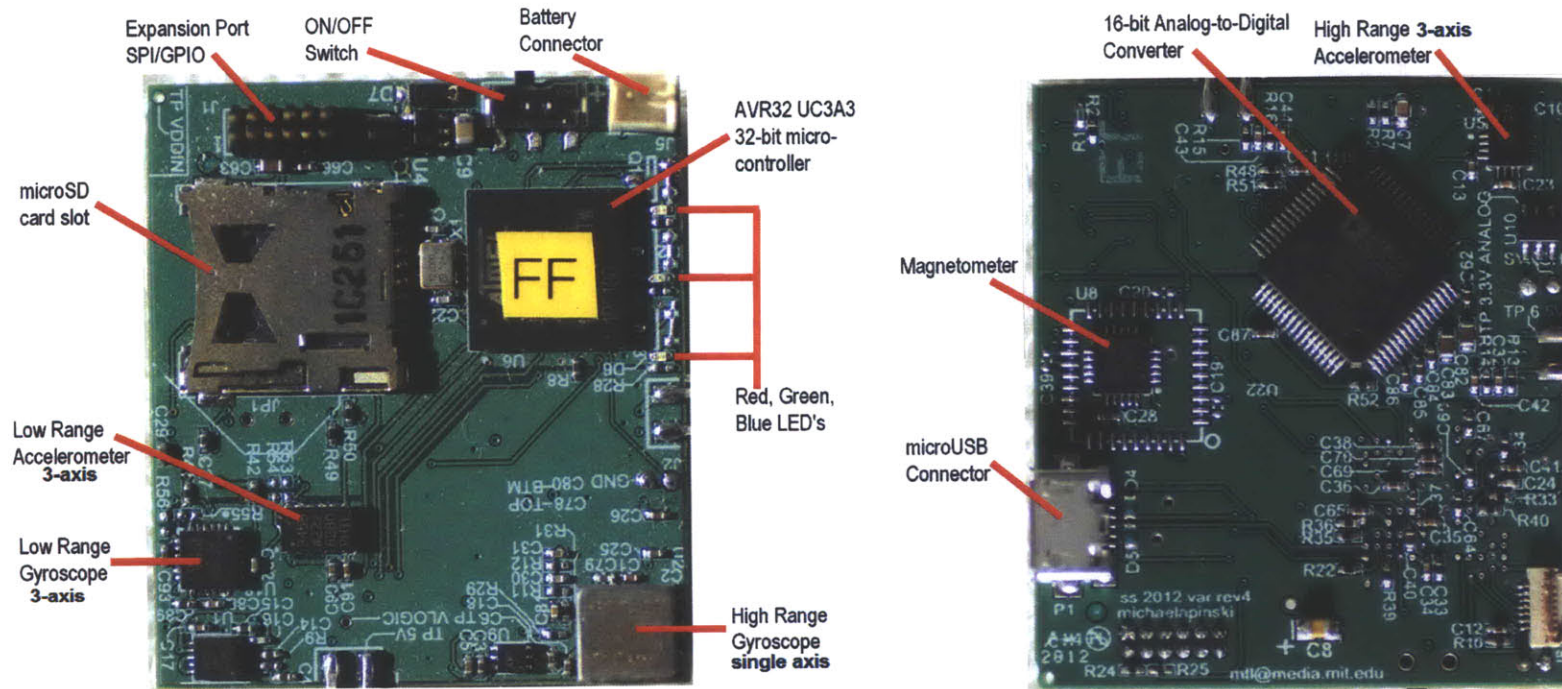
4.1 WIRELESS INERTIAL MEASUREMENT NODE

.....

The wireless inertial measurement node consists of four physical parts: the main board, two identical high range inertial daughterboards and an expansion board for wireless communication. Each node has two tiers of acceleration and angular velocity sensing capability, high and low range. The purpose of this is straightforward. A high range sensor is good at sensing very fast accelerations and angular changes but has low resolution for sensing slow moving accelerations and angular movement, whereas the low range sensors, excellent at sensing slow moving parameters, are incapable of sensing anything past their specified limits. We fuse both low and high range sensor families to attain wide dynamic range with the resolution that we require. This data fusion is non-trivial and the algorithm developed to do so is presented in Section 9.5

Our hardware has gone through 4 generations of design. The first, [74][115] was an adaptation of a low-range design used for interactive dance and only had a single range accelerometer and gyroscope set. The second, [7] was explicitly developed for sports applications and had dual-range sensors, although little onboard memory, hence streamed each collected pitch or swing to the basestation via the wireless link, which would take up to a minute. The subsequent generation [104], had virtually unlimited onboard memory via the SD card. Our final version, described here, has been designed to minimize noise, take advantage of newer and more compact sensing, support rapid data unloading vis USB and enable higher sampling rates.

FIGURE 4-21 Main Board Component Diagram



4.1.1 Main Board

The main board is true to its name as it contains the bulk of power, processing and storage capabilities of each node. There are 4 sources, at various voltages, of power on the board for dividing the supply into analog and digital components. Each node is normally powered by a two cell 7.4V 145 mAh Lithium Polymer battery via the onboard connector. The two high range daughterboards are necessary because the high range gyroscope is a single-axis part, requiring orthogonal attachment to sense on all three axes. A microUSB

connector allows for wired connection of the node to a host computer for command and control of an individual node, or for the connected node to act as a basestation and perform command and control for a network of nodes. The main board has a microSD slot connected to the AVR32 microcontroller via a high speed parallel SDIO interface for storing all sampled sensor data. Additionally, the board is capable of acting as a USB master (via the microUSB port) in order to connect slave devices, such as an external hard drive for storing years of data.

The board is outfitted with a 6-channel Analog Devices AD7606 analog-to-digital converter that interfaces the AVR32 microcontroller via a Serial Peripheral Interface. The sensors connected to the AD7606 are:

- 1 High Range Accelerometer - The Analog Devices ADXL377 has $\pm 200G$ range, 3 orthogonal axes of sensing and analog output for each axis. It is small and has a low power consumption, making it ideal for the system.
- 2 High Range Gyroscope - A single Analog Devices ADXRS649 gyroscope is mounted on the main board. The gyroscope has a range of $\pm 20,000^\circ/\text{second}$ and senses about its Yaw axis, making it ideal for sensing the extreme angular velocities that athletes are capable of producing. Its single analog output is fed into the AD7606.

The low range sensors are also mounted to the main board. These consist of:

- 1 Low Range Accelerometer - The Analog Devices ADXL345 running in $\pm 16G$ mode has a 400kbit/s I²C digital communication interface that is directly connected to the AVR32 microcontroller. It has 3 orthogonal axes of sensing and is ideal for recording the slow moving accelerations that most activity is composed of.
- 2 Low Range Gyroscope - A 3-axis Invensense IMU-3000 is configured in $\pm 1,000^\circ/\text{second}$ mode and shares an I²C communication bus with



FIGURE 4-22 High Range Daughterboard

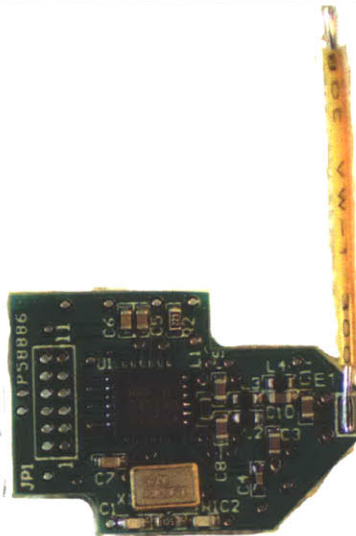


FIGURE 4-23 nRF2401 Based Wireless Expansion Board

the ADXL345. Again, its purpose is to record slow moving angular velocities that the ADXRS649 is not capable of sensing.

- 3 Magnetometer - While not a low range sensor per se, the Honeywell HMC5843 is limited to a 50Hz sampling rate. This puts it into the category of sensors that cannot be relied on during extremely high speed motion. It is used to determine the initial and final angles of each node relative to the local vector of the Earth's magnetic field.

4.1.2 Inertial High Range Daughterboards

The two high range daughterboards, depicted in FIGURE 4-22 , are identical pieces of hardware and contain only one significant component, an ADXRS649 gyroscope. The single sensing axis nature of this gyroscope mandates these daughterboards and also requires that they are both orthogonal to each other and the ADXRS649 on the main board.

4.1.3 Wireless Expansion Board

While hardware portion of this dissertation is focused on wearable wireless sensor networks, it is important to note that the main board and daughterboards are combined to form a standalone high-range/low-range 6 Degree-of-Freedom IMU. Using the 12 pin GPIO header to mate the main board with the wireless expansion board brings the entire system to its full operational level.

The main component of this board is Nordic Semiconductor's nRF2401[76] single chip 2.4GHz transceiver. The analog RF portion of the board's layout is based on Ryan Aylward's Senseable [74] radio board. The antenna (yellow in FIGURE 4-23) is a wire cut to one quarter of a 2.4GHz wavelength (31.25mm).

The rest of the layout is designed to offer mechanical strength to withstand up to 200Gs of force and match up with the expansion port of the main board. The 12-pin header connector, visible in FIGURE 4-23 is complemented by 2 additional header pins, FIGURE 4-24 , to prevent the board from cantilevering on the 12-pin end. This prevents the solder joints from flexing and eventually failing, which we had seen occur regularly on previous iterations of our hardware which lacked these additional pins.

Communication and power for the wireless board to the AVR32 microcontroller is via the Serial Peripheral Interface that is broken out on the 12-pin connector. Digital 3.3V power and ground pins are also broken out.

4.1.4 Putting It All Together

FIGURE 4-26 depicts a completely assembled wearable node. It is important to note the orientation of the two inertial daughterboards in relation to the high-range gyroscope on the main board. As previously mentioned, this allows for high-range angular velocity sensing on all three axes.

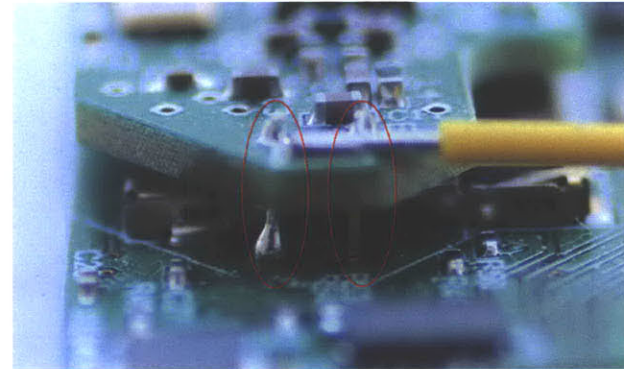
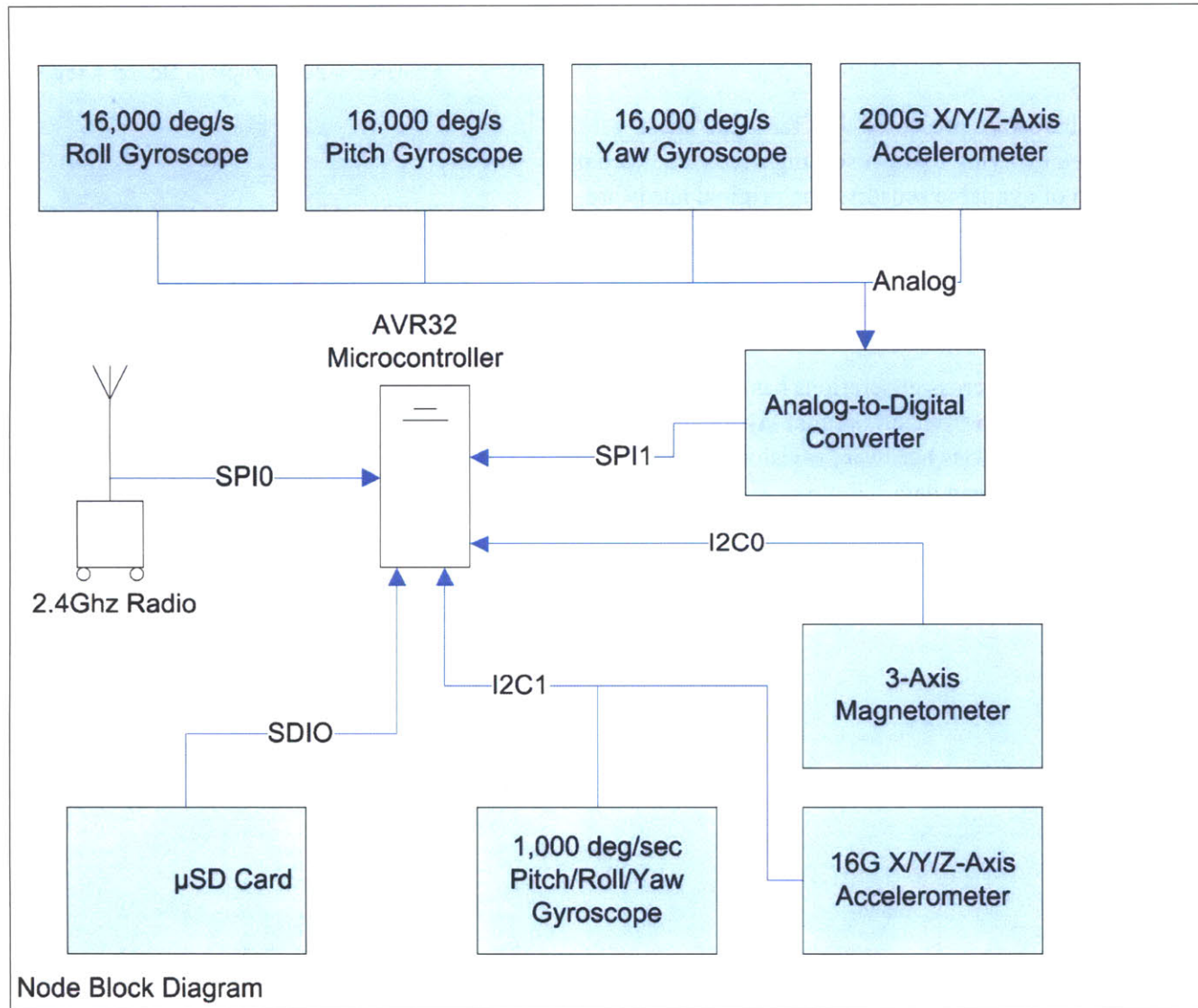


FIGURE 4-24 **Wireless Expansion Board Mechanical Support Headers**

FIGURE 4-25 Wearable Inertial Node Block Diagram

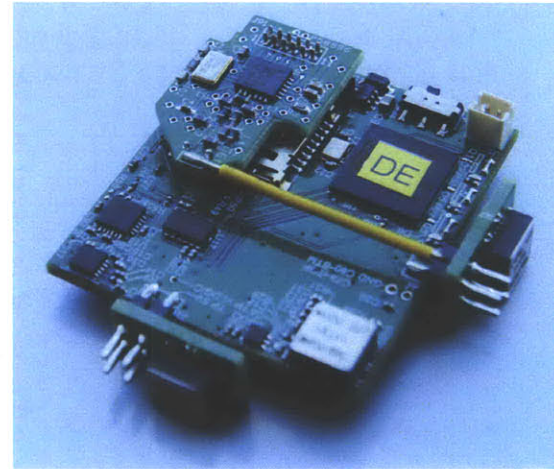


4.1.5 System Evolution

As mentioned earlier, the hardware presented thus far is the latest revision of a system that has been evolving to meet sensing needs and keep up with the technological evolution of available sensors. The original hardware leveraged was Ryan Aylwards 2006 Senseable [74][115] system for instrumenting ensembles of dancers (FIGURE 4-27). The current revision shares only the wireless transceiver chip; all other components have been replaced with newer, smaller, less power hungry parts.

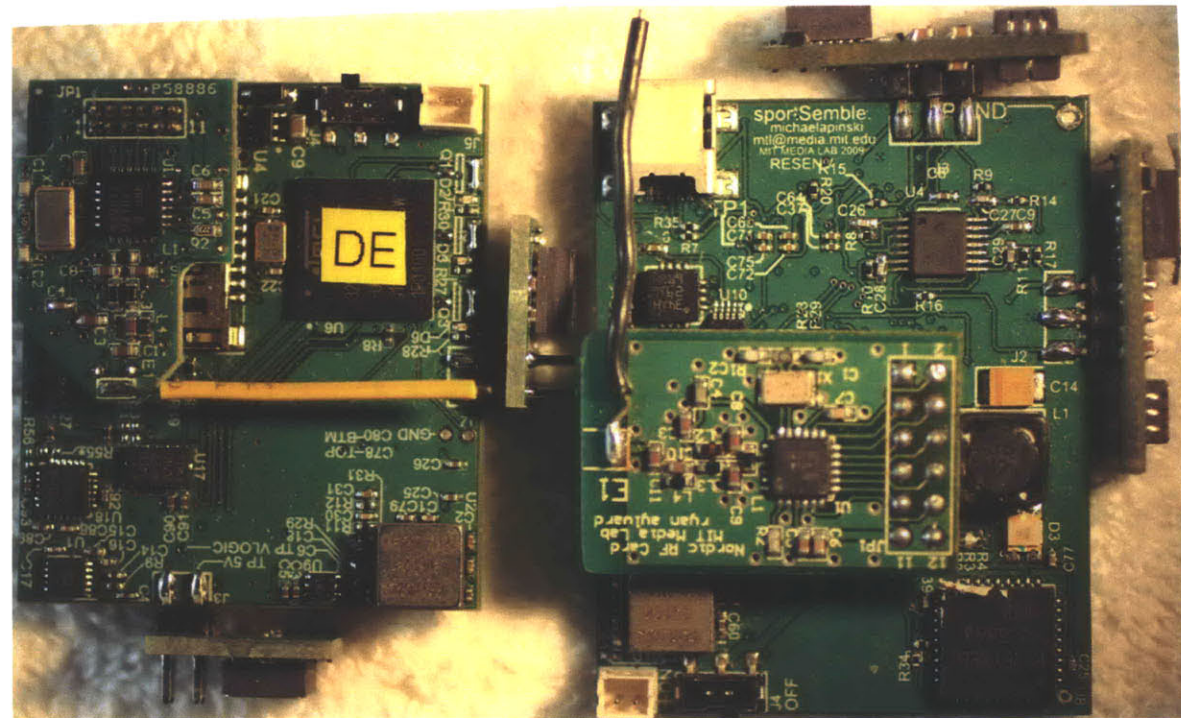
The improvement in data quality across generations has been significant. Background noise due to induced pickup from suboptimal layout and power supply conditioning was present in previous hardware revisions. The newer nodes remedy these and produce very clean data.

FIGURE 4-26 Complete Board Assembly



(37.5x42mm)

FIGURE 4-27 Our current board (left), its predecessor (right)



4.2 CALIBRATION

Every sensor manufacturer publishes a data sheet for each sensor they produce with specifications that include the sensor's range, sensitivity and expected analog output at a given angular velocity, heading or acceleration. Unfortunately, from the authors experience, these numbers are based on

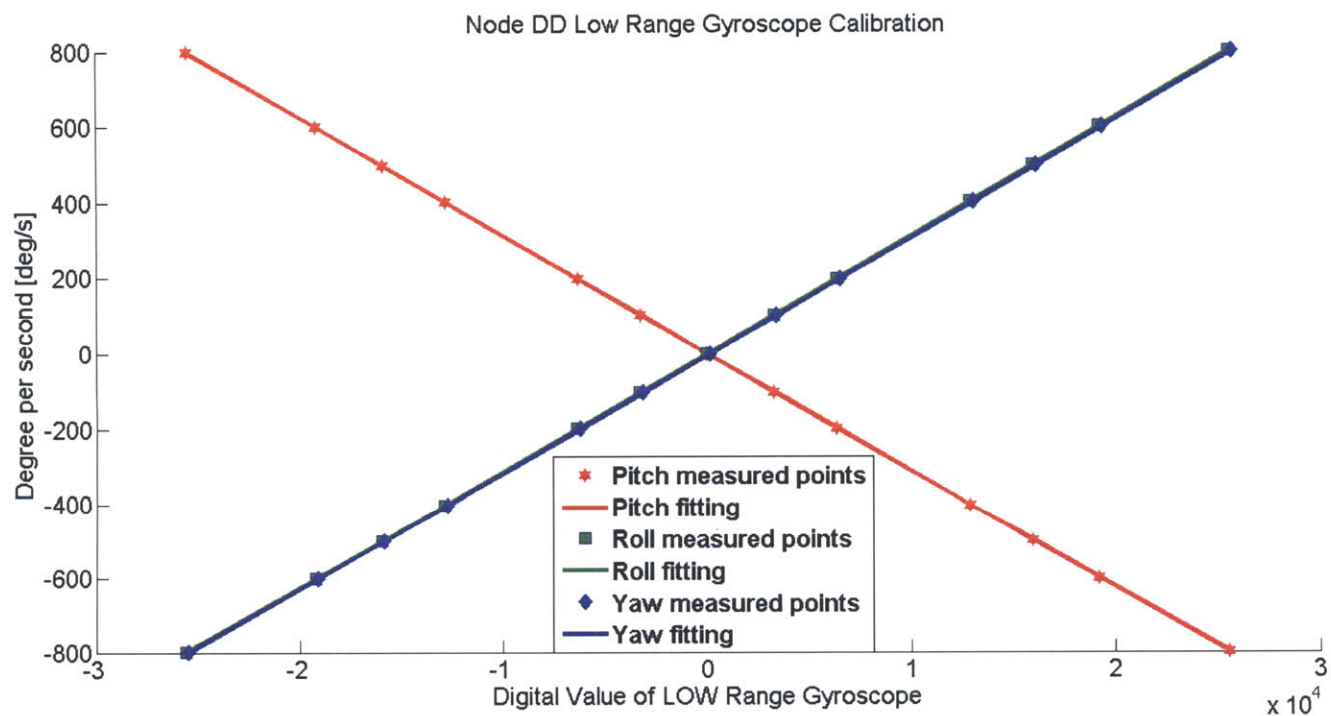
averages taken from several different batches of manufactured units and lack sufficient accuracy. This dictates the necessity of calibrating each axis of each sensor on each node and development of a transfer function for all sensed axes in order to ensure accurate translation from analog to inertial values. The approach used is a rotation based calibration to apply angular velocity for gyroscopes and to simulate acceleration for accelerometers. Magnetometers have their own specific calibration that involves rotation and random data input. A picture of the rig built to perform calibration is show in FIGURE 4-31 .

4.2.1 Rotation Based Calibration

4.2.1.1 Gyroscopes

For gyroscopes, the rotation-based calibration concept is straightforward, because a gyroscope measures angular velocity and outputs an analog value. If the applied angular velocity is known, a transfer function can be developed to map from the analog value to the real angular velocity. Taking several samples at various angular velocities allows fitting of a curve to generate a transfer function that is generic for the specific axis of a particular sensor. Due to the inclusion of both high and low range gyroscopes on all three axes of each node, six individual gyroscope calibrations must be performed for each node built. For each axis that is calibrated a residual to a linear fit is calculated and stored, indicating the quality of the fit. For low range gyroscopes, the calibration points used were $798^\circ/\text{s}$, $600^\circ/\text{s}$, $498^\circ/\text{s}$, $402^\circ/\text{s}$, $198^\circ/\text{s}$, $0^\circ/\text{s}$, $-198^\circ/\text{s}$, $-402^\circ/\text{s}$, $-498^\circ/\text{s}$, $-600^\circ/\text{s}$ and $-798^\circ/\text{s}$. For the high range gyroscopes, the calibration points used were $16998^\circ/\text{s}$, $16002^\circ/\text{s}$, $12000^\circ/\text{s}$, $7998^\circ/\text{s}$, $4002^\circ/\text{s}$, $1998^\circ/\text{s}$, $0^\circ/\text{s}$, $-1998^\circ/\text{s}$, $-4002^\circ/\text{s}$, $-7998^\circ/\text{s}$, $-12000^\circ/\text{s}$, $-16002^\circ/\text{s}$ and $-16998^\circ/\text{s}$.

FIGURE 4-28 Sample Low Range Gyroscope Data and Fitting



4.2.1.2 Accelerometers

Accelerometer calibration is more difficult than for the gyroscope, especially at higher accelerations. It requires the ability to produce a specific linear acceleration in a controlled manner for a defined amount of time. The simplest way to create linear acceleration is to move the accelerometer along a straight line at the desired acceleration.

This is much easier said than done, especially when the desired acceleration is at 150G's for 8 seconds of sampling. The approach taken to calibrate each node's accelerometers exploits centripetal acceleration that occurs when an object is rotated at some radius greater than zero. The general formula for centripetal acceleration is:

$$a = \omega^2 r$$

where acceleration is a , ω is angular velocity and r is the radius. It is easy to observe that a larger radius produces a larger acceleration and a larger ω also results in a larger acceleration. The equation can be rearranged to act as a function of angular velocity based on a desired acceleration:

$$\sqrt{\frac{a}{r}} = \omega$$

Given a static radius of 0.05 m, inputting a desired acceleration into the equation yields the angular velocity necessary to produce it.

Table 1: Desired Acceleration Expressed in Angular Velocity (radius of 5mm)

Acceleration (G)	Angular Velocity (°/s)	RPM
12.0	8,790	1465

Table 1: Desired Acceleration Expressed in Angular Velocity (radius of 5mm)

Acceleration (G)	Angular Velocity (°/s)	RPM
8.0	7,177	1196
6.0	6,215	1036
4.0	5,075	846
2.0	3,589	598
0.0	0	0
-2.0	3,598	598
-4.0	5,075	846
-6.0	6,215	1036
-8.0	7,177	1196
-12.0	8,790	1465

The accelerations used for the low range accelerometer are listed in Table 1 on page 72. It is important to note that positive and negative accelerations all require a positive angular velocity (the node orientation is swapped using a second bracket to reverse sign). This is because centripetal acceleration is independent of direction of rotation. A similar table can be constructed for the high range accelerometer and its desired calibration points.

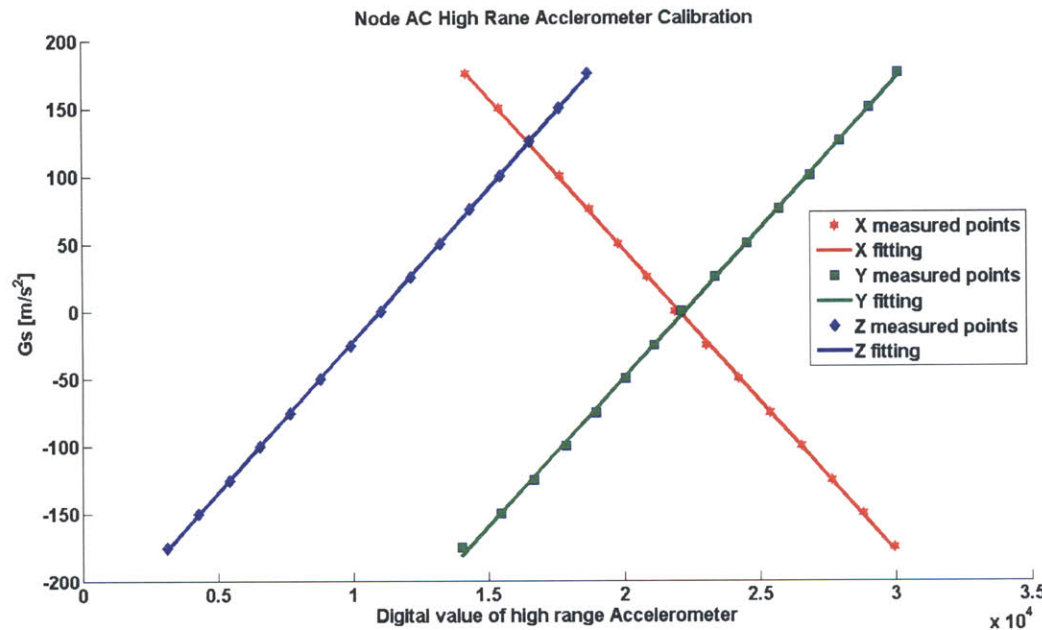
The same fitting technique as for gyroscopes is utilized, and a sample fit is presented in FIGURE 4-29

Table 2: Desired Acceleration Expressed in Angular Velocity (radius of 20mm)

Table 3:

Acceleration (G)	Angular Velocity (°/s)	RPM
175	16,784	2797
150	15,539	2590
125	14,185	2364
100	12,687	2115
75	10,987	1831
50	8,971	1495
25	6,344	1057
0	0	0
-25	6,344	1057
-50	8,971	1495
-75	10,987	1831
-100	12,687	2115
-125	14,185	2364
-150	15,539	2590
-175	16,784	2797

FIGURE 4-29 Sample High Range Accelerometer Data and Fitting



4.2.2 Calibration Rig

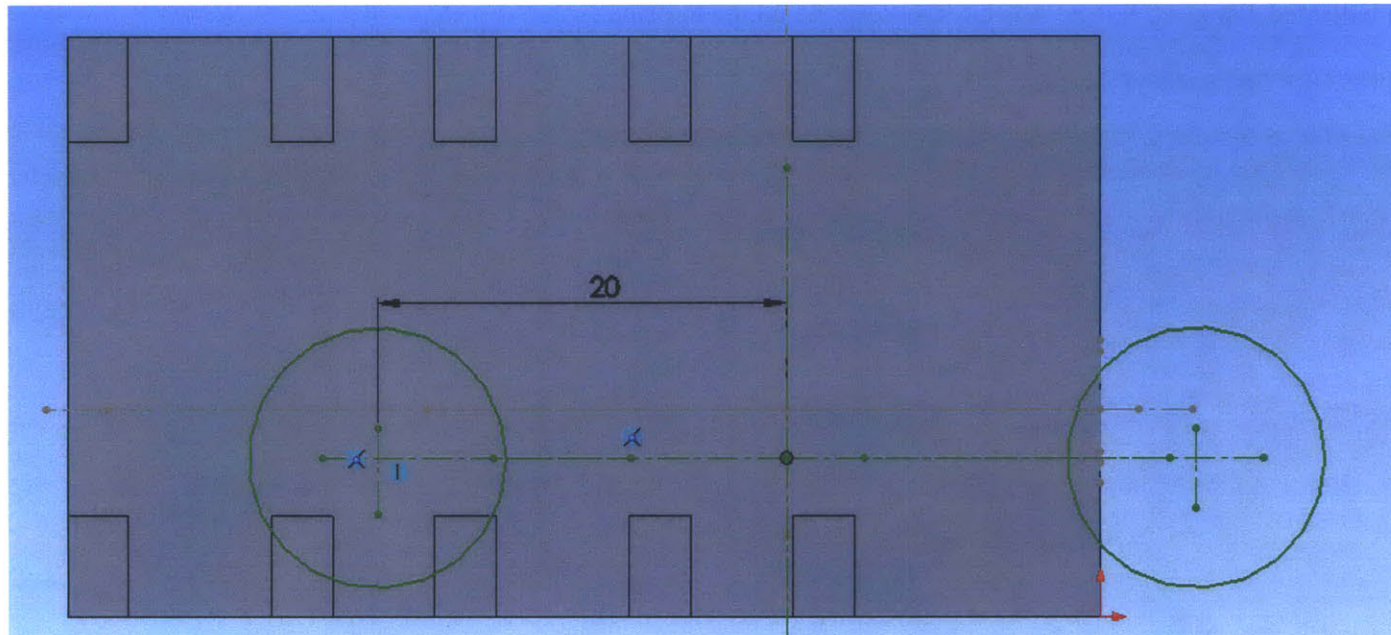
Examining Table 2 on page 74 tells us the angular velocity necessary to generate 175G's of acceleration at a radius of 20mm is 16,784°/s. In order to gather enough samples of data at each angular velocity and acceleration to make an adequately accurate measurement, this angular velocity must be controlled and sustained for at least several seconds. This requires a constant feedback loop controlling an electric motor powerful enough to generate 2,797RPM. This is the first of three issues that a calibration rig needs to address. The second issue is that of containing, or clamping down, a motor that rotates this fast. The last issue is to address a method of attaching the node to

the rotating shaft of the motor with significant accuracy in positioning to meet our design constraints for each type of sensor. The constraint for gyroscopes is that each must be rotated about its center in order to avoid acceleration induced error¹⁰.

In the case of accelerometers there are two constraints or sub-problems that need to be addressed. The first of which requires the accelerometer to be rotated at a known radius from its center axis. The second sub-problem is that of generating both positive and negative acceleration. In order to achieve this the accelerometer must be rotated with its axis of rotation in a position that is positively displaced on the plane orthogonal from its center axis to produce positive acceleration. To create the negative acceleration the accelerometer must be rotated with its axis of rotation negatively displaced on the same orthogonal plane. FIGURE 4-30 illustrates this concept. The center of each green circle is the off-center axis of rotation spaced 20mm from the actual accelerometer's center axis. When rotated about these off-center axes, the accelerometer experiences positive centripetal acceleration at one and negative at the other.

¹⁰ Acceleration induced error in gyroscopes occurs when they are rotated about an axis that is other than its center axis. This error can be mathematically characterized and subtracted. However, this adds unnecessary complexity to the calibration process and is avoided.

FIGURE 4-30 Positive and Negative Axes of Acceleration Spaced at a Known Radius From its Center



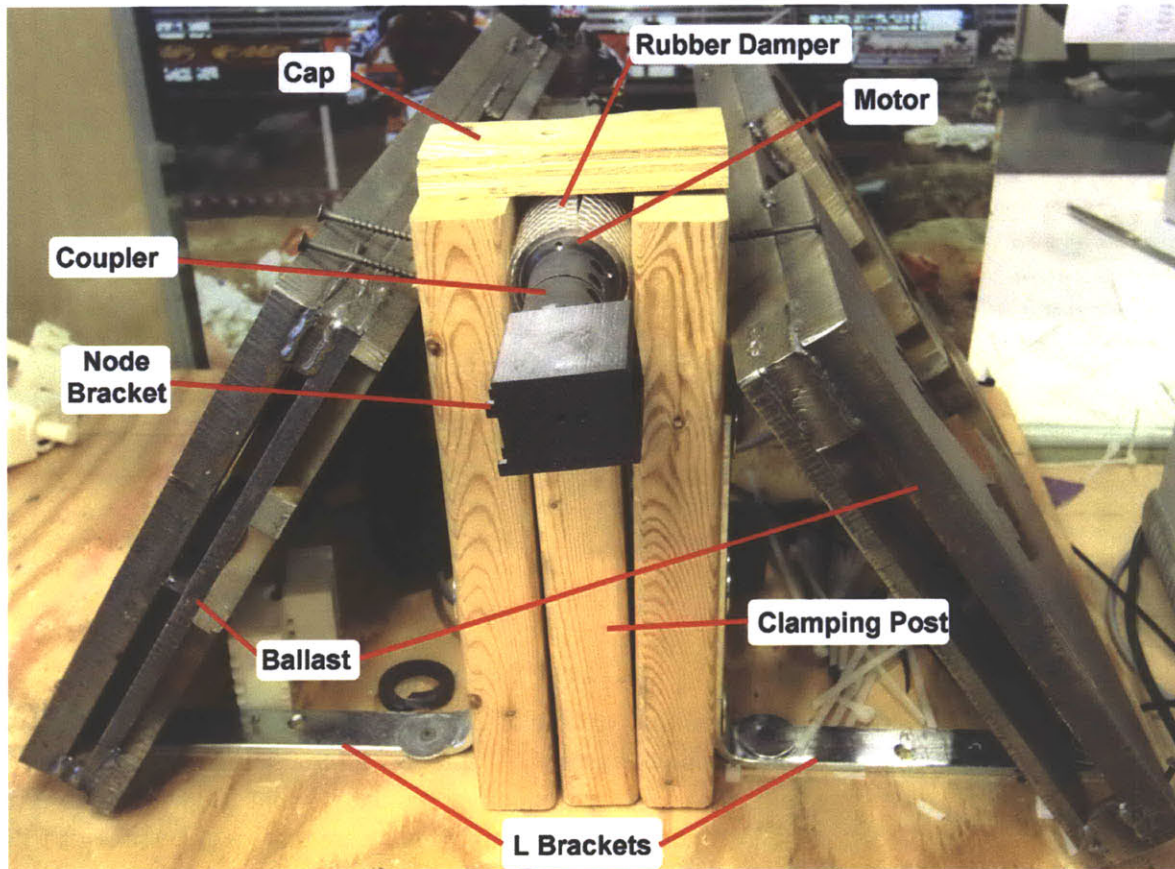
4.2.2.1 Motor and Controller

An electric motor capable of generating the necessary angular velocities was the easiest problem to solve. A suitable motor, the EC-max 40, was readily available from Maxon Motor. It comes standard with a 1000 count per turn precision HEDL encoder. Both components were mated with Maxon's EPOS2 Motor controller operating at 50V. Maxon also offers a Windows application programming (API) interface that allows for automated control of all parameters of the motor. This proved useful in automating the calibration process.

4.2.2.2 Motor Containment

Securing a motor that rotates at over 2700 RPM is no trivial task. A custom ballasted clamping fixture was built to keep the motor in place.

FIGURE 4-31 Calibration Fixture



The fixture evolved in order to meet the angular velocities that it was required to handle. Initially it consisted of only the *L Brackets*, *Clamping Posts*, *Rubber Damper* and *Motor* with its *Coupler*. The motor is sleeved in the

Rubber Damper and then clamped in place by using screws to squeeze the 3 2x4s of the *Clamping Posts* around it. Note the gap between the right and center parts of the *Clamping Post*; all clamping force of the 3 2x4's is exuded on the motor via the damper. This scheme worked well for the low RPM (1465 max.) calibration of low range sensors.

Helloooooo Mr. Dr1scoll, this ones for you.

Unfortunately, calibration of the high range sensors brought to light two issues. First, the *Node Brackets* that hold each node in place required a counterweight to in order to balance the mass while spinning. The counterweight on each bracket does not perfectly balance the bracket, and vibration occurs during high speed rotation. The second was directly related to the high RPM needed to perform calibration (2833 max) where the vibration from imperfectly balanced bracket caused the *Clamping Post*, along with the table it is attached to, to also vibrate. To address this issue 1/2" to 3/4" steel sheets were scavenged from the scrap pile near the MIT Media Lab's water jet cutter and welded together. These *Ballast* sheets, weighing about 150lbs, are attached to the *Clamping Posts* damp the vibration. This ballast alone does not fully solve the problem. The *Node Brackets* were still unbalanced and caused a lot of vibration, addressing this is covered in the following section.

The *Cap* element was added after an incident in which the motor vibrated itself free from the grip of the post and disaster ensued, breaking the bracket.

4.2.2.3 Per Axis Node Motor Attachment

The clamped motor has an un-keyed exposed shaft with a relatively small diameter (6mm). A 6mm to 24mm coupler was attached to the shaft, allowing the attachment of 3D printed plastic *Node Brackets* to the motor. The reason for increasing the diameter via the coupler is due to weakness in the 3D printer's material that required a much larger diameter shaft for strength.

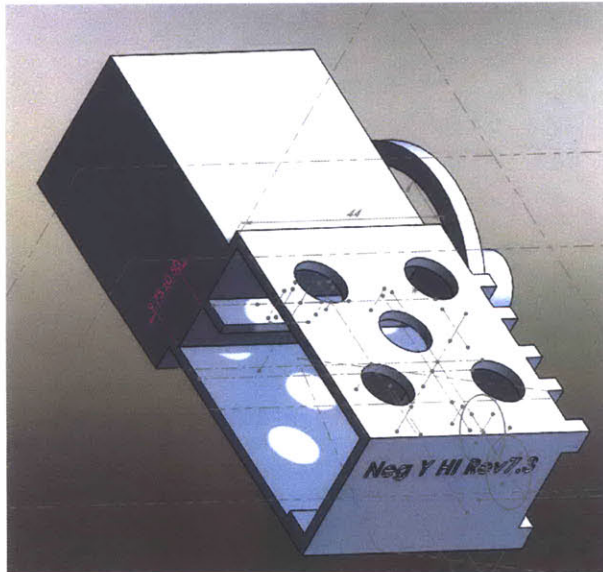


FIGURE 4-32 High Negative Y Axis Bracket CAD Model

As mentioned in beginning of Section 4.2, each axis of each sensor needs to be calibrated. As described in Section 4.2.2 and illustrated by FIGURE 4-32, each accelerometer requires dual calibration, for negative and positive acceleration. Lastly, as also mentioned in Section 4.2.2, for a gyroscope it is desirable to rotate about the center of its axis to avoid acceleration-induced errors.

These parameters dictate that each axis of gyroscope requires its own custom bracket and that each axis of accelerometer requires two, for a total of 6 gyroscope and 12 accelerometer brackets.

A 3D CAD model was developed and refined for each bracket; a sample model is visible in FIGURE 4-32. Each model had an approximated balancing mass added to prevent vibration. An approximation was made because performing the calculations to perfectly balance each bracket is a non-trivial task. Once a bracket was 3D printed, it was manually balanced using a trial and error process of adding and removing material from the bracket. FIGURE 4-33 shows two manually balanced brackets. One needed a significant amount of mass added to balance it and the other had a small amount of mass removed by drilling holes.

4.2.3 Calibration Process

Having defined a process in which about 15 datapoints are taken for each sensed axis to perform a fit, and considering that there are 18 brackets that need to be applied for each node, it quickly becomes apparent that applying roughly 270 different bracket and acceleration/angular velocity measurements **per node** is intractable. Fortunately, Maxon provides an application programming interface (API) for its EPOS2 motor controller that enables programmatic control of the controller and motor via USB.

A module that enabled the PC to control the motor was added to the network control application that manages the network (Section 6.1). This

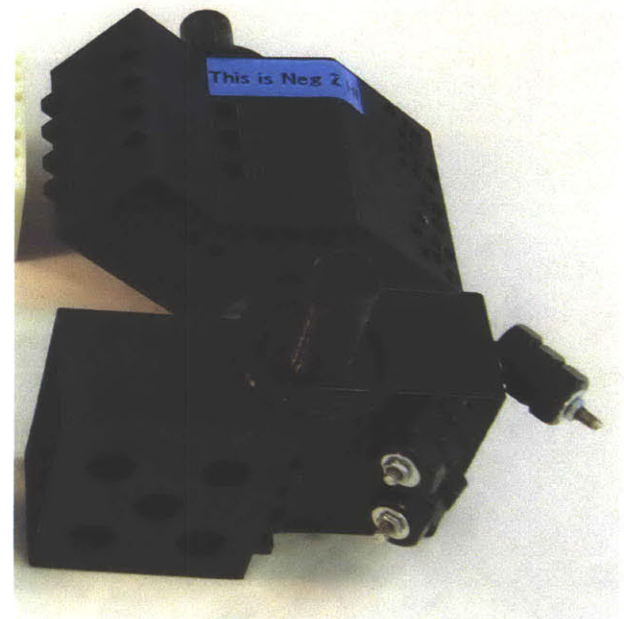
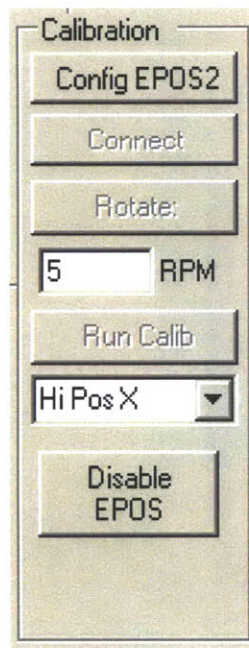


FIGURE 4-33 Hand Balanced Brackets. Removal of mass via drilling holes (Upper Bracket). Addition of mass by placing nuts on threaded screws (Lower Bracket).

centralization of command and control of both the network and the motor allowed automation of the calibration process for each bracket.

A simple user interface (FIGURE 4-34) is presented to the calibration operator. The *Config EPOS2* button opens a configuration dialog for the USB driver that communicates with the motor controller. Once the controller is configured, clicking the *Connect* button creates a connection to the motor and configures its parameters, such as maximum acceleration rate, which is set to 500 RPM/sec. A manual speed control routine is built into the interface for one-off motor rotation, and is activated by filling out the field at left and clicking the *Rotate* button.

FIGURE 4-34 Calibration User Interface



For accelerometer calibration, the details of angular velocity to acceleration mapping for each accelerometer axis are hidden from the operator. The operator simply attaches the appropriate bracket to the coupler, chooses the axis (in the drop down menu below the *Run Calib* button) that matches the bracket, and clicks the *Run Calib* button. The software module coordinates control of starting and stopping data sampling with changing the speed of the motor and iterates through each of the necessary motor speeds while recording data. The same process applies to gyroscope calibration, except there is no need to switch between brackets for positive and negative acceleration or rotation in the gyroscope case.

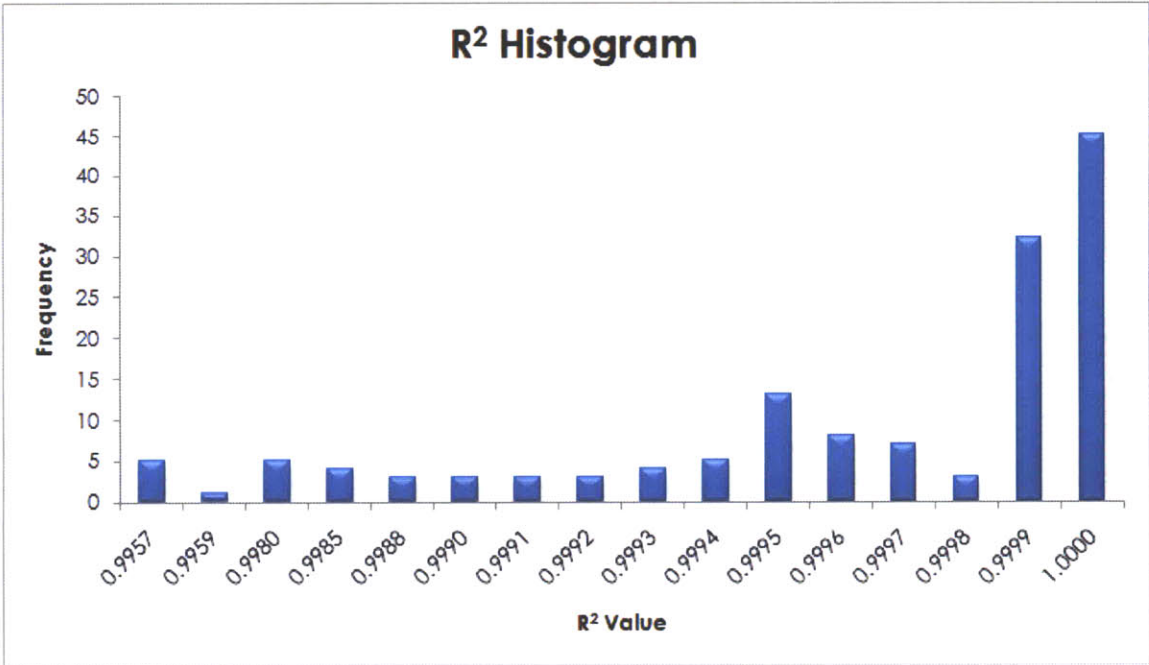
4.2.4 Calibration Results

Calibration yields about 15 datapoints per axis; each of these datapoints are matched to their inertial values and because of the linear nature of all sensors used) a first order polynomial fit is performed using Matlab. This produces a slope and an intercept that are used to generalize mapping of the analog sensor value to true inertial values. A coefficient of determination (R^2 value) is calculated for each to measure the goodness of the fit. Node and axis-specific values are presented in FIGURE 4-35 .

FIGURE 4-35 Sample R² Values For Calibrated Nodes. X, Y, Z are in G's and Pitch, Roll, Yaw are in degrees/sec.

NODE_ID	HI_X	HI_Y	HI_Z	HI_PITCH	HI_ROLL	HI_YAW	LO_X	LO_Y	LO_Z	LO_PITCH	LO_ROLL	LO_YAW
EA	0.993936	0.999616	0.99912	0.999904	0.999845	0.999871	0.999008	0.999503	0.995698	1	1	1
CF	0.999265	0.999487	0.999214	0.999952	0.999841	0.99991	0.998114	0.998759	0.997956	1	1	1
DA	0.999331	0.999519	0.999401	0.999896	0.999835	0.999818	0.998306	0.999387	0.998871	0.999999	1	1
AC	0.999429	0.999524	0.998571	0.999838	0.999887	0.999854	0.998457	0.999678	0.996106	0.999999	1	1
BB	0.999435	0.999592	0.999772	0.99992	0.999815	0.99985	0.999345	0.999896	0.998498	1	1	1
EF	0.9996	0.999369	0.999226	0.999881	0.999854	0.999893	0.998906	0.996621	0.996083	0.999995	1	1
DC	0.999622	0.99954	0.99945	0.999888	0.999858	0.99986	0.999012	0.999424	0.995481	0.999999	1	1
CB	0.999624	0.999026	0.998717	0.9999	0.999903	0.999882	0.99665	0.999892	0.994402	0.999997	1	1
AA	0.999659	0.999556	0.999156	0.999904	0.999856	0.999908	0.999367	0.999287	0.995876	1	1	1
BA	0.99967	0.999474	0.999439	0.999885	0.999814	0.999859	0.999908	0.999482	0.999181	0.999999	1	1
FA	0.999771	0.99948	0.999917	0.999896	0.999893	0.999868	0.999714	0.999566	0.99962	1	1	1
DB	0.999867	0.9995	0.998892	0.999895	0.999853	0.999848	0.999416	0.999491	0.994984	1	1	0.999999

FIGURE 4-36 Generalized Histogram of R² Values in FIGURE 4-35



The fit for the low range gyroscope is 1.0 for nearly all nodes and overall the minimum coefficient of determination is 0.993936. This minimum is still a very good fit and indicates that the calibration excellently maps from analog to inertial values and that the output of each sensor is near linear. The histogram in FIGURE 4-36 shows this. A detailed analysis and quantification of the error introduced during calibration is presented in Section 8.1.1.

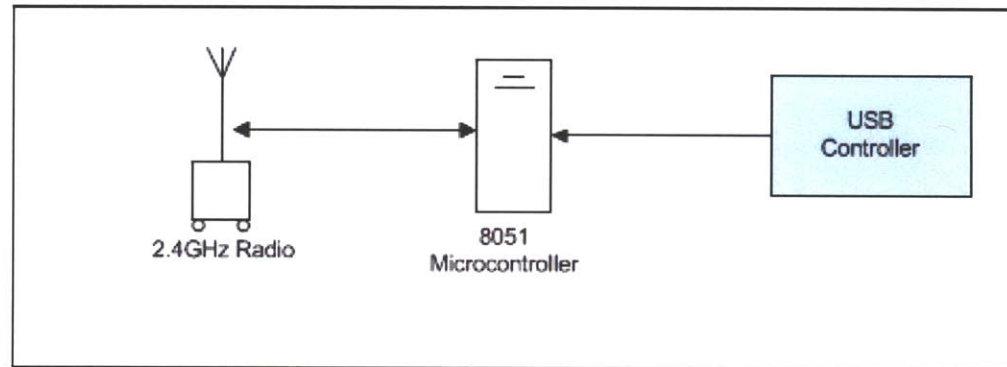
4.3 NETWORK CONTROL BASESTATION

.....

Although the RF protocol has been entirely re-designed, the basestation is the only piece of hardware that is reused from the Senseble project and a high level summary will be presented here. A detailed description is available in Ryan Aylwards Masters Thesis [74] and the author's Masters Thesis [7]. It is important to note that only the hardware has been reused. The firmware and client side code that controls the basestation are all specific to the new node hardware and athletic activity.

The basestation has essentially 2 pieces of hardware, a limited capability microcontroller that can act a a USB slave and a wireless transceiver. The wireless transceiver is the same Nordic nRF2401[76] that is used in the node. The microcontroller is a Silicon Labs C8051F320 [77] running at 24MHz. It reads commands via a USB connection to a host PC, interprets them and instructs the nRF2401 to transmit the data wirelessly to the network of nodes via a Serial Peripheral Interface.

FIGURE 4-37 Basestation Block Diagram



4.3.1 Optical System Synchronization

The basestation is in real time communication with the network and is the hardware gateway into the network and into the host PC, which makes it the ideal place to implement hardware synchronization with external optical systems. Because it is the chosen optical platform by my MGH collaborators, Vicon is the system with which synchronization capability has been built for. The Vicon system provides a method of configuring a digital output on their custom hardware that pulls the pin to logic high when the system starts capture and goes low when the capture stops. This output pin is wired to an available GPIO pin on the basestation's MCU. The firmware of the basestation monitors this pin for changes, calculates synchronization offsets and transmits them to the host PC via its USB peripheral. The details of this are documented in the basestation firmware section (5.1).

4.4 DATA TRANSLATOR

As briefly described in 3.2.2, a custom data retrieval interface needed to be implemented in order to read data from the μ SD, because it is written to the card as raw sectors, not a standard filesystem. Instead of building a custom piece of hardware, the Atmel EVK1101 [78] development board was leveraged. The EVK1101 is an all-in-one platform for developing test applications for the Atmel UC3B0256 microcontroller, the same microcontroller used in hardware revision 2 of the wireless inertial node. Having the development environment and familiarity with the board made it a natural choice. Other than a μ SD to SD adapter, no hardware modifications were made to the board and it was used as-is.

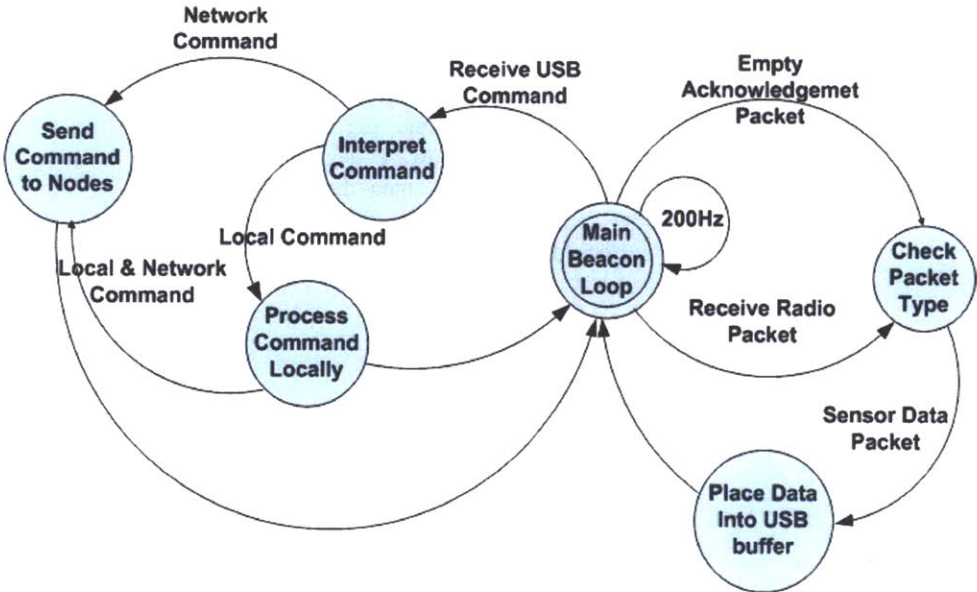
THE INTANGIBLE

The intangible is something that cannot be seen or touched. Here it consists of the firmware that operates the tangibles. The operating principals of three hardware devices are described, starting with the basestation, then the inertial node(s) and lastly, the data translator, in order to better understand how the system functions as a whole.

5.1 BASESTATION

The basestation is the starting point in describing the intangible, because it is the gateway from the graphical user interfaces into the intangible world of microcontrollers and wireless communication. Its behavior is dictated by a USB host master running a control application. All communication between the PC and basestation is based on a command protocol. The hardware for the basestation is described in 4.3 and [7][74]. A state diagram of the basestation is presented in FIGURE 5-38 .

FIGURE 5-38 Basestation State Machine



The basestation microcontroller (MCU) operates at 24MHz and its *Main Beacon Loop* runs at 200Hz based on internal *Timer 1*. Every time an interrupt is fired from *Timer 1*, the MCU updates the current global system timestamp and transmits a packet to the network. This beaconing is also used to synchronize the network. Each beacon packet contains a timestamp, which is logged on each node when recording data. Because of this timestamp, the precision of the network’s synchronization is on the order of microseconds.

While not servicing the *Main Beacon Loop*, the MCU is servicing any requests and commands that are delivered via the USB peripheral. These commands fall into two categories, *Local* and *Network*. *Local* commands are used to configure the basestation and its behavior and do not get sent over the wireless link to the network. *Network* commands, as their name indicates, are transmitted wirelessly to the network of nodes.

FIGURE 5-39 Basestation Local Commands

Command Hex	Command name	Command Short Description
0xDE	NUM_NODES_CMD	Set the number of nodes that are present in the network.
0xAA	RF_CONFIG_CMD	Set the Radio Frequency base channel and the number of channels that will be used.
0xCA	RESET_RF_STATS	Reset packet loss counters for RF channel testing.
0xFF	IDLE	Do nothing; only beacon.
0xDF	NODE_ACTIVE_CMD	Set a specific node as active in gathering data.
0xDD	RESET_CAMERA_SYNCH_DATA_CODE	Reset all optical system synchronization counters.

Local commands are presented in **FIGURE 5-39** and *Network* commands are presented in **FIGURE 5-40** . The mechanism for the basestation to communicate back to the host PC is a *USB Buffer* that is filled and transmitted to the host PC via the MCU's USB peripheral.

The *NUM_NODES_CMD* informs the basestation as to how many nodes will be operating in the network. It is complemented by the *NODE_ACTIVE_CMD* command, which specifies whether a specific active node is gathering data. This is a crucial mechanism for allowing the network to continue operation even with a node that maybe misbehaving and not able to gather data.

The *IDLE* command instructs the basestation to do nothing. The commands *RF_CONFIG_CMD* and *RESET_RF_STATS* are used to configure the communication frequencies used and reset counters and parameters related to testing the RF environment quality. The *RESET_CAMERA_SYNC_DATA_CODE*, is covered in the optical system synchronization sections **5.1.1**, **6.1.8** and **7.4**.

FIGURE 5-40 Basestation Network Commands

Command Hex	Command Name	Command Short Description	Reply Expected
0xBA	NEXT_PACKET	Request for specific sample number	Yes
0xBB	SAMPLE_2_FLASH	Sample data to <u>microSD</u> Card	Yes
0xBC	ERASE_FLASH	Erase <u>microSD</u> Card	No
0xAA	RF_CONFIG_CMD	Set the Radio Frequency base channel and the number of channels that will be used	No
0xCB	TEST_RF_CHANNEL	Insert TX/RX packet counts into packet.	Yes
0xCA	RESET_RF_STATS	Resets RF channel test packet loss counters	No
0xAB	GET_SAMPLE_CNT_CMD	Queries the network for how many files and sample counts	Yes
0xDC	GET_FILE_NAME	Ask a specific node for a specific filename	Yes
0xBE	GET_ERROR_COUNT	Get number of errors recorded by a specific node	Yes
0xC0	GET_ERROR_CODE	Get code for a specific error from a specific node	Yes

Network commands have the additional property of determining whether or not a reply is expected from the node once it has received and processed the packet. A reply is not expected from all commands except the *RF_CONFIG_CMD* command. This is because, if the network is reconfigured to a different frequency, the node will be broadcasting on the new frequency, which the basestation is not yet utilizing. Further, the *RF_CONFIG_CMD* is considered to be a *Local* and *Network* command because both the basestation and nodes must process it. The *TEST_RF_CHANNEL* command adds additional data to all packets that allow for calculating packet loss metrics for the network. The *RESET_RF_STATS* command resets received/transmitted packet counters on the node. These counters are used to measure the RF channel quality.

The *NEXT_PACKET* command, whose purpose was to send a specific data sample wirelessly, has been deprecated because the packet length can no longer handle all of the sampled sensor data. The expected reply packet contained the analog sensor data from a given sample number, and when this data was received it was placed into the *USB Buffer* and transmitted to the host PC.

The *SAMPLE_2_FLASH* command instructs the network to begin sampling data. The basestation continues to beacon this command until interrupted via USB by the host PC or until it has received a packet indicating from every node in the network that it finished its sampling loop. Which nodes are expected to reply is based on previous *NUM_NODES_CMD* and *NODE_ACTIVE_CMD* commands.

The *ERASE_FLASH* command instructs each node in the network to erase its μ SD card and the MCUs own internal flash, which stores various counters and memory allocation information for previously sampled data. A reply is expected from each node when the data has been erased. Again, which

nodes are expected to reply is based on previous *NUM_NODES_CMD* and *NODE_ACTIVE_CMD* commands.

¹¹Please refer to Section 3.1.0.3 for definition of a gesture

The *GET_SAMPLE_CNT_CMD* requests the number of *gestures*¹¹ of data that have been recorded by each node and also the number of samples per *gesture*¹¹.

The *GET_FILE_NAME* command requests a specific filename from a specific node based on a numerical index. This index is sent by the PC host and inserted into the outgoing packet. The index indicates which name in the list of filenames is to be transmitted back by the node.

A *GET_ERROR_COUNT* command requests the value of a specific node's internal error counter - a count of how many errors the node has experienced. It is complemented by the *GET_ERROR_CODE* command, which is sent to a specific node with a specific error code *index*. The specified node selects the *index* error code in its error code list and transmits it back to the basestation.

It is easy to see that the basestation is an arbiter between the host PC and the network of nodes that does some simple bookkeeping to track which nodes are present on the network and how they are expected to behave.

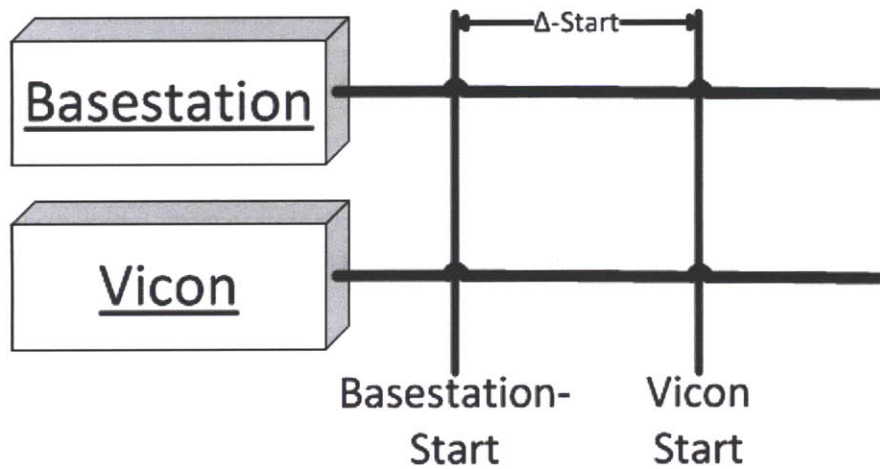
5.1.1 Optical System Synchronization

Section 4.3.1 describes the hardware interface between the wearable network and the Vicon optical capture system in order to synchronize them. The bulk of the synchronization is handled by the basestation firmware and the logic is based on monitoring the Vicon output pin (an input to the basestation) to see if the optical system is recording or not.

The synchronization starts when the basestation receives a *SAMPLE_2_FLASH* command from the host PC and the Vicon GPIO pin is logic zero. When this command is seen, the basestation starts a counter that

measures the number of milliseconds that have elapsed since it was received; the start of this timer indicates the start time of data recording. The only delay that is present is that of transferring the data packet to the nRF2401 and its wireless transmission. This delay is on the order of μ seconds and presents negligible error into the synchronization. Once the Vicon GPIO pin changes state to logic high, indicating the optical system has start recording, the counter is stopped and read. This reading yields Δ -Start, which represents the amount of time that the wearable inertial system was recording before the optical system started. In order to synchronize the two systems, Δ -Start milliseconds of data must be pruned from the start of any inertial data stream.

FIGURE 5-41 Optical Synchronization Timing Diagram

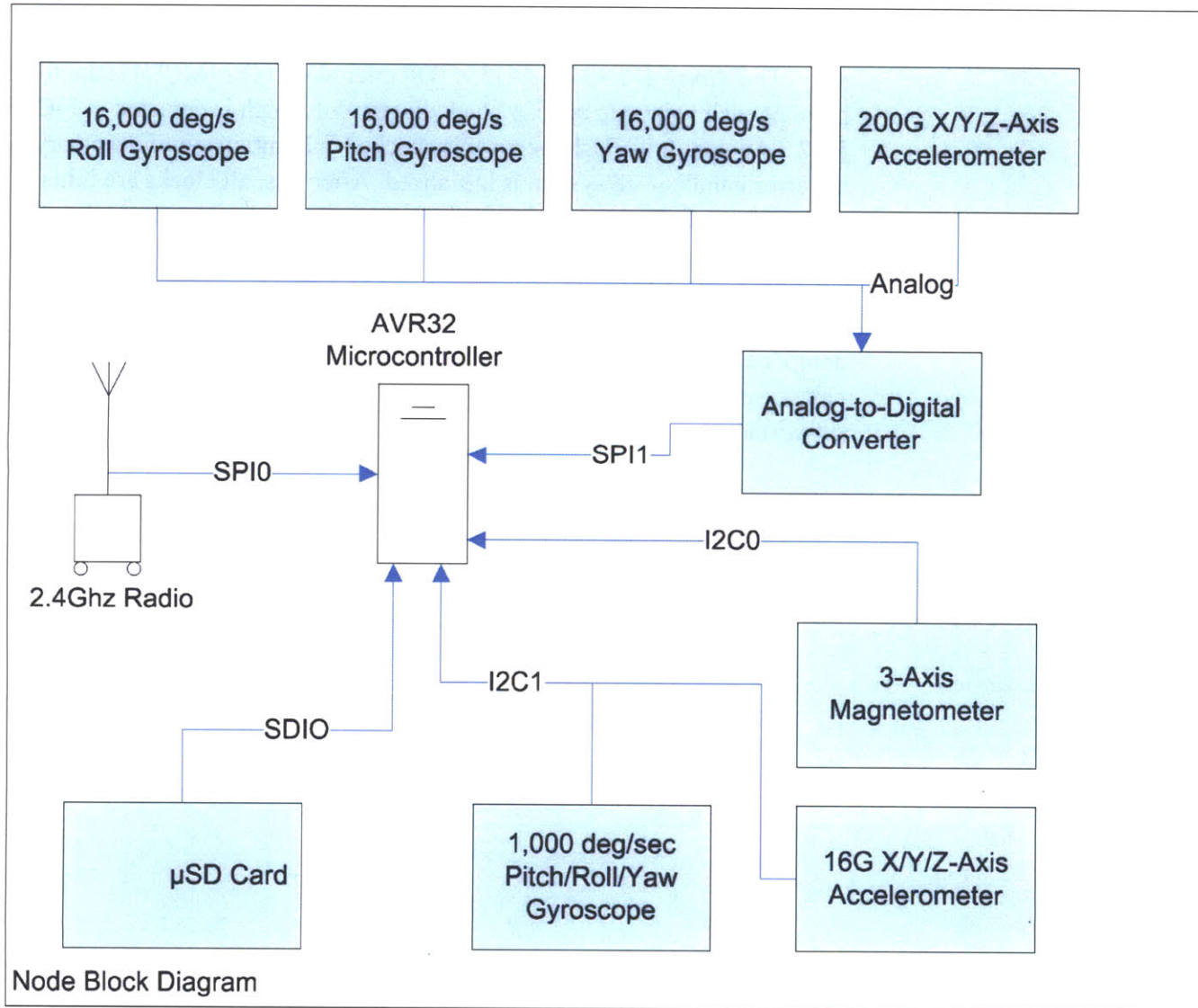


5.2 NODE STARTUP

.....

The *Atmel AVR32 UC3A3256* [79] microcontroller (MCU) is the focal point of each wearable node, a block diagram of which is depicted in **FIGURE 5-42**. At startup its flash memory is checked and initialized, if necessary, and the error handling subsystem is initialized. After this, all clocks are initialized and configured. With properly configured clocks, all communication peripherals can be configured and tested. Once communication buses have been made available, each connected hardware device can be configured for operation and queried to ensure it is operating properly. Once all hardware components and subsystems have been confirmed to be properly working, the node begins servicing interrupts and processing command data packets from the wireless transceiver.

FIGURE 5-42 Wearable Inertial Node Block Diagram



5.2.1 Flash Memory

The MCU's internal flash memory is used as persistent storage for several system level variables; their organization is documented in Table 4 on page 97. Once a node has been freshly programmed with firmware and booted, the first action of the MCU is to check for a specific *SIGNATURE_BYTE* value in the flash memory. If the *SIGNATURE_BYTE* value is not found, the flash memory is allocated, initialized and the *SIGNATURE_BYTE* is set.

Table 4: Flash Memory Variables

Name	Description	Size
SIGNATURE	Signature Byte	1 x byte
startSector	List of μ SD card sector numbers where a datasets start	MAX_DATA_SET_CNT x int
endSector	List of μ SD card sector numbers where datasets end	MAX_DATA_SET_CNT x int
fileName	Operator specified filename	char x MAX_DATASET_CNT x 6
dataSetIndex	Index of next dataset to be recorded	1 x int
resetCount	Number of times the node has been booted up	1 x short
errorCount	Number of errors recorded by the node	1 x int
errorCodes	List of error codes	MAX_DATASET_CNT x byte

5.2.2 Error Handling Subsystem

With the flash memory properly configured, the error handling subsystem can operate correctly. In the node firmware there are two types of

errors, *RECOVERABLE* and *FATAL*. Additionally, there is a predefined list of *ERROR_CODES* that are unique to a specific piece of logic in the code. This

allows for rapid diagnosis of any problems that arise during node operation. For example, if there is a problem establishing communication to the radio transceiver, a *NRF_SELECT_SPI_ERROR* (unique HEX value 0x16) error is generated. Because each error code is unique to a piece of logic, doing a lookup of HEX error code 0x16 pinpoints the communication problem instantly. A partial list of error codes is available in **FIGURE 5-43**.

When a *RECOVERABLE* error is encountered, its error code is written to the *errorCodes* array in flash memory, the *errorCount* is incremented, written to flash and the node continues operation. When a *FATAL* error is encountered, the error code is also written to the *errorCodes* array and the *errorCount* incremented. However, the node then goes into a infinite loop and flashes 2 LED's alternately to indicate that is in an unrecoverable error state.

This method for recording errors is complemented by the *GET_ERROR_COUNT* and *GET_ERROR_CODE* commands that are used by the Host PC application and basestation to read the codes from the node.

5.2.3 Clocks and Peripheral Bus

When the MCU powers up, its main clock is switched from an internal oscillator to an external crystal and the chip runs at 60MHz. Additionally, Oscillator 0 is configured to run at 12MHz and Peripheral Bus A is configured to run at 30 MHz.

5.2.4 Communication Peripherals

There are five communication interfaces that are utilized on the AVR32 MCU, two Serial Peripheral Interfaces (SPI) [80], two two-wire interfaces (also known as I²C) [81] and one Secure Digital Input Output (SDIO) interface [82].

FIGURE 5-43 Partial List of Error Codes

NRF_SELECT_SPI_ERROR	0x16
NRF_DATA_WAITING_ERROR	0x17
NRF_ENABLE_GPIO_INT	0x18
NRF_ENABLE_GPIO_MODULE	0x19
NRF_SETUP_CHIP_ERROR	0x1A
NRF_SELECT_SPI_ERROR_2	0x1B
NRF_ENABLE_GPIO_INT_2	0x1C
MAIN_ERROR_SDIO_WRITE_OPEN_1	0x21
MAIN_ERROR_SDIO_WRITE_SECTOR_1	0x22
MAIN_ERROR_SDIO_WRITE_CLOSE_1	0x23
MAIN_ERROR_SDIO_WRITE_OPEN_2	0x24
MAIN_ERROR_SDIO_WRITE_SECTOR_2	0x25
MAIN_ERROR_SDIO_WRITE_SECTOR_3	0x26
MAIN_ERROR_SDIO_WRITE_SECTOR_4	0x27
SAMPLE_DATA_MUX_ERROR	0x31
SAMPLE_TIMER_ERROR_1	0x32
SAMPLE_TIMER_ERROR_2	0x33
START_LO_ACCEL_ERROR	0x34
STOP_LO_ACCEL_ERROR	0x35
START_LO_GYRO_ERROR	0x36
STOP_LO_GYRO_ERROR	0x37
GPIO_INTERRUPT_ERROR	0x41
DATASET_SPI_WRITE_OPEN_ERROR	0x42
DATASET_SPI_WRITE_SECTOR_ERROR	0x43
TWI_ENABLE_GPIO_MODULE	0x44
TC_READ_RC_ERROR	0x45
TC_READ_RC_ERROR_2	0x46
INIT_FAT_ERROR	0x47

All three are bus interfaces supporting multiple devices, however in this implementation the bus feature is not used for all interfaces. In all cases the MCU is the master, while the connected devices are slaved.

The zeroth SPI bus (SPI0) is used to communicate with the radio transceiver. It is clocked at 4MHz and is exclusively used by the radio to allow for servicing of incoming radio packets at any time. One clock pin and two data lines (one input and one output) are utilized for communication. A chip select pin is also dedicated to each specific device on the bus. In this case, there is a chip select pin wired to the transceiver.

The first SPI bus (SPI1) is used to communicate with the analog-to-digital converter. Is it also clocked at 4MHz and exclusively dedicated to the analog-to-digital converter because no other SPI devices exist in the system. As with SPI0, one clock pin and two data lines are used for communication.

The one and only SDIO bus has one μ SD card slot wired to it, and, because it is a high speed interface, it operates at 30MHz. The node design exploits the parallel mode of operating the SDIO interface and has a command pin, clock pin and four data pins dedicated to it.

I²C bus zero is dedicated to the on-board magnetometer and operates at a clock speed of 400 kHz for communication. As the two-wire interface name suggests, there are two pins dedicated to an I²C device, one as a clock and one for data.

I²C bus one makes use of the multi-device bus feature and communicates with the low- range gyroscope and the low-range accelerometer. Each of these devices is also clocked at 400 kHz. Again, two pins are dedicated to I²C1, one for clocking and one for data.

5.2.5 Hardware Devices

Once all communication peripherals are have been initialized without error, individual device configuration can occur.

5.2.5.1 μ SD Card

The μ SD card is connected via the *SDIO* bus. In previous versions of the node hardware, *SPI*-based communication was used to read and write from the SD card and its serial nature created a bottleneck in the system while writing sampled data to the card. One of the motivations for choosing the UC3A3 MCU was that it features a dedicated and parallel, therefore much faster, *SDIO* bus. Along with the hardware peripheral, *Atmel* provided a software framework [82] and a library for programmers and took the complicated process of implementing the *SDIO* Specification[83] upon themselves. Once the *SDIO* peripheral has been configured, the programmer calls a single function to negotiate and establish communication with the card. After this, the card can be opened/closed and sectors can be written and deleted.

5.2.5.2 High Range Gyroscopes

The *ADXRS649* [84] high range gyroscope has an analog output and does not communicate directly with the MCU, hence it does not have any software-based configuration. However each gyroscope uses external filtering capacitors to limit its output bandwidth to 500Hz, to avoid aliasing. The output of the three onboard *ADXRS649* gyroscopes is sampled by the *Analog Devices AD7606* [85] analog-to-digital converter and transmitted to the MCU via *SPI1*.

5.2.5.3 High Range Accelerometer

As with the high range gyroscopes, the *Analog Devices ADXL377* [88] high range accelerometer only has analog outputs, which are sampled by the analog-to-digital converter. It is also bandwidth limited by external filtering

capacitors, which are matched to chip-internal resistors for anti-aliasing to 500Hz.

5.2.5.4 Analog-to-Digital Converter

The *Analog Devices AD7606* 16-bit analog-to-digital (A2D) converter is connected to the MCU via *SPII*. It has no other software based configuration, and all of its functionality and communication is based on GPIO pins that are wired from the A2D to the MCU. The *SPII* bus is used only to transmit six 16-bit analog-to-digital conversion values to the MCU. The GPIO pins that are used are as follows:

- 1 *CONV_CTRL* - wired to the chip's *CONVST A* and *CONVST B* pins. The MCU drives this pin and a transition from logic 0 to logic 1 starts the analog-to-digital conversion process.
- 2 *A2D_BUSY* - while the conversion is active, this pin is held in logic 1, and when finished the A2D transitions the pin to logic 0. The MCU internally polls this pin to determine when conversion data is available.
- 3 *A2D_RESET* - The MCU can pull this pin low to reset the A2D.

Specific configuration parameters are configured using external pins present on the *AD7606* chip itself. Other than power and ground pin connections, there are three other pins that control the A2D's behavior. They are:

- 1 Communication Interface - the $\overline{PAR/SER/BYTE SEL}$ pin is pulled up to logic 1. The puts the chip in SPI communication mode.
- 2 Standby - the \overline{STDBY} pin is pulled up to logic 1, keeping the chip out of standby mode at all times.
- 3 Reference Voltage Selection - set to logic 0, allowing the A2D to use its own internally-generated reference voltage.

5.2.5.5 Low Range Gyroscope

The *Invensense IMU-3000* [87] 3-axis gyroscope is the first part we discuss that is exclusively¹² controlled and configured via software and does not require any external parts to configure its sensing capability. The process for configuring the *IMU-3000*, is by setting specific values in registers that are stored in its own EEPROM. As a sanity check after each register is written to the *IMU-3000* it is then read back and compared to the expected value. If there is an inconsistency, a *FATAL* error code is generated.

The target sampling rate for the *IMU-3000* is its maximum rate of 5Hz and its desired range is $\pm 1,000^\circ/\text{second}$. Because of this, the register that controls its low pass filters and scale (0x16) is set to 0x10, which yields a 256Hz low pass filter and $\pm 1,000^\circ/\text{second}$ range.

When the low pass filter register is configured for the *IMU-3000* internally to cutoff at 256Hz, the internal analog gyroscopes are sampled at 8kHz. This sampling rate must be scaled down via a sample rate register to match the desired sample rate of 500Hz. This is achieved by writing a value of 0x0F to the appropriate register (0x19).

Now that the behavior of the *IMU-3000* has been configured, the interrupt it generates for the MCU to inform it when gyroscope data is ready is configured. The interrupt is physically enabled by wiring the *IMU-3000's AD0* pin to a GPIO pin on the MCU. Additionally, the *IMU-3000* is configured to generate an interrupt when data is ready and clear the interrupt when any register is read by setting a value of 0x31 to register 0x17.

5.2.5.6 Low Range Accelerometer

Similarly to the low range gyroscope, the *Analog Devices ADXL345* [88] low range accelerometer is also fully configured using a software interface¹², and has an interrupt pin wired to the MCU to inform it when data is available. It also has a set of registers that are written to configure its operation.

¹²except for a pin that is pulled down to specify I²C address

As with the *IMU-3000*, the desired sampling rate for the *ADXL345* is 500Hz, however the chip only supports 400Hz and 800Hz sampling. The 800Hz option was chosen to maximize the amount of data available. This required setting the bandwidth rate register (0x2C) to 0x0D.

The interrupt map register (0x2F) is configured to transition the *ADXL345*'s *INT1* pin from logic 0 to logic 1 when data is available by setting its value to 0x7F. The interrupts are enabled by setting a separate register (0x2E) to 0x80.

5.2.5.7 Magnetometer

The *Honeywell HMC5843* [89] magnetometer is configured via software in the same EEPROM register-writing manner as the low range gyroscope and accelerometer. Two registers need to be written to configure the magnetometer as desired. The sampling rate is set to the maximum of 50Hz by writing 0x18 to Configuration Register A (0x00). The device is started and set to continuous-conversion mode by writing 0x00 to the mode register (0x02).

5.2.5.8 RF Transceiver

In addition to communicating on *SPI0*, the *Nordic NRF2401* [76] has three additional pins that are wired to the MCU for proper radio operation. These are a chip enable pin (*CE*), a power up pin (*PWR_UP*) and a data ready pin (*DR*). The *CE* pin is used to toggle the radio between standby and receive/transmit modes. The *PWR_UP* pin is used to turn the radio on and off. The *DR* pin indicates when the radio has received a full data packet and is ready for the MCU master to read it from the radio. All of these pins are configured in the MCU as general purpose input/output (GPIO). Additionally, a service interrupt is associated with the *DR* pin transitioning from logic zero to logic one.

With a properly configured SPI bus and associated GPIO pins, the radio is set to standby mode and the configuration data (packet length, network address, operating frequency, datarate) is sent over the SPI bus. Once configured, the transceiver is set to receive mode and the MCU waits for an interrupt on the *DR* pin.

5.3 NODE OPERATION

.....

Each wearable node is controlled by the *Network* commands (FIGURE 5-40) broadcast by the basestation. An interrupt is fired when the radio receives a valid data packet. The packet is read from the radio by the MCU and decoded to determine what command it contains. Based on the command, the MCU reacts and takes action. The behavior of the node will be documented here for all commands except those that pertain to RF configuration and testing.

5.3.0.1 Error Commands

The *GET_ERROR_COUNT* and *GET_ERROR_CODE* commands are used together to read errors from the node. When *GET_ERROR_COUNT* is received by the node, the *errorCount* (Section 5.2.1) is read from the flash memory, packaged into the next RF packet to be transmitted and sent back to the basestation. A *GET_ERROR_CODE* command is accompanied by an integer *index*. This index is used to read the *index* error code in the *errorCodes* flash memory array (Section 5.2.1) and copy them into the next outgoing RF packet such that it can be transmitted back to the basestation.

5.3.0.2 Idle Command

When an *IDLE* command is received by a node, the global *SYSTEM_STATE* of the node is set to *SYS_IDLE*, to indicate that the node is idle, and a packet with no payload is transmitted back to the basestation.

5.3.0.3 Next Packet Command

As mentioned in 5.1, the *NEXT_PACKET* command is deprecated and is no longer tractable to support. When a node receives a command of this type it is treated in the same manner as a *SYS_IDLE* command.

5.3.0.4 Erase Flash Command

The *ERASE_FLASH* command erases the contents of the MCU's internal flash that is used for storing data (Section 5.2.1) and also erases the sectors of the μ SD card that have sampled data stored on them. After this, all counters used to keep track of sector position on the μ SD card and those stored in the MCU's flash are re-initialized to zero and the *SIGNATURE_BYTE* is re-written to flash.

5.3.0.5 Sample to Flash Command

The most complicated of all commands is the *SAMPLE_2_FLASH* command. When received, the node goes into a data gathering loop and gathers data for a predetermined number¹³ of seconds at 1000Hz for the high range sensors, 500Hz for the low range sensors and 50Hz for the magnetometer. The global *SYSTEM_STATE* variable is set to *SAMPLING_TO_FLASH*.

All data is stored in two RAM buffers that are 512 bytes in size. Which buffer is currently being used to store data is determined by what buffer is currently being written to the μ SD card. If a buffer is in the process of being written, new data cannot be added to it, as this would cause inconsistencies in the data. There are two types of data: magnetometer and inertial. Both types

¹³Typically 8 seconds.

have a set length of 28 bytes. This is the minimum number of bytes that can be used to store a *SAMPLE_NUMBER*¹⁴, a global timestamp (provided by the basestation in the incoming packet) and the analog inertial sensor data. Rather than deal with the overhead needed to handle variable length data packets, the 10 bytes of magnetometer data are padded to make the data length 28 bytes. A global index into the data buffer is kept, and before any data is stored into a RAM buffer, a check is done to ensure that storing 28 bytes will not exceed the 512 byte length of the buffer. If a store will exceed the 512 length, the current buffer is marked to be stored to the μ SD card and the other buffer is utilized.

Each *SAMPLE_2_FLASH* command packet is accompanied by a 6-byte filename. This filename is written to the first sample section of the current 512-byte data buffer. It is uniquely identified by 4 signature bytes and is called the *HEADER_DATA*.

The entire process is managed by an internal timer that fires once every millisecond. When a *SAMPLE_2_FLASH* command is received, this timer is started. Each time the timer is fired, a series of decisions and actions are taken based on the current *SAMPLE_NUMBER*¹⁴.

The first check that is performed is to determine whether the magnetometer should be read or not. This is done by taking the modulus of *SAMPLE_NUMBER* by 20. If the result is zero, the compass' 50Hz sampling should have data ready, then a Direct Memory Access (DMA) transaction is initiated and started. If the result of the modulus is not zero, a global variable that stores the state of the magnetometer's DMA transaction is read. If this variable indicates that the transaction has completed, the magnetometer data is copied to the current μ SD card buffer. If neither condition is met, no action is taken.

Every time the timer fires, the *AD7606* is queried for new high range data from the *ADXL377* and the *ADXRS649*'s. This data is stored into the current RAM buffer. After sampling high range data, the GPIO pins for the

¹⁴ *SAMPLE_NUMBER* is simply a counter that is initialized to zero when the timer is configured and started. It is incremented by one every time the timer fires.

ADXL345 and *IMU-3000* are checked to determine if data is ready. If data is available from the *ADXL345*, its data registers are read and the results are stored in the current RAM buffer. Otherwise, NULL values are stored into the current RAM buffer. The same approach is taken with the *IMU-3000*.

If the current *SAMPLE_NUMBER* has reached the global maximum number of samples, the timer is stopped and the global *SYSTEM_STATE* variable is updated to *FLASH_FULL*. A full dataset has been successfully recorded and relevant data that is stored in flash memory (Section 5.2.1) can be appended and updated. This means that the *startSector* of the currently completed dataset is appended, as is the *endSector* and *fileName*. The *dataSetIndex* is read, incremented by 1, and written again. Additionally, sector 1 of the μ SD card is reserved for metadata and is written out. This metadata consists of the *dataSetIndex*, which is useful when the μ SD card is being read by other devices to know how many datasets the device should expect to read. Additionally, this sector has a unique *NODE_ID* and *NODE_LOCATION* written to it. *NODE_ID* is a hexadecimal globally unique identifier and *NODE_LOCATION* ranges from one to five and indicates where on the body the node is attached.

5.3.0.6 Pseudo-Command Continuous Mode

Continuous mode is not a discrete command, however it enables enough functionality to be considered a pseudo-command. The continuous mode command allows the system to record data in a continuous manner, only pausing briefly to maintain synchronization with other nodes on the network.

The continuous mode command is enabled (or disabled) by setting a byte in the *SAMPLE_2_FLASH* command. If this byte is set, the node also expects a 1 byte *SEQUENCE_NUMBER* to be set in the packet.

When sampling to flash is initiated and the *CONTINUOUS_MODE* byte is set, the node reads the *SEQUENCE_NUMBER* from the packet and places it

into the *HEADER_DATA*¹⁵ sector that is to be written to the μ SD card. While sequence numbers could be auto incremented in the node, a decision was made to allow the host PC to increment the sequence number in case any nodes become very desynchronized from the network.

During a single sampling window, the node's behavior is identical to that of the normal sampling process described in the previous section. Once a window has been concluded, the node pauses sampling and waits for a packet from the basestation. When received, this packet will contain a new timestamp and possibly the *SAMPLE_2_FLASH* command will cause the *CONTINUOUS_MODE* byte to be set. If it is, another sampling window is executed with an updated *SEQUENCE_NUMBER*. If not, the node sets its *SYSTEM_STATE* variable to *FLASH_FULL*.

¹⁵ *HEADER_DATA* is described in Section 5.3.0.5

5.3.0.7 Sample Count Command

The *GET_SAMPLE_CNT_CMD* command is used to determine how many datasets have been recorded by the node. When received, the node reads the *dataSetIndex* flash variable (Section 5.2.1), and places the read value into the next packet to be transmitted back to the basestation. The *dataSetIndex* counts how many datasets have been recorded and also the pointer used to index the *startSector*, *endSector* and *fileName* arrays stored in flash.

5.3.0.8 Get Filename Command

The *GET_FILE_NAME* command is accompanied by an *index* value that is stored in the incoming packet. This value is read from the packet, and the filename that is stored in the *index* location of the *fileName* flash array is copied into the next packet to be transmitted back to the basestation.

5.4 DATA TRANSLATOR

The data translator (described in Section 4.4) is a crucial piece of hardware responsible for reading the raw data sectors from the μ SD card, which contain all sampled data on a given node, and transferring them over USB to a host PC that can decode the data and store it into a database.

Similarly to the basestation, the card reader is simply an arbiter between the host PC and the μ SD card itself. Also similarly to the SDIO portion of the node firmware (Section 5.2.5.1), the USB configuration is handled by leveraging an *Atmel*-provided library that conforms to USB communication standards. The same SDIO library is used to communicate and read sectors from the μ SD card, as was introduced in Section 5.2.5.1.

Once USB connectivity has been established with the host PC and the SDIO peripheral has been initialized, the μ SD card is opened and the MCU awaits commands requesting sectors.

When the host PC application asks for a specific sector from the data translator, the translator accesses and reads that sector into a RAM buffer. This RAM buffer is copied into an outgoing USB buffer that is transmitted to the host PC over the established USB connection.

TANGIBLE INTANGIBLES

Tangible intangibles? This term refers to the runtime software, which is visually “tangible”, an operator or user can see and manipulate on the screen. Yet this software cannot be touched and is comprised of intangible binary data and instructions a computer executes.

With a complete description of the hardware and firmware systems in chapters 4 and 5, the next logical step is to examine the software used to interact with and manipulate the two. There are three interfaces that an operator interacts with to run the system, and two that a user interacts with. In one case there is overlap.

The operator interacts with a network control application that communicates with the network control basestation (4.3, 5.1) and a data translation application that interacts with the data translation card reader (4.4, 5.4) to convert encoded μ SD card data (5.3.0.5) to human-readable files. Lastly, the operator uses a main data processing and import application to create *players* (3.1.0.1), *sessions* (3.1.0.2), load raw analog *gesture* (3.1.0.3) data into the database, apply calibration constants (4.2) to that data and annotate gathered *gestures*.

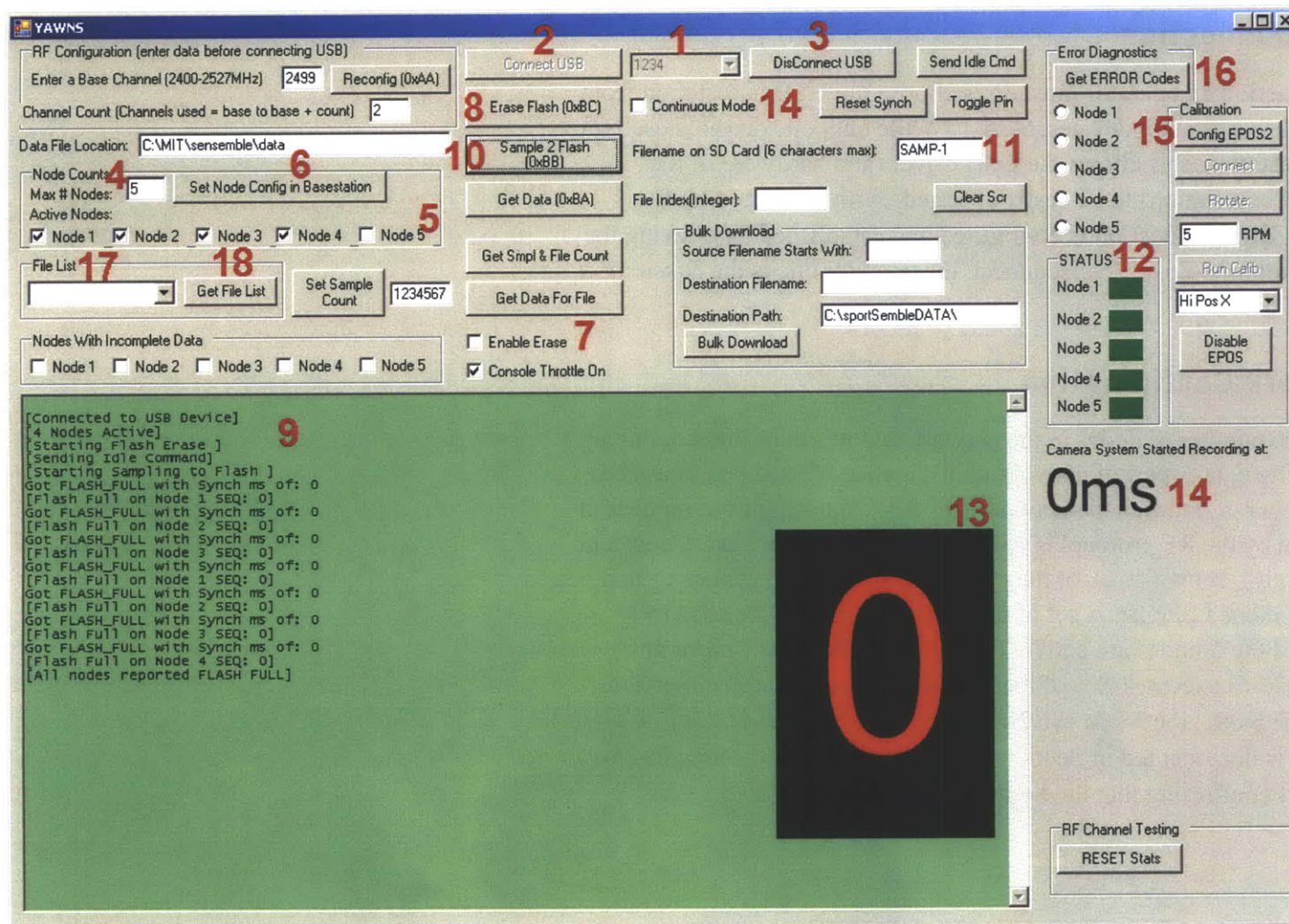
The user also interacts with the data processing and import application, but in a different manner. The user's goals are not to gather data, but to view and perform various analyses of the data, therefore a user interacts with different parts of this application. The second user application is the *Visual3D* [65] environment. Via a custom plug-in, *Visual3D* imports our kinematic and inertial data, then this data is used to perform kinetic analyses of the upper body.

6.1 NETWORK CONTROL APPLICATION

The network control application, FIGURE 6-44, is a Visual Basic graphical user interface (GUI) that uses a *Silicon Labs USB Express* [92] dynamic link library (DLL) in order to communicate (via USB) to the network

control basestation (4.3). It is used to configure, command and control the network of wearable wireless inertial nodes.

FIGURE 6-44 Network Control Application Operator Interface (Large red numbers are for annotation purposes)



Documenting the functionality and operation of the network control application will heavily rely on **FIGURE 6-44** and the red numbers that are present in the figure. The notation used to point at a specific number in the figure will simply be 6-26-*<number>*.

6.1.1 USB Connection

The first action an operator must do is choose the USB basestation from a list of available basestation devices, 6-26-1. While only one driver is used for our current basestation, this allows the USB driver (and hardware of the network control basestation) to be easily changed. With a selected USB basestation, the USB connection is configured and established by clicking the *Connect USB* button, 6-26-2. To disconnect, the operator clicks the *Disconnect USB* button, 6-26-3

6.1.2 Network Configuration

Setting the number of nodes in the network and which of these nodes are actively gathering data is part of network configuration. A text box is used to specify the number of nodes in the network (6-26-4). The maximum number of nodes supported by the RF protocol is 15 (enough to instrument every segment of the human body). However, all of the current software supports only 5 nodes needed to instrument a pitcher. A set of checkboxes (6-26-5) are used to specify which of the 5 nodes are active. Clicking the *Set Node Config in Basestation* (6-26-6) executes two of the commands documented in Section 5.1 and **FIGURE 5-39**, the *NUM_NODES_CMD* and *NODE_ACTIVE_CMD*. This command is documented in Section 5.1. The main message area (6-26-9) will display text confirming that the network has been configured.

6.1.3 Erasing Flash

An erase of all data in the MCU's internal flash and on the μ SD card should be performed before beginning data gathering on a *player*. In order to avoid mistaken erasure of the data on all nodes (something that the author learned the hard way), a simple two phase process is employed. The first phase is to check the *Enable Erase* checkbox (6-26-7) that is placed geographically far away from the *Erase Flash* button, which can only be clicked with the prior checkbox checked. When clicked, a *ERASE_FLASH* command is generated and sent to the basestation. This command is documented in Section 5.1. The main message area (6-26-9) will display text confirming that the memory is being erased.

6.1.4 Sampling Gesture Data

With a configured network and clean memory to store *gesture* data, the operator enters a filename in the *Filename on SD Card* textbox (6-26-11) and clicks the *Sample 2 Flash* button (6-26-10). It is important to note that the maximum filename length is 6 characters, as dictated by the payload size of the wireless data packet. The click of the button triggers a *SAMPLE_2_FLASH* command to be sent to the basestation, along with the operator-entered filename.

During the sampling process, the operator observes two areas of the screen: the main message area (6-26-9) and the STATUS area (6-26-12). The main message area will display a message for every node that has replied that its flash is full. The STATUS area has a green/red box to the right of each node name. If the box is green, a packet has been received from that given node in the last 50ms. If the box is red, the node has not been heard from in the past 50ms. This is an excellent way of diagnosing which node(s) are misbehaving.

6.1.5 Continuous Sampling

The ability to continuously sample is desirable in order to better fit into the workflow and routines of athletes. Pitchers, for example, throw at their own pace and, as mentioned previously, a goal of the system is to fit into routine athletic activity as seamlessly as possible. Dictating when to start and stop impacts their, for lack of a better word, “mojo” and may affect performance.

Continuous mode is activated by checking the *Continuous Mode* checkbox (6-26-14), this sets the continuous mode byte in the outgoing packets that the basestation sends and enables continuous mode in the nodes, the mechanics of which are detailed in Section 5.3.0.6. While the checkbox is checked, the *SEQUENCE_NUMBER* will be incremented with every new dataset and displayed on the large red-on-black sequence number field (6-26-14). The reason that the sequence number field is so large and has a high contrast is to ease viewing when recording data in sunny outdoor environments. The system will stay recording in continuous mode until the *Continuous Mode* checkbox is unchecked. When this occurs, the current dataset recording completes, the *SEQUENCE_NUMBER* is reset to zero, and the system goes into the *IDLE* state.

6.1.6 Error Management

When errors do occur, they are recorded in the flash memory of each node, and the error handling subsystem is explained in Section 5.2.2. In order to retrieve errors, the operator first selects the node from the radio button list (6-26-15) and then clicks the *Get ERROR Codes* button (6-26-16).

When this occurs, a *GET_ERROR_COUNT* command is issued in order to retrieve the number of errors the specific node has experienced. Then a loop is executed, sending a *GET_ERROR_CODE* command from zero to the number of errors. As the error codes are transmitted back, each is displayed in the main message area (6-26-9) in hex.

6.1.7 Reading Node Contents

In order to see what datasets each node has recorded, there exists a mechanism to retrieve a list of files (datasets) from the node. The mechanics of the two commands used, *GET_SAMPLE_CNT_CMD* and *GET_FILE_NAME* are described in Sections 5.3.0.7 and 5.3.0.8, respectively.

The operator first selects a node from the drop down menu (6-26-17) in the *File List* section of the GUI, then clicks the *Get File List* button (6-26-18). A similar process is followed to that of retrieving an error list. A *GET_SAMPLE_CNT_CMD* count command is issued and a count of the number of datasets is obtained. Then a loop is executed from zero to this count, issuing a *GET_FILE_NAME* command with the index of the loop. For each iteration through the loop a filename is transmitted back by the node and printed in the main message area (6-26-9).

6.1.8 Optical System Synchronization

The hardware connectivity and generation of synchronization offsets are described in Sections 4.3.1 and 5.1.1. The synchronization constant that is calculated and transmitted to the host PC is displayed under the *Camera System Started Recording at* label (6-26-14). If synchronization is ongoing, this data is normally recorded as part of normal data gathering procedures and entered into the database.

6.2 DATA TRANSLATION APPLICATION

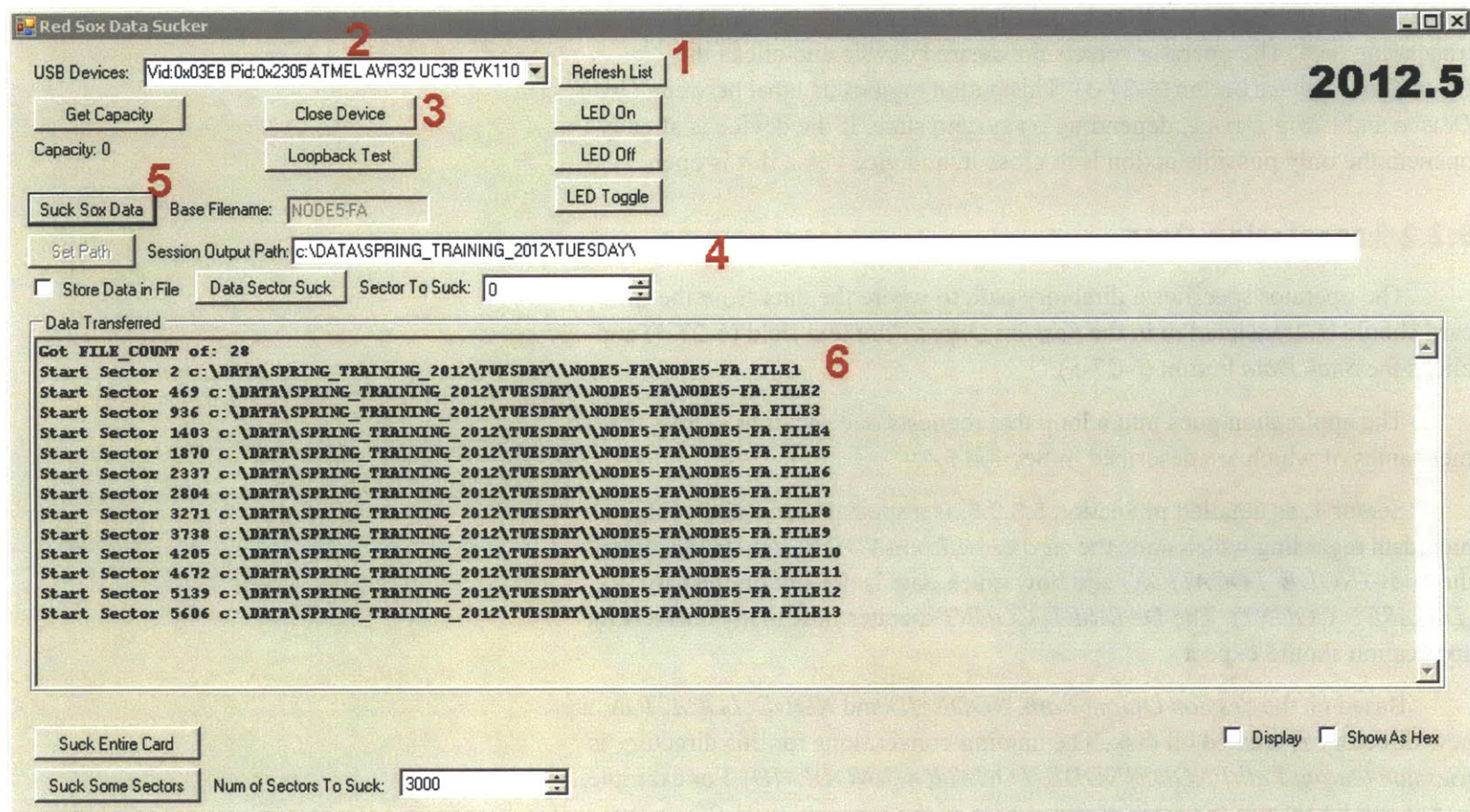
.....

The data translation application is used in conjunction with the Data Translator (4.4, 5.4). The purpose of these two is to translate the data stored on

μSD cards, as raw sectors, to something that is human readable and machine parseable. To connect the application via USB to the hardware translator, a customized version of an open source USB library, *libusb*[93], is used. A device driver matched to the EVK1101 (4.4) is compiled and installed on the host PC.

The same notation scheme used for **FIGURE 6-44** in Section 6.1 will be used here, [FIGURE NUMBER]-[RED INDEX NUMBER].

FIGURE 6-45 Data Translator Application Operator Interface (Large red numbers are for annotation purposes)



6.2.1 USB Connection

Once the μ SD card has been removed from the node and inserted into the translator, the first action an operator takes after opening the application is to click the *Refresh List* button (6-27-1). This causes a hardware refresh of all

USB devices that match the *DeviceID* of the Data Translator hardware and populates it into the *USB Devices* list (6-27-2). This list allows operating more than one data translator at a time to parallelize the time-consuming task of translating data. The operator selects the desired device and clicks the *Open/Close Device* button (6-27-3). This button toggles its label between *Open Device* and *Close Device*, depending on system state. If the device is already opened, the only possible action is to close it, and vice versa if it is open.

6.2.2 Translating Data

The operator specifies a directory path to where the data from the μ SD card should be translated to in the *Session Output Path* text field (6-27-4) and clicks the *Suck Data* button (6-27-5).

The application goes into a loop that requests one sector at a time, the mechanics of which are described in Section 5.4.

Sector 1, as detailed in Section 5.3.0.5, is a special sector and contains metadata regarding which node the card came from (*NODE_ID*), its location on the body (*NODE_LOCATION*) and how much data is present on the card (*DATASET_COUNT*). The *DATASET_COUNT* dictates how many datasets the application should expect.

Based on the *Session Output Path*, *NODE_ID* and *NODE_LOCATION*, a new directory is created on disk. The naming conventions for this directory is *[Session Output Path]\NODE[NODE_LOCATION]-NODE_ID*. For example, and as can be seen in the main message area of the application (6-27-6), the *Session Output Path* is C:\DATA\SPRING_TRAINING_2012\TUESDAY and the read *NODE_LOCATION* is 5 and the *NODE_ID* is FA. This yields the directory C:\DATA\SPRING_TRAINING_2012\TUESDAY\NODE5-FA\ for storing all data from this card.

Once sector 1 has been processed, the application begins to sequentially request sectors from the data translator. With each received sector, it reads 28 bytes at a time and processes the contents. 28 bytes are read because this is the length of the data packets that are placed onto the card by the nodes, and the format and information regarding card writing is located in Section 5.3.0.5.

Once 28 bytes are read, 4 *HEADER_BYTES* are checked to determine what kind of data is contained in the given packet. There are three types of packets: *header*, *inertial* and *magnetometer*.

The first packet for any *gesture* dataset is a *header* packet that contains the 6-character *FILENAME* and *SEQUENCE_NUMBER*. These two are used to create 4 different files, with different *DATATYPES* for each recorded *gesture*.

- 1 Synchronization File - *SEQDATA* - Timestamp and synchronization data
- 2 High Range Inertial File - *NO DATATYPE STRING* - High range X, Y, Z and Pitch, Roll, Yaw data is contained in this file
- 3 Low Range Inertial File - *LOWG* - High range X, Y, Z and Pitch, Roll, Yaw data is contained in this file
- 4 Magnetometer File - *COMPASS* - Magnetometer X, Y, Z data is contained in this file

Additionally, when a *header* packet is encountered, a global *FILE_COUNTER* is incremented by one. The naming convention for the filenames is:

NODE[*NODE_LOCATION*]-[*NODE_ID*].FILE[*FILE_COUNTER*].[*FILENAME*].SEQ[*SEQUENCE_NUMBER*].[*DATATYPE*].txt

An example of the four files for a single *gesture* is:

NODE1-AC.FILE4.ZupDn.SEQ0.SEQDATA.txt - Synchronization

NODE1-AC.FILE4.ZupDn.SEQ0.txt - High range inertial

NODE1-AC.FILE4.ZupDn.SEQ0.LOWG.txt - Low range inertial

NODE1-AC.FILE4.ZupDn.SEQ0.COMPASS.txt - Magnetometer

The *header* packet also contains a global timestamp, this timestamp is written out to the Synchronization file and is later used to perform a global synchronization for all data gathered. Once the four files are created and opened, processing of data packets can begin.

If the packets' *HEADER_BYTES* match an *inertial* packet, the encoded inertial data from high range X, Y, Z and pitch, roll, yaw and low range X, Y, Z and pitch, roll, yaw is decoded. This data is output in comma-separated-value (CSV) format into the low range inertial data file for low range data and the high range inertial data file for the high range data.

If the *HEADER_BYTES* contain the *magnetometer* code, magnetometer data is decoded from the packet and written out to the magnetometer file.

When the current sector has been iterated through in 28 byte increments, the next sector is requested from the translator, and the same process is followed for packets in the sector. If a new *header* packet (representing the next recorded *gesture*) is encountered, the current data files are closed and new ones, based on the information in the packet, are created.

The translation process terminates when a pre-determined number of sectors are read without a *header* packet being read from the card. When this occurs, a message is written out to the main message area (6-27-6).

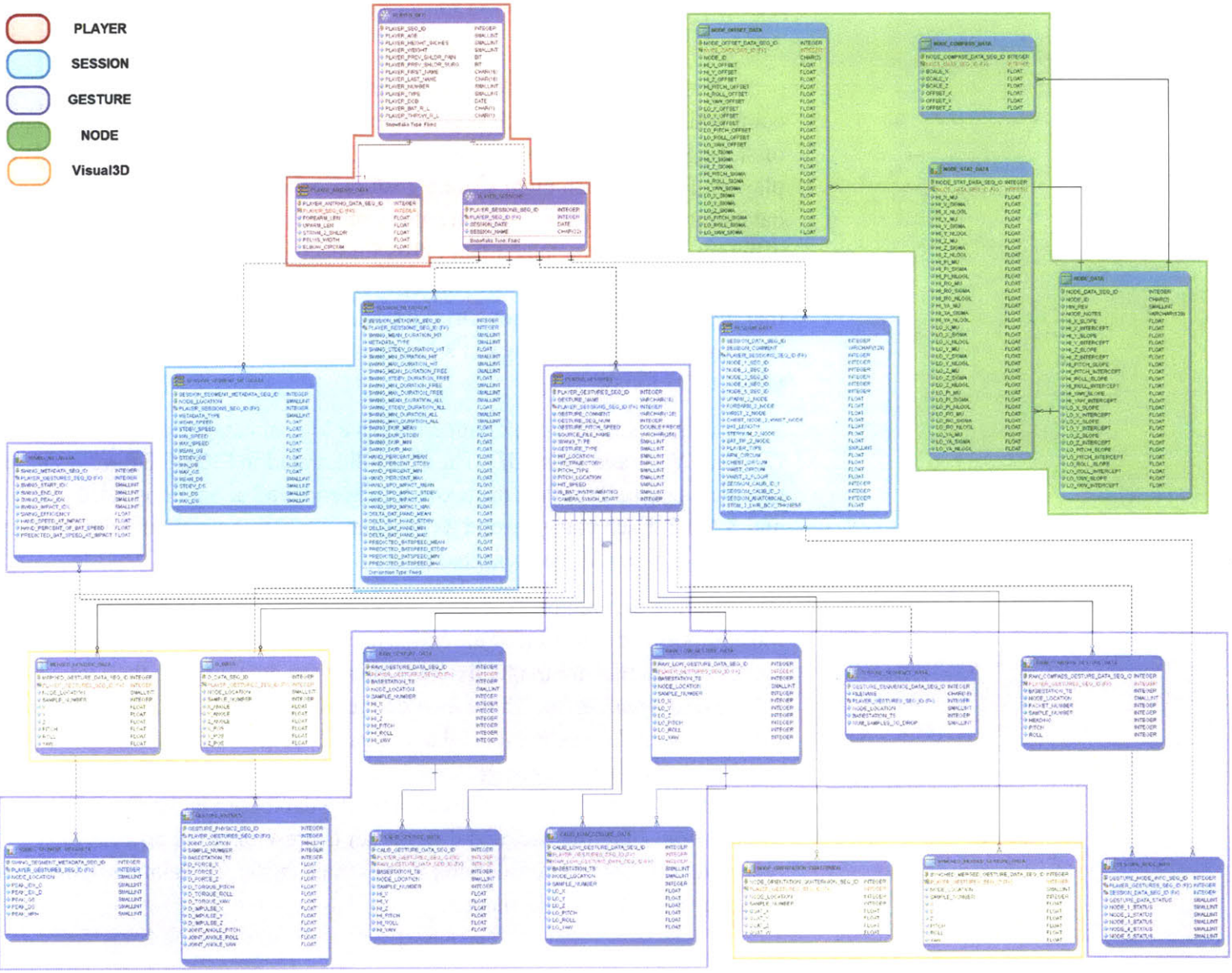
6.3 DATA MODEL

It is important to understand the inherent data demands and data complexity of a system such as this. The system's data storage must be capable of storing data for hundreds, possibly thousands, of gestures for hundreds of players. Further, each eight second gesture consists of roughly 40,000 raw datapoints and 40,000 calibrated datapoints. Not only this, but there are several different pieces of metadata that exists for each gesture and each sample. This amount of data quickly grows into millions of records, hence it is easy to see that managing all of it is not a trivial task. A model to store all of this data has been evolving since the project's inception in 2008 and has grown from 9 tables to 25 today.

This data model can be divided into five logical categories; *Player*, *Session*, *Gesture*, *Node* and *Visual3D*. These are illustrated in FIGURE 6-46 . These categories partially reflect the taxonomy introduced in Sections 3.1.0.1, 3.1.0.2 and 3.1.0.3. Each category and its associated tables, accompanied by a human-readable figure, will be presented in the following sections.

Before delving into the data model, it is important to note that while most import and insertion of the raw sensor data is automated, there are several pieces of data that are manually entered into the database via the *Data Processing Application*. These include the biometric and anthropometric information and measurements that are gathered for each *player* before each *session*. Additionally, each *gesture*, be it a pitch or swing, has metadata associated with it that is also entered into the database via the *Data Processing Application*. Here the backend data model is presented; the process of recording this data in our logbook is presented in the *Experimental Methods* Chapter that follows this chapter.

FIGURE 6-46 Complete Data Model



6.3.1 Player Data Model

The player data model consists of two tables, *PLAYER_INFO* and *PLAYER_ANTHRO_DATA*. The *PLAYER_INFO* table contains general biometric data; the specific information that is present in this table mirrors numbered points 1 to 12 in Section 3.1.0.1. *PLAYER_ANTHRO_DATA* contains anthropometric information, namely the information outlined by numbered points 13 to 18 in the previously-mentioned section. A mandatory one-to-one relationship exists between these tables, meaning that for every player, there must exist anthropometric data. The primary key of the *PLAYER_INFO*, *PLAYER_SEQ_ID*, is a unique identifier for all *Players*, and is a foreign key in *PLAYER_ANTHRO_DATA*.

FIGURE 6-47 Player Data Model

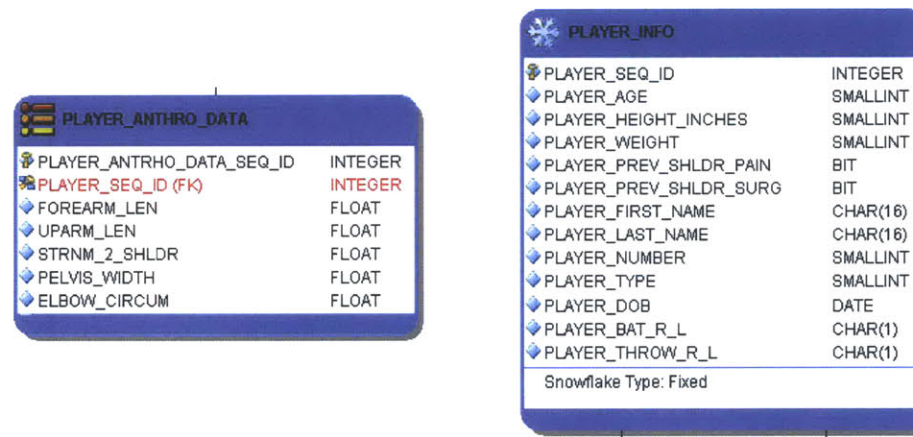


FIGURE 6-48 Session Data Model



6.3.2 Session Data Model

The *Session* concept is defined and described Section 3.1.0.2; the data model consists of four tables, *PLAYER_SESSIONS*, *SESSION_DATA*, *SESSION_SEGMENT_METADATA* and *SESSION_METADATA*.

PLAYER_SESSIONS has a foreign key from *PLAYER_INFO*, and its relationship to *PLAYER_INFO* is, from *PLAYER_INFO* to *PLAYER_SESSIONS*, one to many. This indicates that for one *Player*, there exist one or more *Sessions*. This table contains its primary key, *PLAYER_SESSION_SEQ_ID*, the session name and session date (number points 1 and 2 in Section 3.1.0.2). The bulk of the information outlined in the numbered list of the *Session* description is contained in the helper table *SESSION_DATA*.

PLAYER_SESSION_SEQ_ID is a foreign key in *SESSION_DATA*, and as the relationship between these two tables is mandatory one-to-one, session data must exist for each *Session*. The data contained in this table is outlined in numbered points 3 through 21 in Section 3.1.0.2.

The two metadata tables contain post-processed data and statistics that are generated on a per-session level. *SESSION_METADATA* reflects statistics generated inter-node, for example, the mean delta between peak angular velocity for the hand and forearm nodes. *SESSION_SEGMENT_METADATA* contains statistics that are on a per-node basis. For example, the mean G-Force experienced by the hand node for this *Session*. Data for these tables is generated by the Analytics Engine described in Section 9.3 and will be covered in more detail in that section.

6.3.3 Gesture Data Model

Core data directly related to what each nodes sensors read (Sections 4.1.1 and 4.1.2) and is later translated to the filesystem (Section 6.2.2) is stored

in five tables: *PLAYER_GESTURES*, *RAW_GESTURE_DATA*, *RAW_LOW_GESTURE_DATA*, *GESTURE_SEQUENCE_DATA* and *RAW_COMPASS_GESTURE_DATA*¹⁶.

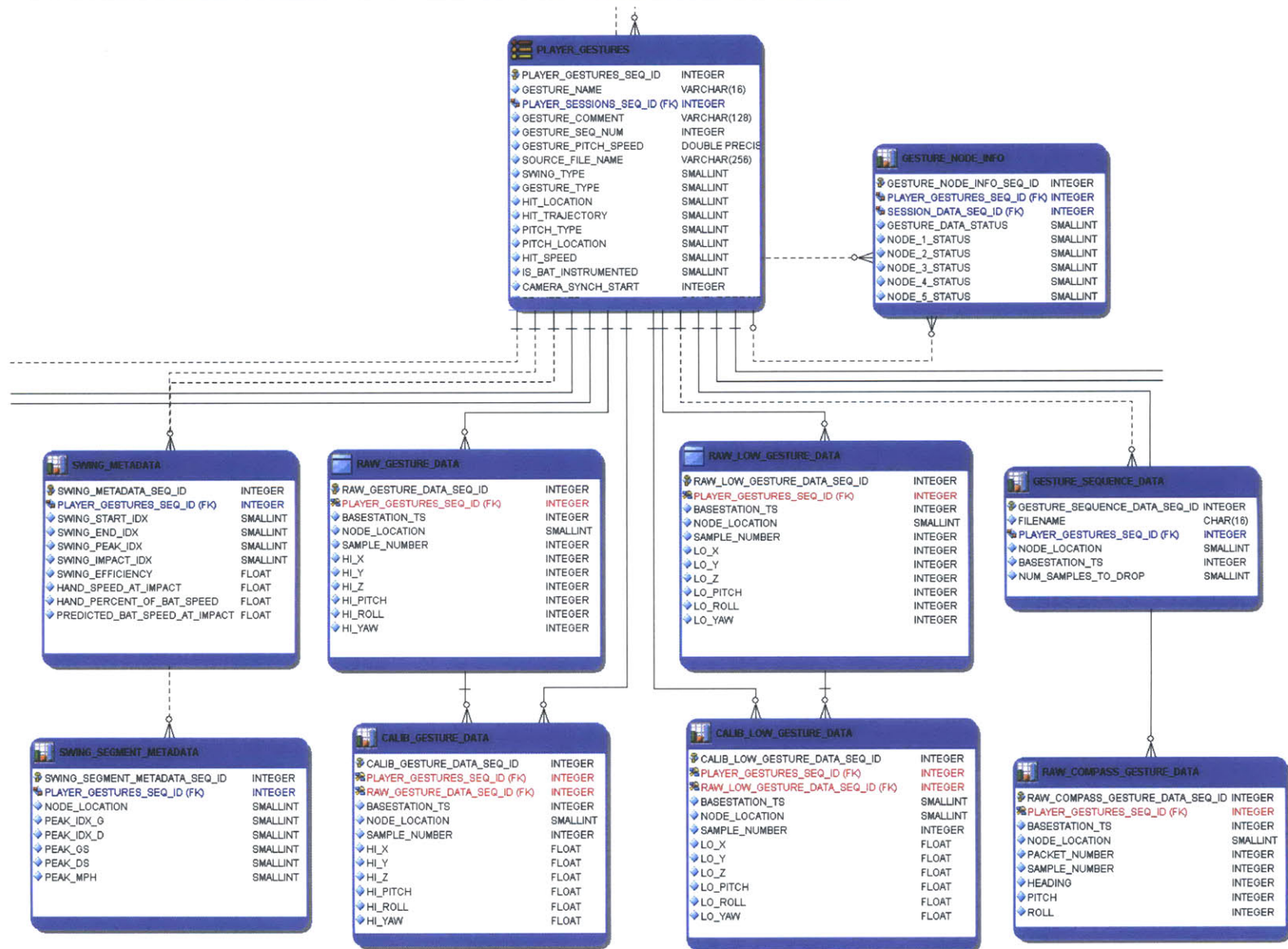
The root table, *PLAYER_GESTURES*, has a foreign key from the *PLAYER_SESSIONS* table and a one-to-many relationship exists between the two, indicating that one *Session* is associated with multiple *Gestures*. *PLAYER_GESTURES* has its own primary key, *PLAYER_GESTURES_SEQ_ID*, whose purpose will be clear once all tables related to *Gesture* data are described. As with *Player* and *Session*, the data stored in the *PLAYER_GESTURES* table also mirrors what is enumerated in the *Gesture* taxonomy section (3.1.0.3), specifically, numbered points 1 through 13 in that section. This is general information pertaining to the physical gesture, and the actual data sampled from the sensors is stored in the *RAW_** tables.

The *RAW_** tables are directly correlated with the four files per gesture that are created in the filesystem by the translator (6.2.2). Each of these has a many-to-one relationship with *PLAYER_GESTURES*, meaning that each of the many samples of data that is inserted are related to only one *Gesture*. In order to identify what gesture the data is part of, *PLAYER_GESTURES_SEQ_ID* has a foreign key in each *RAW_** table.

Data from the *High Range Inertial File* is inserted into the *RAW_GESTURE_DATA* table. Data from the *Low Range Inertial File* is inserted into the *RAW_LOW_GESTURE_DATA*. Data from the *Synchronization File* is inserted into the *GESTURE_SEQUENCE_DATA* table. And, finally, data from the *Magnetometer File* is inserted into the *RAW_COMPASS_GESTURE_DATA*¹⁶ table.

¹⁶*RAW_COMPASS_GESTURE_DATA* is a misnomer, since magnetometer data is gathered. It is a naming relic from previous hardware [7] that used a digital compass in place of a magnetometer.

FIGURE 6-49 Gesture Data Model



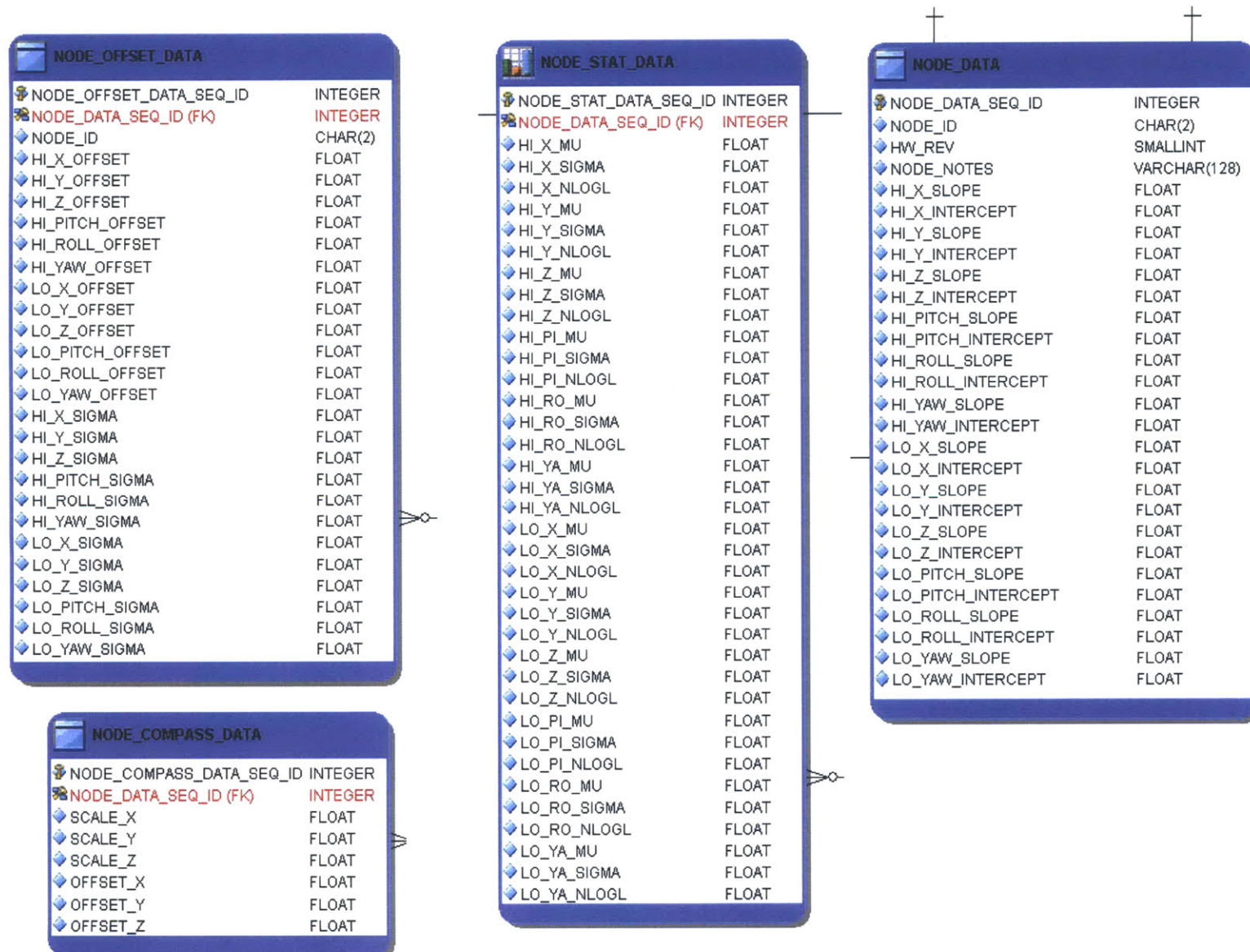
The naming convention of *RAW* indicates that the data stored is in a raw format. In the case of *RAW_GESTURE_DATA* and *RAW_LOW_GESTURE_DATA*, it is in fact raw analog data that needs to be converted using calibration constants (described in Section 4.2). In order to keep both raw and calibrated data, for archival purposes and in case re-calibration becomes necessary, the calibrated data is inserted into two new tables, aptly named *CALIB_GESTURE_DATA* and *CALIB_LOW_GESTURE_DATA*. The *GESTURE_SEQUENCE_DATA* and *RAW_COMPASS_GESTURE_DATA*¹⁶ do not have matching *CALIB_* tables because this data is in a final format. However, post-processing of this data does occur to calculate heading, from *RAW_COMPASS_GESTURE_DATA*, and node synchronization offsets, from *GESTURE_SEQUENCE_DATA*. This will be addressed in Section 7.2.

The third tier of storage for gestures are the two **_METADATA* tables and are similar in purpose to the **_METADATA* tables for *Sessions*. The “*SWING*” name portion of the tables *SWING_METADATA* and *SWING_SEGMENT_METADATA* is a misnomer because the metadata in these tables is not only related to swings. Initially, it only was swing related (i.e. for batters) and as the system evolved the table was used for both swings and pitches. *SWING_METADATA* contains *Gesture* level information, such as the start and end samples of the given gesture. *SWING_SEGMENT_METADATA* contains segment-specific information, such as the peak angular velocity for a given segment for a given gesture.

6.3.4 Node Data Model

Section 4.2 describes, in depth, the calibration process each axis of each node and the process of generating calibration constants for each axis. The generated constants, along with their coefficients of determination (FIGURE 4-35), statistical noise data and magnetometer calibration data are all stored as part of the Node Data Model. These four tables are shown in FIGURE 6-50

FIGURE 6-50 Node Data Model



The calculated linear calibration constants are stored in the *NODE_DATA* table. These include slope and Y intercept for each inertial axis, a unique node identifier and a primary key, *NODE_DATA_SEQ_ID*, that will be a foreign key to link data to a specific node in the other tables.

*NODE_COMPASS_DATA*¹⁶ contains scale and offset values for each of the three axes of the magnetometer. *NODE_DATA_SEQ_ID* is a foreign key to identify which node this data is for. The relationship between this table and *NODE_DATA* is one-to-one.

The *NODE_OFFSET_DATA* table has a “dual personality”, as it contains offset data and coefficients of determination for each inertial axis. Offset data is occasionally calculated for inertial sensors that drift severely over short periods of time. The coefficients of determination (R^2) are calculated at calibration time to examine the goodness of the correlation and are stored here for future analysis. As with the previous table, *NODE_OFFSET_DATA* also has a foreign key of *NODE_DATA_SEQ_ID*, which establishes the data uniqueness and a one-to-one relationship with *NODE_DATA*.

NODE_STAT_DATA is information used for generating covariance statistics that are used by orientation estimation algorithms and kinematic estimation Kalman filters. There are three components for each inertial axis, μ sigma and the negative log likelihood. *NODE_DATA_SEQ_ID* is a foreign key and the two tables have a one-to-one relationship.

6.3.5 Visual3D Data Model

Visual3D [65] and its connection to this work is briefly described in Section 3.4 and an in-depth description is featured in Section 9.7.1. The custom plug-in developed to import inertial data uses inertial data to compute dynamics and previously calculated kinematic *Q-Data* to drive the upper body model.

The *Q-Data* is stored in the *Q_DATA* table. It contains the three Euler angles that represent joints, which dictate segment-to-segment rotations to set the orientation of each body segment. Additionally, X, Y, Z translation data is stored for any segments that are allowed to translate in 3D space. Each record in the table represents one calculated orientation between two segments (one joint) for one time step. *PLAYER_GESTURES_SEQ_ID*, from the *PLAYER_GESTURES* table, is a foreign key, establishing a mandatory one-to-one relationship between these two tables.

The low range and high range data exists in separate tables and as separate data streams for each inertial axis and require fusion (Section 9.5) before the *Visual3D* plug-in can access them via the *SYNCHED_MERGED_GESTURE_DATA* table. Each low range and high range inertial axis is fused and placed into its respective column. This data is stored on a per segment, per sample basis for each *PLAYER_GESTURES_SEQ_ID*, a foreign key in this table. The *MERGED_GESTURE_DATA* table has the same structure and a similar purpose. The difference between the two is that synchronization offsets from the *GESTURE_SEQUENCE_DATA*, which contains calculated offset information for each node in the network.

Segment orientations are calculated as intermediate data and stored in the *NODE_ORIENTATION_QUATERNION* table. The four parts that represent a Quaternion [105] are stored along with which segment (*NODE_LOCATION*) and sample number the orientation is for. *PLAYER_GESTURES_SEQ_ID* is a foreign key and establishes a one-to-one relationship.

6.4 DATA PROCESSING AND IMPORT APPLICATION - OPERATOR VIEW

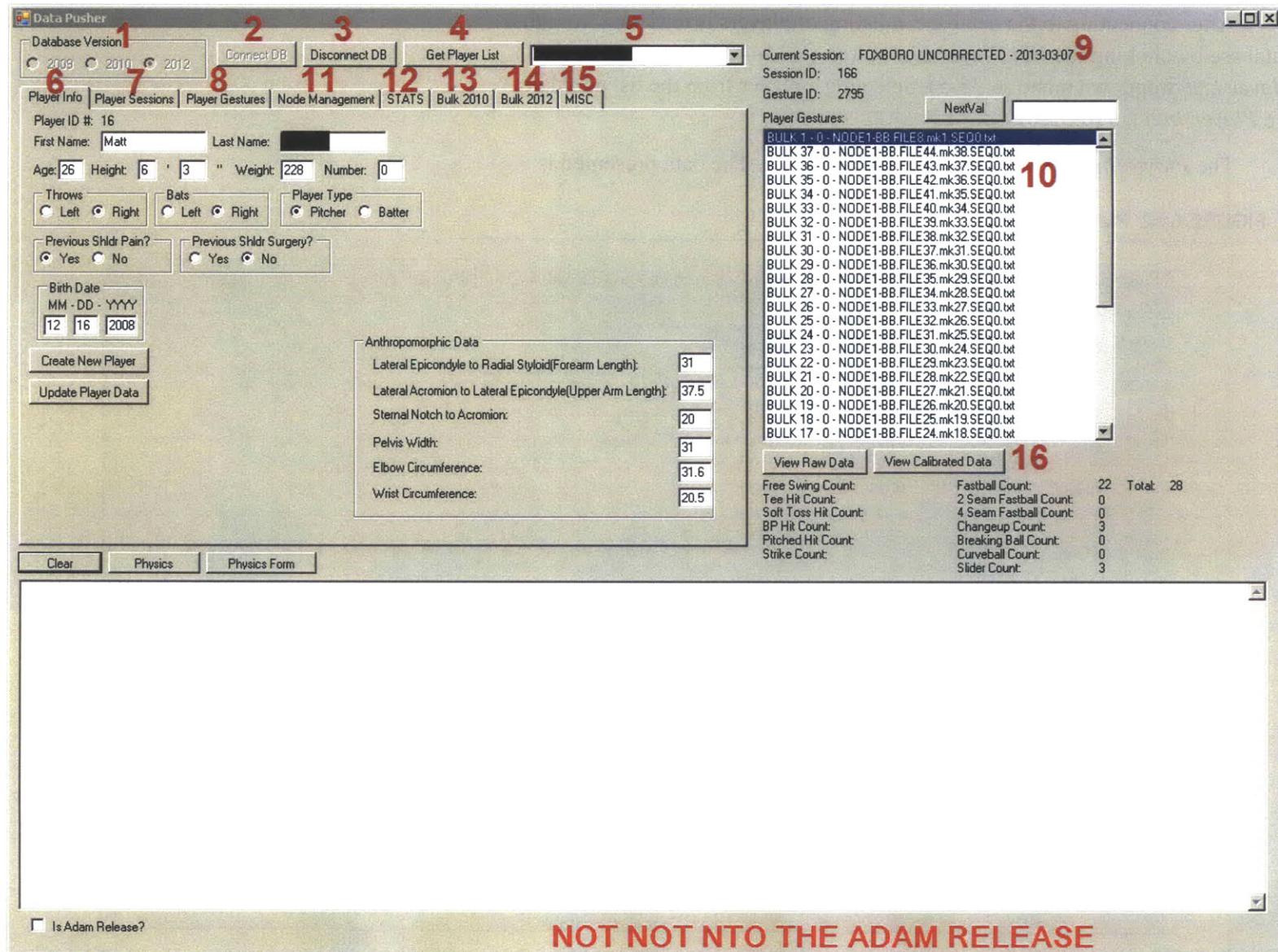
.....

Details of the data processing application will be broken up into the two logical viewpoints that reflect the different types of interaction with the application, the user and the operator. This section will focus on the operator and will cover creation of *players*, *sessions*, *gestures*, *nodes* and the process of importing the data provided by the translator into the relational database.

6.4.1 Database Connectivity

As the system has evolved, there have been three different instances of the database, *2009*, *2010* and *2012*. All three have slight differences in data structure, but backwards compatibility has been built into the *Data Processing Application*. Only the latest schema is considered here, as it has the most features. The same notation will be used here to identify different graphical features that was used in Sections 6.1 and 6.2. To connect to the database, the operator selects the desired database version in the *Database Version* radio button group (6-33-1) and then clicks the *Connect DB* button (6-33-2). To change databases, the operator clicks the *Disconnect DB* button (6-33-3) and follows the process just outlined.

FIGURE 6-51 Data Processing Application Main View (Large red numbers are for annotation purposes)



6.4.2 Player Management

After connecting to the database, a listing of players is retrieved from the database by clicking the *Get Player List* button (6-33-4). This populates the *Player List* dropdown menu (6-33-5). Selecting a player from the list populates the *Player Info* tab (6-33-6).

The *Player Info* tab is shown in FIGURE 6-52 . The data presented is

FIGURE 6-52 Player Info Tab

Player Info | Player Sessions | Player Gestures | Node Management | STATS | Bulk 2010 | Bulk 2012 | MISC

Player ID #: 16
 First Name: Last Name:

Age: Height: ' " Weight: Number:

Throws: Left Right Bats: Left Right Player Type: Pitcher Batter

Previous Shldr Pain?: Yes No Previous Shldr Surgery?: Yes No

Birth Date: MM - DD - YYYY

1
 2

Anthropomorphic Data	
Lateral Epicondyle to Radial Styloid(Forearm Length):	<input type="text" value="31"/>
Lateral Acromion to Lateral Epicondyle(Upper Arm Length):	<input type="text" value="37.5"/>
Sternal Notch to Acromion:	<input type="text" value="20"/>
Pelvis Width:	<input type="text" value="31"/>
Elbow Circumference:	<input type="text" value="31.6"/>
Wrist Circumference:	<input type="text" value="20.5"/>

selected from the database (Section 6.3.1) and described in Section 3.1.0.1. The two possible actions that can be taken on a *Player* are player creation (*Create New Player* button (6-34-1)) and updating a player's information when it has been changed via the *Update Player Data* button (6-34-2). When a player is created, new data is inserted into the database, when updated, existing data is modified.

FIGURE 6-53 Player Sessions Tab (Large red numbers are for annotation purposes)

Player Info | Player Sessions | Player Gestures | Node Management | STATS | Bulk 2010 | Bulk 2012 | MISC

Sessions for Player: **7** **FOXBORO UNCORRECTED - 20** Session Name: **FOXBORO UNCORR**

Session Comments go here

9 BB	Node 1(hand)	Radiocarpal to Node 1:	6
BA	Node 2(forearm)	Lateral Epicondyle to Node 2:	27.5
AA	Node 3(upper arm)	Later Acromion to Node 3:	18
DA	Node 4(chest)	Sternal Notch to Node 4:	17.5
FA	Node 5(waist/bat)	Node 4 to Node 5:	35.5

1 Add New Session

2 Update Session

3 Delete Session

Bat Length: 0

Bat Tip to Node 5: 0

Arm Circumference: 38

Chest Circumference: 104

Waist Circumference: 98

Waist Node to Floor: 110.5

Chest Thickness: 25.5

Stomache to Lower Back Thickness: 25.3

Stomache to Sternum Depth: 0.2

Calib Gesture 1 ID: -1

Calib Gesture 2 ID: -1

Anatomical Gest ID: -1

4 **8** Allow Delete?

5 **6** Generate Visual3D Model

Valid Range Values are 0 to 37

Range Start: **5**

Range End: **6**

Compass Fix

Change Gesture Drive Letter

Re-Run Calibration for Gesture Range

Re-Run Calibration for Selected Gesture

Mike is Dumb

Check Sample Count

Custom Session (for adding old data)

MM - DD - YYYY

03 07 2013

Add Custom Session

6.4.3 Session Management

Session management actions are contained under the *Player Sessions* tab (6-33-7); the tab is presented in **FIGURE 6-53** . As with Player Info, the presented information is described in Section 3.1.0.2. An operator specifies a session name, selects which nodes are located on which body segment (6-35-9) and measured anthropometric data. There are options to create (6-35-1), update (6-35-2) and delete (6-35-3) existing sessions. Deletion is a two phase process and requires the *Allow Delete?* checkbox (6-35-8) to be checked.

Additionally, the output of the *Visual3D* model file, which is based on the measured anthropometric data for each player and session, is executed by clicking the *Generate Visual3D Model* button (6-35-4). Sessions are selected by choosing them from the *Sessions for Player* dropdown menu (6-35-7). When a session is selected, the information in the Main View (**FIGURE 6-51**) for the *Current Session* (6-33-9) and the *Player Gestures* list (6-33-10) is updated with the gestures for the selected session.

There are two features that make use of the raw data that is kept in the database, the ability to re-run calibration. If there are any issues with a calibration and new calibration constants are regenerated, any previously gathered data can be reprocessed, making it usable for future study. There is a two phase process for recalibrating, similar to deleting sessions. Next to the *Re-Run Calibration for Selected Gesture* (6-33-6) there is a checkbox that needs to be checked in order for the recalibration to run. There is also an option to specify a range of gestures to be recalibrated and to recalibrate a group of gestures (6-35-5).

6.4.4 Gesture Handling

Gesture management falls into two categories: importing data into the database and annotating, classifying and managing the gestures once they have been imported.

6.4.4.1 Gesture Import Process

The interface for the import process is available via the *Bulk 2012* tab (6-33-14). As documented in Section 6.2.2, there are four files generated by the Data Translator for each recorded gesture, and in order to load this data into the database, the operator clicks the *Add Files* button (6-50-1). This brings up a file selection dialog box and the operator selects any one of the four files for an individual gesture from one node. The operator can use the *Shift+Click* windows feature to select multiple individual files from gestures. Once the dialog is closed, the files are added to the *File List Area* (6-36-2).

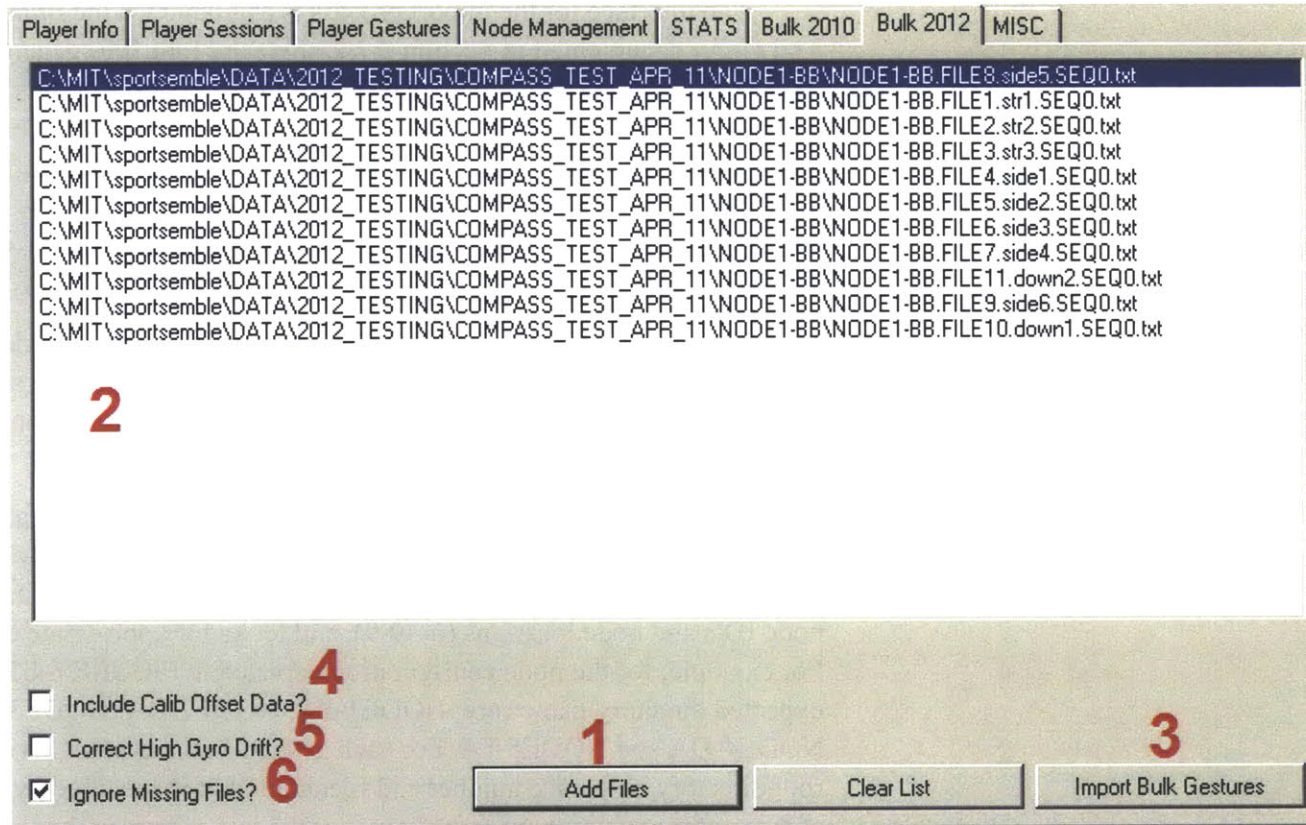
The reason that, for each gesture, only one file from one node needs to be selected is because the algorithms that load data are built to take advantage of the specified file format and node segment placement information that is encoded under the *Player Session* tab (6-33-7).

Once the *Import Bulk Gestures* button (6-36-3) is clicked, a series of checks and verifications occurs based on *Session* data. These rely on the file and directory structure detailed in Section 6.2.2. The algorithm first checks the node ID's and node locations (6-49-9), and looks for appropriate directories. For example, for the node configuration depicted in FIGURE 6-53, the expected directory names are: NODE1-BB, NODE2-BA, NODE3-AA, NODE4-DA and NODE5-FA. For each gesture in the gesture list (6-36-2), a root directory, sequence number and filename (that is specified by the operator at data gathering time) are parsed out. For the last gesture in the list in FIGURE 6-54, the parsed root directory is:

```
C:\MIT\sportsemble\DATA\2012_TESTING\COMPASS_TEST_APR11\
```

and the parsed sequence number is *0* and the parsed filename is *down1*. This information is used to search for files, following the directory structure and node naming rules.

FIGURE 6-54 Bulk Data Import Tab (Large red numbers are for annotation purposes)



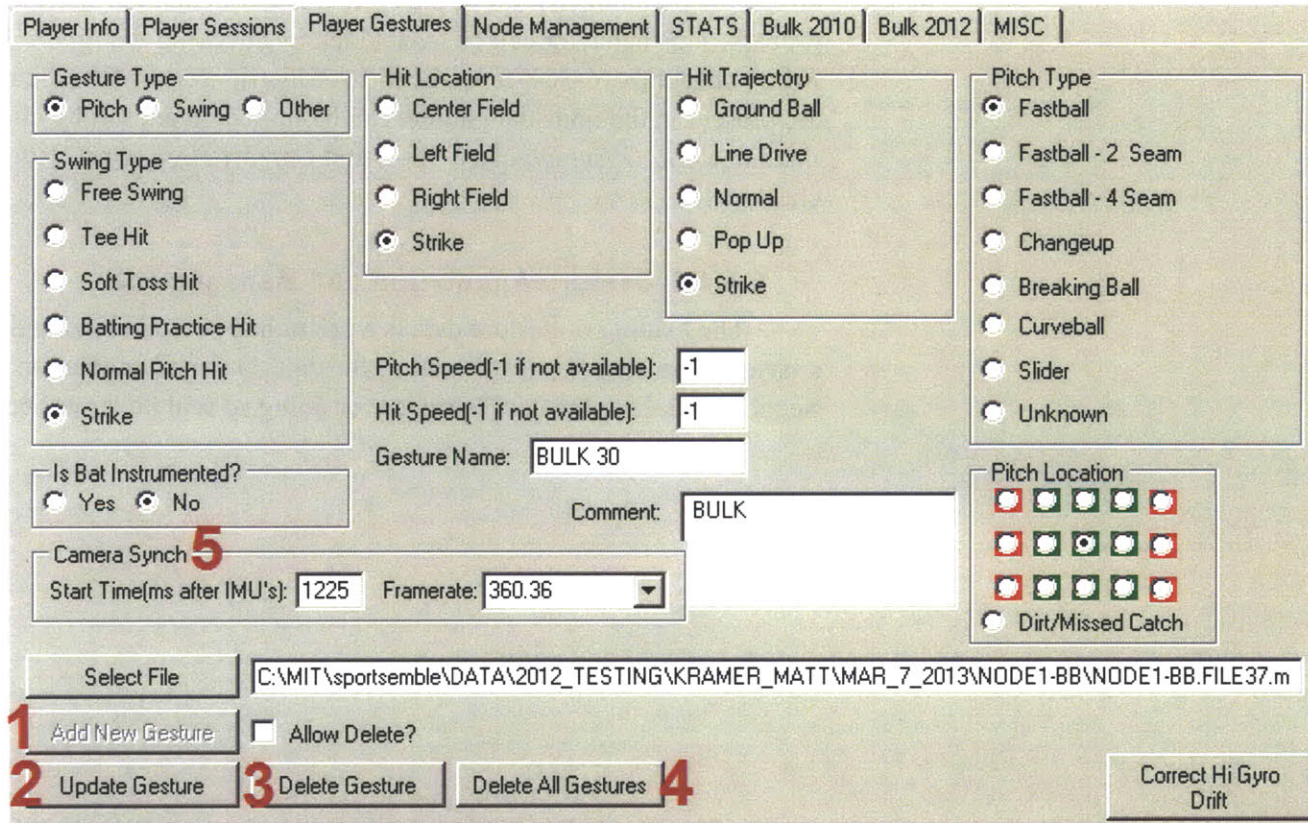
For each node, the found files are opened, parsed line-by-line and inserted, into the *RAW_GESTURE_DATA*, *RAW_LOW_GESTURE_DATA* and *RAW_COMPASS_DATA* tables. It is important to note that the data in the files is raw analog data. As each line is parsed for a specific node, calibration constants (stored in the node data tables, Section 6.3.4) are retrieved and applied for each inertial axis. The resulting calibrated inertial data is stored in the complementary *CALIB_GESTURE_DATA* and

CALIB_LOW_GESTURE_DATA tables. If data is not available from all five nodes, the default behavior of the system is to fail and abort the import process. This behavior can be overridden by checking the *Ignore Missing Files?* checkbox (6-36-6). Application of inertial sensor-specific offsets that are present in the node data model can be turned on and off by clicking the *Include Calib Offset Data?* (6-36-4) and *Correct High Gyro Drift?* (6-36-5) checkboxes.

6.4.4.2 Gesture Annotation and Management

The loading of gesture data is a preliminary step in having data ready for analysis. The next step is to annotate the data. Detailed annotation is covered in Sections 7.5; here the user interface for doing so will be described.

FIGURE 6-55 Player Gesture Tab (Large red numbers are for annotation purposes)



When the *Player Gestures* tab (6-33-8) is clicked by the operator, the user interface in FIGURE 6-55 is presented. This tab displays the annotation information for the currently selected gesture. Gesture selection and listing occurs outside of this tab by clicking the gesture list (6-33-10) which is found in the main application window.

All of the gesture annotation metrics described in Sections 3.1.0.3 and 3.1.0.4 are reflected in the user interface. There are options to update (6-37-2):

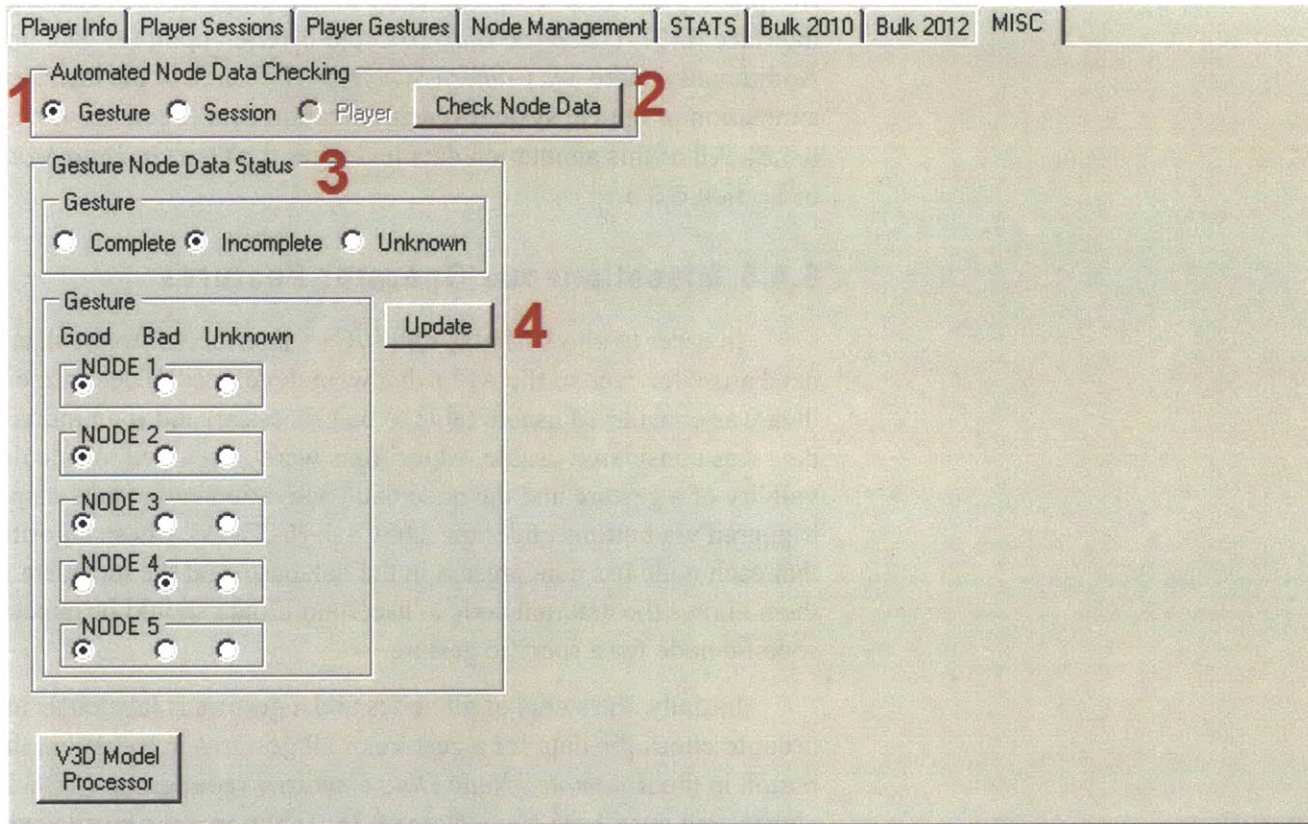
delete individual (6-37-3) and delete all gestures (6-37-4). Deletion is, again, a two phase process. The functionality to add gestures has been disabled in this interface (6-37-1) and the *Bulk 2012* tab is relied upon for data import. Additionally, there is a *Camera Synch* (6-37-5) area in the interface that allows annotation of optical system synchronization data (Sections 4.3.1, 5.1.1 and 6.1.8). All of this annotation data leverages the *Gesture Data Model* described in Section 6.3.3.

6.4.5 Miscellaneous Operator Features

In order to allow Matlab and C/C++ interfaces into the data model, a need arose for each of the API's that were developed to determine if a gesture's data was considered usable (able to be processed) and if an individual node's data was considered usable. Algorithms were developed to calculate the validity of a gesture and the node data; activation and results display is triggered via buttons under the *MISC* tab (6-33-15). These algorithms ensure that each node has data present in the database, and the metadata generated by them allows the external code to ascertain if data should be expected from a specific node for a specific gesture.

Initially, the status of all nodes and a gesture is labeled as unknown. In order to check the data for a gesture or all gestures in a session, the a radio button in the *Automated Node Data Checking* radio group (6-38-1) must be chosen and the *Check Node Data* (6-38-2) button must be clicked. The checks are performed, and status information is inserted into the *GESTURE_NODE_INFO* database table. When selecting a gesture in the gesture selection area in the main application view (6-33-10), the populated information is retrieved and the *Gesture Node Data Status* radio groups (6-38-3) are updated. If there is a need for the operator to update the information manually, the radio groups can be changed, and clicking the *Update* button (6-38-4) will update the information in the database.

FIGURE 6-56 Miscellaneous Tab (Large red numbers are for annotation purposes)



6.5 . DATA PROCESSING AND IMPORT APPLICATION - USER VIEW

.....

Before presenting the user view of the Data Processing and Import Application, it makes more sense to examine the experimental methods that an operator uses to gather data. These methods are presented in Chapter 7



TANGIBLE INTANGIBLES

. Data Processing and Import Application - User View

EXPERIMENTAL METHODS

This chapter is, for the average reader, possibly the most important and could almost be considered a starting point. It describes the way in which the realized network is used to gather data from players and how that data is preprocessed for analysis.

There are three components to executing a successful data gathering session: A reliable and relatively quick method of attaching nodes to the body, a logging methodology for keeping tracking of information that is not gathered by sensors, and a protocol for executing the experiments.

7.1 BODY ATTACHMENT

Wearable, Wireless, Sensor Networks is a term that used to describe the underlying technology that is the basis for this dissertation. Sections 4.1.3 and 5.2.5.8 address the wireless and networks part. The sensors part is well covered in Chapters 4 and 5. Now the time has come to discuss the evolution of the wearable portion of this name.

7.1.1 2009

Initial experimentation, during Spring Training activities in 2009, quickly brought to light many wearable issues. Before describing the problem it is necessary to discuss the first approach to body attachment.

Each body segment was instrumented in a slightly different manner, mainly using two different types of medical tape, 3M brand COBAN and Johnson & Johnson/Cramer pre-wrap. Pre-wrap was used on the skin to slightly buffer the nodes against the skin and also on top of the nodes to initially keep each in place. Pre-wrap is thin foam that is self adhesive, commonly used between the skin and sports equipment, such as knee pads, to avoid chafing. COBAN, which is also self adhesive and much stronger, was placed on top of the pre-wrap.

FIGURE 7-57 COBAN (Left) Pre-Wrap (Middle, Right)



FIGURE 7-58 Empi StimCare Electrodes, Standard (Left), Hook Velcro Attached (Right)



The most delicate approach was taken with the hand. This is because the hand makes contact with the ball and pitchers are sensitive to any changes occurring to the throwing hand, hence the number one goal was to not impede motion and throwing style as much as possible. In order to achieve maximum adhesions with the skin on top of the hand (where the hand node was mounted) an Empi StimCare Carbon FM Electrode (FIGURE 7-58 left) was affixed directly to the skin. The electrical lead from the pad was trimmed and industrial strength adhesive hook velcro was applied to the top of each pad (FIGURE 7-58 right). The loop side of the velcro was applied to the back of the hand node and the two were mated on the hand. This is visible in FIGURE 7-59 . The node was then prewrapped and COBAN'd.

FIGURE 7-59 Node mated to hand with stim pad and about to be pre-wrapped.



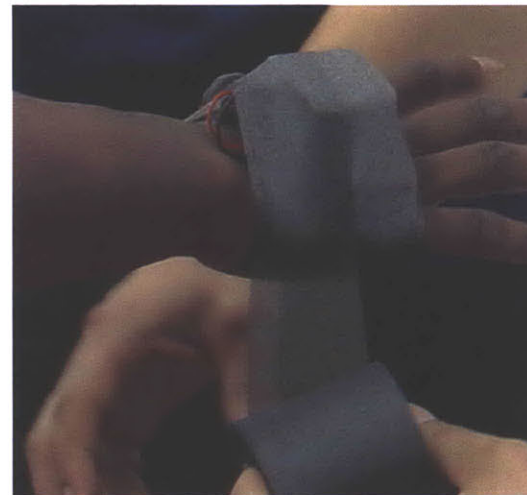
The forearm and upper arm received a similar treatment, however without the stim pad. The chest node was attached using a Polar heart rate monitoring strap that received the same hook velcro as the stim pad. A pre-wrapped arm and the chest strap are visible in **FIGURE 7-61** .

A 8 inch wide lower back support made from elastic was purchased at a pharmacy and cut down to 3 inches in width; this was used to mount the waist node. A benefit of this support was that it already has the hook velcro built into it (as its own attachment mechanism) so the waist node was readily applied to it. The trimmed support with a node and a COBAN'd trunk and arm are visible in **FIGURE 7-62** .

When batting data was being gathered, the bat was instrumented for swings that did not involve ball impact. When this was occurring, the waist node was not applied to the waist and was used for the bat. This received the same treatment as the forearm and upper arm, with an extra thick layer of tape at the end of the bat to keep the node from sliding off during activity. An instrumented bat can be seen in **FIGURE 7-73** .

Instrumenting actual pitching and batting activity was a learning experience, to say the least. The attachment for the hand, forearm and upper arm nodes functioned quite well, when the player was not sweating. The attachment worked well under moderate sweating, but when a player was very hot and became profusely sweaty, everything started to slide down the arm and frequent readjustment was required. The other issue with this approach was that it took quite a bit of time to instrument the arm because of the multiple layers of tape that were applied. The chest and waist node had the problem that both would slide down the body because they were applied on top of the player's jersey. Applying copious amounts of pre-wrap and COBAN helped alleviate the sliding. Some node failures did occur from what is thought to be sweat creating shorts in the node. In general, the takeaway from our first

FIGURE 7-60 Pre-wrapped throwing hand



attempt was that too much time was (10-15 minutes) spent instrumenting the player, which impeded their workflow, and application directly to the skin, even with pre-wrap, caused failures when sweat began to short out the inertial nodes.

FIGURE 7-61 Pre-Wrapped upper arm and chest strap.



FIGURE 7-62 Pitcher with 4 of 5 nodes ready. Waist node still requires COBAN and pre-wrap

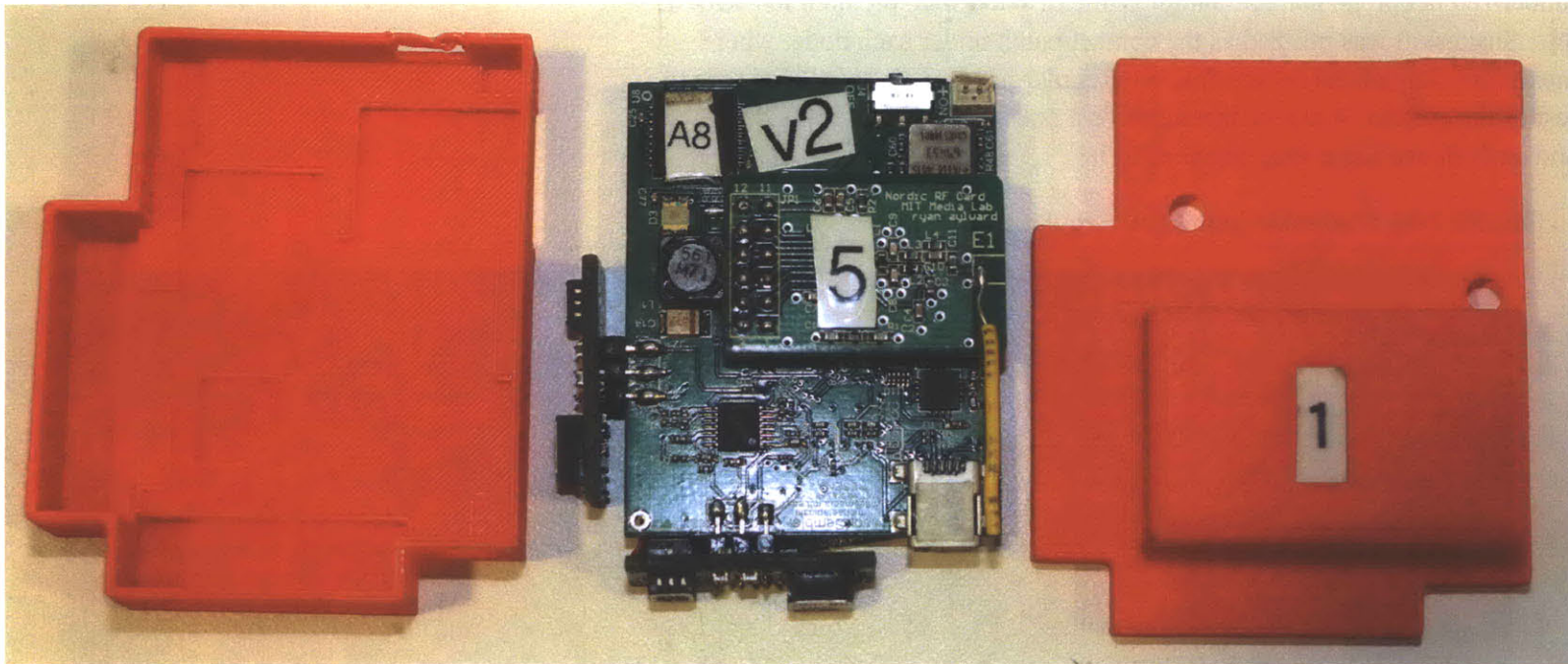


7.1.2 2010

¹⁷A very big thank you goes out to Steve Buckley of Corflex who facilitated and donated the time and materials to build the rapid attachment system.

For 2010, both issues were addressed. A rapid application system that did not slide and a case for each node were developed. The rapid application system was a collaboration between the author and an orthopedic rehabilitation product company named Corflex¹⁷. The case design came via a three dimensional CAD model based on node measurements.

FIGURE 7-63 Node Case (bottom case, left) (lid, right) and Hardware Rev 2 Node



The case was designed to add minimal size to the node placed inside of it and not allow the node to move inside the case. This strategy dictated a complex design that adhered to each surface of the node. This is clearly visible in the case bottom pictured in FIGURE 7-63 . The lid has a large protrusion for the battery and two relief holes to allow viewing of the on-node LED and allow

the antenna to extend outside of the case. Design was done in Solidworks and went through several iterations until an acceptable form factor was finalized. All cases were 3D printed and certain dimensions of the rapid application system were dictated by the case size.

The rapid application system's design started with choosing the appropriate materials. In consulting with Corflex about what material would be best to contact the skin, they suggested a standard material used in braces that has excellent skin adhesion and sweat wicking ability. The material is a rubberized neoprene that has a trade name of *snakeskin*, pictured in FIGURE 7-64 . Snakeskin was utilized as the contact patch under each node, where maximum skin adhesion was desired. Regular neoprene was utilized for the rest of the system. A sleeve that acted as a pocket for the case was designed, and each sleeve has a strap attached to it.

FIGURE 7-64 Snakeskin (right) and Regular Neoprene (left)



FIGURE 7-65 Hand & Forearm Sleeves



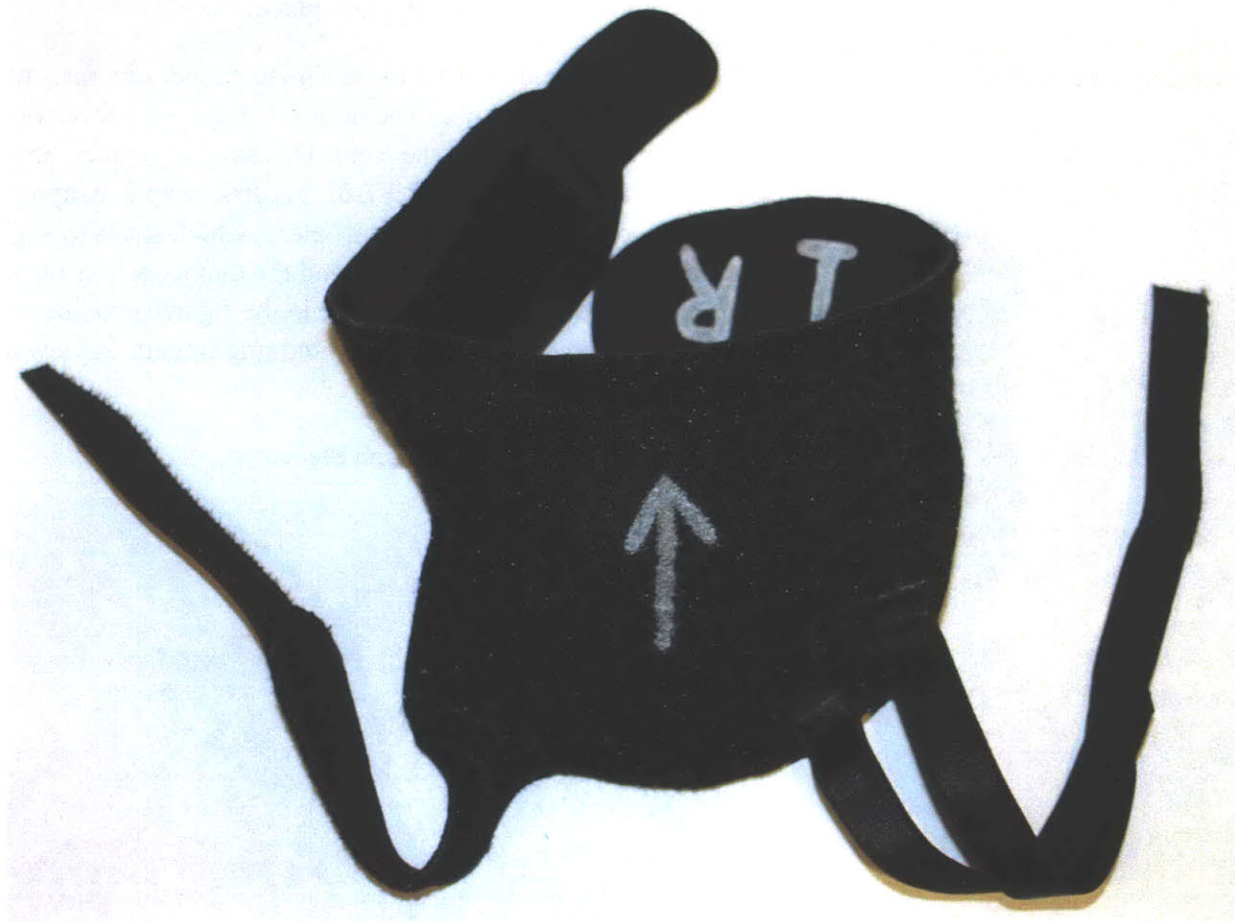
In order to secure the nodes, sleeves and straps into place on body segments, hook velcro was sewn into place.

As in 2009, and in order to maximize pitcher comfort, attachment to the hand was carefully designed. The design focused on not restricting the fingers and not to cover the palm of the hand. This strap is pictured applied in FIGURE 7-65 and standalone in FIGURE 7-67 . A first strap is wrapped around the wrist and is kept in place with hook velcro, which sticks to standard neoprene very well. A second strap wraps around the thumb, across the upper palm area and around the wrist; its end is visible in the figure right above the arrow. A third strap goes in between the pinky and ring fingers. A view of the palm area is shown in FIGURE 7-66 .

FIGURE 7-66 Palm View of Hand Sleeve



FIGURE 7-67 Hand Node Neoprene Sleeve



The sleeves used to attach the forearm and upper arm nodes (FIGURE 7-68) share the same construction. The only difference between the two is that the forearm sleeve is shorter because the forearm has a smaller circumference.

FIGURE 7-68 Forearm and Upper Arm Sleeves



These wrap around the body segment and, again, hook velcro that adheres to neoprene is used to secure them into place.

Due to the very similar attachment requirements the chest and waist node sleeves have the same construction. Pictured in FIGURE 7-69 , these two straps are much wider than others in order to adhere to the body better. They are held in place with a wide-hook piece of velcro (visible attached to the sleeve in the upper are of the figure) and have a pocket that is velcro'd shut once a case is put inside. In order to minimize sliding down the trunk and moving around, the chest sleeve was applied under the loose-fitting jersey of the instrumented athlete.

Corflex generously donated time, materials, and the benefit of their previous experience and executed sewing and construction of the sleeves. The finished product is professionally made and of commercial quality.

FIGURE 7-69 Chest and Waist Node Neoprene Sleeves



During 2010 Spring Training, the finished product performed exceptionally well. There were still some issues with the chest and waist straps sliding down the body during activity. The conclusions that is drawn is that these two sleeves should not be strap style sleeves, but rather integrated into an Under Armour style shirt that is very tight and covers the entire trunk. The

FIGURE 7-70 Carolina Brum Medeiros, a collaborator from McGill, adjusts a node on a 'BRO' instrumented pitcher during hybrid system experiments at the Mass General Orthopedics Sports Performance Center.



waist node would be best applied as a belt that makes use of the eyelets in the athletes pants to prevent movement up or down the pelvis.

The weak links during 2010 were the node cases. More failures occurred than in 2009, and most of them were due to the wireless daughterboard flexing, which, in Rev 2 of the hardware, was cantilevered at the header that it was mounted on only one fixed end of the daughterboard, as shown in FIGURE 7-63 . The solder joints flexed and possibly some pressure point existed that the rigid case exacerbated during extreme activity. The result of this was cracking of the solder joints at the header and wireless communication failing.

After 2010, the cases were no longer utilized and the nodes themselves were placed inside of the rapid attachment systems' sleeves, without any cases. This protected them from sweat and has proven to be the best approach.

During parallel testing with the optical system, where the *player* is required to be shirtless in order to attach optical system markers, it was discovered that the chest mount would slide down the chest. This was because as a *session* was ongoing the *player* would sweat, the shear force of motion overwhelmed the snakeskin's ability to remain adhered to the skin. A node sliding down the chest rendered the initial calibration *gestures* inaccurate.

A modification was made to the rapid attachment system in order to keep the chest node from sliding down a players body. It simply involved using two pieces of COBAN as a suspender FIGURE 7-70 . COBAN, with its excellent skin adhesion (even under sweating conditions), again proved to be an ideal material. The suspender was reminiscent of a *Sienfeld* episode [116] where one of the characters, Kramer, created a bra-like device for males to feed infants. He named this device the 'BRO' here the same name was applied to the suspender.

7.2 PITCHING PROTOCOL

The process for actually gathering data is purposely made to be as simple as possible to involve minimum setup time per player and keep a fast flow of subjects with minimum downtime. In general, an athlete is instrumented, measured and allowed to go about their normal activity.

The pitching protocol starts by instrumenting the athlete with the previously described neoprene sleeves. The next steps involve performing anthropometric measurements and logging pitch data as each ball is thrown. To facilitate this, a custom logbook was created. The logbook consists of a first page for recording the anthropometric and biometric data for each pitcher (FIGURE 7-71). The measurements recorded are described in the *Player* and *Session* sections in Chapter 3 (3.1.0.1 and 3.1.0.2).

Three types of calibration gestures are initially recorded for each *session*. The first of these involves the *player* standing upright, with both hands at their sides. The second involved the *player* standing in anatomic position. The third positioned the *player* with the arms abducted 90 degrees at the shoulder and the elbows at 90 degrees of flexion, forming a plane that is drawn by the shoulder, elbow and wrist joints. Each of these stances are recorded twice and the same calibration protocol is followed for pitchers and batters.

FIGURE 7-71 Pitcher Logbook Page 1



Pitching data Collection Sheet

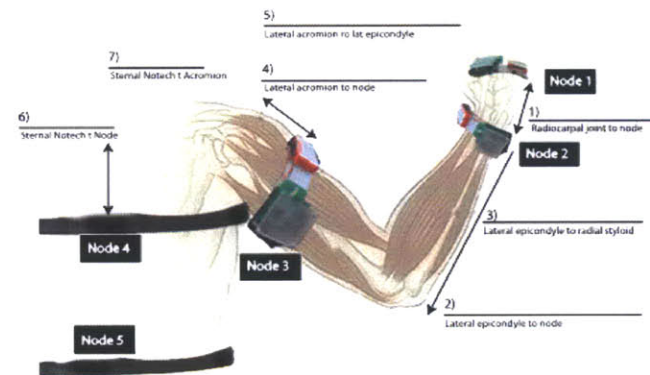
Name: _____ Date: _____

Age: _____ Height: _____ Weight: _____ Number: _____

Previous shoulder pain Y/N Previous surgery: Y/N _____ Throws: R/L Bats: R/L Pitch Types: _____

Set Up

	Node	Label	Comments	Inverted
Hand				
Wrist				Ⓞ Volar Ⓞ Dorsal
Arm				
Chest				
Waist				



1. Radiocarpal to Hand Node(1)		14. Stomach to Lower Back Thickness	
2. Lat Epicondyle to Forearm Node (2)		15. Stomach to Sternum Depth	
3. Lat Epicondyle to Radial Styloid		16. Chest Thickness	
4. Lateral Acromion to UpArm Node(3)		17. Pelvis Width	
5. Lateral Acromion to Lateral Epicondyle		18. Elbow Circumference	
6. Sternal Notch to Acromion		19. Wrist Circumference	
7. Sternal Notch to Chest Node(4)			
9. Chest Node (4) to Waist Node (5)			
10. Arm circumference			
11. Chest circumference			
12. Waist circumference			
13. Waist Node(5) to Floor			

FIGURE 7-72 Pitcher Logbook Pages 2-8



Pitching data Collection Sheet

Name: _____

Date: _____

#	Activity	File Name	Sequence Number	Pitch Type	Pitch Speed	Location	Comments						
1	Calibrate Hands at Side												
2	Calibrate Hands at Side												
3	Anatomic Position												
4	Anatomic Position												
5	Arms Up Elbow 90Degrees												
6	Arms Up Elbow 90Degrees												
7				FB CU BB		<table border="1" style="width: 40px; height: 40px; margin: auto;"><tr><td></td><td></td></tr><tr><td></td><td></td></tr><tr><td></td><td></td></tr></table>							
8				FB CU BB		<table border="1" style="width: 40px; height: 40px; margin: auto;"><tr><td></td><td></td></tr><tr><td></td><td></td></tr><tr><td></td><td></td></tr></table>							
9				FB CU BB		<table border="1" style="width: 40px; height: 40px; margin: auto;"><tr><td></td><td></td></tr><tr><td></td><td></td></tr><tr><td></td><td></td></tr></table>							
10				FB CU BB		<table border="1" style="width: 40px; height: 40px; margin: auto;"><tr><td></td><td></td></tr><tr><td></td><td></td></tr><tr><td></td><td></td></tr></table>							
11				FB CU BB		<table border="1" style="width: 40px; height: 40px; margin: auto;"><tr><td></td><td></td></tr><tr><td></td><td></td></tr><tr><td></td><td></td></tr></table>							

The following pages of the logbook are all identical; an example is presented in FIGURE 7-72 . These are used to record data for each pitch that is thrown. In order to effectively gather all necessary data, 3 people are required. One person is the system operator who monitors and controls the *Network Control Application* (Section 6.1). In continuous pitching mode, the operator is also broadcasting the *Sequence Number* (Section 6.1.5) to the data recorder and radar gun operator. For each pitch, the data recorder is responsible for

logging the *File Name*, *Sequence Number*, *Pitch Type* and *Pitch Location*. The radar gun operator is responsible for standing behind the catcher and recording the *Sequence Number* and the incoming pitch speed in miles per hour. If single gesture capture mode is used, there is no *Sequence Number*, so a filename is recorded for each pitch. Once the pitching *Session* concludes, the radar gun operator's pitch speeds are rectified with the *Sequence Numbers* or *File Names* and added to the data recorder's pitching sheet.

The next steps in the process involve using the *Data Translation Application* (Section 6.2) and the *Data Processing and Import Application* (Section 6.4) to process and load data into the data store. These processes are the same for pitching and batting. Optical system synchronization will be presented in Section 7.5.

7.3 BATTING PROTOCOL

.....

Batting experimentation consists of two different protocols. The first is a directed protocol, where the batter performs free swings with an instrumented bat, hits balls off of the tee with instruction on where the ball should go, then hits some soft toss pitches. The second fits more into the routine training activity of batting practice (BP) and the system runs in continuous mode.

7.3.1 Directed Batting Protocol

Historically, the directed batting took place in the batting cages at the minor league facilities of a major league baseball team, hence the title of the first page of the logbook (FIGURE 7-74) is *Batting Cage Data Collection Sheet*. The portability of a wearable inertial system does not prevent this from

being performed out in the field. As with pitching, a batter is instrumented and also measured

FIGURE 7-73 Dr. Eric Berkson from MGH measures a batter while the author logs measurements. ¹⁸



¹⁸Picture is from 2009, as indicated by the tape-based node attachment scheme. An instrumented bat is visible on the left.

FIGURE 7-74 Directed Batting Protocol Logbook Page 1



Batting Cage Data Collection Sheet

Name: _____ Date: _____ Time: _____

Age: _____ Height: _____ Weight: _____ Number: _____

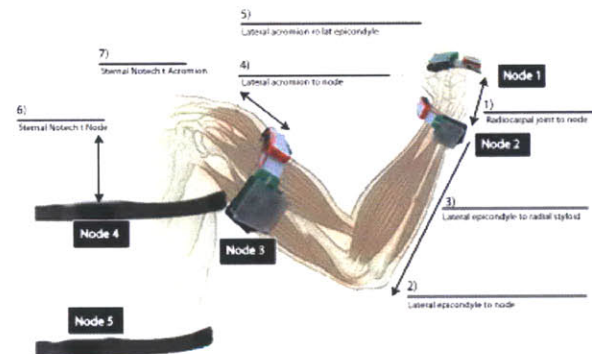
Previous shoulder pain Y/N Previous surgery: Y/N _____ Throws: R/L _____ Bats: R/L _____

Set Up

	Node	Label	Comments
Hand			
Wrist			⊗ Volar ⊙ Dorsal
Arm			
Chest			
Waist			
Bat			



1. Wrist to Node	
2. Lat epicondyle to Node 2	
3. Lat epicondyle to radial styloid	
4. Lateral Acromion to Node 3	
5. Lateral Acromion to node	
6. Sternal Notch to acromion	
7. Sternal Notch to Chest node	
9. Chest Node to Waist Node	
10. Arm circumference	
11. Chest circumference	
12. Waist circumference	
13. Waist node to floor	
14. Bat tip to node	
15. Bat Length	



Batting Cage

Free swing 6 (3 x 2)

Free swing 6 (3 x 2)

Tee

- Normal swing 4 indy
- To right field 2
- To left field 2

Soft toss

- Normal swing 4
- To right field 2
- To left field 2

Pitched balls 6

The directed protocol involves the batter performing a variety of *gestures* at the direction of the system operator. These *gestures* are:

With an instrumented bat at home plate:

- 6 x Free Swing - batter swinging the bat with no impact

With an un-instrumented bat hitting from a batting tee at home plate:

- 4 x Hit From Tee Straight - batter is instructed to hit the ball straight into center field
- 2 x Hit From Tee Right - batter is instructed to hit the ball into right field
- 3 x Hit From Tee Left - batter is instructed to hit the ball into left field

With an un-instrumented bat from home plate and a pitcher throwing underhand from half the distance between the pitching mound and home plate:

- 4 x Hit Straight - batter is instructed to hit the ball straight into center field
- 2 x Hit Right - batter is instructed to hit the ball into right field
- 3 x Hit Left - batter is instructed to hit the ball into left field

With an un-instrumented bat from home plate and a pitcher throwing overhand at a moderate speed (40 - 65 MPH):

- 6 x Hit Ball

As these swings and hits are occurring, an operator is controlling the network and dictating *File Names* to the data recorder and radar gun operator. The data recorder logs *File Name*, *Location* of where the ball went on the field (via a graphic of the field on the sheet) and the trajectory arc of the ball when it was hit. The radar gun operator is recording the outgoing speed of the ball, and in the case of pitched balls the incoming pitch speed and the *File Names*.

FIGURE 7-75 Directed Batting Protocol Logbook Swing Annotation Page



Batting Cage Data Collection Sheet

Name: _____ Date: _____ Time: _____

#	Activity	File Name	Sequence Number	Pitch Type	Pitch Speed	Pitch Location	Location	Comments
1	Calibrate Hands at Side							
2	Calibrate Hands at Side							
3	Anatomic Position							
4	Free swing x 2			FB CU BB			 <input type="checkbox"/> Strike (missed) <input type="checkbox"/> Aborted Swing <input type="checkbox"/> Foul Ball <input type="checkbox"/> Line Drive <input type="checkbox"/> Fly ball <input type="checkbox"/> H.R.	@Instrumented bat
5	Free swing x 2			FB CU BB			 <input type="checkbox"/> Strike (missed) <input type="checkbox"/> Aborted Swing <input type="checkbox"/> Foul Ball <input type="checkbox"/> Line Drive <input type="checkbox"/> Fly ball <input type="checkbox"/> H.R.	@Instrumented bat
6	Free swing x 2			FB CU BB			 <input type="checkbox"/> Strike (missed) <input type="checkbox"/> Aborted Swing <input type="checkbox"/> Foul Ball <input type="checkbox"/> Line Drive <input type="checkbox"/> Fly ball <input type="checkbox"/> H.R.	@Instrumented bat
7	Tee normal swing			FB CU BB			 <input type="checkbox"/> Strike (missed) <input type="checkbox"/> Aborted Swing <input type="checkbox"/> Foul Ball <input type="checkbox"/> Line Drive <input type="checkbox"/> Fly ball <input type="checkbox"/> H.R.	@Instrumented bat
8	Tee normal swing			FB CU BB			 <input type="checkbox"/> Strike (missed) <input type="checkbox"/> Aborted Swing <input type="checkbox"/> Foul Ball <input type="checkbox"/> Line Drive <input type="checkbox"/> Fly ball <input type="checkbox"/> H.R.	@Instrumented bat
9	Tee normal swing			FB CU BB			 <input type="checkbox"/> Strike (missed) <input type="checkbox"/> Aborted Swing <input type="checkbox"/> Foul Ball <input type="checkbox"/> Line Drive <input type="checkbox"/> Fly ball <input type="checkbox"/> H.R.	@Instrumented bat
10	Tee normal swing			FB CU BB			 <input type="checkbox"/> Strike (missed) <input type="checkbox"/> Aborted Swing <input type="checkbox"/> Foul Ball <input type="checkbox"/> Line Drive <input type="checkbox"/> Fly ball <input type="checkbox"/> H.R.	@Instrumented bat

7.3.2 Batting Practice Protocol

Batting practice, or BP as it is called by those in the know, involves a continuous series of moderate speed (45 - 75MPH) overhead pitches thrown by a professional pitcher from halfway between home plate and the pitching mound. This scenario is ideal for utilizing the system's *Continuous Sampling Mode* (Section 6.1.5).

The protocol followed for BP is the same as pitching in continuous mode, with the caveat that pitch data is not logged. The data logged is the same data as is logged with directed batting during overhead soft toss.

FIGURE 7-76 Dual system experiment at the Mass General Orthopedics Sports Performance Center; Collaborator Donna



Scarborough measures pitch speed.

7.4 DUAL SYSTEM EXPERIMENTS

Gathering data from both an inertial and optical system simultaneously for the purposes of comparing the two requires instrumentation of the *player* with inertial nodes as well as optical markers (FIGURE 7-76) and synchronization of data streams from both systems. The synchronization system, which spans the hardware, firmware and software sections of this dissertation, is described in Sections 4.3.1, 5.1.1, 6.1.8.

The activity performed during dual system experiments is only pitching, and the protocol followed is that of non-continuous pitching. Additionally, the protocol follows the sequence of starting and stopping the recording of both systems, as described in the optical system synchronization timing diagram (FIGURE 5-41). Two additional pieces of data are gathered for each *gesture*: the optical system framerate and the offset delta between the start times of both systems. Both of these are utilized during *gesture annotation* (Section 6.4.4.2).

7.5 DATA TRANSLATION AND ANNOTATION

The underlying mechanics of how data moves from sensors via communication busses to a microcontroller and finally to μ SD cards on the nodes attached to body segments has been described in Chapters 4, 5 and 6. The data translation operator interface, used to retrieve data from the μ SD cards, is described Section 6.2.

Once a given data gathering protocol has been executed, the process for translating data is followed. The data is available in flat comma-separated-value format files for processing by the *Data Processing and Annotation Application* (Section 6.4). This application parses the files, applies calibration offsets and inserts all of this data into the database using the *bulk import* (Section 6.4.4.1) feature of the application. The final step is to use the data that is logged during each *Session* and annotate each of the *Gestures* to enable classification, data mining and analysis of the data.

The precursor to annotating gesture data is to create a *Player* and *Session* for that player. Some of the anthropomorphic and all of the biometric data, recorded on *Page 1* in both logbooks, is used in conjunction with the *Player Info Tab* (Section 6.4.2) to create the *Player*. Some of the anthropometric data and node body segment location data, from the same logbook page, are used to create a new *Session* using the *Player Sessions Tab* (Section FIGURE 6-53).

The annotation process involves matching *gesture filenames* with those that are recorded in the logbook and, depending on the gesture type, the proper parameters are entered in the *Player Gesture Tab* (FIGURE 6-55) that is part of the *Data Processing and Annotation Application* (Section 6.4).

FIGURE 7-77 Player Gestures Tab. From Data Processing and Annotation Application. (Large red numbers are for annotation purposes)

The screenshot displays the 'Player Gestures' tab with the following configuration options:

- Gesture Type:** Pitch, Swing, Other
- Swing Type:** Free Swing, Tee Hit, Soft Toss Hit, Batting Practice Hit, Normal Pitch Hit, Strike
- Hit Location:** Center Field, Left Field, Right Field, Strike
- Hit Trajectory:** Ground Ball, Line Drive, Normal, Pop Up, Strike
- Pitch Type:** Fastball, Fastball - 2 Seam, Fastball - 4 Seam, Changeup, Breaking Ball, Curveball, Slider, Unknown
- Is Bat Instrumented?:** Yes, No
- Pitch Speed(-1 if not available):** -1
- Hit Speed(-1 if not available):** -1
- Gesture Name:** BULK 30
- Comment:** BULK
- Camera Synch 5:** Start Time(ms after IMU's): 1225, Framerate: 360.36
- Pitch Location:** A 3x3 grid of colored squares (red, green, white) with Dirt/Missed Catch below it.
- Select File:** C:\MIT\sportsemble\DATA\2012_TESTING\KRAMER_MATT\MAR_7_2013\NODE1-BB\NODE1-BB.FILE37.m
- 1 Add New Gesture**, Allow Delete?
- 2 Update Gesture**, **3 Delete Gesture**, **4 Delete All Gestures**, **Correct Hi Gyro Drift**

7.5.1 Pitch Annotation

For reference purposes, the *Player Gestures* tab is presented again in FIGURE 7-77 and the same figure referencing approach as has been used in previous chapters will be used here.

The first step involves the operator selecting the pitch that has been matched to the filename in the *Player Gestures* list (6-33-10). Annotating a pitch requires translating data from the pitching logbook to the various radio button groups in the *Player Gestures Tab*.

The groups relevant to a pitch are:

- Gesture Type - This is always *Pitch*
- Pitch Type - taken from logbook's *Pitch Type* column and based on the pitch type signaled by the pitcher while throwing.
- Pitch Speed (Text Field) - measured via radar and taken from the logbook's *Pitch Speed* column and entered in the *Pitch Speed text area*.
- Pitch Location - taken from the logbook's *Pitch Location* column and entered in the *Pitch Location* radio group.

Once the correct radio groups are selected, the operator clicks the *Update Gesture* button and annotation has been completed.

7.5.2 Swing Annotation

Annotation a swing also starts with the operator selecting a *filename* matched *gesture* in the *Player Gestures* list (6-33-10) and translating logbook data to the appropriate radio button groups and text fields in the *Player Gestures* tab, FIGURE 7-77 .

The groups relevant to a swing are:

- Gesture Type - This is always *Swing*
- Swing Type - taken from logbook *Activity* column for directed batting; there are also options for swings during BP and at off-mound pitches.
- Pitch Speed (Text Field) - measured by radar, recorded in the *Pitch Speed* column and entered in the *Pitch Speed text area*; this is incoming pitch speed.
- Hit Speed (Text Field) - Also measured by radar and logged as outgoing hit speed. Data is entered into the *Hit Speed* text field.
- Hit Location - where the ball went, if it was struck. If not, the swing is recorded as a strike.

- Hit Trajectory - the arc that the ball flew in if struck or a strike if the ball was not struck.
- Bat Instrumentation - For *Free Swings*, the bat is instrumented and the *Yes* radio button is chosen, otherwise *No*.

Once the correct radio groups are selected the operator clicks the *Update Gesture* button and annotation has been completed.

7.5.3 Dual System Annotation

When a dual system experiment, using the inertial and optical system in parallel, is performed two pieces of additional data are logged: synchronization offset and framerate. These are entered into the *Camera Synch* area of the *Player Gestures* tab. The remaining annotation process follows the same procedure as described in the previous two sections.

VALIDATION AND ERROR SOURCES

This chapter seeks to answer one question, “How good are we?”, mainly by presenting measurement techniques. A validation methodology is developed and results are presented that compare the inertial system to an established optical one. But first, an examination of the sources and quantification of error that are present using an inertial approach is given.

8.1 ERROR QUANTIFICATION

Four sources of error are identified. Calibration error involves any error introduced at calibration time. Application error refers to error that will be introduced to the kinematic model by improperly aligning nodes at application time to the body segment's coordinate system. This is followed by a brief discussion of soft tissue artifacts and how they impact measurements. Lastly, acceleration-induced error in the gyroscopes is addressed.

8.1.1 Calibration

The process of individual node axis calibration, including the goodness of the linear fit for each, is documented in detail in Section 4.2. Here the calculated error bounds of each axis will be presented and discussed.

It is important to understand that this node calibration yields a linear function for each sensor axis that inputs an analog value and outputs an absolute acceleration/angular velocity. Please note that this inertial value is a prediction or interpolation based on a linear function, because the calibration does not sample every possible analog output from the sensor. Each of these predictions has some uncertainty associated with it, and this uncertainty is expressed in terms of a confidence interval. This uncertainty is comprised of two parts. The first is error in calibration, such as node alignment when rotating the node about a given axis. The second is the noise present in the sensor itself. Separation of these two is not possible and the uncertainty estimation performed here takes both into account.

The process for determining the functional confidence interval for each sensor axis that is calibrated uses standard statistical techniques based on residuals from the linear fit. The calculated confidence intervals for the nodes most commonly used in experimentation are presented in **FIGURE 8-1**. These

intervals allow stating of what the worst-case error is in our analog to absolute prediction. In lay terms, based on the table, we can state that “For any predicted acceleration value for the X axis, Node FA has a worse case error bound of $\pm 1.93\text{m/s}^2$.” or “For any predicted angular velocity for Node AA’s Yaw axis the worst case error bound is $\pm 120.93\text{degrees/s}$ ”.

FIGURE 8-1 Confidence Intervals For The Most Commonly Used Nodes

Node ID	High X	High Y	High Z	High Pitch	High Roll	High Yaw	Low X	Low Y	Low Z	Low Pitch	Low Roll	Low Yaw
FA	1.76	2.63	1.93	130.79	137.42	144.80	0.19	0.21	0.19	0.26	0.16	0.25
DA	3.01	2.57	5.43	130.29	172.85	171.14	0.32	0.25	0.32	0.43	0.04	0.12
BA	2.11	2.72	5.14	137.17	183.19	152.71	0.27	0.23	0.27	0.44	0.04	0.11
BB	2.76	2.37	3.28	114.70	180.56	155.30	0.37	0.11	0.37	0.38	0.26	0.19
AA	2.15	2.42	6.31	125.41	160.03	120.93	0.50	0.14	0.50	0.39	0.12	0.25
EF	2.33	2.94	5.92	139.31	160.01	131.83	0.39	0.82	0.39	1.31	0.39	0.22
EA	9.10	2.27	6.17	125.46	166.16	147.99	0.48	0.21	0.48	0.22	0.34	0.28
AC	2.78	2.48	8.01	162.69	142.27	155.22	0.37	0.15	0.37	0.44	0.15	0.36

Each node axis is separately calibrated and fit. These fits differ from node-to-node and are never used as generalized numbers to ensure maximum precision in per-node prediction. Looking at the standard deviation and mean of confidence intervals (FIGURE 8-2) indicates, in general, how good the calibration process is for the entire population of nodes.

FIGURE 8-2 Overall Per Axis Mean and Standard Deviation of Confidence Intervals (Gs for XYZ, °/s for others)

	High X	High Y	High Z	High Pitch	High Roll	High Yaw	Low X	Low Y	Low Z	Low Pitch	Low Roll	Low Yaw
Mean	3.25	2.55	5.27	133.23	162.81	147.49	0.36	0.26	0.36	0.48	0.19	0.22
StdDev	2.40	0.21	1.89	14.14	16.58	15.42	0.10	0.23	0.10	0.34	0.13	0.08

While the numbers presented in FIGURE 8-1 and FIGURE 8-2 allow for an accurate statement of data confidence, they do not really give an idea of how ‘good’ our system is. Taking the confidence interval as a percentage of the entire range of the sensor (FIGURE 8-3) gives a perspective of ‘goodness’.

FIGURE 8-3 Confidence Interval as a Percentage of Sensor Range (Gs for XYZ, °/s for others)

Range(±)	200	200	200	17000	17000	17000	16	16	16	1000	1000	1000
Node ID	High X	High Y	High Z	High Pitch	High Roll	High Yaw	Low X	Low Y	Low Z	Low Pitch	Low Roll	Low Yaw
FA	0.440%	0.657%	0.482%	0.385%	0.404%	0.426%	0.597%	0.653%	0.597%	0.013%	0.008%	0.012%
DA	0.752%	0.642%	1.357%	0.383%	0.508%	0.503%	1.009%	0.768%	1.009%	0.021%	0.002%	0.006%
BA	0.528%	0.681%	1.284%	0.403%	0.539%	0.449%	0.835%	0.710%	0.835%	0.022%	0.002%	0.005%
BB	0.691%	0.593%	0.819%	0.337%	0.531%	0.457%	1.159%	0.328%	1.159%	0.019%	0.013%	0.010%
AA	0.538%	0.605%	1.578%	0.369%	0.471%	0.356%	1.550%	0.450%	1.550%	0.019%	0.006%	0.012%
EF	0.582%	0.734%	1.481%	0.410%	0.471%	0.388%	1.215%	2.567%	1.215%	0.065%	0.020%	0.011%
EA	2.274%	0.567%	1.543%	0.369%	0.489%	0.435%	1.488%	0.656%	1.488%	0.011%	0.017%	0.014%
AC	0.694%	0.621%	2.001%	0.478%	0.418%	0.457%	1.166%	0.480%	1.166%	0.022%	0.008%	0.018%

Taking the min and max of the entire population (FIGURE 8-4) of calibrated nodes indicates the worst and the best performance of nodes. It is easy to observe that the low-range gyroscope has a extremely high confidence, best of ±0.002% and worst of ±0.018%. The low range gyro also demonstrates high confidence with a single outlier of ±1.550%; removing the outlier gives a worst case error of ±.768% and best of ±.328%. Similarly, the high-range accelerometer has an outlier that, if removed, gives a worst case accuracy of ±2.001% and best of ±0.440%. In general, the worst confidence (with outliers removed) is ±2%.

FIGURE 8-4 Minimum and Maximum (Best and Worst) Confidence in Predicted Sensor Data

Node ID	High X	High Y	High Z	High Pitch	High Roll	High Yaw	Low X	Low Y	Low Z	Low Pitch	Low Roll	Low Yaw
Min	0.440%	0.567%	0.482%	0.337%	0.404%	0.356%	0.597%	0.328%	0.597%	0.011%	0.002%	0.005%
Max	2.274%	0.734%	2.001%	0.478%	0.539%	0.503%	1.550%	2.567%	1.550%	0.065%	0.020%	0.018%

8.1.2 Application (Coordinate System Misalignment)

When performing an inertial to optical system comparison, an important assumption is made. That the coordinate systems of each segment (or limb that a node is attached to) in each system are aligned. This alignment is crucial for comparing segment orientations of both systems. Error in the alignment occurs when the inertial nodes are applied to an athlete's body. The sources of the error are due to varying body types and physical dimensions of athletes and difficulty in perfectly aligning the axes of the inertial node to skeletal landmarks.

The hand and forearm nodes do not suffer from a great deal of misalignment because both are placed on relatively flat surfaces on those segments. These surfaces happen to align very well with the planes that are used to define optical system coordinate systems.

For the upper arm, which is modeled as a cone and in reality has a cylindrical shape without flat surfaces, it is more difficult to ascertain the exact coordinate system orientation and apply the node accordingly. The Z-Axis is easy, as it runs along the humerus, and the X-axis is more difficult, as it is defined by the line drawn from the medial to lateral epicondyle. At application time, a best effort is made to align these axes, however this alignment is not perfect.

Measuring the alignment error on all three axes requires a common global coordinate system between both systems. Otherwise, it is only possible to measure the error about the X and Y axes. The two-axis approach is possible by considering that any global coordinate system has the plane defined by the X and Y axes orthogonal to gravity (if the floor defining the coordinate system is flat). By nature, the accelerometer measurement of the nodes is also orthogonal to Earth's gravity vector. Therefore, a calculated tilt and roll of an inertial node relative to gravity (given by the projection of Earth's 1G Gravitational field onto the three accelerometer axes) when the node is not

moving can be compared to the optical system's tilt and roll in relation to the global lab coordinate system.

For the inertial node, the Z axis for stationary subjects is calculated using magnetometer data to determine a Yaw relative to Earth's magnetic North. However, in order to create the common coordinate system, it is necessary to relate the optical system's coordinates to magnetic north. This is performed by placing the inertial nodes at the optical system's operator-defined (0, 0, 0) coordinates and recording data with them.

Once the data is recorded it is possible to determine how many degrees off of true north the optical coordinate systems Yaw components is. Subtracting this offset from every inertial reading yields a common coordinate system. The only assumption here is that the floor in the laboratory is level. If it is not, the same procedure must be repeated for the Pitch and Roll axes using data from the low range accelerometer.

8.1.3 Soft Tissue Artifacts

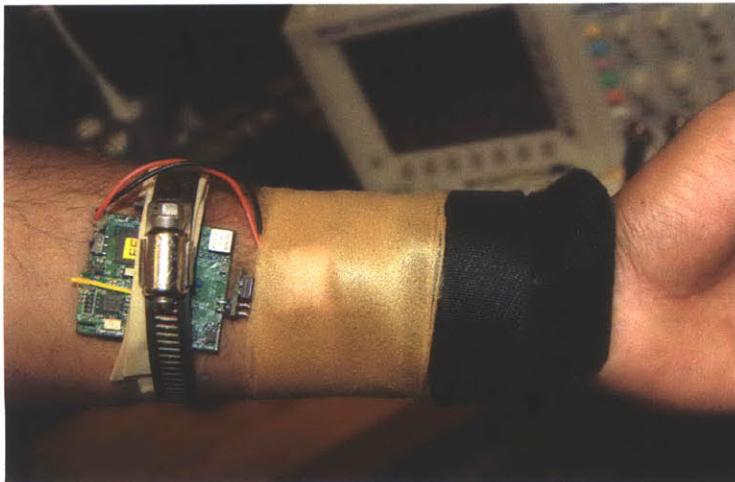
The effects of soft tissue artifacts (STAs) on optical markers attached to the skin are discussed in Section 2.1.5.1. The inertial nodes may also suffer from STAs because the neoprene sleeve mounting system developed to attach the IMU's is attached to surface skin and not rigidly mounted to bone.

While it is far beyond the scope of this work, the proper way to characterize STAs present in the neoprene system is to compare neoprene mounted inertial nodes to nodes attached to surgically mounted bone pins [46][48][97]. Bone pin attachment is the only way to exactly ascertain the accelerations and angular velocities that a segment experiences.

In an attempt to characterize inertial node STAs without the use of bone pins, one node was mounted using the standard neoprene and another was rigidly mounted using a thin rubberized buffer and a standard hose clamp. Both

nodes were mounted to the volar surface of the forearm (FIGURE 8-5) and the hose clamp was tightened on test subjects to the pain level they could tolerate. Four amateur subjects were instrumented and each completed four gestures. Three of the subjects were instrumented twice and have two sessions of four gestures. The subjects instrumented twice each had different mounting configurations. In the first configuration, the clamped node was distal from the elbow joint and the neoprene mounted proximally. In the second configuration, the mounting was swapped.

FIGURE 8-5 Soft Tissue Artifact Testing Configuration. Clamped node is proximal and sleeve-attached node is distal.



Data from each configuration was examined for the dominant acceleration axis, Z, and is presented in FIGURE 8-6

The magnitudes of the peaks of each node cannot be compared directly because each node is mounted at a different location on the forearm, hence this changes the radius of the circle each node draws as someone throws, thus it should be expected that the acceleration of the distal node will always be higher. This is confirmed by swapping the locations of the nodes.

A visual examination of the structure of the curves shows that for low accelerations the output of both nodes is similar. While under high accelerations the magnitudes differ, the general structure of the curves are very similar. After examining several curves the general conclusion is that the neoprene curves appear to be smoother than the clamped curves, which may indicate that the elasticity of the neoprene functions as a filter or spring, subtracting information at given frequencies or adding it. To examine this the Fourier transform was taken of each configuration to examine how much information exists at each frequency for each node.

FIGURE 8-6 Acceleration Curves For Both Testing Configurations

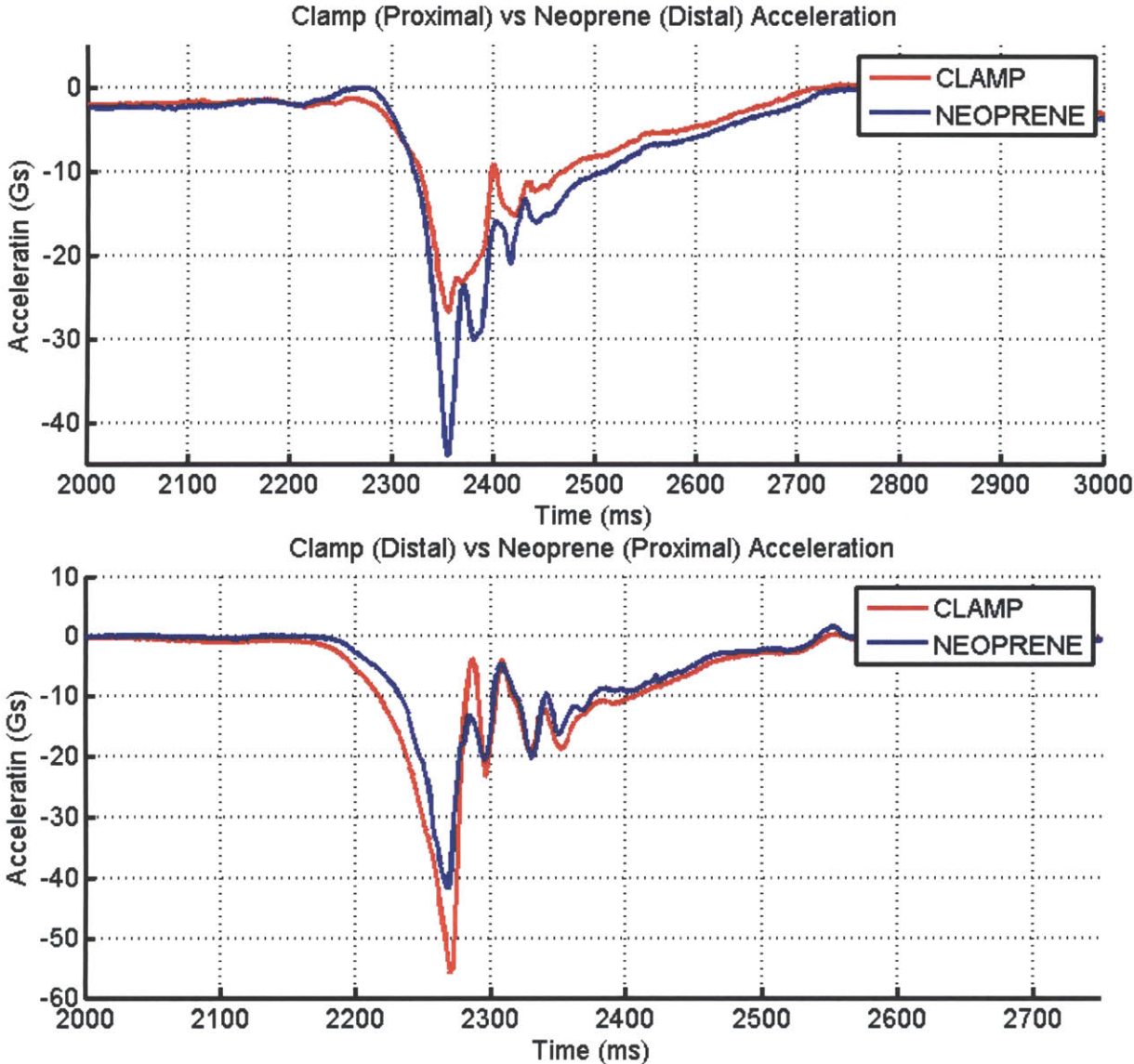
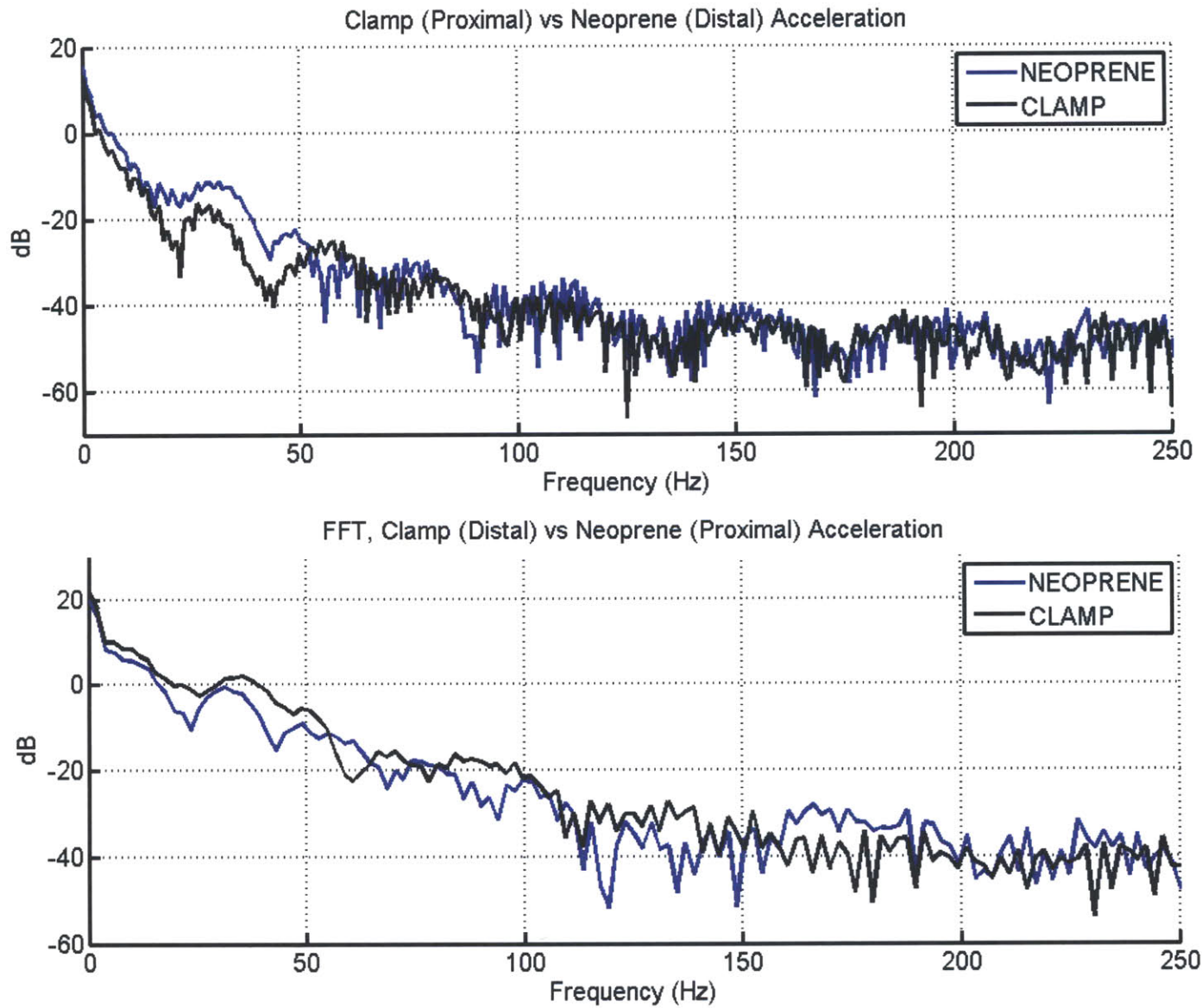


FIGURE 8-7 FFT of each node configuration



The main phenomena that can be observed for each of the FFT's (FIGURE 8-7) is that the distal node has more low frequency information from 5 to 55Hz. There exists a notch, from 55-62Hz, where the proximal node contains more information. Around 90Hz the distal node again has more information present.

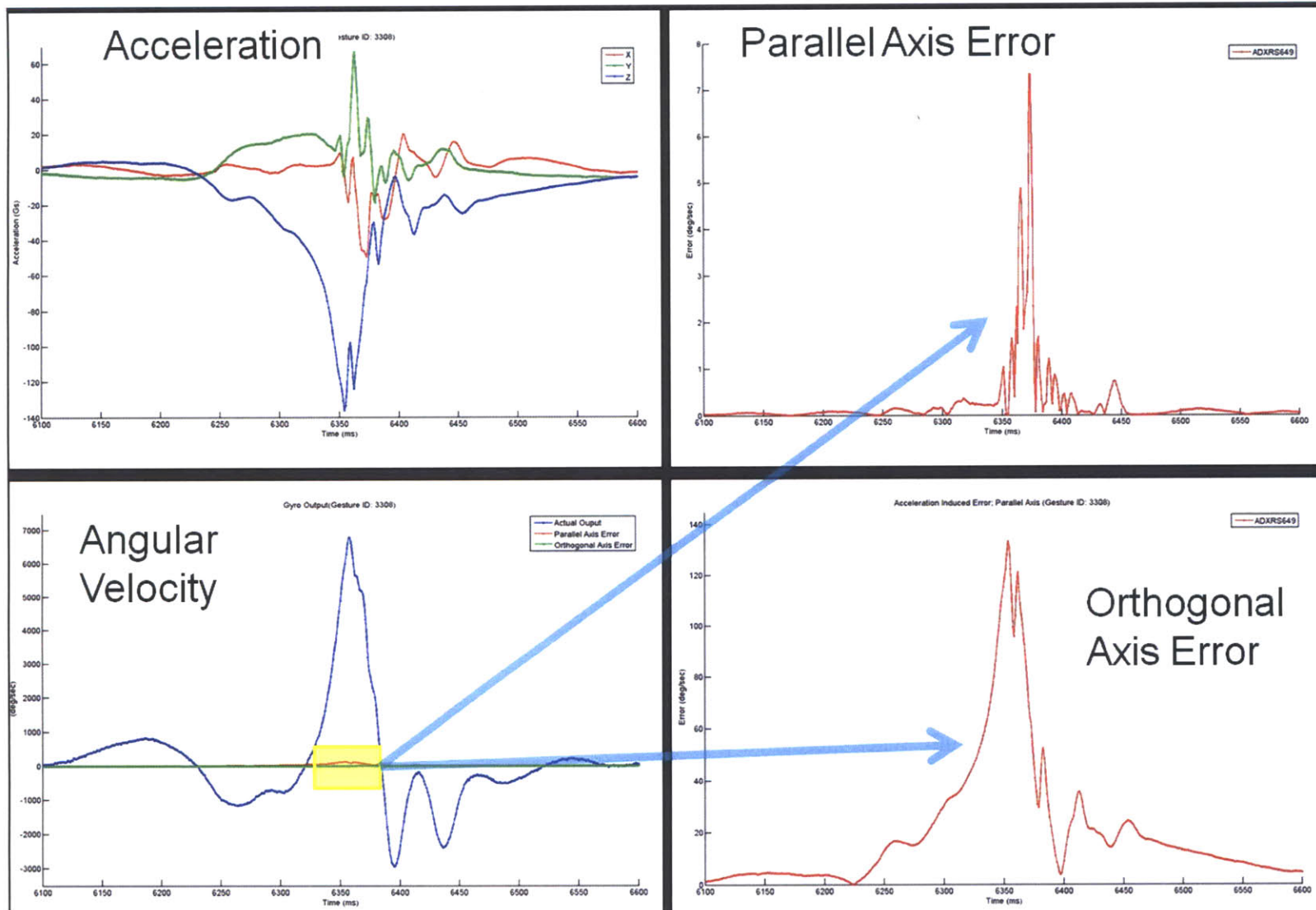
Both sets of data presented in FIGURE 8-6 and FIGURE 8-7 have differences based on node position rather than the mechanism used to attach the node to the body. This experiment affirms the need for surgically mounted bone pins to truly study the effects of soft tissue artifacts associated with the neoprene application system, and/or comparison of this data to the predictions of a numerical model that account for expected skin stretch, bounce, and other mechanisms and its effects on node measurement. In reality, such study is not possible, and a new area of research is exposed in characterizing the behavior of skin when placed under high acceleration as there is no existing body of work that addresses this¹.

8.1.4 Acceleration Induced Gyroscope Error

Due to the physical structure of micro-electromechanical gyroscopes, they are susceptible to false angular velocity being sensed when the sensors experience high acceleration. This false angular velocity is proportional to acceleration along (parallel to) the axis the gyroscope senses on and both axes orthogonal to the gyroscope axis. Fortunately, each inertial node is equipped with an accelerometer aligned with gyroscope axis and orthogonal to it. This allows for acceleration induced angular velocity be mathematically calculated and subtracted from the measured angular velocity [106]. This calculation for the high-range Analog Devices gyroscope (ADXRS649) used in the current hardware revision of the inertial node was performed using actual gesture data and the results are presented in FIGURE 8-8 .

¹This statement is based on conversations with Dr. Berkson, MGH Sport Medicine.

FIGURE 8-8 Acceleration Induced Error Sample Data



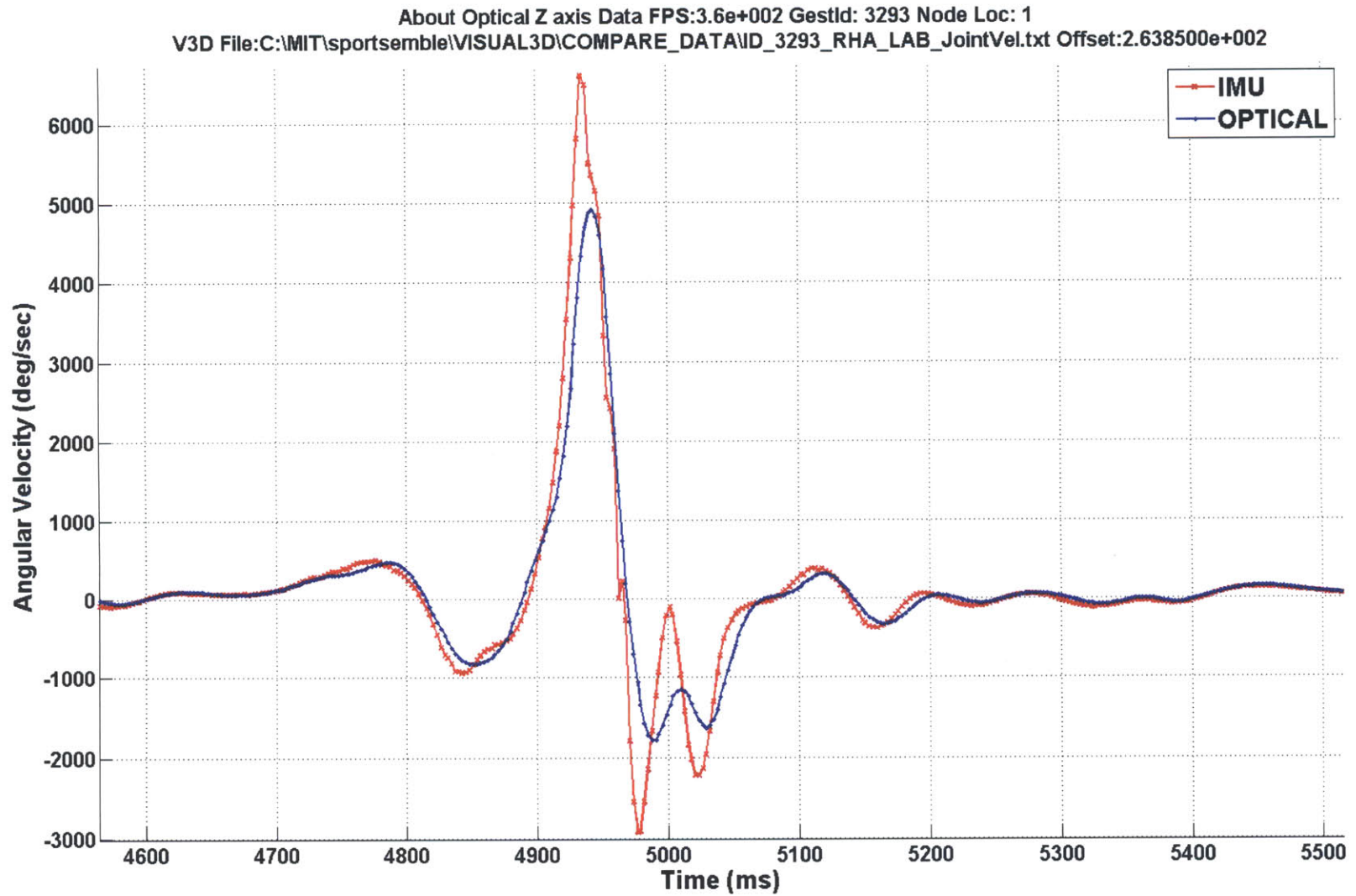
The ADXRS649 is a newer part and is used in the latest revision of the inertial node, thus it is the focus of analysis here. A peak angular velocity of around 7,000 degrees/sec is seen at this gesture, and the parallel axis false angular velocity is less than 135 degrees/sec. At the same angular velocity, the acceleration at the orthogonal axes adds less than 8 degrees/sec of false angular velocity. This gives a total of 143 degrees/sec of false angular velocity which is 1.8%, if data is left uncorrected. However, because the error can be calculated and all parameters necessary to do so are readily available we accommodate this in our analysis, and this phenomena does not present a source of system error.

8.2 SYSTEM VALIDATION

Comparison of the inertial system against the optical is another indication as to how ‘good’ the inertial system is. However, a tricky question arises when this comparison is performed: What if, for certain parameters, the inertial system is better than the optical?

Optical systems directly observe segment position and orientations via marker positions, and because of this they are better at providing these parameters. Their accuracy and precision is discussed in Section 2.1.5 in detail. Because of this, the kinematic calculations of the inertial system must use the optical as a ‘gold standard’ ground truth. When inertial parameters are considered, it is necessary to answer the above question. If the inertial system is better, then it is necessary to compare the optical system to the inertial and examine how ‘good’ it is at estimating inertial parameters and use the inertial system as the ‘gold standard’.

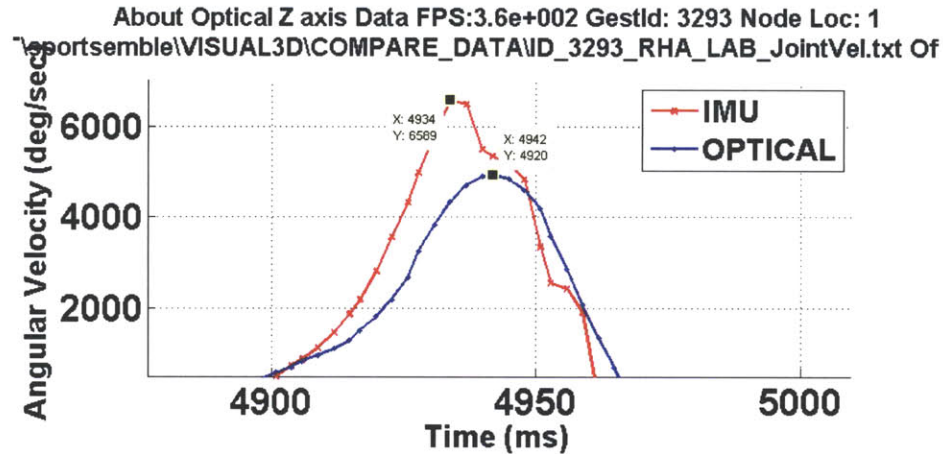
FIGURE 8-9 Synchronized Inertial & Filtered (13Hz Butterworth) Optical Data (Z Axis Hand)



8.2.1 The Inertial Gold Standard

The inertial gold standard starts with examining synchronized, coordinate system rectified data from both systems, such as that in **FIGURE 8-9** . Of particular interest are peak maxima and minima present in each of the data sets, **FIGURE 8-10** . The first important observation is the difference in peak amplitude, $6589^\circ/\text{sec}$ inertial vs. $4920^\circ/\text{sec}$ optical, a delta of $1669^\circ/\text{sec}$. The optical data appears to be attenuated. The second observation is the smoothness of the optical curve, as there is very little high frequency change in the optical data.

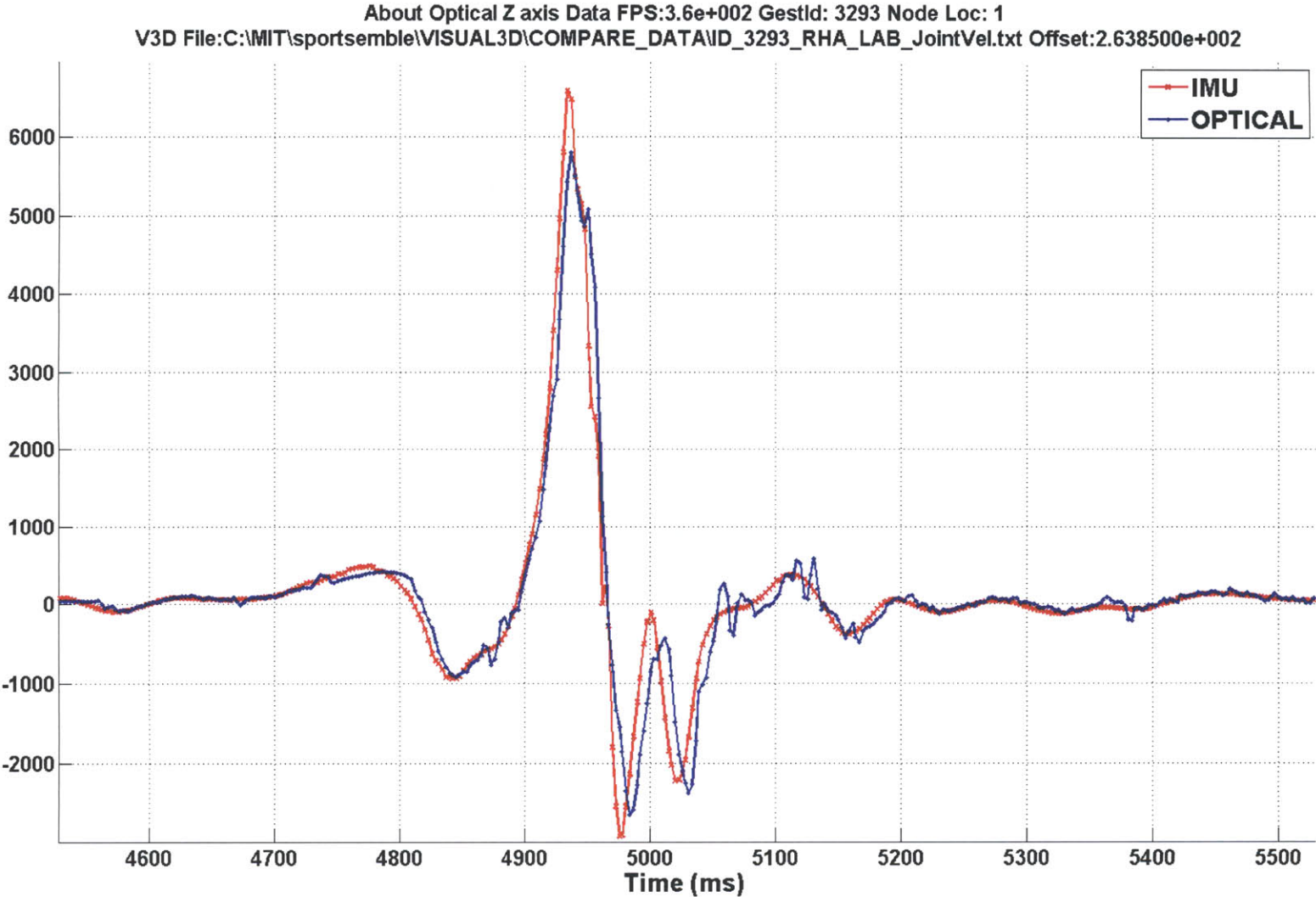
FIGURE 8-10 Zoomed Peak of Filtered Synchronized Inertial & Optical Data (Z Axis Hand)



This smoothness and attenuation are explained by the standard procedures for processing optical data for biomechanical studies, application of a 13Hz Butterworth filter on the data [\[\[12\]\[30\]\[31\]\[32\]\[33\]\]](#). This is to de-noise data and provide smooth derivatives (velocity and accelerations) in order to obtain smooth kinetics (forces and moments) when processing *gesture* data.

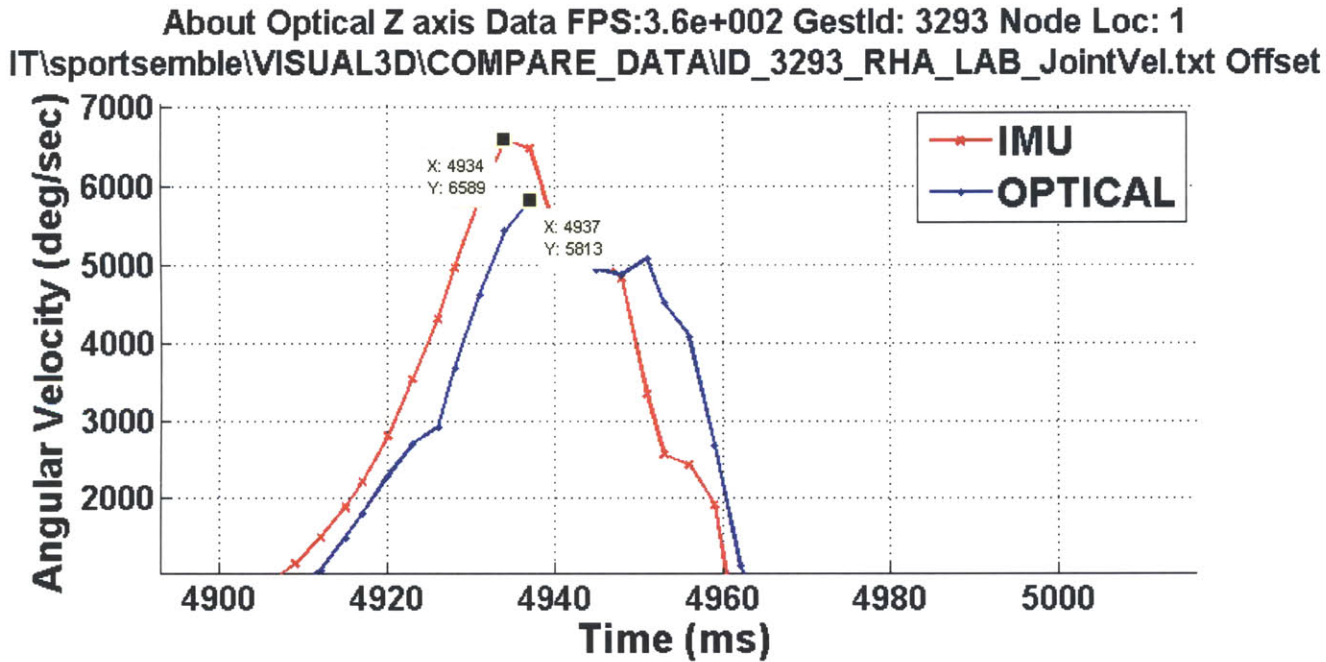
Logically, the next step is to not filter the optical data and compare the two datasets again. The expected result is that the amplitude of the signal will not be attenuated at the cost of additional noise. Unfiltered data is presented in **FIGURE 8-11** and the hypothesis holds true.

FIGURE 8-11 Unfiltered, Synchronized Inertial & Optical Data (Z Axis Hand)



Zooming and examining the peaks (FIGURE 8-12) shows that there is less attenuation in the signal and the peak amplitude of the optical data is higher, 5813°/sec, which now yields a delta of 776°/sec, which is 13% of the peak. Interestingly we have ‘found’ 893°/sec (almost 26%) of angular velocity by not filtering the data.

FIGURE 8-12 Zoomed Peak of Unfiltered Synchronized Inertial & Optical Data (Z Axis Hand)



This trivial analysis shows that filtering high frequency activity like pitching drastically skews (from one example by 26%) any angular velocity

results that are obtained. This is independent of any inertial system or data and bears large scale future investigation.

However, we are not done yet, as the inertial confidence interval has not been considered. The worst case interval of $\pm 2\%$ yields a worst case error in the inertially measured peak of $6589 \pm 131.7^\circ/\text{sec}$. The best case delta, from unfiltered optical data is $776^\circ/\text{sec}$. We still need to ‘find’ $645^\circ/\text{sec}$ of angular velocity. This search started by consulting an expert in optical motion capture, Tom Kepple, who has over 25 years experience in all facets of motion capture and is Chief Science Officer of C-Motion Inc.² After discussion and examination of the data, he confirms that, yes, additional attenuation is occurring somewhere along the datapath from the camera lens to the final graphs provided here. However, he is not able to state accurately where it is occurring. In order to determine where and how it is occurring a view into the optical system’s algorithms is necessary. As these are proprietary to each commercial system, the likelihood of obtaining this is low.

Considering the worst case $\pm 2\%$ confidence that exists in the inertial, Tom’s advice for system comparison at the inertial level was to use the inertial system as the gold standard and see how ‘good’ the optical system is compared to the inertial at these extreme rates. Further, because the standard practice is to use filtered data for all dynamics (kinetic) calculations, that the optical data used to compare should be filtered, rather than more accurate unfiltered data.

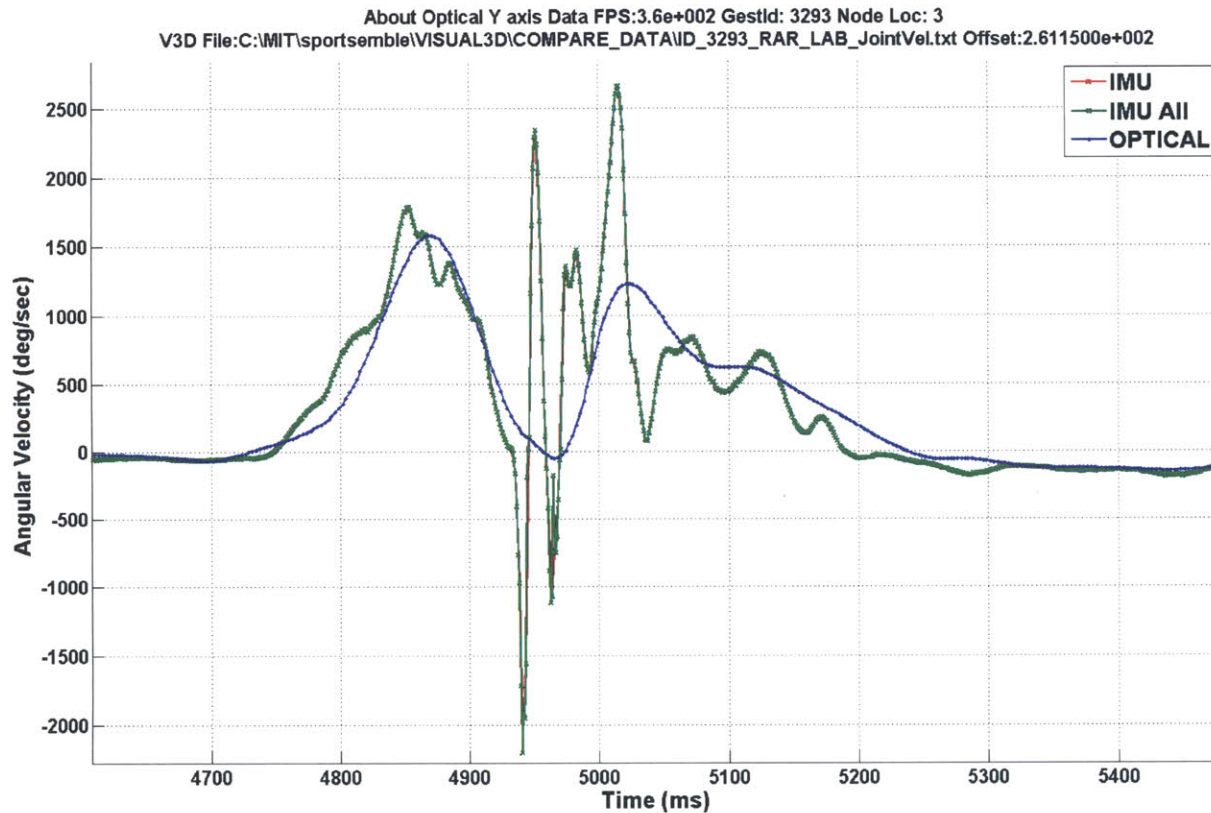
8.2.2 The Eyeball Comparison

Sections 8.2.3 and 8.2.4 statistically compare the optical and inertial systems on each sensed axis for each body segment. This section takes a step back and performs what is called an eyeball analysis, visually looking at the synchronized data from each system to see how the two compare to each other. The purpose of eyeball analysis is help develop an intuition as to what is really

²C-Motion produces optical system analysis software and works closely with vendors of these systems. If any bias were to be present in Tom’s opinion it would lean towards supporting optical systems as these are the focus of his life work.

going on in order to aid understanding of the statistical analysis. The first part of the eyeball analysis occurred above, when comparing a specific peak from the inertial to an optical system. As noted before, it was observed that there exists an attenuation in the optical system that is due to the low frequency filtering on tracked marker data.

FIGURE 8-13 Angular Velocity, Optical and Inertial; Upper Arm. Optical is missing information due to low



frequency filtering.

The second artifact of this filtering is presented in **FIGURE 8-13**. An initial eyeball comparison shows that the curves for both are similar at the

beginning and end of the motion. Further comparison yields the conclusion that there is more information (more happening) in the inertial system curve while the optical curve is subdued.

The high frequency changes in the inertial curve may very well be present in raw optical data observed, however the 13Hz filter being applied is probably responsible for destroying this information. This portion of the data is most important to those studying high-speed motion, as it is where angular velocities and accelerations are high, but is missing from the optical curve. In general, this curve does not pass the eyeball comparison very well since the data we care about the most is not present and the magnitudes of highest peaks and lows are missing. This is significant because it is theorized that most stress and repetitive microtrauma occurs during peak angular velocities and accelerations. If these are undermeasured, the true severity of the trauma is also undermeasured. Again, some of these oscillations may be due to soft tissue artifacts; any exploitation of its detailed structure will need to take these into account.

FIGURE 8-14 Angular Acceleration Inertial (green), Optical and downsampled Inertial (red) for a fastball.

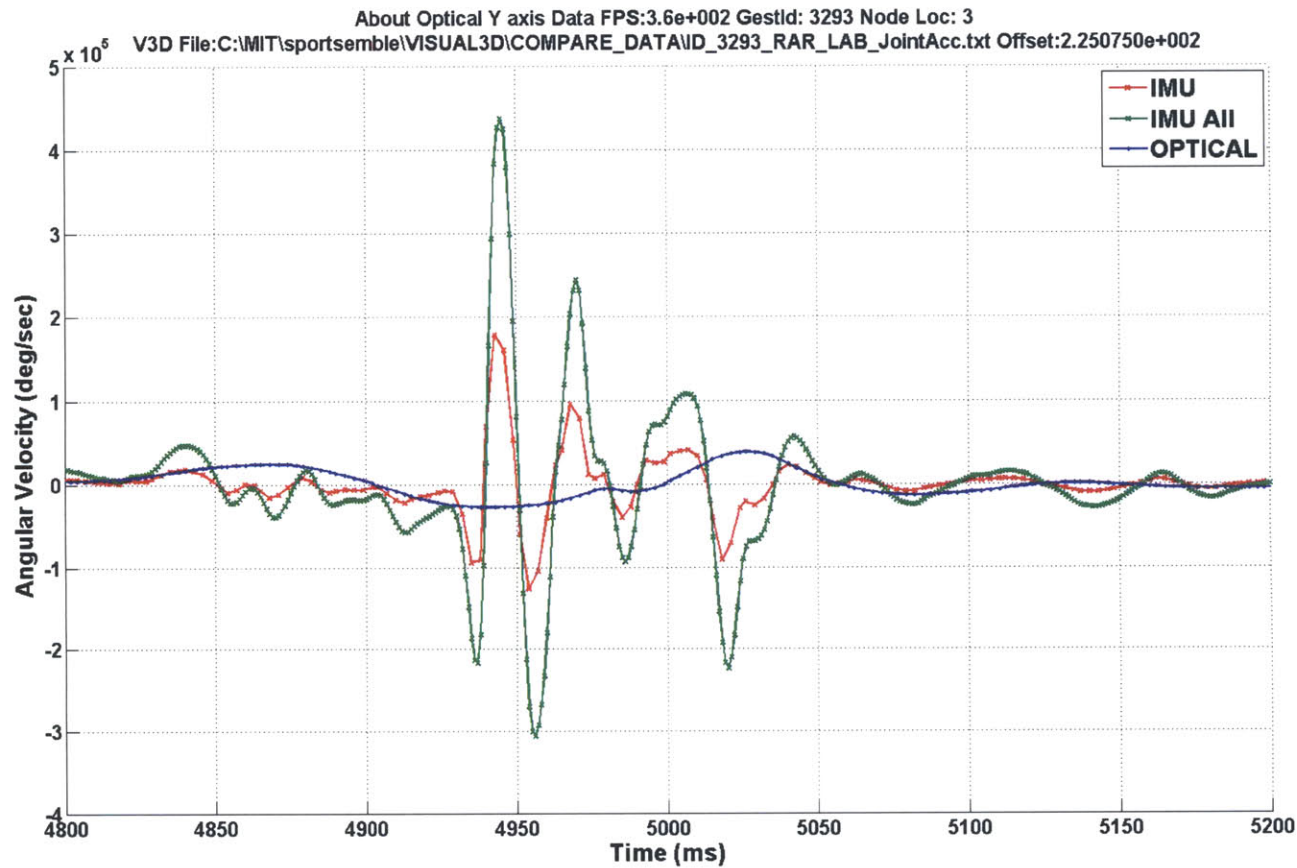


Figure FIGURE 8-14 presents the angular acceleration (*IMU All*, *OPTICAL*), from the same motion presented in FIGURE 8-13 . The red *IMU* curve is data that is downsampled to the sampling frequency of the optical system, 360Hz in this case. The purpose of this downsampling is to perform a Root Mean Squared Error analysis of the two systems. *IMU All* has a sampling

frequency of 1000Hz. Unfiltered optical angular acceleration data is not considered as it is almost all noise.

Applying the same eyeballs to these curves two things are quickly obvious. The first, that the angular acceleration calculated by the optical system is dwarfed by the *IMU All* angular acceleration. The explanation for this is simple, if you start with a smooth (heavily filtered) curve and differentiate the resulting curve will also be smooth. Data was destroyed in the filtering and will be lost for any future processing. The unfiltered, high frequency changes in the *IMU All* curve are a much better indicator of the true angular acceleration because they are based on a tight accuracy confidence interval ($\pm 2\%$) and directly measured angular velocity data.

The second observation that can be made is that of the effects of sampling rate on angular acceleration. The red *IMU* curve is downsampled to the 360Hz sampling rate of the optical system. While the red curve more closely matches the green in terms of structure, its range is closer to that of the blue optical curve. This indicates that not only does the initial filtering of the optical data effect angular acceleration results, but that sampling frequency also plays a role. It also indicates that the optical systems need to improve or that other avenues for obtaining angular velocity data to complement the optical system need to be explored.

8.2.3 Angular Velocity Comparison

The root mean squared error (RMSE) and delta between maximum/minimum peaks for each *gesture* are the two metrics used to compare the optical system to the inertial. The RMSE is an indicator of how good the fit is between the studied *gestures*. The delta between the maxima/minima is an indicator of how much attenuation is occurring. Further, most biomechanical analysis focuses on peak inertial values; as they are

indicators of maximum microtrauma, the accuracy of these directly effects reported results and validity of calculated data. In general, both are indicators of how far off calculated optical angular velocities and angular accelerations are from the real physical world.

RMSE, the delta between the maximum peaks and delta between minimum peaks of 26 gestures for one pitcher were calculated. A standard score (Z Score) and P Value were also extracted for the peaks and lows of each axis of each instrumented segment.

FIGURE 8-15 Mean Angular Velocity RMSE of Optical vs.Inertial (Per-Segment Per-Axis) (°/sec)

P1	HAND		FOREARM		UPARM		CHEST		WAIST	
	MEAN	STDEV	MEAN	STDEV	MEAN	STDEV	MEAN	STDEV	MEAN	STDEV
X	99.2	17.5	117.9	26.4	93.8	14.0	62.2	16.7	25.9	3.0
Y	94.7	22.0	113.8	16.8	127.9	13.4	21.8	3.7	23.8	8.2
Z	189.3	28.8	192.3	28.5	165.9	23.5	64.3	13.1	25.1	13.3

Mean RMSE error and its standard deviation, is presented in **FIGURE 8-15** for each segment. The highest error appears in Z axis of the forearm with the Z axis of the hand closely following. However, the segments that experience the highest forces during throwing all have an RMSE above or almost at 100 °/second on all three axes. The chest and waist both have drastically less error and it is important to note that they do never move as fast as the other three segments. This may be an indication that the optical system is much better at calculating per-axis angular velocities for slower-moving segments.

FIGURE 8-16 Hand Segment Attenuation Percentage, Z Scores and P Values for Peaks and Lows (°/sec)

P1	HAND											
	Max Delta X	MaxValX	Max Delta Y	MaxValY	Max Delta Z	MaxValZ	Min Delta X	MinValX	Min Delta Y	MinValY	Min Delta Z	MinValZ
MEAN	178.9	4317.8	126.2	2187.0	2070.7	6465.6	382.8	1754.5	984.6	3390.8	1063.0	2730.1
STDEV	146.8	169.9	42.5	62.3	491.0	331.6	91.3	116.5	524.6	362.8	436.1	408.1
% Attenuation	4.1%		5.8%		32.0%		21.8%		29.0%		38.9%	
Z Score	4.6		8.8		27.2		14.3		11.8		11.4	
P Value	0.00		0.00		0.00		0.00		0.00		0.00	

FIGURE 8-17 Forearm Segment Attenuation Percentage, Z Scores and P Values for Peaks and Lows (°/sec)

P1	FOREARM											
	Max Delta X	MaxValX	Max Delta Y	MaxValY	Max Delta Z	MaxValZ	Min Delta X	MinValX	Min Delta Y	MinValY	Min Delta Z	MinValZ
MEAN	2242.1	4771.9	545.9	2042.8	1015.2	5336.0	464.9	1581.5	814.3	3002.8	897.1	2692.9
STDEV	432.3	482.0	197.7	150.3	586.8	361.1	90.1	103.9	204.3	144.2	341.0	407.2
% Attenuation	47.0%		26.7%		19.0%		29.4%		27.1%		33.3%	
Z Score	20.3		15.8		12.3		19.5		24.6		38.4	9.6
P Value	0.00		0.00		0.00		0.00		0.00		0.00	0.00

FIGURE 8-18 Upper Arm Segment Attenuation Percentage, Z Scores and P Values for Peaks and Lows (°/sec)

P1	UPARM											
	Max Delta X	MaxValX	Max Delta Y	MaxValY	Max Delta Z	MaxValZ	Min Delta X	MinValX	Min Delta Y	MinValY	Min Delta Z	MinValZ
MEAN	791.8	1926.5	870.0	2436.1	1196.0	3950.9	93.7	763.7	1786.0	1960.0	849.1	2080.1
STDEV	394.8	314.8	181.4	189.2	361.1	327.7	285.5	295.1	247.9	242.6	419.1	379.5
% Attenuation	41.1%		35.7%		30.3%		12.3%		91.1%		40.8%	
Z Score	11.0		20.0		15.9		1.4		32.1		9.8	
P Value	0.00		0.00		0.00		0.08		0.00		0.00	

FIGURE 8-19 Chest Segment Attenuation Percentage, Z Scores and P Values for Peaks and Lows (°/sec)

P1	CHEST											
	Max Delta X	MaxValX	Max Delta Y	MaxValY	Max Delta Z	MaxValZ	Min Delta X	MinValX	Min Delta Y	MinValY	Min Delta Z	MinValZ
MEAN	352.6	636.7	134.7	254.3	38.3	978.0	497.9	833.1	37.5	144.3	25.3	161.1
STDEV	236.6	248.6	154.3	75.6	87.6	94.4	121.5	137.4	46.1	75.7	118.1	69.4
% Attenuation	55.38%		52.99%		3.91%		59.77%		25.97%		15.71%	
Z Score	6.2		7.8		1.8		15.8		2.2		1.6	
P Value	0.00		0.00		0.04		0.00		0.02		0.06	

FIGURE 8-20 Waist Segment Attenuation Percentage, Z Scores and P Values for Peaks and Lows (°/sec)

P1	WAIST											
	Max Delta X	MaxValX	Max Delta Y	MaxValY	Max Delta Z	MaxValZ	Min Delta X	MinValX	Min Delta Y	MinValY	Min Delta Z	MinValZ
MEAN	65.5	154.8	39.3	54.7	17.1	766.7	36.3	226.7	69.7	245.7	11.3	123.2
STDEV	39.0	36.4	136.4	8.7	22.0	26.6	45.6	22.4	85.0	21.5	46.6	41.5
% Attenuation	42.4%		71.7%		2.2%		16.0%		28.4%		9.1%	
Z Score	7.8		19.8		2.8		7.1		14.2		1.2	
P Value	0.00		0.00		0.00		0.00		0.00		0.12	

Based on percentage distance from the mean, peak and low, attenuation in the optical system is quite drastic for all segments. Some axes demonstrate low attenuation, < 10% is seen in the peak X and Y attenuation for the hand, the peak Z of the chest and in three axes of the waist. Most other axes (20 of 30 axes) show a drastic 15 to 50% attenuation, while certain axes are extremely attenuated. Extreme attenuation (> 50%) is present in the waist peak/max Y, upper arm low/min Y, chest peak/max X, Y low/min X and waist peak/max Y. Calculated Z scores and p values also reflect this and show that there is a statistically significant difference (p value <0.05) between peak/maximum values for any of the 15 studied axes. For low/minimum values there is no statistically significant difference (p value > 0.05) for three of the 15 axes.

In general, it can be ascertained that standard optical system and its associated standard data processing methodology to obtain angular velocities

have a significant amount of error associated with them. Further, using this methodology to study real-world peak/minimum angular velocity values has no statistical correlation, as demonstrated by 0.00 p values, with what is happening in the real world (as measured by the inertial gold standard).

We must point out that effects of node bounce when attached to soft skin need to be properly understood before confidently quantifying these errors.

8.2.4 Angular Acceleration and Deceleration

The same analysis performed on the angular velocity data was also applied to angular acceleration data. As show in the eyeball comparison section, a general angular acceleration curve from the inertial system dwarfs the optical angular accelerations. This disparity in magnitude is to be expected in the statistical calculations presented here.

FIGURE 8-21 Mean Angular Acceleration RMSE of Optical vs.Inertial (Per-Segment Per-Axis) ($^{\circ}/\text{sec}^2$)

Column1	Column2	Column3	Column4	Column5	Column6	Column7	Column8	Column9	Column10	Column11
P1	HAND		FOREARM		UPARM		CHEST		WAIST	
RMSE	MEAN	STDEV	MEAN	STDEV	MEAN	STDEV	MEAN	STDEV	MEAN	STDEV
X	19245.3	1559.1	12469.8	1137.8	7267.0	846.2	2690.6	858.4	1045.3	242.4
Y	12663.6	971.4	12328.6	975.6	10683.5	1197.4	804.5	385.9	990.0	567.8
Z	20120.8	2824.1	21750.1	2609.6	21874.8	2172.4	2865.1	515.6	1834.4	363.1

Examining the RMS error moving up the kinetic chain from the pelvis to the hand show that at each link of the chain the error gets worse and worse. Mean waist error ranges from 1,000 to 2,000 $^{\circ}/\text{second}^2$ while mean hand error ranges from 12,000 to 20,000 $^{\circ}/\text{second}^2$. The hand, forearm and upper arm are much worse than the chest and waist. Examining **FIGURE 8-14** it is easy to understand why there is so much error present in this comparison.

FIGURE 8-22 Hand Segment Attenuation Percentage, Z Scores and P Values for Peaks and Lows ($^{\circ}/\text{sec}^2$)

P1	HAND											
	Accel Delta X	Max Accel X	Accel Delta Y	Max Accel Y	Accel Delta Z	Max Accel Z	Decel Delta X	Max Decel X	Decel Delta Y	Max Decel Y	Decel Delta Z	Max Decel Z
MEAN	304,086	437,098	229,103	315,146	235,009	418,454	395,467	699,786	383,665	559,321	467,737	683,921
STDEV	230,254	231,645	71,784	69,146	123,098	109,171	108,715	121,439	69,463	67,373	204,716	191,602
% Attenuation	99.4%		103.8%		112.8%		89.5%		103.1%		106.8%	
Z Score	5.7		14.4		9.4		14.2		24.8		10.6	
P Value	0.00		0.00		0.00		0.00		0.00		0.00	

FIGURE 8-23 Forearm Segment Attenuation Percentage, Z Scores and P Values for Peaks and Lows ($^{\circ}/\text{sec}^2$)

Column1	Column2	Column3	Column4	Column5	Column6	Column7	Column8	Column9	Column10	Column11	Column12	Column13
P1	FOREARM											
	Accel Delta X	Max Accel X	Accel Delta Y	Max Accel Y	Accel Delta Z	Max Accel Z	Decel Delta X	Max Decel X	Decel Delta Y	Max Decel Y	Decel Delta Z	Max Decel Z
MEAN	352,044	425,209	406,686	475,925	215,485	393,606	576,421	739,785	524,810	679,114	614,158	829,316
STDEV	145,898	146,001	117,407	118,799	83,513	86,811	196,354	202,037	171,764	170,854	186,916	185,112
% Attenuation	99.9%		98.8%		96.2%		97.2%		100.5%		101.0%	
Z Score	10.5		14.9		10.8		12.4		13.4		14.5	
P Value	0.00		0.00		0.00		0.00		0.00		0.00	

FIGURE 8-24 Uparm Segment Attenuation Percentage, Z Scores and P Values for Peaks and Lows ($^{\circ}/\text{sec}^2$)

P1	UPARM											
	Accel Delta X	Max Accel X	Accel Delta Y	Max Accel Y	Accel Delta Z	Max Accel Z	Decel Delta X	Max Decel X	Decel Delta Y	Max Decel Y	Decel Delta Z	Max Decel Z
MEAN	503,421	535,144	973,145	1,010,110	442,193	730,244	350,766	384,888	623,497	650,039	773,238	1,005,358
STDEV	162,022	162,334	233,606	236,237	335,437	339,342	103,551	102,862	255,819	255,626	460,450	447,859
% Attenuation	99.8%		98.9%		98.8%		100.7%		100.1%		102.8%	
Z Score	13.5		18.0		5.7		14.9		10.6		7.5	
P Value	0.00		0.00		0.00		0.00		0.00		0.00	

FIGURE 8-25 Chest Segment Attenuation Percentage, Z Scores and P Values for Peaks and Lows ($^{\circ}/\text{sec}^2$)

P1	CHEST											
	Accel Delta X	Max Accel X	Accel Delta Y	Max Accel Y	Accel Delta Z	Max Accel Z	Decel Delta X	Max Decel X	Decel Delta Y	Max Decel Y	Decel Delta Z	Max Decel Z
MEAN	119,637	125,183	29,187	32,185	128,016	143,628	140,102	146,903	17,725	25,613	109,308	127,087
STDEV	76,461	76,835	13,432	13,596	111,573	105,441	121,258	121,308	29,835	11,605	113,202	113,571
% Attenuation	99.5%		98.8%		105.8%		100.0%		257.1%		99.7%	
Z Score	6.8		9.4		5.3		5.0		6.7		4.2	
P Value	0.00		0.00		0.00		0.00		0.00		0.00	

FIGURE 8-26 Waist Segment Attenuation Percentage, Z Scores and P Values for Peaks and Lows ($^{\circ}/\text{sec}^2$)

P1	WAIST											
	Accel Delta X	Max Accel X	Accel Delta Y	Max Accel Y	Accel Delta Z	Max Accel Z	Decel Delta X	Max Decel X	Decel Delta Y	Max Decel Y	Decel Delta Z	Max Decel Z
MEAN	10,464	17,798	302	9,411	9,484	22,172	9,746	17,652	1,414	6,861	768	17,589
STDEV	5,660	6,108	9,621	1,907	8,315	4,024	7,006	4,456	10,713	1,299	4,992	3,196
% Attenuation	92.7%		504.4%		206.6%		157.2%		824.5%		156.2%	
Z Score	7.5		0.7		10.3		9.5		4.7		1.0	
P Value	0.00		0.24		0.00		0.00		0.00		0.15	

Again, the attenuation percentage calculated by taking the mean delta between the inertial and optical systems and dividing it by the mean peak value from the inertial system. This yields a percentage of how far off the optical peak angular acceleration is from the inertial. In general the percentage error is about 100%, the minimum error was 89.5% (hand X axis), while the maximum is 824%, at the waist Y axis. The numbers clearly show that using an optical system to calculate angular acceleration has such large error bounds that the information is meaningless.

All P values, but two at the waist, were zero. This indicates that, although we see decent correlation in angular velocities, there is no statistically significant correlation between the peak angular acceleration from the optical to the inertial system, for any segment, on any axis.

ANALYTICS AND BIOMECHANICAL METRICS

A system is only as good as the tools that are provided to analyze, manipulate and view the data that it provides. The analytics section presents a set of algorithms, tools and user interfaces for doing just this. For each tool, interface or algorithm results are also presented.

9.1 DATA PROCESSING FUNDAMENTALS

Guidelines for processing data were laid out in Section 1.3.3. These include three abilities (*Viewability*, *Aggregatability* and *Repeatability*) and one *ality* (*Neutrality*).

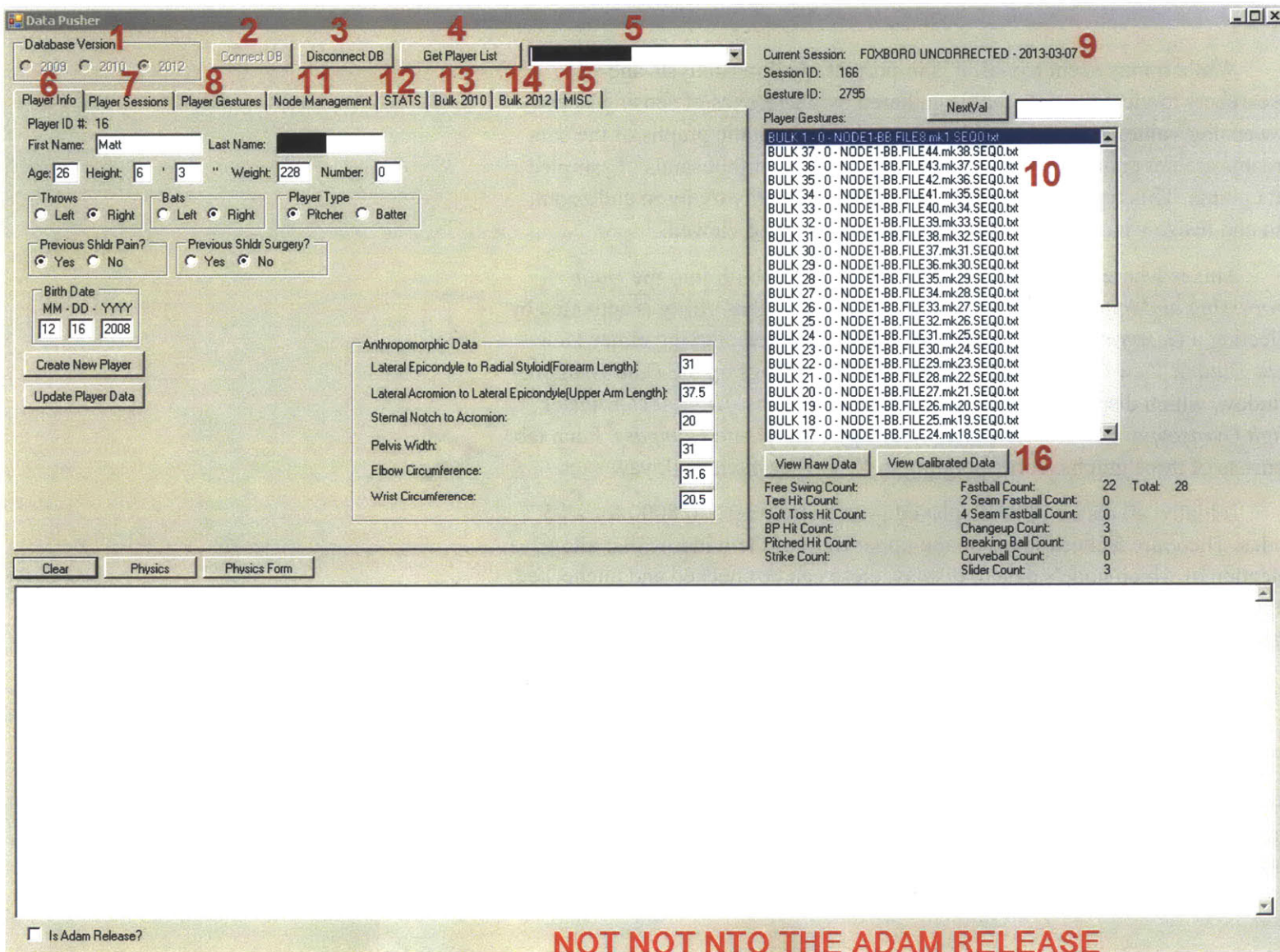
Neutrality and *repeatability* are fulfilled by a set of data access application programming interfaces (APIs) that were developed for *C/C++*, *Matlab* and *Visual Basic*. These APIs abstract away the complex data model (presented in Section 6.3) and its underlying PostgreSQL relational database in an object oriented manner and allow uniform access to the data on the level of *Players*, *Sessions* and *Gestures*. The analyst developing algorithms only has to think at this level to access and manipulate data.

Graphical user interfaces, such as the *Data Processing and Import Application*, leverage the Visual Basic API and allow for *viewability*. Further *viewability* is enabled by the system's integration with *Visual3D*, which uses the C++ API to import data, then further process it and display it to the user.

The Matlab API is heavily used by numerically-intensive analysis algorithms, such as data fusion and synchronization, that perform *aggregation* of data and then use the API to reinsert results into the database

These four concepts will be referred to throughout this section as each interface, algorithm and tool is described.

FIGURE 9-27 Data Processing Application Main View (re-presented)



9.2 DATA VIEWING

While it may seem trivial, it is important to allow analysts and researchers to view the data that is gathered by all 15 axes of sensing as both raw analog values and real-world calibrated values. Static graphs of the data streams are not enough, as each data series consists of thousands of sampled data points. This type of information begs for the ability to dig in and zoom, pan and resize what portion of the data stream is being viewed.

This is where the *Data Grappper* utility that is built into the *Data Processing and Import Application* comes into play. This utility is activated by selecting a *Gesture* in the gesture list (9-1-10) and then clicking either *View Raw Data* or *View Calibrated Data* buttons. This brings up the *Data Grappper* window, which displays the data across 5 separate tabs, *High Acclerometer*, *High Gyroscope*, *Low Accelerometer*, *Low Gyroscope* and *Compass*. Each tab consists of three graphs, corresponding to X, Y, Z or pitch, roll, yaw axes.

Initially, all data will be displayed from sample zero to 8000 for all 5 nodes. There are 5 checkboxes on the upper right of the window that allow selection of which node's data to display, these can be checked and unchecked, depending on what data the users wishes to see. In order to manipulate the displayed graphs, the following key keys are use along with the mouse:

- Alt + mouse - allows drawing of a window to zoom to
- Ctrl + mouse - allows for dynamic zooming
- Shift + mouse - allows to pan the graph up, down, left and right.

FIGURE 9-28 depicts zoomed and panned data in the upper and lower graphs and an entire dataset in the middle graph. All of this functionality falls under the umbrella of *viewability*.

FIGURE 9-28 Data Grappher Calibrated Data View

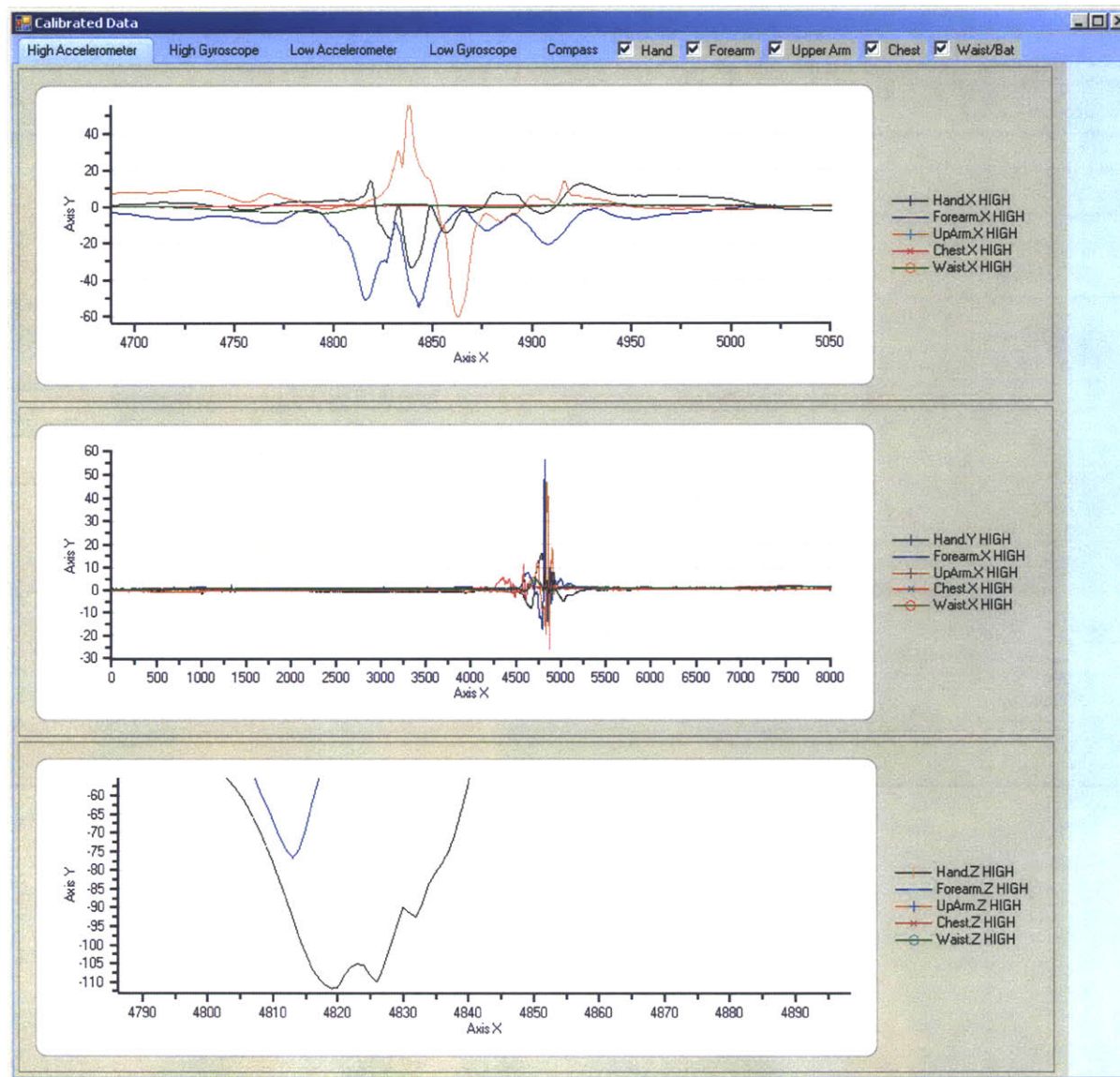


FIGURE 9-29 Statistics Generation Tab in the Data Processing Application

Player Info | Player Sessions | Player Gestures | Node Management | **STATS** | Bulk 2010 | Bulk 2012 | MISC

1

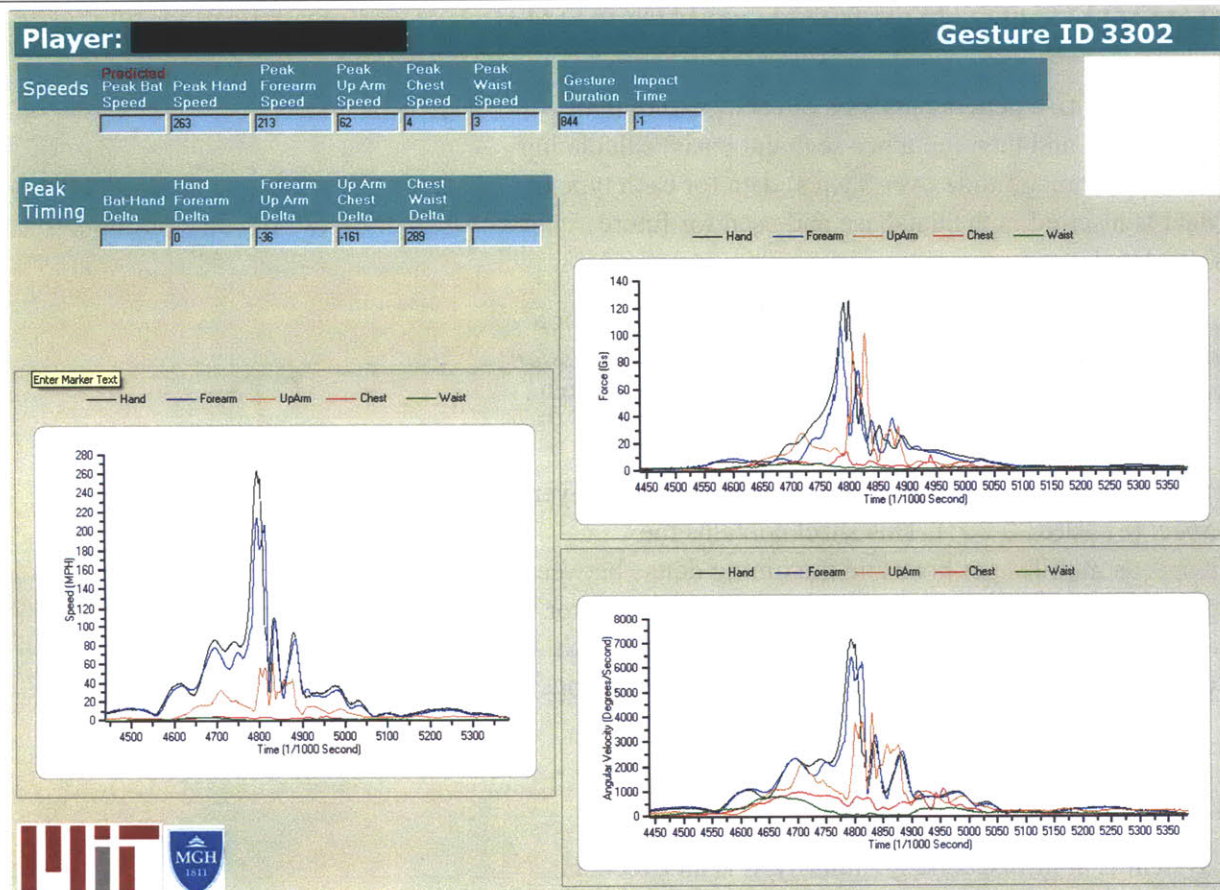
 2

3

Batter Session Stats
Enter Gesture IDs to Configure Stat Sheet
 Free Swing Gesture ID:
 First or second Free Swing? (1/2)
 G Forces Gesture ID:
 MPH Gesture ID:

Pitcher Session Stats
 G-Force Gesture ID:
 Ds Gesture ID:

FIGURE 9-30 Gesture Stat Sheet



9.3 SEGMENT GESTURE STATISTICS

Gesture analysis starts with a general analysis of each *gesture* that includes determining its length and then (on a per-segment basis) calculating statistics on aggregated (vector magnitude over 3 axes) data for each type of inertial sensor. This data is inserted in the database and used for future processing at the *session* level.

Sections 9.3.1 and 9.3.2 document what are termed general stats for a session. Their behavior is executed by clicking the *Generate Stats for Session* (9-3-1) button under the *STATS* tab in the *Data Processing Application* (9-1-12).

The data for any gesture is presented to clinicians, coaches and players via the *Gesture Stat Sheet* (FIGURE 9-30). This sheet contains the extrapolated segment speeds in miles per hour and the timing deltas between the peaks of each segment's speed. Three graphs are also presented: vector magnitude acceleration, angular velocity and extrapolated speeds for each segment. Lastly, the calculated gesture duration and impact time (for swings) is also displayed.

9.3.1 Gesture Duration Determination

As the inertial system is at millisecond granularity, it is an excellent platform for examining the amount of time that a single pitch or swing takes to execute. Further, having an algorithmic process for trimming any unnecessary data from a *gesture* allows for analysis to focus on only the relevant motion contained in the inertial data streams.

This algorithm finds the peak for the vector magnitude of all the axes (gyroscope or accelerometer) and iterates backwards and forwards until the

inertial value falls below a given threshold. For gyroscopes, 300 degrees/second and accelerometers 3.2G's. Iterating backwards from the peak yields a sensor specific start time for each gesture in terms of gyroscope and accelerometer. The minimum of these two values is taken and is used as the start time of the gesture. The same process occurs iterating forward, however the maximum value of the two is taken as the end time for the gesture.

This process is applied for all body segments and rolled up into a *gesture*-level start and end time by taking the minimum of all segment start times and maximum of each segment end time, respectively. This information is stored in the database as part of the *gesture* metadata that is presented in Section 6.3.3, *Gesture Data Model*.

9.3.2 Individual Segment Analysis

Two vector magnitudes, one of the three axes of accelerometers and one of the gyroscope's three axes, are used to calculate and present most metrics. The reasoning behind this is twofold. First, because it represents the integrated acceleration and angular velocity, giving an general idea of how much motion is occurring at each segment. Secondly, it is much easier to have two numbers per segment when looking at general statistics instead of six per segment. For a five node upper body network, there are 10 numbers that represent the motion, rather than 30.

For each sample of each segment of each gesture the vector magnitude is calculated for the gyroscope axes and the accelerometer axes. The formula for an individual datapoint's vector magnitude is:

$$\text{magnitude} = \sqrt{X^2 + Y^2 + Z^2}$$

where X, Y and Z are accelerometer axes of gyroscope pitch roll and yaw values

Once the magnitude has been calculated over all samples, for both types of sensor, the peak value is found along with the time that the peak occurred. This data is inserted into the database as part of the *Gesture Data Model*, Section 6.3.3.

9.3.3 Inter-Segment Timing

Inter-segment peak timing is calculated on the fly from the data that is stored for each segment in the previous section. The time differences between segment peaks are considered by trainers and coaches as an indicator of how well a pitcher or batter delivers power through the kinetic chain to the bat or ball. The smaller the difference, the more efficiently the power is delivered. The deltas are calculated between each pair of segments in the kinetic chain. The segment timing application (Section 9.4.2) was developed to study this phenomena in detail.

9.3.4 Segment Velocity Estimation

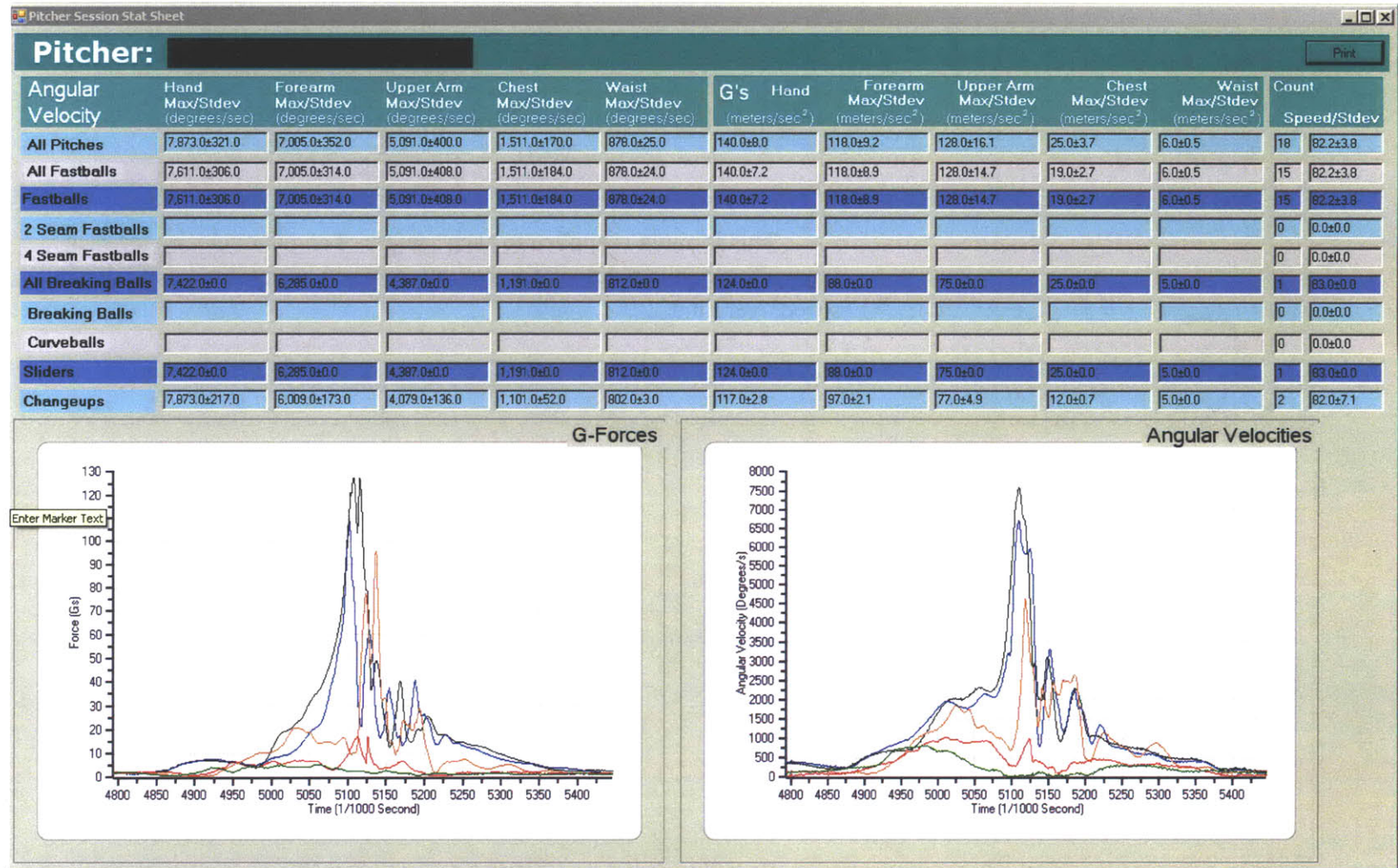
Segment velocity estimation is a tool that is used to translate angular velocity into lay terms. The approach is named an estimation because it makes one broad assumption about the mechanical structure of the arm when it is swinging or throwing. This assumption is that the arm is fully extended at the peak of the *gesture*, and allows for a simplified calculation of segment speed based on each inertial node's location in the segment. Node location is measured and stored in the database as part of *session* annotation, thus these number are readily available. The derived formula for converting the

centimeter radius (r) and degrees/second angular velocity (ω) to miles per hour is:

$$\text{MPH} = \frac{\left(\frac{180}{\pi}\omega\right) \times r}{30.48} \times 3600$$
$$\text{MPH} = \frac{\quad}{5280}$$

This formula is applied to each sample of angular velocity for each segment using the segment's own radius to provide an estimate of segment speed over time.

FIGURE 9-31 Session Stat Sheet



9.4 SESSION AGGREGATION AND STATISTICS

9.4.1 Session Stat Sheet

For each *player's session*, metrics are generated to give insight into what the inertial forces and angular velocities are for different groupings of pitches and all pitches for that session. *Session* level data depends on what is calculated in the previous section and is a second level of post-processing. This data is presented to clinicians, coaches or players in the form of a graphical *Session Stat Sheet* (FIGURE 9-31).

The data access API allows for selection of *gestures* based on their *type*. *Type* is defined by the annotation and classification process that occurs at the time *gesture* data is inserted in the database. This feature is leveraged to first select all *pitches*, then the subcategory of all *fastballs*, then the sub-sub-category of all 2 *seam fastballs*, then the sub-sub-category of all 4 *seam fastballs*. This same behavior applies to all *breaking balls* and their sub-sub-categories of *breaking balls* and *curveballs*. *Sliders* and *changeups* are individual sub-categories.

Each of these selections yields a group of pitches and the metadata that was generated and stored. at the gesture level. For each selection's *gesture* and each segment, the mean angular velocity and the standard deviation are calculated. The same calculations are performed for accelerations.

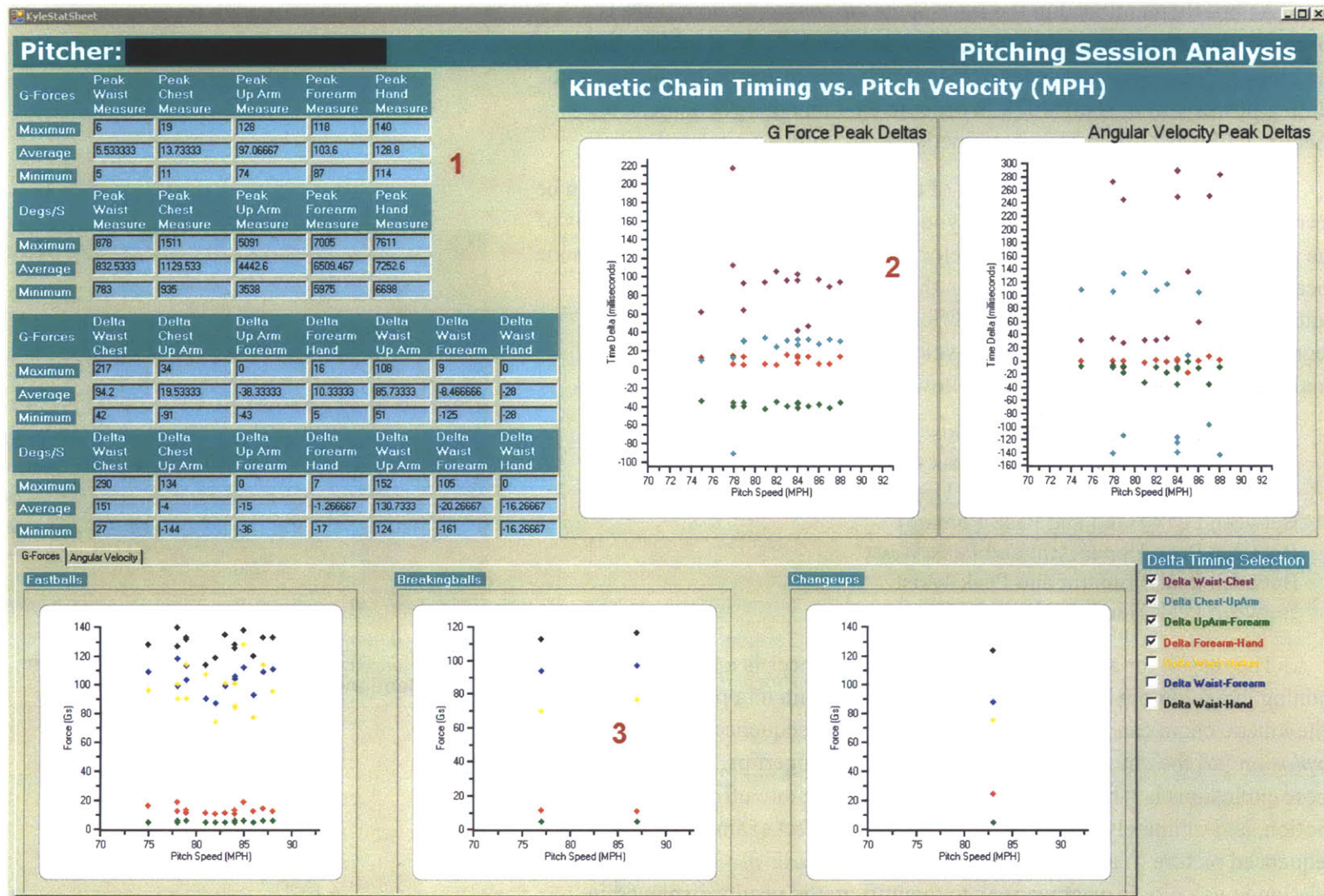
The analysis is executed by clicking the *Run Pitcher Session Analysis* button (9-3-2). Its resulting data is stored in the database as part of *session* metadata, Section 6.3.2. When the *View Stat Sheet* button (9-3-3) is clicked, the *Session Stat Sheet* stat sheet is displayed populated with the calculated data. The two graphs in the stat sheet are user-selectable gestures that are displayed

in vector magnitude form in units of Gs and angular velocity. Lastly, the number of pitches in each pitch category and the mean pitch speed are in the leftmost column.

The pitcher stats sheet allows for instant comparison of per-segment angular velocities and accelerations for different pitch types. This analysis takes only a couple of minutes and is a large step forward in terms of en masse data analysis. The same algorithms can be applied to hundreds of pitches and enable a big data approach to pitching analysis previously not possible.

For the particular pitcher presented in (FIGURE 9-31), one can quickly ascertain that, for fastballs, the acceleration the upper arm experiences are higher than those of the forearm: mean 128G upper arm vs. mean 118G forearm. For all other pitch types the mean accelerations are always less in the forearm than the upper arm.

FIGURE 9-32 Segment Timing Analysis Application



9.4.2 Segment Timing Analysis Application

As briefly mentioned in the *Inter-Segment Timing* section, there is a long-standing coaching rule-of-thumb that the closer, in time, each segment of the kinetic chain reaches its peak velocity, the more efficient the pitcher is at putting power into the ball [107]. In order to examine this phenomena a specific tool was built to compare kinetic chain timing to pitch velocity.

In FIGURE 9-32 , a screenshot of the segment timing application can be seen. In section 1 of FIGURE 9-32 , you can find a brief statistical analysis of the peak g-forces and peak angular velocities captured at each of the five node locations across all fastballs thrown in the player's bullpen session. In the bottom half of section 1, the timing difference is given between certain segment's peak g-forces and angular velocities. The timing differences analyzed in the application are the following:

- Between Peak Chest and Peak Waist
- Between Peak Upper Arm and Peak Chest
- Between Peak Forearm and Peak Upper Arm
- Between Peak Hand and Peak Forearm
- Between Peak Upper Arm and Peak Waist
- Between Peak Forearm and Peak Waist
- Between Peak Hand and Peak Waist

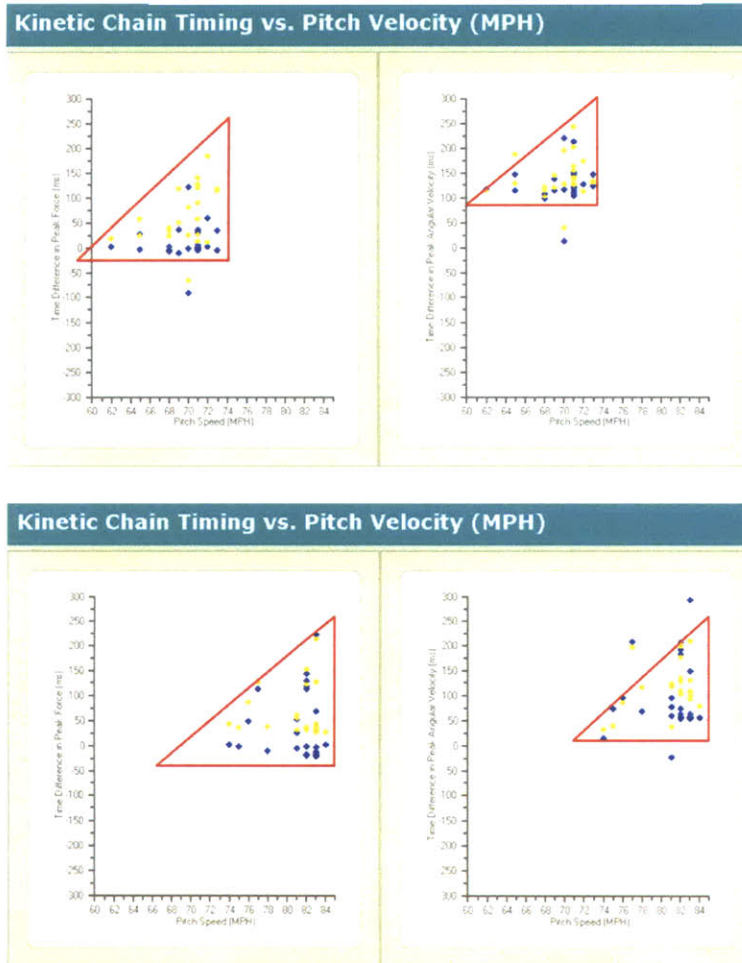
The reason for analyzing these timing differences is a starting point for gaining insight into what is known as the kinetic chain of a pitcher in baseball. The kinetic chain can generally be described as the sequenced “*athletic explosion*” of the entire human body from feet to fingertips. Proper timing of these explosions is what leads to better mechanics, more efficient athletic motion, and ultimately higher pitch velocity. A perfect example of this is the sequenced picture of a major league pitcher in FIGURE 9-33 . This direct relation to velocity is what we seek to quantify in the results displayed in Section 2 of FIGURE 9-32 . This section plots each pitching gesture's pitch



FIGURE 9-33 Example of Kinetic Chain Sequence (Source: ESPN)

speed versus the timing peaks described above for both peak G-forces and peak angular velocity. Finally in Section 3 of [FIGURE 9-32](#), we analyze the peak magnitudes in g-forces and angular velocity.

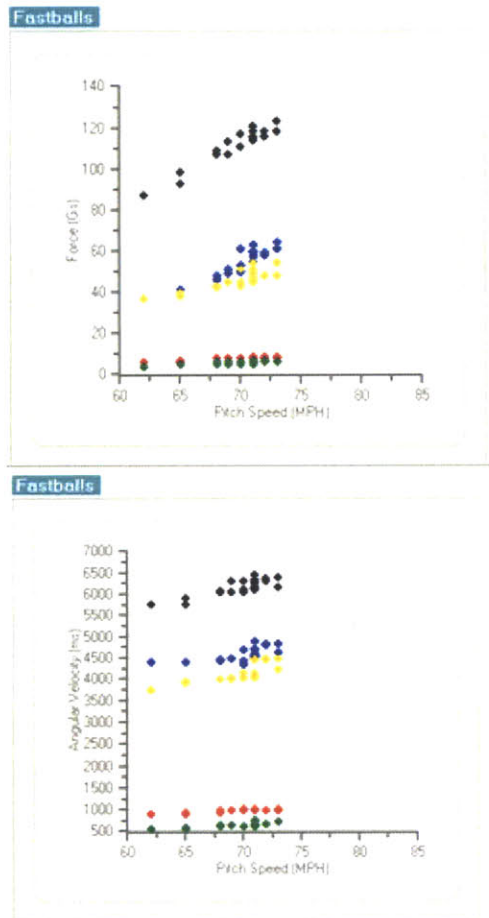
FIGURE 9-34 Formation of Delta Triangle (Hand Drawn). Angular Velocity (Upper), Acceleration (Lower)



In looking towards trends in the results, we are going to focus on the data plots of Sections 2 and 3 in [FIGURE 9-32](#) above. Looking first at the timing differences plotted versus pitch speed, one interesting trend we noticed across different bullpen sessions had to do with the timings calculated between the waist and the various other body segments. As pitch speed increased (measured with a standard doppler radar gun), the percent variation between the timings increased almost forming a neat triangle as shown in [FIGURE 9-34](#). It didn't matter what the actual velocity was, but rather what the velocity was relative to the other pitches in the session. As you can see below, the triangle is formed on both sessions from both the G-forces and angular velocity plots. For the first pitcher, the pitch speeds ranged between low-60s and mid-70s, while for the second pitcher, speeds were about 10MPH faster ranging between low-70s and mid-80s (miles per hour). Despite the difference in velocity, a similar general delta triangle is formed on the graph. I believe this difference may be correlated to the actual quality of the pitch thrown, with the definition of quality incorporating not just pitch velocity, but also pitch location and some other qualitative judgments of the pitch. In other words, on the higher end of the pitch speeds, where most of the pitches fall, the differences in timing between peaks may be attributed to the quality of the pitch. On one side of the delta timing spectrum could be good pitches thrown to their intended location, while on the other side of spectrum could be pitches that are thrown unintentionally far away from the strike-zone (in the dirt for example). This observation goes back towards our discussion of the proper timing of the kinetic chain for pitchers. When looking at peak differences in the proper timing of a pitcher's kinetic chain, location or "pitch quality" may be most impacted by these timing differences, while other attributes of the kinetic chain may contribute more towards actual pitch velocity. Attributes of

these graphs worth exploring further would be how fast the body segments reach their peak magnitudes and how long the magnitudes are sustained using

FIGURE 9-35 Linear Velocity Trends in Kinetic Chain (G's upper, degrees/s lower)



some sort of power calculation, as to how much power has been put into the thrown ball.

Now let us take a look at our results for peak magnitudes plotted against pitch speed. One interesting result is that our data confirms the generally accepted baseball wisdom that the more explosive the kinetic chain is in absolute terms, the faster the pitcher will throw. As shown in FIGURE 9-35, there is a linear trend between both the peak magnitudes of G-forces and the peak magnitudes of angular velocity. Each color is the time difference between two segments. The black is between the waist and hand, blue between waist and forearm, yellow between waist and upper arm, red between forearm and hand and the green is between the upper arm and forearm. This result in and of itself is fantastic, but what is more interesting is how the slope of those five lines steepens as the body segment gets closer to the hand. The increasing slopes of these lines across the body segments suggests there is a multiplier effect moving along the kinetic chain from hips to the release at the hand. This trend confirms a lot of the emphasis experts in pitching biomechanics have placed on examining the kinetic chain. The evidence of a potential multiplier effect along the kinetic chain would be a major area of further research to explore in the future.

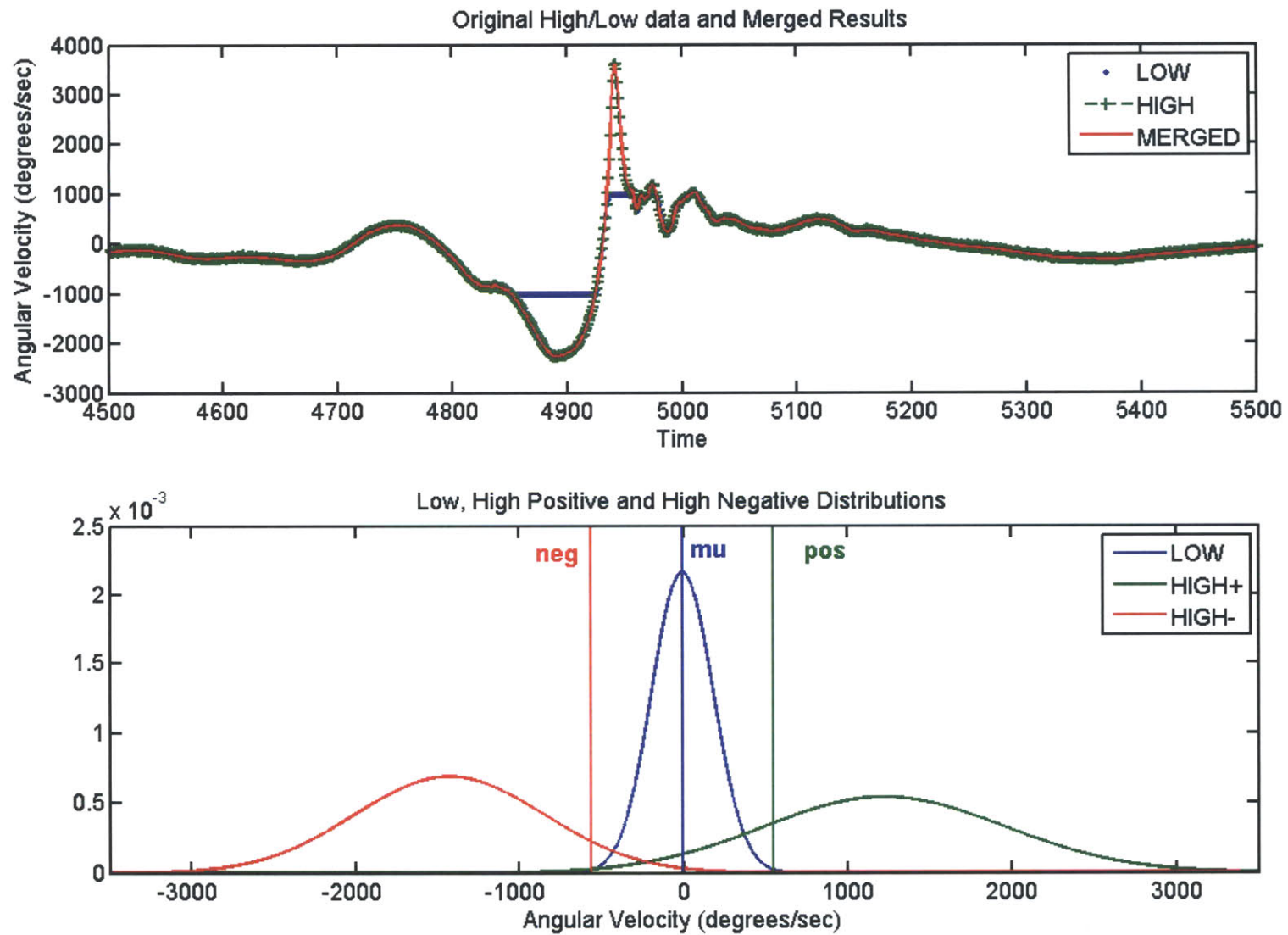
9.5 LIKE MODALITY SENSOR FUSION

One of the strong points of the inertial nodes developed for this work is that acceleration and angular velocity sensing is done on two levels, high range and low range. The reasoning for this is explained in 4.1 and will be restated

here. A high range sensor is good at sensing very fast accelerations and angular changes, but not very good at sensing slow moving accelerations and angular movement. A similar concept applies to the low range sensors, excellent at sensing slow moving parameters, incapable of sensing anything past their specified ranges. Thus, there is a need for both types of sensors to be present on inertial nodes for high-speed activity. The presence of both like sensing modalities requires that at some point data processing algorithms stop using the low range data and begin using the high range. Previous to this section, only the data based on high range sensors has been used. As the high range sensor poorly senses low range information ($< 1,000$ degrees/s gyroscope, $< 16G$ s accelerometer) there is too much variability (noise) in the high range to simply create a rule-based system of thresholds for when to use which sensor. This technique was initially attempted by the author and produced a system with so many rules and caveats that it became untractable while still producing poor fusion.

The second try at addressing the problem was with the help of the Responsive Environments Research Assistant Matt Aldrich. Matt suggested a statistical approach that calculated blending factors for each dataset to be merged and can be generically applied to any two datasets.

FIGURE 9-36 Merged High and Low Range Data (upper) Data Fusion Distributions (lower)



The process starts with two vectors of data, high range and low range. Using the low range data, a normal distribution is generated, yielding a μ (μ) and sigma-squared (σ^2) value. These two parameters are matched with a user-defined tuning parameter (final value of 3) to define two dividing thresholds for the high range data. The formula for determining the thresholds is:

$$\text{threshold} = \mu \pm P \times (\sqrt{\sigma^2})$$

where P is the tuning parameter and \pm is dependant on whether positive or negative high range calculations are being made. The thresholds, along with μ , are show in FIGURE 9-36 as vertical lines *neg*, *mu* and *pos* in the lower graph.

In the next step, high range data is partitioned into positive and negative. The partitioning is based on the thresholds; all data less than *neg* is put into one partition and above *pos* is placed into a second. This effectively removes any data that is $\pm P$ standard deviations from μ in the high data. Using the partitioned positive and negative data, two more normal distributions are fit.

Now there are three distributions: positive high, low and negative high, and two original sets of data: high and low.

The probability density function for each distribution is calculated using low range data with the low normal distribution and all high data for both positive and negative distributions. This effectively gives a weight for each datapoint in the low dataset and two weights for each high-range data point in the form of 3 vectors of data, *distHiPos*, *distLo*, *distHiNeg*. These weights are applied to their respective data sets and the results are summed. The general equation for this is:

where hiData is the high-range sensor data and lowData is the low-range sensor data.

It is important to note that, because of how the distributions are generated, the weight for a positive high value will be zero in the negative weight vector and vice versa. Moreover, the weights where the distributions intersect will create a blending effect on the data and the end effect is a smooth fusion that is dependant on the actual data itself, not predetermined thresholds. Resultant data is shown in the upper graph of [FIGURE 9-36](#).

9.6 BIOMECHANICAL METRICS

Session and gesture level analysis and data presentation both are in the category of data *viewability* and *aggregatability*. This section will explore some metrics that are relevant to traditional biomechanical analysis that are published in orthopedic literature.

9.6.1 Jerk

One concept that does not exist in current medical literature is that of Jerk, the derivative of acceleration. Jerk is the third derivative of position, the rate at which something is accelerated. Section 8.2.4 presents an in-depth analysis of the poor ability of optical systems to calculate the second derivative of position (acceleration); this analysis indicates that any jerk number derived from an optical system would be meaningless. Further, if this metric cannot be measured there has been no avenue to use it to study human motion. The unit of measure for jerk is m/s^3 .

A jerk value indicates the rate of acceleration. To better understand jerk, the example of removing a band-aid from the human skin can be considered. When a low jerk is used to remove a band-aid, slowly pulling it off of the skin, the skin continues to adhere to the band-aid in an attempt to keep the two materials together. When a high jerk value is used, the band-aid is yanked, the skin cannot deform fast enough to adhere to the band-aid and it releases. If the band-aid is of poor quality, it may tear in half when jerked because it cannot handle a high jerk force.

This concept can be transferred to that of a ligament that connects two bones, or a muscle to a bone. If the ligament is lightly jerked, it pulls whatever bone it is attached to along with it. If a ligament is jerked hard (or one of the segments it is attached to is accelerated quickly), its tensile strength may not be able to handle the change in force and it may tear. Further, consider that repeated jerks are analogous to repetitive microtrauma; multiple mild or medium jerks may lead to fatigue in the ligament and eventual failure. Based on this I theorize that examining the actual jerk, as opposed to previous study of linear and angular acceleration, to be a better indicator of repetitive microtrauma severity.

Which component of jerk and how it can be used in biomechanical study is an unanswered question. Here we will present the first jerk data taken for the human body and some related metrics with their analysis.

Note that STA's may contribute to this data; future work must ascertain the magnitude of these effects.

FIGURE 9-37 Per Segment Z Axis Jerk and Acceleration for a Fastball

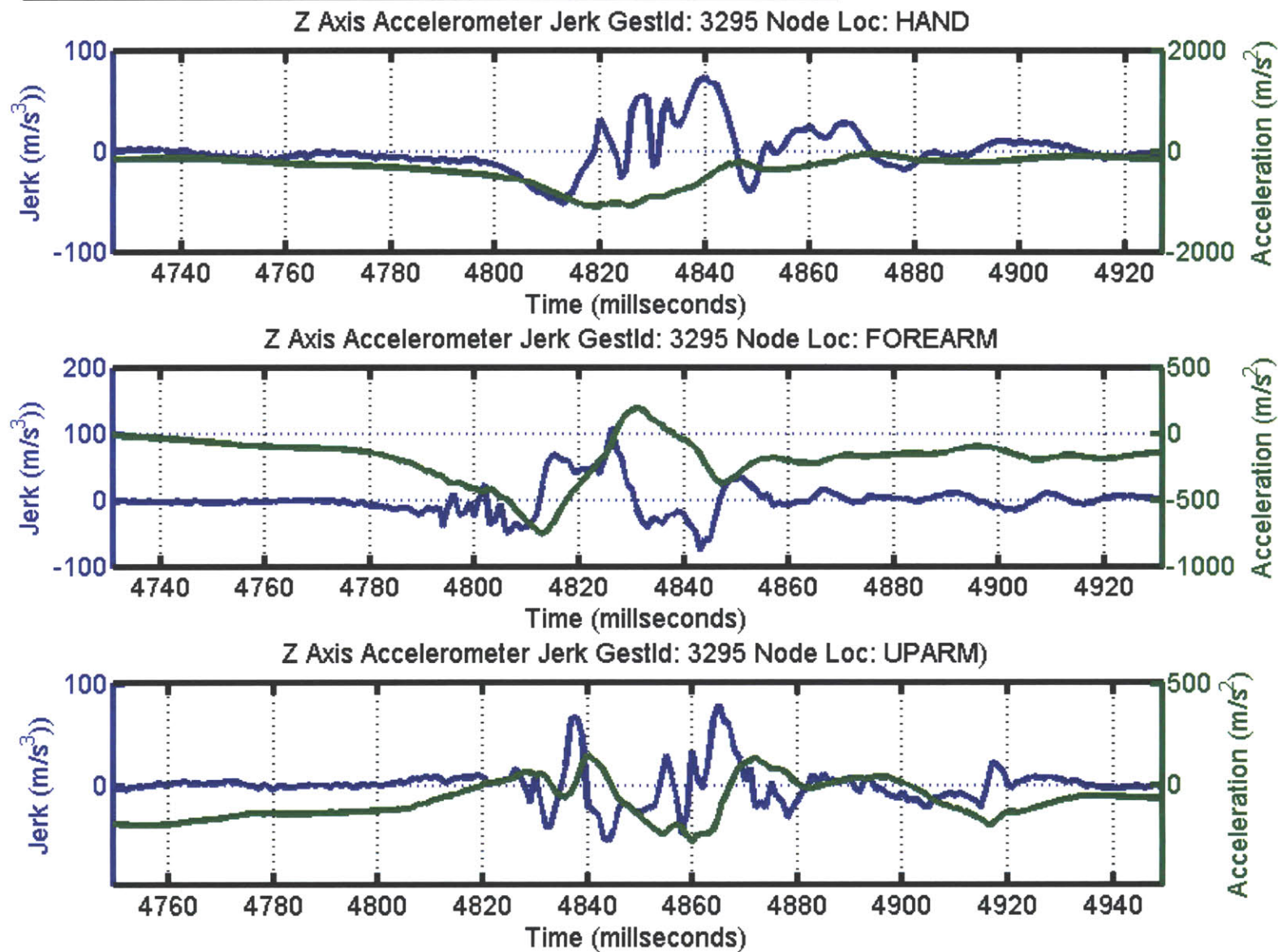


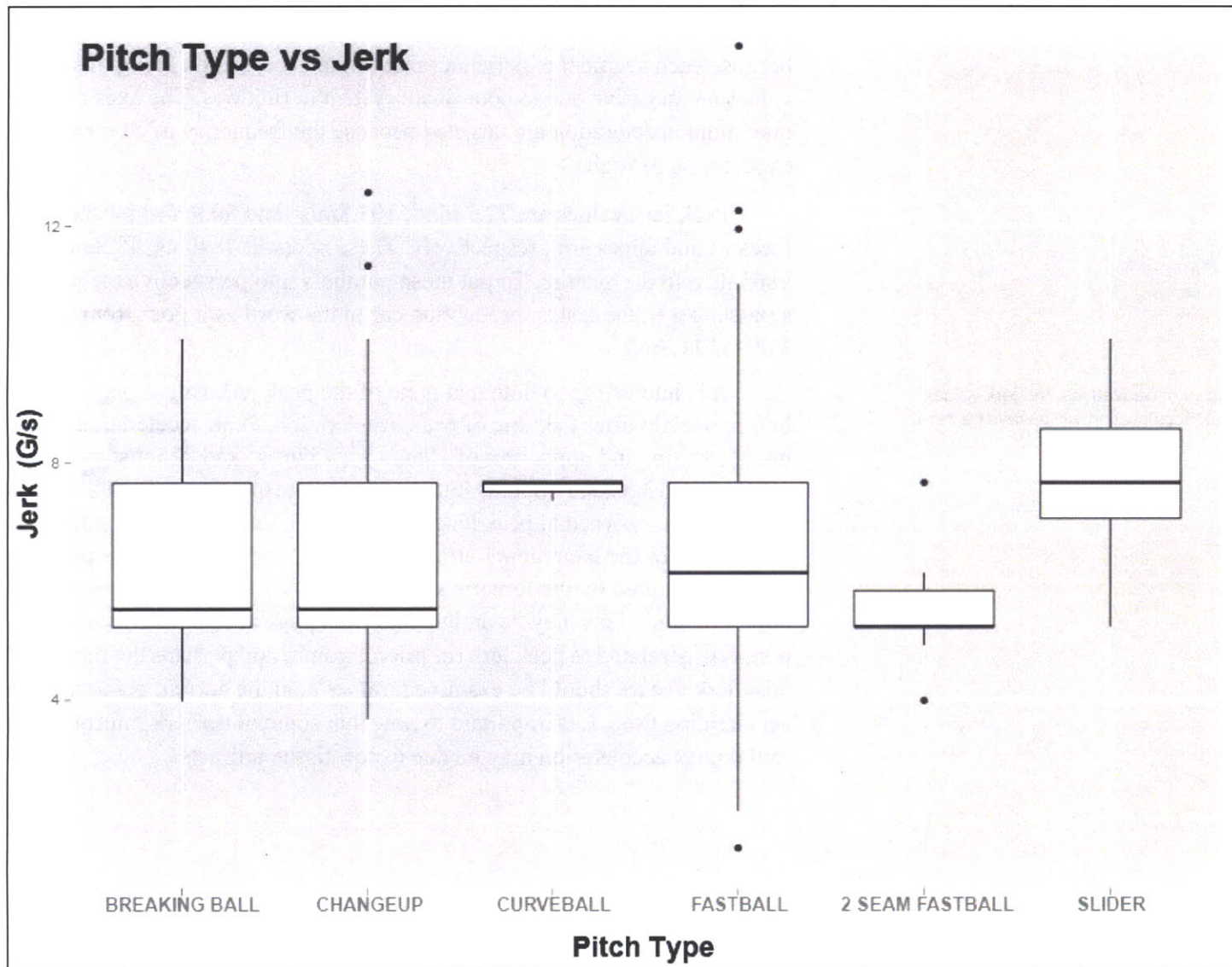
FIGURE 9-37 presents Jerk (blue) that has been derived from acceleration data from the Z-axis of the hand, forearm and upper arm nodes. The Z-axis is aligned with the long axis of each segment and was chosen because each segment experiences maximum acceleration along this axis; values are negative due to coordinate system definitions. The axes of maximum acceleration are targeted because the frequency of change is also expected to be high.

Peak jerk values are 72.7 m/s^3 , 107.8 m/s^3 and 80.9 m/s^3 for the hand forearm and upper arm, respectively. These occur at 4840ms, 4826ms and 4865ms into the gesture. To put these numbers into perspective the jerk felt by a passenger in the fastest production car in the world as it goes from 0 to 60 MPH is 11.7 m/s^3

³Due to the nature of derivatives, the jerk values exactly at peak acceleration will always be zero.

It is interesting to note that none of the peak jerk values occurred right before or right after the time of peak acceleration. Peak acceleration for the hand, forearm and upper arm of 1096 m/s^2 , 752 m/s^2 and 275 m/s^2 occurred at 4819ms, 4813ms and 4860ms into the gesture, respectively. In fact, the actual acceleration recorded at peak jerk time was 553.2 m/s^2 , 95.0 m/s^2 and 152.3 m/s^2 for the hand upper arm and forearm, respectively. This phenomena is best illustrated by the forearm where jerk is 107.8 m/s^3 and acceleration is only 95.0 m/s^2 . This may be an indicator that peak acceleration is not necessarily related to peak jerk (or microtrauma) and perhaps the time at which peak jerk occurs should be examined, rather than the current practice of peak acceleration time. It is important to note that some of the jerk information after initial peak acceleration may be due to soft tissue artifacts.

FIGURE 9-38 Jerk Data for the Shoulder Distraction Axis (Z) Categorized by Pitch Type



9.6.2 Shoulder Distraction Jerk

The peak linear jerk along the long axis of the humerus was calculated using accelerometer data from a population of 6 minor league pitchers throwing a total of 206 pitches of various pitch types. Distractive force pulling the arm out of the shoulder is concentrated along the long axis of the humerus, hence it was the chosen point of study.

The calculated jerk was classified by pitch type (fastball, 2 seam fastball, changeup, slider, breaking ball) and analyzed for Z score and P Value in order to determine if a correlation exists between jerk and different pitch types. All pair-wise combinations of pitch type were considered, and statistically relevant combinations are presented in FIGURE 9-39. The 2 seam fastball demonstrates a significant statistical difference in the amount of jerk over all other pitch types. It also had the lowest mean jerk value (53.6m/s^3) of any of the studied pitch types. The slider also has a significant difference in its jerk value when compared to all other pitch types. It had the highest (76.3m/s^3) jerk value. The fastball, breaking ball and changeup had mean jerk values that are all very similar (66.8m/s^3 , 62.3m/s^3 and 65.0m/s^3 , respectively). This data confirms previously published work [98] and it is a well know rule-of-thumb in

FIGURE 9-39 Jerk Correlation by Pitch Type

	Z score	P Value
Fastball - 2 Seam Fastball	6.96	0.00
Fastball - Breaking Ball	2.38	0.01
Changeup - 2 Seam Fastball	3.84	0.00
Slider - Fastball	1.69	0.05
Slider - Changeup	2.00	0.02
Slider - 2 Seam Fastball	4.00	0.00
Slider - Breaking Ball	2.48	0.01
Breaking Ball - 2 Seam Fastball	2.19	0.01

baseball that the slider “is the most dangerous pitch in the game... refer[ing] to the tax that it puts on the elbow...” [99].

9.6.3 Shoulder Internal and External Rotation Acceleration

Examining FIGURE 9-40 , shoulder internal rotation is defined as motion from the neutral 90 degree position towards 0 degrees. External rotation is defined as motion from the neutral towards 180 degrees. Essentially, this motion coincides with the Z axis of the upper arm inertial node and is a one-dimensional measurement easily measured by the inertial system (FIGURE 9-41). This concept is a measure of how fast the head of the humerus is moving in the shoulder joint, and is based on the inertial properties of the arm as it moves.

Briefly examining FIGURE 9-41 , it is almost trivial to determine the speed of external and internal rotation, Negative rotation is external and positive is internal, each is marked by the shaded boxes in the figure. Integrating the area under the red or green areas allows calculation of the amount of each.

FIGURE 9-40 Shoulder Rotation

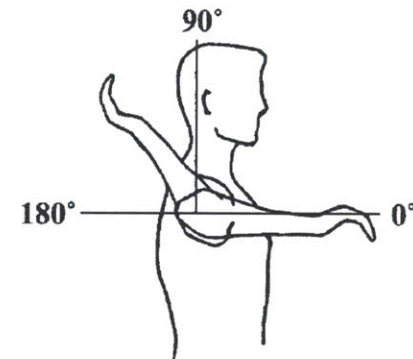
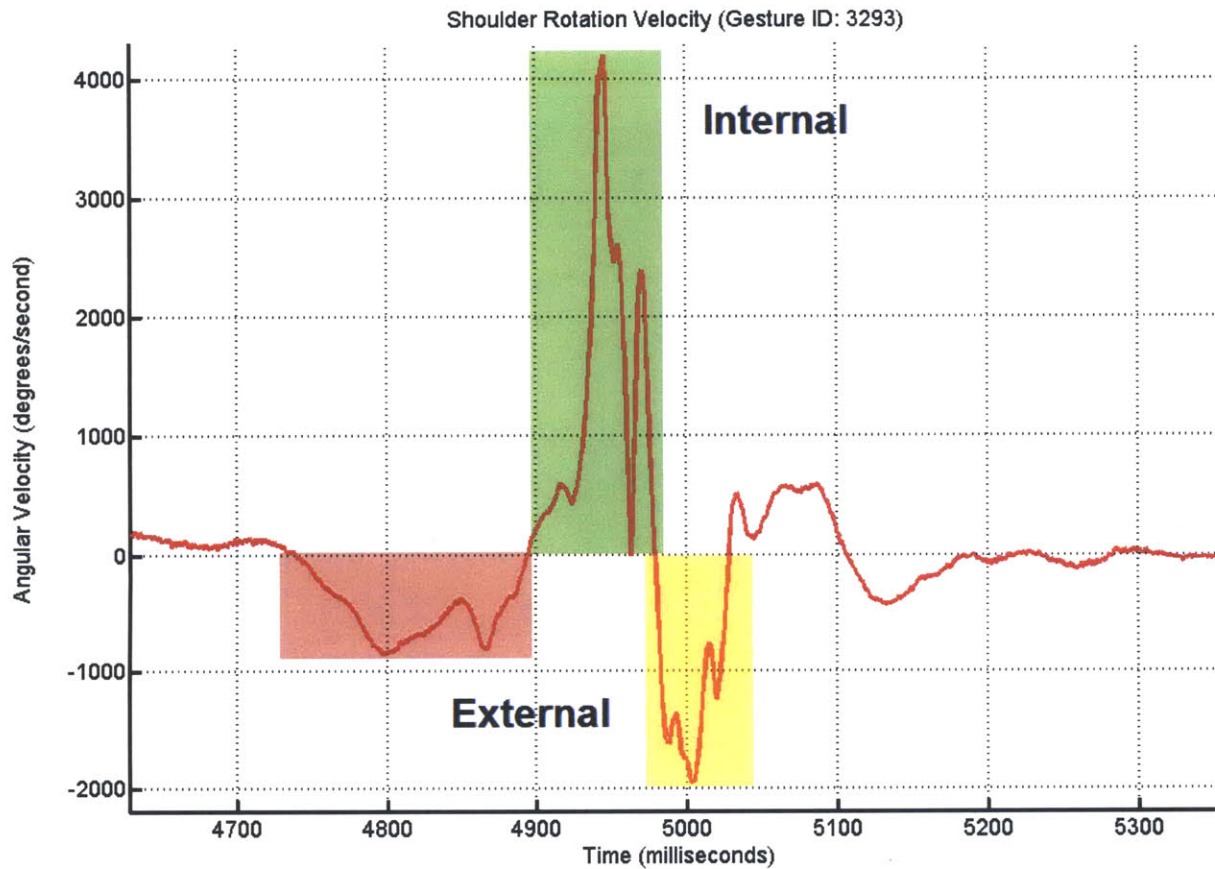


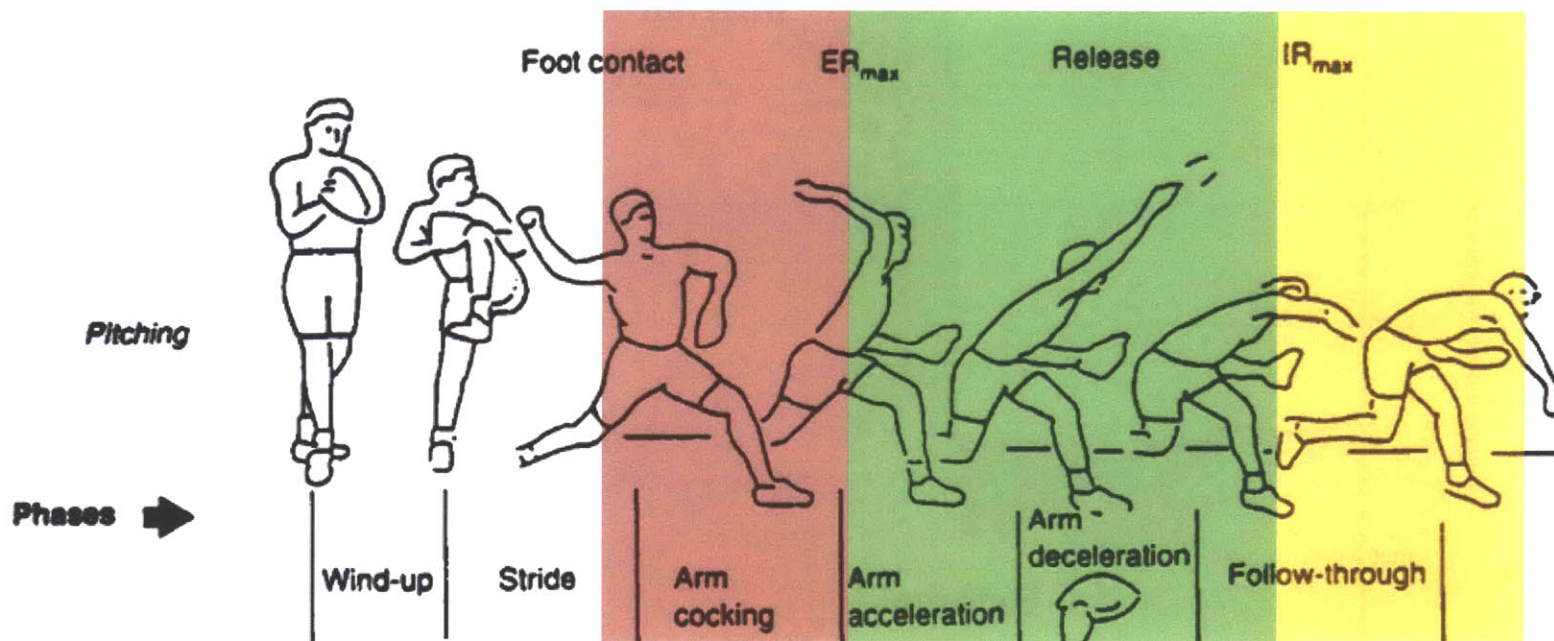
FIGURE 9-41 Shoulder Rotation Velocities. Internal (Positive), External (negative).



Mapping these internal and external rotation peaks and lows to the standard definition of the six phases of a pitch (FIGURE 9-42) shows that, in inertial terms, the boundary between acceleration is blurred. An interesting performance question that arises when looking at this mapping is whether the ball is released from before, at, or after the peak angular velocity is reached? Further, is this time of ball release, in inertial terms, an indicator of how much

power a pitcher is putting into the ball, and what are the effects on pitch speed? Perhaps the internal rotation peak should be partitioned based on the time of ball release and the dividing line compared to where the peak occurs.

FIGURE 9-42 Current Definition of the Phases of a Pitch

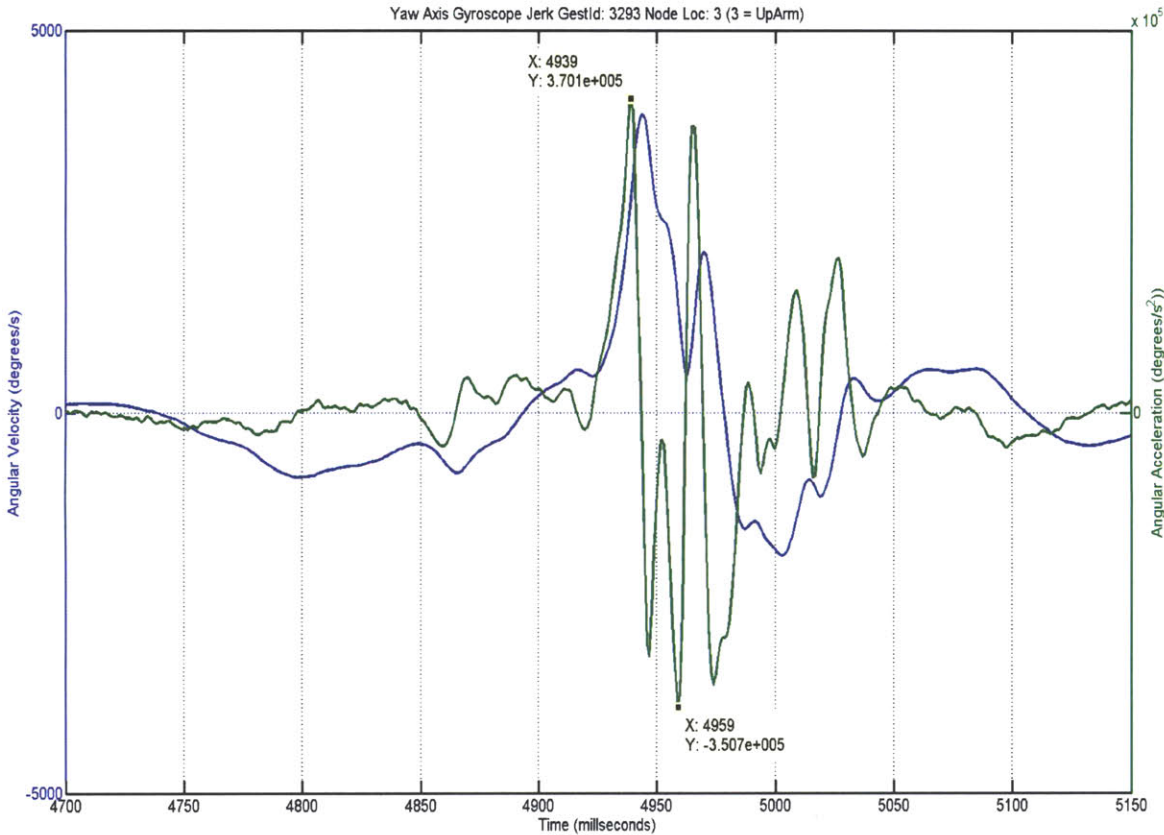


The speed and degree of internal and external rotation is an indicator of how much torque and stress must be absorbed by the soft tissue in the shoulder during pitching to keep the humerus in the joint. This one dimensional measurement has been heavily studied in medical literature [11][100][101][102][103] in terms of angular velocity. However, internal and external rotation has never been examined in terms of angular acceleration. This is because there have been no accurate means of measuring this parameter available until the author's inertial platform was created.

The internal and external rotation velocity simply parameterizes how fast the humeral head is moving inside the shoulder joint. It does not measure the acceleration and deceleration of the humeral head. The magnitude of internal and external angular acceleration, when the shoulder tissue must contain the humerus in the joint, is possibly a better indicator of the magnitude of microtrauma, rather than just velocity alone.

FIGURE 9-43 shows shoulder rotation velocity and the rate of shoulder acceleration. The peak acceleration is $370,100^\circ/\text{sec}^2$ and the peak rate of deceleration $-350,700^\circ/\text{sec}^2$. The angular velocities at the time of these two datapoints are $3058^\circ/\text{sec}$ and $1105^\circ/\text{sec}$, respectively. The delta time between these two is 20 milliseconds. This means that the humerus was accelerating at $370,100^\circ/\text{sec}^2$ and within 20 milliseconds was decelerating at $350,700^\circ/\text{sec}^2$. This is an acceleration delta of $720,800^\circ/\text{sec}$ and indicates that during the transition from peak angular velocity during the acceleration phase to the deceleration phase the shoulder performs the maximum amount of work to stabilize the humerus and keep it in the joint.

FIGURE 9-43 Shoulder Rotation Velocity (blue) and Acceleration. (green)



9.7 CALCULATION OF KINETICS AND DYNAMICS

All sections of this chapter prior to this one demonstrate several medically relevant uses of the inertial network without any context for the relationships between body segments. The next level of analysis involves calculating the kinetic forces that are being experienced between the body segments at the joints. Calculation of these requires knowledge of the context between the segments, or joint angles, over time, the forces and angular velocities, centers of mass of segments and the appropriate dynamics algorithms. An architecture for doing so has been designed and is presented here.

9.7.1 Visual3D Integration

C-Motion Incorporated's Visual3D is introduced in Section 3.4. It is an important part of obtaining kinetic information because the complex mechanical algorithms necessary for doing so are implemented in the software. There is no need to ‘reinvent’ the analysis and this author is not even close to being qualified to do so. However making use of the existing algorithms requires that inertial data be somehow brought into Visual3D and that data be used when specific kinetic calculations are performed.

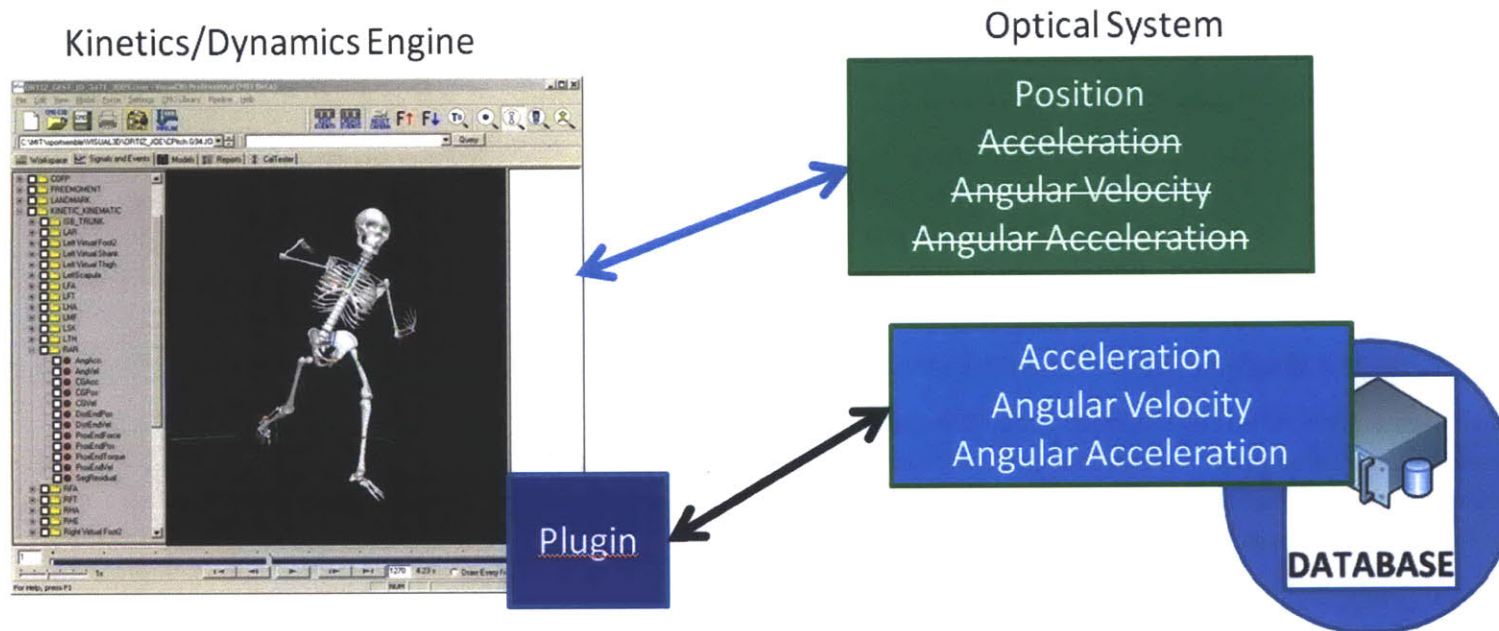
The initial approach was to calculate orientations and joints angles for the segments using only inertial data and to import this data along with inertial data into Visual3D to create a system that is standalone from any optical tracker. The task of properly calculating joint angles for segments over time is non-trivial and a large amount of effort was put forth to realize a system such

as this. Although some commercial products on the market actually do this (i.e. XSens), the demands of our application are severe, hence the problem is much more difficult than it appears on the surface and was not solved. A detailed discussion of why is presented in the following chapter. Instead a hybrid inertial-optical system was created. This system exploits the strengths of both systems and uses the precise joint angles available from the optical tracker as the positional information when calculating kinetics. For the portions of the calculation that require accelerations, angular velocities and angular accelerations, it uses data from the inertial node sensor network. The inertial data has been shown to be more precise than optical for determining forces and torques in Chapter 8 and is the logical choice to obtaining the best results.

The first step in bringing data into Visual3D involves preprocessing it to ensure that it is synchronized with optical data. This involves reading synchronization offset information (in milliseconds) from the database and subtracting it from the inertial data. The high and low range data also need to be fused, and the algorithm for doing so is presented in Section 9.5. Angular acceleration data is calculated based on angular velocity data and filtered lightly with a 250Hz Butterworth filter to remove noise present in the derivative.

With fused and synchronized data available, a plugin to Visual3D was built that would import it from the database into the program's memory. This data is then transformed into the same coordinate systems as the individual body segments and is available to Visual3D's dynamics engine. This architecture is presented in [FIGURE 9-44](#) .

FIGURE 9-44 Visual3D Hybrid System Plugin Architecture



With the help of Tom Kepple (Chief Scientist at C-Motion Inc.), the algorithms in the dynamics engine that calculate joint forces and torques for the wrist, elbow and shoulder were modified to discard the inaccurate optical system accelerations, angular velocities and angular accelerations and use the inertial analogs in performing these calculations.

All of this culminates in the first of its kind system that is capable of providing forces and torques from end-to-end in three dimensions that are based on inertial data. Tom Kepple and his 25 years of pioneering the state of the art in motion capture indicated after the first torques and forces were extracted:

“This is the future of motion capture”

Two biomechanically-relevant metrics that are specific to baseball pitching were targeted to prove the systems ability to provide meaningful data for clinical researchers. These are shoulder distraction and compression forces and elbow valgus and varus torques.

Before continuing, its is extremely important to note that the Visual3D plugin architecture is capable leveraging all features of Visual3D's dynamics engine. This allows application of the more precise inertial information to any metrics that involve the shoulder, elbow and wrist, and is not limited elbow torques and shoulder forces.

9.7.2 Example Data

Sample data from the wrist joint is presented in [FIGURE 9-45](#) and [FIGURE 9-46](#) ; one optical data set is filtered, one is not. There are two noticeable differences in graph that contains filtered optical data. The first are the peak values of each curve and the second are oscillations present in the IMU data after 3000ms. In order to see if the optical system filtering is attenuating such high-frequency oscillations, unfiltered optical data is

presented in **FIGURE 9-46** . Examining the unfiltered graphs shows that there are similar oscillations present in unfiltered optical data. Whether these are actually biomechanically relevant motion or soft tissue artifacts (Section 8.1.3) remains an open research question, but as seen in the figure, any strap-on sensor will exhibit these effects.

FIGURE 9-45 Wrist X Axis Force for a Pitch. IMU data is unfiltered, Optical is filtered.

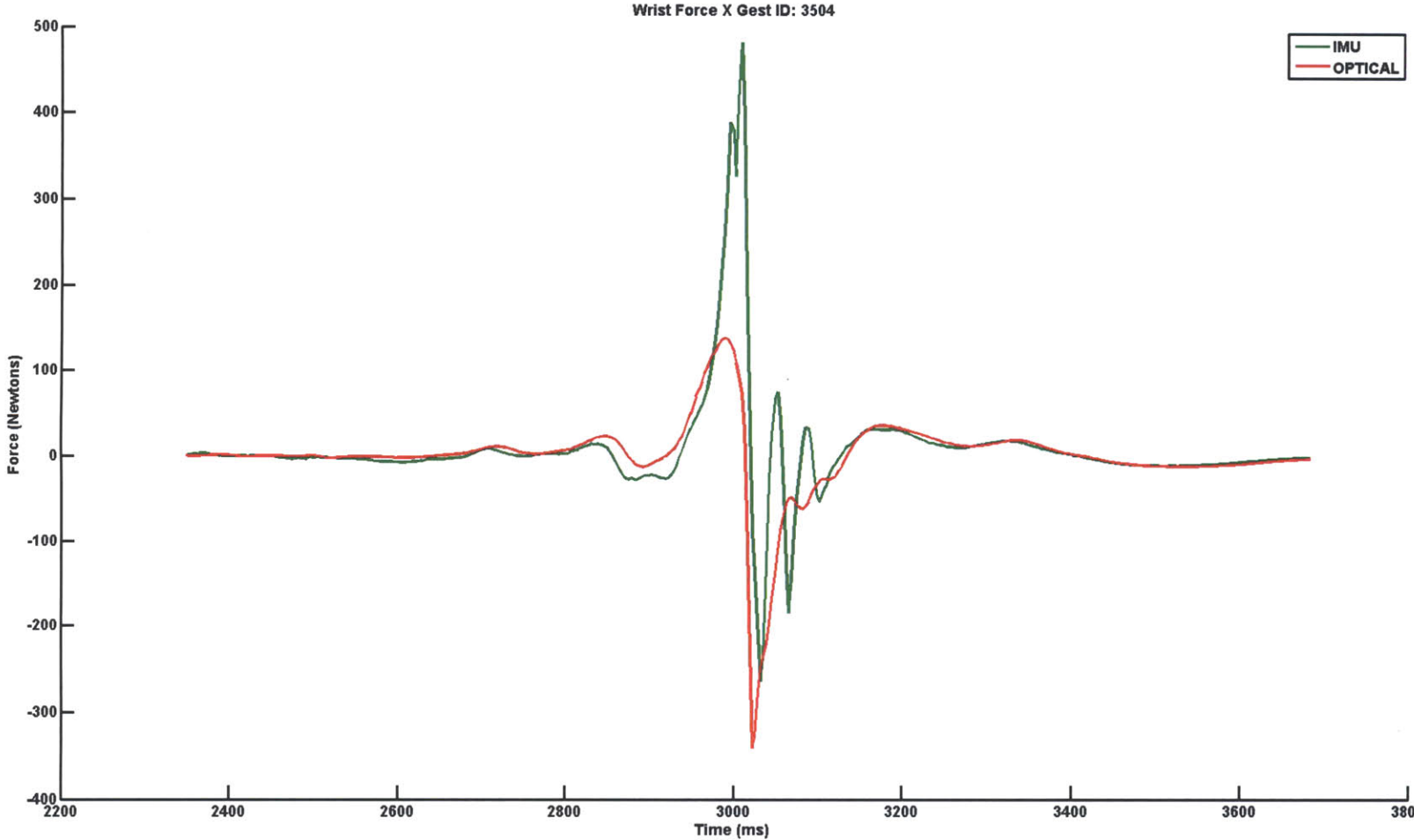
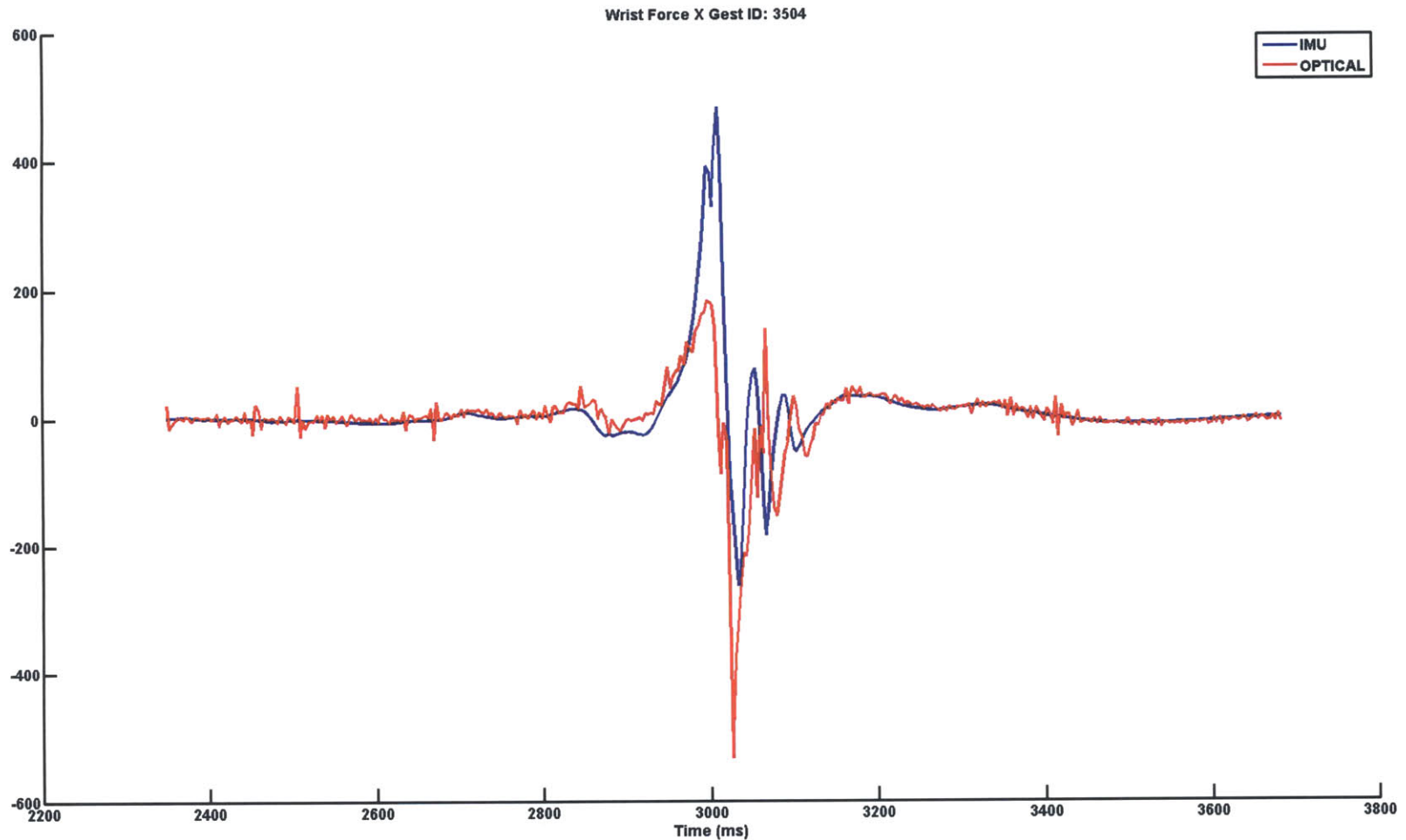


FIGURE 9-46 Wrist X Axis Force for a Pitch. Both IMU and Optical Unfiltered.



In general, examining the shape of the curves for both force and torque in the wrist, elbow and shoulder for both optical and IMU data are similar on a per axis basis. There are some differences that can be attributed to coordinate system misalignment (8.1.2) that require examination of the data in the form of

a vector magnitude. Taking the vector magnitude removes any alignment error or dynamic couplin from sensor rocking and allows for an unbiased comparison.

FIGURE 9-47 Wrist Force Vector Magnitude for a Pitch

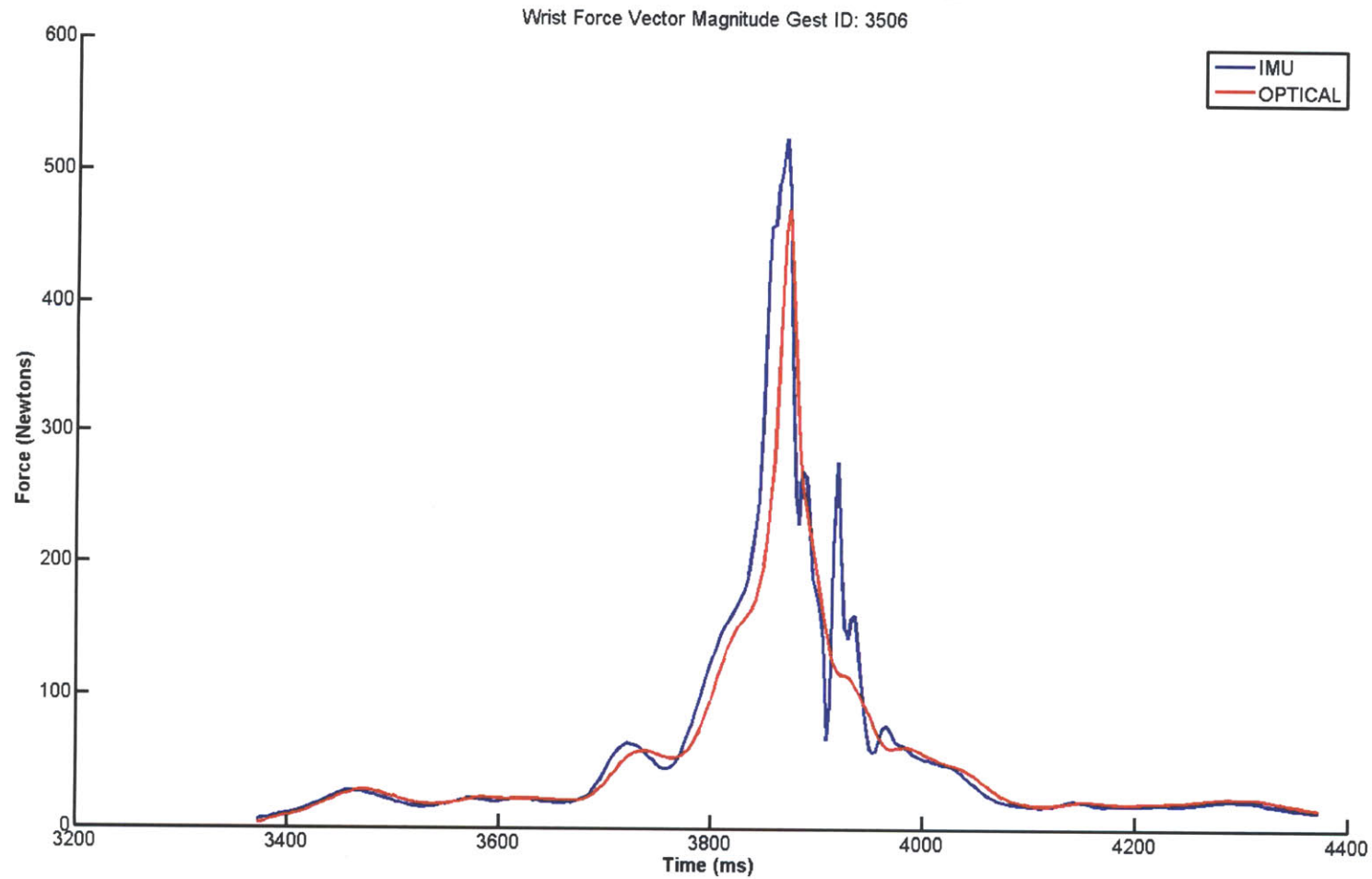
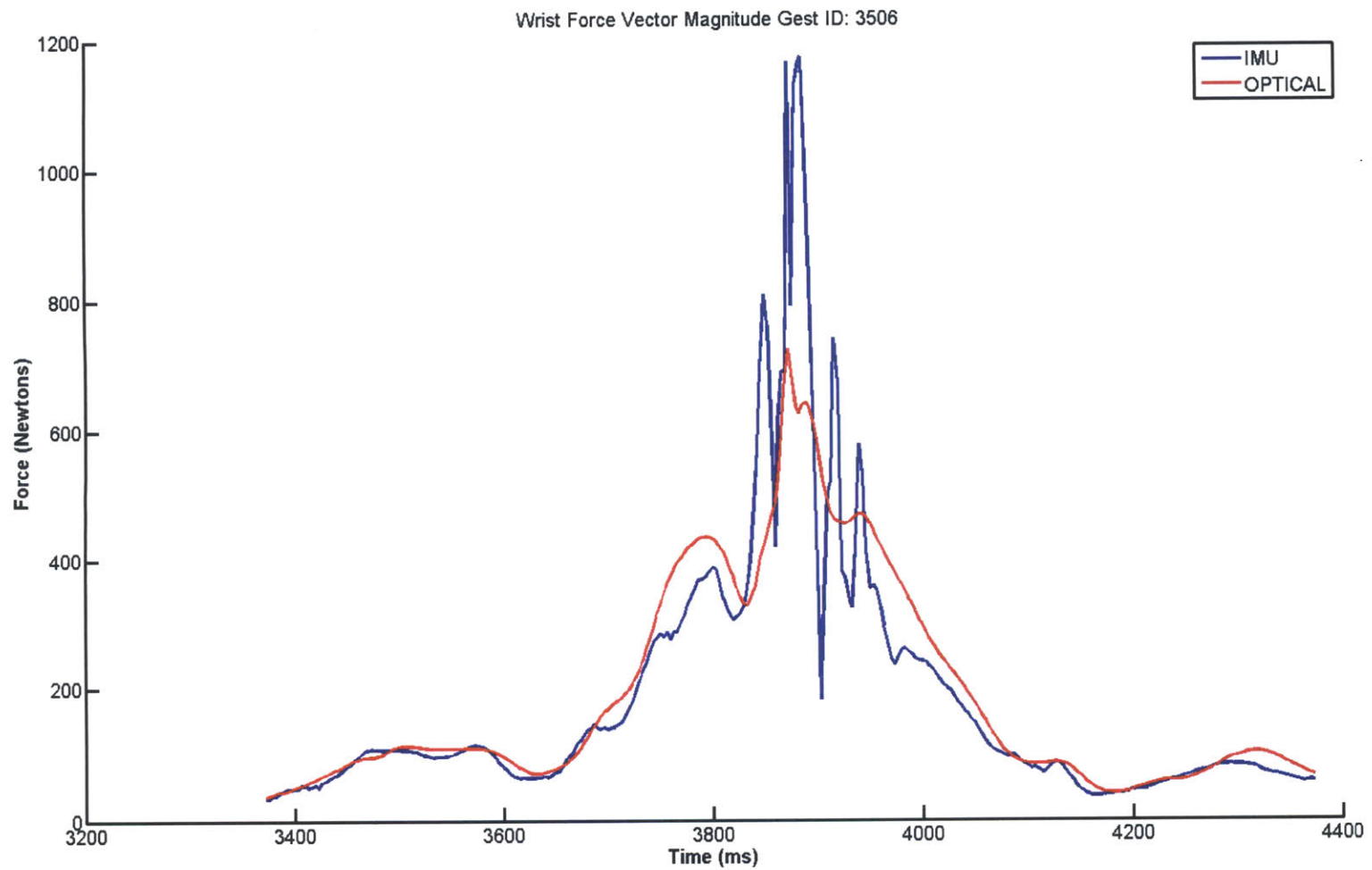


FIGURE 9-48 Shoulder Force Vector Magnitude for a Pitch



Applying the ‘eyeball comparison’ introduced in Section 8.2.2 we can see that in at lower calculated forces the inertial and optical data matches quite well. However, there does exist divergence at the higher forces.

9.7.3 Shoulder Distraction and Compression Forces

Shoulder compressive force is the force that tendons and ligaments must be capable of producing in order to prevent the arm from dislocating (distracting) during a throw [30]. This metric has been the focus of a great deal of research for youth [32] [98] [108] and adult pitchers [35][109][110][111]. The general consensus, based on optical system data, is that “During overhead throwing, high rotator cuff muscle activity is generated to help resist the high shoulder distractive forces 80–120% bodyweight during the arm cocking and deceleration phases.” [110].

The hybrid system allows comparison of the compressive force between the inertial system and the optical. I contend that the compressive forces measured to-date have been lower than previously thought because of the attenuation (partially due to low frequency filtering) present in optical data; this attenuation is documented in Section 8.2.

Sample data for this metric is presented in FIGURE 9-50 , negative values are the distractive force, positive are compressive force. Visual examination of the two curves shows that the inertial values are much higher than the optical. An analysis of the differences in the two forces for the two systems for two pitchers was performed and is presented in FIGURE 9-51 .

It is important to note that the mass difference between the two pitchers is 82lbs, which has an effect on the magnitudes of the forces that are observed for each pitcher. This makes sense, being that a larger pitcher will have larger body segments which require more force to be generated by muscles and ligaments to keep them in place.

FIGURE 9-49 Shoulder Distractive Force

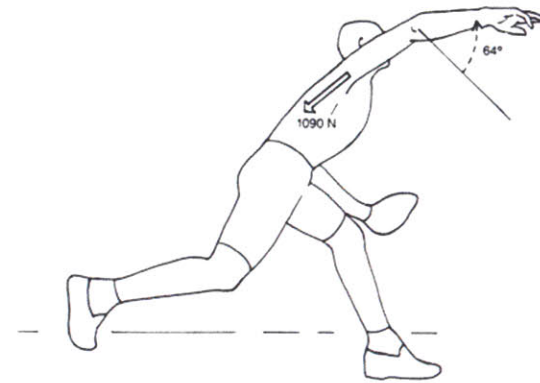


FIGURE 9-50 Shoulder Distractive Force (Negative is distractive)

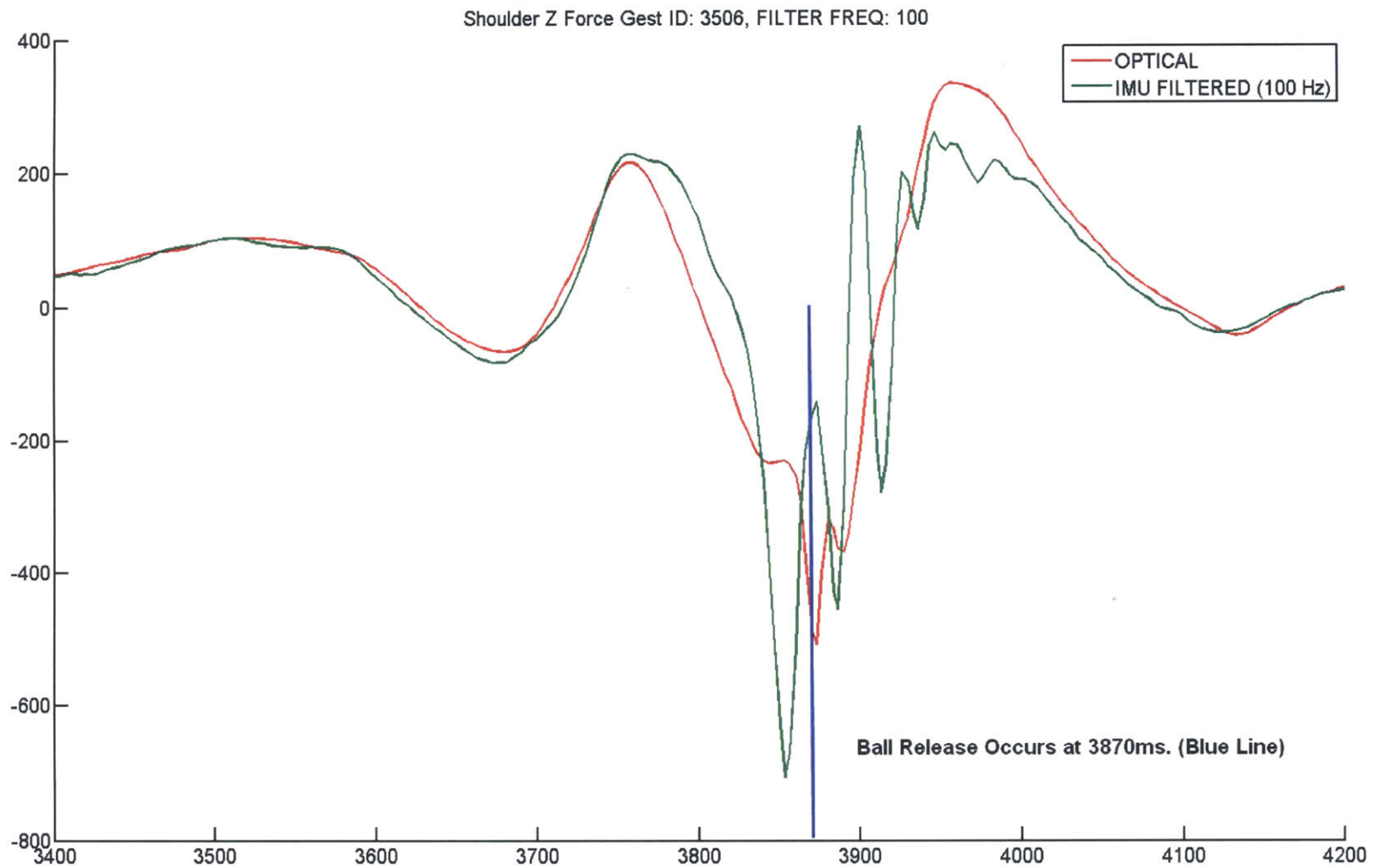
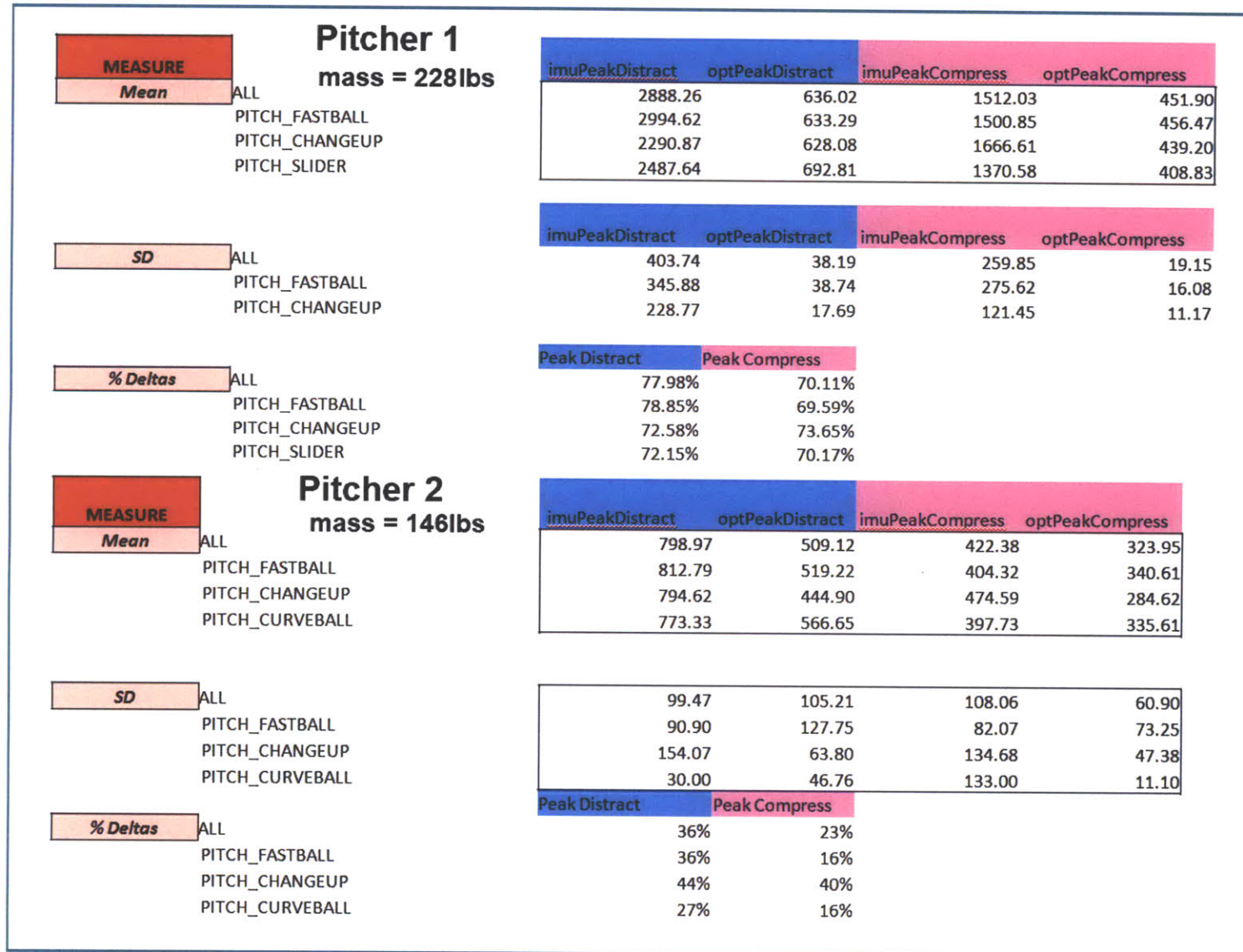


FIGURE 9-51 Shoulder Force Analysis for Both Systems for Two Pitchers (Forces are in Newtons)



The parameters *imuPeakDistract* and *optPeakDistract* are the mean peak distraction values over all pitches for each pitcher. For the IMU system, *Pitcher 2* has an average distraction force of $798.7N$ while the average optical system distraction force is $509.1N$; this is a difference of 36%. For *Pitcher 1*, the average IMU distraction force is $2888.2N$ and the average optical distraction force is $636.0N$, this is a difference of 78%.

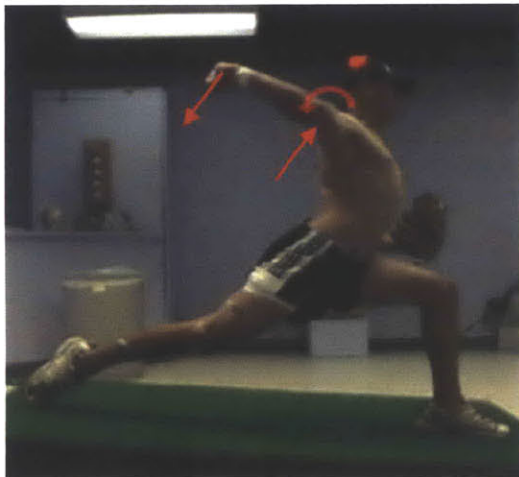
The parameters *imuPeakCompress* and *optPeakCompress* are the mean peak distraction values over all pitcher for that pitcher. The compressive forces are lower than distractive, with an average optical compressive force of $452N$ and $324N$ for *Pitcher 1* and *Pitcher 2*, respectively. The inertial compressive forces are $1512N$ and $422N$ for each pitcher, again respectively. This is a difference of 70% and 23% for *Pitcher 1* and *Pitcher 2*, again respectively.

A minimum distraction difference of 36% is significant and examining these two example pitchers shows that the average difference in force can be as high a 78%. This disparity demonstrates that the measurement by the optical system is heavily attenuated. While this shows that the inertial system gives a better approximation (based on calibration confidence) of what is really happening to the shoulder, two sets of pitches are not enough to draw concrete conclusions and more data is required.

9.7.4 Elbow Valgus and Varus Torque

As with the shoulder distraction force, the torques that are experienced by the elbow have also been heavily studied [112][113][114]. The varus and valgus torque on the elbow is of specific interest as it is directly related to the amount of loading that the ulnar collateral ligament (UCL) experiences. A repair of a torn UCL is commonly known as *Tommy John Surgery*. The Valgus load is depicted in FIGURE 9-52 by the red counter-clockwise arrow and is calculated by building a composite coordinate system from the forearm and upper arm segments, and multiplying each component vector of this coordinate

FIGURE 9-52 Elbow Valgus Load (Counter-Clockwise), Varus Load (Clockwise)



system by the torque at the proximal end of the forearm, starting at the hand body segment. The exact formula for this is as follows:

$$\tau_{\text{v}}^{\text{X}} = \text{RAR}_{\text{X}}^{\text{LAB}} \bullet \tau_{\text{RFA}}$$

$$\tau_{\text{v}}^{\text{Y}} = \left[\text{RFA}_{\text{X}}^{\text{LAB}} \times \text{RAR}_{\text{Z}}^{\text{LAB}} \right] \bullet \tau_{\text{RFA}}$$

$$\tau_{\text{v}}^{\text{Z}} = \text{RFA}_{\text{Z}}^{\text{LAB}} \bullet \tau_{\text{RFA}}$$

The way these are intended to be read are that the torque in the valgus coordinate system for the X-axis is equal to the RAR (right upper arm segment) X-axis vector in the LAB coordinate system multiplied by the torque at the proximal end of the RFA (right forearm). The same can be applied to both the Y and Z axes, with the caveat that the Y axis vector is composed of the cross product of the RFA X axis and the RAR Z axis. The axis that represents the valgus and varus load is the Y axis of this newly formed coordinate system.

Published values for valgus torque are 50 ± 29 Nm [112]. For varus torque, published values range from 82 ± 13 Nm [113] to 55 ± 12 Nm [114]. In order to compare the output of the inertial and optical systems, the same style of analysis that was performed for shoulder distraction force for the same two pitchers using valgus and varus torque. Results from this analysis are presented in [FIGURE 9-53](#) .

FIGURE 9-53 Inertial and Optical System Valgus and Varus Torque Comparison (Values are in Newton-meters)

Pitcher 1		imuPeakValgus		optPeakValgus		imuPeakVarus		optPeakVarus	
MEASURE									
Mean	ALL	151.60	99.18	104.07	33.92				
	PITCH_FASTBALL	159.66	100.22	107.15	34.02				
	PITCH_CHANGEUP	108.76	93.96	109.87	34.79				
	PITCH_SLIDER	116.48	94.04	46.30	30.70				
SD	ALL	41.28	6.94	28.04	4.92				
	PITCH_FASTBALL	40.61	7.17	26.24	5.34				
	PITCH_CHANGEUP	1.56	0.73	13.51	0.54				
	PITCH_SLIDER								
% Deltas	ALL		35%		67%				
	PITCH_FASTBALL		37%		68%				
	PITCH_CHANGEUP		14%		68%				
	PITCH_SLIDER		19%		34%				
Pitcher 2		imuPeakValgus		optPeakValgus		imuPeakVarus		optPeakVarus	
MEASURE									
Mean	ALL	82.80	51.66	54.51	38.03				
	PITCH_FASTBALL	75.84	45.39	56.65	36.98				
	PITCH_CHANGEUP	97.57	65.97	56.91	44.56				
	PITCH_CURVEBALL	79.99	47.86	46.70	32.22				
SD	ALL	21.68	23.66	10.24	14.49				
	PITCH_FASTBALL	22.67	6.77	8.69	9.82				
	PITCH_CHANGEUP	20.68	43.76	5.87	23.67				
	PITCH_CURVEBALL	14.20	4.25	15.57	8.16				
% Deltas	ALL		38%		30%				
	PITCH_FASTBALL		40%		35%				
	PITCH_CHANGEUP		32%		22%				
	PITCH_CURVEBALL		40%		31%				

As with the shoulder distraction force, the torques are higher for the larger pitcher. For the *Pitcher 1* the mean valgus torque was $151.6Nm$ and $99.2Nm$ for the inertial and optical systems, respectively. *Pitcher 2*'s values are $82.8Nm$ and $51.7Nm$, respectively. While the actual values are quite different, the amount of attenuation, in terms of a percentage, between the *Pitcher 1* and *Pitcher 2* are 35% and 38%.

Mean varus load for *Pitcher 1* is $104.1Nm$, inertial, and $34.0Nm$, optical, and for *Pitcher 2* $54.6Nm$, inertial, and $38.0Nm$, optical. In percentages, these differences are 67% and 30%, with the larger disparity being for the player who has more mass.

As with previous metrics that utilize inertial data, the high confidence in calibration is used to state that the inertial-based data is considered to be more accurate. Based on this limited dataset, I can confidently state that the previously calculated optical system elbow torques fall at least 30% short and that the stress on the elbow is much greater than previously thought.

9.7.5 The Fine Print

There are means through which the node attachment to the arm could artificially increase the measured peak value. For example, the mechanical characteristics of skin appear to be fairly compliant and soft until the skin is displaced maximally, where the displacement encounters rapid resistance forming something of a “hard stop”. In the course of a rapid motion, the node could be forced against the stop, experiencing large deceleration encountered by the node but not the arm. Additionally, if the node attachment is mechanically resonant, it could experience overshoot in response to a physical impulse as seen in a pitch. Such resulting ambiguities need to be explained in future measurements and simulations of the arm-node attachment and soft tissue dynamics.

CONTRIBUTIONS & CONCLUSIONS

All good things must come to an end.

- Thornton Wilder

This chapter summarizes the contributions and advancements in the state-of-art that this thesis has provided. It also presents new directions for continuing this work and challenges that will be faced by those attempting to push further.

10.1 CONTRIBUTIONS

This thesis presents a novel end-to-end research platform that extends the capabilities of current biomechanical analysis.

The inertial measurement unit (IMU) network and hardware developed to enable measurement of the extreme forces is the only wearable IMU array that is capable of obtaining these measurements currently in existence. It has been designed to be robust to extreme activity and has been proven, because of rigorous calibration, to be a scientific tool accurate enough to perform life sciences quality research that brings more confidence to biomechanical analysis. By sampling at 1000Hz, it addresses the aliasing problem. With the developed rapid application system, it fits into the athletic workflow smoothly and increases the throughput of how much data can be gathered; unlike optical systems my IMU array can be easily deployed anywhere. Lastly, by leveraging the precision of inertial sensors the IMU system allows for the introduction of a new biomechanically relevant, never before considered, metric, jerk.

The platform allows clinical researchers to focus on research topics that are of interest to them and does not require any sensor network or inertial sensing expertise in order to leverage the capabilities of the system. It provides a true end-to-end solution with graphical user interfaces, that abstract away the details of such systems, for every step of the process.

These interfaces start with network command and control, continue onto translation of gathered data into biomechanically relevant parameters (G-forces and angular velocities). They handle synchronization of the network itself and with other systems, allowing for realization of a hybrid inertial/optical system that leverages the strengths of both systems. The next level of interface integrates with an industry standard kinetics engine and allows feeding of more accurate inertial data into the kinetics algorithms. This

integration provides clinically relevant inertial-based biomechanical metrics and provides the only existing mechanism for checking, and extending, the current accuracy of existing optical systems.

As part of the platform, a *Player*, *Session* and *Gesture* taxonomy and its underlying data model has been invented and realized. This provides a generic biomechanical data model that captures all the information needed for storing inertial information and all associated metadata for any physical activity. Due to this data-centric approach the system scales from tens to tens of thousands of gesture without any additional work. Further, application programming interfaces have been developed, in several computer programming languages, to allow access to this model in a language and platform independent manner. They allow for a query-based approach for defining clinical research populations based on any of the metadata parameters, such as pitch type or age or weight, that are enumerated in the data model.

The entire platform has been proven to work and is considered by experts in the field as “the future of motion capture”.

The system has been used to perform novel biomechanical measurements, (i.e. shoulder and elbow forces and torques, jerk forces, shoulder internal rotation, etc.) and have shown indications that widely accepted force/torque magnitudes in baseball pitching are consistently larger than previously work has shown.

10.2 FUTURE WORK

10.2.1 Differentiation Between Real Motion & Soft Tissue Artifacts

As explained in Section 9.7.2, there are unexplained oscillations that are present in the unfiltered inertial data that appear to also be present in the unfiltered optical data. These oscillations have not been previously considered, because the low-frequency filtering of optical data removed them. A need exists to determine if they are real motion that is part of the pitch, or soft tissue artifacts. Soft tissue mounting could also affect the peak values of measured acceleration and rate and dynamic rocking of the IMU on the skin can couple axes. Soft tissue artifacts are covered in Section 8.1.3, which explains that the established way to answer this question is to surgically implant bone pins, or pursue the new research area of studying the effects of high linear acceleration on human skin when inertial nodes are fixed to it through a combination of mathematical modeling, simulation and actual measurement.

10.2.2 Coordinate System Alignment Protocols

The pitfalls of coordinate system misalignment are described in Section 8.1.2. While this problem has not yet been solved, as part of this thesis initial steps were taken to characterize misalignment. A common coordinate system between the optical and inertial system has been defined at the Massachusetts General Hospital Sports Performance Center and some initial data has been gathered. Carolina Brum Medeiros, a callaborator from McGill University, has begun to define a gesture taxonomy to dynamically calculate the orientation misalignment angles for each node and her work is currently ongoing.

10.2.3 Joint Angles

The next logical step in the current hybrid system is to remove the optical portion and calculate the joint angles using the standalone inertial system to drive the skeletal model. This is conventionally done by integrating the gyroscope signals using a Kalman Filter, getting initial angles and nulling offsets/noise via “ground sensor truth” from the magnetometer. This was attempted and the results were only partially successful. However, there are some difficult issues that need to be addressed in order to realize this system.

The first of these is the orientation representation system for each of the joint angles between body segments that was required to bring them into Visual3D. Visual3D required that each orientation be represented as an Euler angle. Euler angles suffer from gimbal lock, when two axes are rotated into the same plane, and it cannot be determined which axis is which. In order to deal with these singularities there are different angle application schemes (such as ZXZ) that require tracking of each angle over time, detecting and working around any gimbal lock that occurs. While these singularities are not a problem for Visual3D, they are a problem for the external algorithms that were developed to compute joint angles (using inertial data) outside of the Visual3D environment.

Clinically-defined research models prefer a particular set of coordinate systems. The inertial system prioritizes the comfort of the instrumented players and uses the best placement to avoid skin tissue artifacts. These two coordinate systems are not aligned and require transcription of initial angles from the inertial node coordinate system to the clinical coordinate system. Implementation of this transcription is not only a rotation, but also a change of basis.

Initial segment orientation relies heavily on fusion of magnetometer and low range accelerometer data. These algorithms were developed during the course of this thesis, unfortunately indoor magnetometer data in practice has

shown to be inaccurate and there is another level of (better) calibration required to obtain accurate initial orientation.

Assuming accurate enough initial orientation information, tracking the orientation of an individual segment over time via a Kalman filter has been shown to be feasible [63]. Additionally, the next step is to build a second level of Kalman filtering to determine the joint angle by building an estimator that uses the orientations of two nodes to observe a joint center. This leverages algorithms that are used by GPS satellite tracking, and no previously built wearable systems do this, as they simply assume a quaternion representation of each segment and calculate a joint angle based on the difference between the two quaternions. This approach is not sufficiently accurate in order to perform life sciences quality research.

10.2.4 Lower Cost Hybrid Systems

As optical capture technology has continually evolved since its inception, so has the cost of purchasing such a system. The faster the motion, the more cameras, with higher framerates, that are required to capture as much information as possible. A 500Hz system with enough cameras to capture pitching comes at a cost in the hundreds of thousands of dollars.

One hypothesis is that a high-end optical system isn't needed if it is complemented by an inertial network. Considering a hybrid inertial and optical system running at 100Hz, the hardware necessary to realize such a system is much cheaper to build than its high-end counterpart. An interesting question is how well would such a system work? While the aliasing problem would still exist, the accuracy of the sensors and their ability to provide high-quality inertial parameters would definitely help provide better data than a standalone optical system running at 100Hz, and help to properly interpolate the optical results.

While the quality would not be that of the high-end system, such a low-cost system creates a market that would make it tractable for enable smaller organizations, such as little league teams, to perform biomechanically relevant motion capture.


10.2.5 Continued Data Acquisition

The final piece of future work involves building a large body of data from various populations and various sports. Adding a layer of data mining on top of such a body of data would exploit the full power of the data-centric approach along with the full power of the inertial system to enable fine grained clinical research to draw more accurate conclusions and performance and injury predictions than previously has been possible.


REFERENCES



The *References* chapter provides the bibliographic information cross-referenced to the text.

- 
- [1] The Computer for the 21st Century. Mark Weiser. Scientific American, September 1991. Pgs 94-104.
- [2] *Body sensor networks for baseball swing training*. Ghasemzadeh, H. and Jafari, R. 2010. Pervasive Computing and Communications Workshops. pp. 792-795.
- [3] Roetenberg, D. Slycke, P. J. Veltink, P. H. Ambulatory position and orientation tracking fusing magnetic and inertial sensing. In Biomedical Engineering, IEEE Transactions on, pages 883 { 890, May 2007.
- [4] Xsens Technologies B.V. Xsens motion technologies.
<http://www.xsens.com>.
- [5] Animazoo UK Ltd, Animazoo Motion Capture,
<http://www.animazoo.com/products>
- [6] Great Lakes Neurotechnologies, KinetiSense Motion Capture,
<http://www.glneurotech.com/KinetiSense/>,
<http://glneurotech.com/support/brochures/kinetisense.pdf>
- [7] Lapinski, M., *A Wearable, Wireless Sensor System for Sports Medicine*, 2008, Masters Thesis, MIT Media Lab
- [8] **Vicon MotionSystems**. Polygon. [Online]
<http://www.vicon.com/products/documents/Polygon4.pdf>
- [9] Jarrett MO, Andrews BJ, Paul JP. A television-computer system for the analysis of human locomotion, in: I.E.R.E. Golden Jubilee Conference. An exhibition on Application of Electronics in Medicine. Southampton University, Southampton, England, 1976.
- [10] Qualisys Motion Capture Systems. [Online] ,
<http://www.qualisys.com/products/>

- [11] **Fleisig, Glenn, Escamilla, Rafael and Andrews, James.** Biomechanics of Throwing. [book auth.] James E. Zachazewski and David J Magee. *Athletic Injuries and Rehabilitation*. s.l. : Saunders, 1996.
- [12] *Implications for the Development of Proximal Humeral Epiphysiolysis and Humeral Retrotorsion.* **Michelle B. Sabick, PhD, Young-Kyu Kim, MD, Michael R. Torry, PhD.** 11, s.l. : The American Journal of Sports Medicine , 2005, Vol. 33.
- [13] McFarland, J. (1990). *Coaching pitchers*. Champaign, Ill: Leisure Press.
- [14] Kindall, J., & Winkin, J. (2000). *The baseball coaching bible*. Champaign, IL: Human Kinetics.
- [15] ST Microelectronics. (2008). Application Note AN2768: LIS331DL 3-axis digital MEMS accelerometer: translates finger taps into actions. http://www.st.com/st-web-ui/static/active/en/resource/technical/document/application_note/CD00196199.pdf
- [16] Vicon Motion systems. T-Series Camera Documentation. (2010). <http://www.vicon.com/products/documents/TSeriesSedition.pdf>
- [17] Zoopraxiscope. Wikipedia. [Online] 12 31, 2005. [Cited: 11 11, 2011.] <http://en.wikipedia.org/wiki/Zoopraxiscope>.
- [18] Rotoscoping. Wikipedia. [Online] Oct 14, 2003. [Cited: 11 11, 2011.] <http://en.wikipedia.org/wiki/Rotoscoping>.
- [19] Edgerton, Harold E. Abrupt change of load on a synchronous machine. Cambridge, MA : MIT Thesis, 1927.
- [20] Mocapture, Society. History of Motion Capture. Mocap History. [Online] 2011. [Cited: 11 11, 2011.] <http://motioncapturesociety.org/resources/industry-history>.
- [21] A clinically viable electrogoniometer. Cousins, S J, Hannah, R E and Foort, J. Atlanta, GA : s.n., 1979. 2nd Annual International Conference on Rehabilitation Engineering.

- 
- [22] Toward a Language for Human Movement. Calvert, Thomas W. 1986, Computers and the Humanities, pp. 35-43.
- [23] Linder, Wilfred. Digital Photogrammetry. s.l. : Springer, 2006.
- [24] Wikipedia. Bob Sabiston . Wikipedia. [Online] May 10, 2006. [Cited: 11 27, 2011.] http://en.wikipedia.org/wiki/Bob_Sabiston.
- [25] Sabiston, Walter Roberts. Extracting 3D motion from hand-drawn animated figures. Cambridge, MA : MIT Thesis, 1991.
- [26] Intra-rater and inter-rater reliability of gait measurements with CODA mpx30 motion analysis system. Maynard, V, et al. 2003, Gait & Posture, pp. 59-67.
- [27] Prakash: lighting aware motion capture using photosensing markers and multiplexed illuminators. Raskar, Ramesh, et al. 3, s.l. : ACM TRANSACTIONS ON GRAPHICS, 2007, Vol. 26.
- [28] McFarland, Joe. Coaching Pitchers. Champaign, Ill: Leisure Press, 1990.
- [29] Carroll, Will. Saving the Pitcher: Preventing Pitching Injuries in Modern Baseball. Chicago: Ivan R. Dee, 2004.
- [30] Fleisig, Glenn, Escamilla, Rafael and Andrews, James. Biomechanics of Throwing. [book auth.] James E. Zachazewski and David J Magee. Athletic Injuries and Rehabilitation. s.l. : Saunders, 1996.
- [31] Implications for the Development of Proximal Humeral Epiphysiolysis and Humeral Retrotorsion. Michelle B. Sabick, PhD, Young-Kyu Kim, MD, Michael R. Torry, PhD,. 11, s.l. : The American Journal of Sports Medicine , 2005, Vol. 33.
- [32] The Effect of Pitching Biomechanics on the Upper Extremity in Youth and Adolescent Baseball Pitchers. J. T. Davis, Orr Limpisvasti, Derrick Fluhme, Karen J. Mohr, Lewis A. Yocum, Neal S. ElAttrache and Frank W. Jobe. 8, s.l. : Sage, 2009, Vol. 37. 10.1177/0363546509340226.

[33] Werner SL, Murray TA, Hawkins RJ, et al. Relationships between throwing mechanics and shoulder distraction in professional baseball pitchers. In American Journal of Sports Medicine, 2001.

[34] Tullos HS, King J. Throwing mechanism in sports. In Orthopedic Clinic of North America; 4, pages 709-720, 1973.

[35] Fleisig GS, Kingsley DS, Loftice JW, et al. Kinetic comparison among the fastball, curveball, change-up, and slider in collegiate baseball pitchers. In American Journal of Sports Medicine, 2005.

[36] Body sensor networks for baseball swing training. Ghasemzadeh, H. and Jafari, R. 2010. Pervasive Computing and Communications Workshops. pp. 792-795.

[37] Vadim Gerasimov. Swings That Think. <http://vadim.oversigma.com/stt/bat.html>

[38] Gerasimov, Vadim. Every sign of life. Cambridge: Massachusetts Institute of Technology, 2003. <http://hdl.handle.net/1721.1/28776>.


[39] Feltner ME: Kinematic and kinetic parameters of the shoulder joint during the overarm baseball throw. Masters thesis. Indiana University, Bloomington, Indiana, 1984

[40] Feltner ME, Dapena J: Three-dimensional interactions in a two-segment kinetic chain. Part I: General model. Int J Sport Biomech 5: 403-419, 1989


[41] Feltner ME, Dapena JJ: Dynamics of the shoulder and elbow joints of the throwing arm during a baseball pitch. Int J Sport Biomech 2: 235-259, 1986

[42] M.E. Feltner, J. Dapena, Segmental interactions affecting the flexion/extension motion of the elbow during fastball baseball pitching, Journal of Biomechanics, Volume 21, Issue 10, 1988, Page 869,


[43] Eugene J. Alexander, Thomas P. Andriacchi, Correcting for deformation in skin-based marker systems, Journal of Biomechanics, Volume 34, Issue 3, March 2001, Pages 355-361

- 
- [44] Hansen C., Honeine J., et al. Low-cost motion capture systems in practice. *Computer Methods in Biomechanics and Biomedical Engineering*, Vol. 15, Iss. sup1, 2012
- [45] Helen Liu, Cathy Holt, Sam Evans, Accuracy and repeatability of an optical motion analysis system for measuring small deformations of biological tissues, *Journal of Biomechanics*, Volume 40, Issue 1, 2007, Pages 210-214
- [46] C. Reinschmidt, A.J. van den Bogert, B.M. Nigg, A. Lundberg, N. Murphy, Effect of skin movement on the analysis of skeletal knee joint motion during running, *Journal of Biomechanics*, Volume 30, Issue 7, July 1997, Pages 729-732
- [47] Markus Windolf, Nils Götzen, Michael Morlock, Systematic accuracy and precision analysis of video motion capturing systems—exemplified on the Vicon-460 system, *Journal of Biomechanics*, Volume 41, Issue 12, 28 August 2008, Pages 2776-2780
- [48] Michael S. Andersen, Daniel L. Benoit, Michael Damsgaard, Dan K. Ramsey, John Rasmussen, Do kinematic models reduce the effects of soft tissue artefacts in skin marker-based motion analysis? An in vivo study of knee kinematics, *Journal of Biomechanics*, Volume 43, Issue 2, 19 January 2010, Pages 268-273
- [49] Stephane Armand, Morgan Sangeux, Pierre Hoffmeyer, Richard Baker, Optimal markers' placement on the thorax for clinical gait analysis—A preliminary study, *Gait & Posture*, Volume 30, Supplement 2, November 2009, Page S54
- [50] Steven Stanhope, John Holden, John Orsini, Effect of Target Attachment Techniques on Estimates of Shank Skeletal Motion., *Gait & Posture*, Volume 2, Nr. , 1994. Page 58
- [51] Inge Söderkvist, Per-Åke Wedin, Determining the movements of the skeleton using well-configured markers, *Journal of Biomechanics*, Volume 26, Issue 12, December 1993, Pages 1473-1477, ISSN 0021-9290, 10.1016/0021-9290(93)90098-Y.

- [52] T.-W. Lu, J.J. O'Connor, Bone position estimation from skin marker coordinates using global optimisation with joint constraints, *Journal of Biomechanics*, Volume 32, Issue 2, February 1999, Pages 129-134,
- [53] Rita Stagni, Silvia Fantozzi, Angelo Cappello, Double calibration vs. global optimisation: Performance and effectiveness for clinical application, *Gait & Posture*, Volume 29, Issue 1, January 2009, Pages 119-122
- [54] Cappello, A.; Stagni, R.; Fantozzi, S.; Leardini, A., "Soft tissue artifact compensation in knee kinematics by double anatomical landmark calibration: performance of a novel method during selected motor tasks," *Biomedical Engineering, IEEE Transactions on* , vol.52, no.6, pp.992,998, June 2005
- [55] Yeadon, MR (1990) The simulation of aerial movement - I: The determination of orientation angles from film data, *Journal of Biomechanics*, 23, pp.59-66, ISSN: 0021-9290.
- [56] Yeadon, MR (1990) The simulation of aerial movement - II: A mathematical inertia model of the human body, *Journal of Biomechanics*, 23, pp.67-74, ISSN: 0021-9290.
- [57] Yeadon, MR (1990) The simulation of aerial movement - III: The determination of the angular momentum of the human body, *Journal of Biomechanics*, 23, pp.75-83, ISSN: 0021-9290.
- [58] Yeadon, MR, Atha, J, Hales, FD (1990) The simulation of aerial movement - IV: A computer simulation model, *Journal of Biomechanics*, 23, pp.85-89, ISSN: 0021-9290.
- [59] A. Ahmadi , D. Rowlands, J. Daniel, (2010) Development of inertial and novel marker-based techniques and analysis for upper arm rotational velocity measurements in tennis., *Journal of Sports Engineering*, 8, pp179-188
- [60] Shanshan Chen; Cunningham, C.L.; Lach, J.; Bennett, B.C., "Extracting Spatio-Temporal Information from Inertial Body Sensor Networks for Gait Speed Estimation," *Body Sensor Networks (BSN)*, 2011 International Conference on , vol., no., pp.71,76, 23-25 May 2011

- 
- [61] Chun-Hao Wu; Yuan-Tse Chang; Yu-Chee Tseng, "On Optimization of Accelerometers Deployment for Human Posture Tracking," Body Sensor Networks (BSN), 2011 International Conference on , vol., no., pp.186,190, 23-25 May 2011
- [62] Burchfield, R.; Venkatesan, S., "A Framework for Golf Training Using Low-Cost Inertial Sensors," Body Sensor Networks (BSN), 2010 International Conference on , vol., no., pp.267,272, 7-9 June 2010
- [63] A. D. Young, M. J. Ling, and D. K. Arvind. 2007. Orient-2: a realtime wireless posture tracking system using local orientation estimation. In Proceedings of the 4th workshop on Embedded networked sensors (EmNets '07). ACM, New York, NY, USA, 53-57.
- [64] Arvind D K and Bates C A, "The Speckled Golfer", 3rd Int. Conf. on Body Area Networks, Tempe AZ, USA, IEEE March 13 - 17, 2008.
- [65] Visual3D, C-Motion Inc.:Research in Biomechanics. <https://www.c-motion.com/products/visual3d/>
- [66] Winter, David A., "Biomechanics and motor control of human movement", 2009, Hoboken, N.J. : Wiley
- [67] Phadke, V., Braman, J. P., LaPrade, R. F., & Ludewig, P. M. (January 01, 2011). Comparison of glenohumeral motion using different rotation sequences. *Journal of Biomechanics*, 44, 4, 700-705.
- [68] International Shoulder Group, <http://internationalshouldergroup.org/>
- [69] Polhemus Motion Tracking Technical Comparisons. Polhemus Motion Tracking. http://www.polhemus.com/polhemus_editor/assets/polhemus-motion-tracking-technical-comparisons.pdf
- [70] Arvind, D. K.; Valtazanos, A., "Speckled Tango Dancers: Real-Time Motion Capture of Two-Body Interactions Using On-body Wireless Sensor Networks," Wearable and Implantable Body Sensor Networks, 2009. BSN 2009. Sixth International Workshop on , vol., no., pp.312,317, 3-5 June 2009

- [71] Nissen CW, Westwell M, Ounpuu S, Patel M, Tate JP, Pierz K, Burns JP, Bicos J., "Adolescent baseball pitching technique: a detailed three-dimensional biomechanical analysis." *Med Sci Sports Exerc.* 2007 Aug;39(8):1347-57.
- [72] Aguinaldo AL, Buttermore J, Chambers H., "Effects of upper trunk rotation on shoulder joint torque among baseball pitchers of various levels." *J Appl Biomech.* 2007 Feb;23(1):42-51.
- [73] Ge Wu, Frans C.T. van der Helm, H.E.J. (DirkJan) Veeger, Mohsen Makhsous, Peter Van Roy, Carolyn Anglin, Jochem Nagels, Andrew R. Karduna, Kevin McQuade, Xuguang Wang, Frederick W. Werner, Bryan Buchholz, ISB recommendation on definitions of joint coordinate systems of various joints for the reporting of human joint motion—Part II: shoulder, elbow, wrist and hand, *Journal of Biomechanics*, Volume 38, Issue 5, May 2005, Pages 981-992, ISSN 0021-9290, 10.1016/j.jbiomech.2004.05.042.
- [74] Ryan Aylward. *Senseable: A Wireless Inertial Sensor System for Interactive Dance and Collective Motion Analysis*. Master's thesis, Media Laboratory, Massachusetts Institute of Technology, 2006
- [75] Quotes by clarinetist Jack Brymer. [Online]
http://thinkexist.com/quotes/jack_brymer/
- [76] Nordic Semiconductor. nRF2401A Transceiver [Online]
[http://\[76\]\[76\]www.nordicsemi.com/eng/Products/2.4GHz-RF/nRF2401A](http://[76][76]www.nordicsemi.com/eng/Products/2.4GHz-RF/nRF2401A)
- [77] Silicon Laboratories C8051[Online]
<http://www.silabs.com/Support%20Documents/TechnicalDocs/C8051F320-Short.pdf>
- [78] Atmel EVK1101 Development Board [Online]
<http://www.atmel.com/tools/evk1101.aspx>
- [79] Atmel AVR32 UC3A3 Series Microcontrollers [Online]
<http://www.atmel.com/devices/AT32UC3A3256.aspx>
- [80] Serial Peripheral Interface Bus [Online]
https://en.wikipedia.org/wiki/Serial_Peripheral_Interface_Bus

- 
- [81] I²C [Online] <https://en.wikipedia.org/wiki/I%C2%B2C>
- [82] Atmel Software Framework [Online]
<http://www.atmel.com/tools/avrsoftwareframework.aspx?tab=documents>
- [83] Secure Digital Input/Output Specification [Online]
https://www.sdcard.org/developers/overview/sdio/sdio_spec/Simplified_SD_IO_Card_Spec.pdf
- [84] Analog Devices ADXRS649 Gyroscope [Online]
<http://www.analog.com/en/mems-sensors/mems-gyroscopes/adxrs649/products/product.html>
- [85] Analog Devices AD7606 Analog-to-Digital Converter [Online]
<http://www.analog.com/en/mems-sensors/mems-gyroscopes/adxrs649/products/product.html>
- [86] Analog Devices ADXL377 3-Axis Analog Accelerometer [Online]
<http://www.analog.com/en/mems-sensors/mems-accelerometers/adxl377/products/product.html>
- [87] Invensense IMU-3000 3-Axis Gyroscope [Online]
<http://www.invensense.com/mems/gyro/imu3000.html>
- [88] Analog Devices ADXL345 3-Axis digital Accelerometer [Online]
<http://www.analog.com/en/mems-sensors/mems-inertial-sensors/adxl345/products/product.html>
- [89] Honeywell 3-Axis Digital Compass [Online]
http://www51.honeywell.com/aero/common/documents/myaerospacecatalog-documents/Defense_Brochures-documents/HMC5843.pdf
- [90] Direct Memory Access [Online]
https://en.wikipedia.org/wiki/Direct_memory_access
- [91] Clemens Satzger. Fusion of Six-Dimensional Sensor Data Using Physics Engines (Diplom - TU München) January 2010.

- [92] Silicon Labs USB eXpress Application Programmers Interface [Online] <http://www.silabs.com/products/mcu/Pages/USBXpress.aspx>
- [93] libusb-win32 USB Library [Online] <http://sourceforge.net/apps/trac/libusb-win32/wiki>
- [94] Hirashima M. Induced acceleration analysis of three-dimensional multi-joint movements and its application to sports movements. In: *Theoretical Biomechanics*, V. Klika, ed. (InTech), pp. 303-318, 2011.
- [95] Hirashima M, Yamane K, Nakamura Y, and Ohtsuki T. Kinetic chain of overarm throwing in terms of joint rotations revealed by induced acceleration analysis. *Journal of Biomechanics*. 41 (13):2874-2883, 2008.
- [96] Hirashima M, Yamane K, Nakamura Y, and Ohtsuki T. Kinetic chain of overarm throwing in terms of joint rotations revealed by induced acceleration analysis. *Journal of Biomechanics*. 41 (13):2874-2883, 2008.
- [97] Lafortune AM, Cavanagh RP. The measurement of normal knee joint motion during walking using intracortical pins. In: Whittle M, Harris D, eds. *Biomechanical Measurements in Orthopaedic Practice*. Oxford, U.K.: Clarendon; 1985;234–243.
- [98] Effect of Pitch Type, Pitch Count, and Pitching Mechanics on Risk of Elbow and Shoulder Pain in Youth Baseball Pitchers. *The American Journal of Sports Medicine* 30 (4): 463-468, 200
- [99] The Filthiest Pitches in Baseball, Blake Murphy, Oct 17 2012, [Online] <http://www.beyondtheboxscore.com/2012/10/17/3514442/MLB-best-pitches-ranked-filthy-dickey-kershaw-darvish>
- [100] Werner SL, Murray TA, Hawkins RJ, et al. Relationships between throwing mechanics and shoulder distraction in professional baseball pitchers. In *American Journal of Sports Medicine*, 2001.
- [101] Fleisig GS, Kingsley DS, Loftice JW, et al. Kinetic comparison among the fastball, curveball, change-up, and slider in collegiate baseball pitchers. In *American Journal of Sports Medicine*, 2005.

- 
- [102] Berkson E., Aylward R., Zachazewski J., Paradiso J., Gill T.J. Imu arrays: The biomechanics of baseball pitching. In *The Orthopaedic Journal at Harvard Medical School*, Vol. 8, pages 90-94, June 2007.
- [103] Dillman CJ, Fleisig GS, Andrews JR. Biomechanics of pitching with emphasis upon shoulder kinematics. In *Journal of Orthopedic Sports Physical Therapy*, pages 402-408, Aug 1993.
- [104] Wearable Wireless Sensing for Sports and Ubiquitous Interactivity, Lapinski, M., Feldmeier, M. and Paradiso, J.A., in 2011 IEEE SENSORS Conference, 2011.
- [105] Dunn F., Parberry I., *3E Math Primer for Graphics and Game Development*. Worldware Publishing. 2002
- [106] Geen, John. Progress in Integrated Gyroscopes. IEEE PLANS 2004
- [107] The Kinetic Chain: Strength and Conditioning of the Baseball Athlete. UConn Health Center [Online]
http://uconnsportsmed.uchc.edu/injury/prevention/kinetic_chain.html
- [108] Biomechanics of the Shoulder in Youth Baseball Pitchers: Implications for the Development of Proximal Humeral Epiphysiolysis and Humeral Retrotorsion, M. B. Sabick; *American Journal of Sports Medicine* 33(11):1716-1722 (2005)
- [109] "Pitching Biomechanics as a Pitcher Approaches Muscular Fatigue During a Simulated Baseball Game", R. F. Escamilla; *The American Journal of Sports Medicine* 35(1):23-33 (2006)
- [110] Shoulder Muscle Recruitment Patterns and Related Biomechanics during Upper Extremity Sports", Rafael F. Escamilla; *Sports Medicine* 39(7):569-590 (2009)
- [111] Werner SL, Guido JA Jr, Stewart GW, McNeice RP, VanDyke T, Jones DG. Relationships between throwing mechanics and shoulder

distraction in collegiate baseball pitchers. J Shoulder Elbow Surg. 2007;16(1):37-42.

- [112] Arnel L. Aguinaldo and Henry Chambers. Correlation of Throwing Mechanics With Elbow Valgus Load in Adult Baseball Pitchers. Am J Sports Med 2009 37
- [113] Fleisig GS, Barrentine SW, Zheng N, Escamilla RF, Andrews JR. Kinematic and kinetic comparison of baseball pitching among various levels of development. J Biomech. 1999;32:1371-1375.
- [114] Fleisig GS, Kingsley, DS, Loftice, JW, Dinnen, KP, Andrews JR. et al. Kinetic Comparison Among the Fastball, Curveball, Change-up, and Slider in Collegiate Baseball Pitchers Am J Sports Med. 2006 Mar;34(3):423-30.
- [115] Sensemble: A Wireless, Compact, Multi-User Sensor System for Interactive Dance, Ryan Aylward, and Joseph A. Paradiso, in Proc. of NIME 2006, The 2006 International Conference on New Interfaces for Musical Expression, Paris, France, June 4-8, 2006, pp. 134-139.
- [116] Seinfeld Episode #104: “The Doorman” [Online] https://en.wikipedia.org/wiki/The_Doorman

